

OBSERVATIONS OF INTERACTION BETWEEN THE INTERNAL WAVEFIELD
AND LOW FREQUENCY FLOWS IN THE NORTH ATLANTIC

by

BARRY RAYMOND RUDDICK
B.Sc., University of Victoria
1971

SUBMITTED IN PARTIAL FULFILLMENT
OF THE REQUIREMENTS FOR THE
DEGREE OF DOCTOR OF
PHILOSOPHY

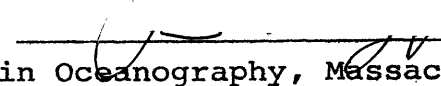
at the

MASSACHUSETTS INSTITUTE OF TECHNOLOGY

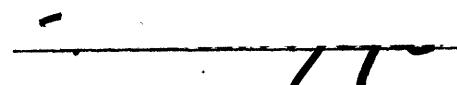
and the

WOODS HOLE OCEANOGRAPHIC INSTITUTION
April, 1977

Signature of Author

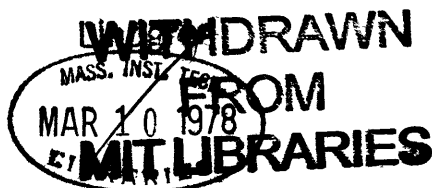

Joint Program in Oceanography, Massachusetts Institute
of Technology-Woods Hole Oceanographic Institution, and
Department of Earth and Planetary Sciences, Massachusetts
Institute of Technology, April, 1977, *Dept. of Meteorology.*

Certified by

 Thesis Supervisor

Accepted by

Chairman, Joint Oceanography Committee in Earth
Sciences, Massachusetts Institute of Technology-
Woods Hole Oceanographic Institution.





Room 14-0551
77 Massachusetts Avenue
Cambridge, MA 02139
Ph: 617.253.5668 Fax: 617.253.1690
Email: docs@mit.edu
<http://libraries.mit.edu/docs>

DISCLAIMER OF QUALITY

Due to the condition of the original material, there are unavoidable flaws in this reproduction. We have made every effort possible to provide you with the best copy available. If you are dissatisfied with this product and find it unusable, please contact Document Services as soon as possible.

Thank you.

Due to the poor quality of the original document, there is some spotting or background shading in this document.

2

OBSERVATIONS OF INTERACTION BETWEEN THE INTERNAL WAVEFIELD
AND LOW FREQUENCY FLOWS IN THE NORTH ATLANTIC

by

Barry Raymond Ruddick

Submitted to the Massachusetts Institute of Technology -
Woods Hole Oceanographic Institution Joint Program in
Oceanography on April 11, 1977 in partial fulfillment of
the requirements for the degree of Doctor of Philosophy.

Abstract

A total of four moorings from POLYMODE Array I and II were analyzed in an investigation of internal wavefield-mean flow interactions. In particular, evidence for wave-mean flow interaction was sought by searching for time correlations between the wavefield vertically-acting Reynolds stress (estimated using the temperature and velocity records), and the mean shear. No significant stress-shear correlations were found at the less energetic moorings, ($\bar{u} \lesssim 10 \text{ cm s}^{-1}$), indicating that the magnitude of the eddy viscosity was under $200 \text{ cm}^2/\text{sec}$, with the sign of the energy transfer uncertain. This is considerably below the $0(4500 \text{ cm}^2/\text{sec})$ predicted by Müller (1976). An extensive error analysis indicates that the large wave stress predicted by the theory should have been clearly observable under the conditions of measurement.

Theoretical computations indicate that the wavefield "basic state" may not be independent of the mean flow as assumed by Müller, but can actually be modified by large-scale vertical shear and still remain in equilibrium. In that case, the wavefield does not exchange momentum with a large-scale vertical shear flow, and, excepting critical layer effects, a small vertical eddy viscosity is to be expected. Using the Garrett-Munk (1975) model internal wave spectrum, estimates were made of the maximum momentum flux (stress) expected to be lost to critical layer absorption. Stress was found to increase almost linearly with the velocity difference across the shear zone, corresponding to a vertical eddy viscosity of $-100 \text{ cm}^2 \text{ s}^{-1}$. Stresses indicative of this effect were not observed in the data.

Abstract (Contd.)

The only significantly non-zero stress correlations were found at the more energetic moorings ($\bar{u} \sim 25 \text{ cm s}^{-1}$). Associated with the 600 m mean velocity and the shear at the thermocline were a positively correlated stress at 600 m, and a negatively correlated stress at 1000 m. These stress correlations were most clearly observable in the frequency range corresponding to 1-8 hour wave periods. The internal wavefield kinetic and potential energy modulated with the mean flow at both levels, increasing by a factor of two with a factor of ten in the mean flow. The observed stress correlations and energy level changes were found to be inconsistent with ideas of a strictly local eddy viscosity, in which the spectrum of waves is only slightly modified by the shear. When Doppler effects in the temperature equation used to estimate vertical velocity were considered, the observations of stress and energy changes were found to be consistent with generation of short (40 - 300 m) internal waves at the level of maximum shear, about 800 m. The intensity of the generated waves increases with the shear, resulting in an effective vertical eddy viscosity (based on the main thermocline shear) of about $+100 \text{ cm}^2 \text{ s}^{-1}$. The stresses were not observable at the 1500 m level, indicating that the waves were absorbed within 500 m of vertical travel.

The tendency for internal wave currents to be horizontally anisotropic in the presence of a mean current was investigated. Using the Garrett-Munk (1975) model internal wave spectrum, it was found that critical layer absorption cannot induce anisotropies as large as observed. A mechanical noise problem was found to be the cause of large anisotropies measured with Geodyne 850 current meters. It could not be decided, however, whether or not the A.M.F. Vector Averaging Current Meter is able to satisfactorily remove the noise with its averaging scheme.

Thesis Supervisor: Terry Joyce

Title: Assistant Scientist

4

ACKNOWLEDGEMENTS

I would like to thank most of all, Dr. Terry Joyce, of the Woods Hole Oceanographic Institution, for gently guiding me into a fruitful research area which closely matched my interests, for many invaluable discussions and criticisms about my work, and for his supreme efforts in reading my often boring early drafts.

I thank Dr. Melbourne Briscoe for many long and interesting discussions about internal waves in general, and the Garrett-Munk spectrum in particular. Dr. Glenn Flierl and Dr. Peter Rhines were most helpful and encouraging in their comments, and I am very grateful for their help.

I thank Dr. Claude Frankignoul for allowing reproduction of several of his figures, and for his friendly interest and helpful comments.

I thank Dr. Peter Müller for his advice and encouraging comments regarding my theoretical ideas. Without his theoretical study as a guide, my ideas about the internal wave field would be much less clear.

I thank Nancy Bauchmann for several rush computations, Mary Raymer for doing much of the drafting, and David Porter for painstakingly proof-reading the largest chapter of the manuscript.

Bob Frazel did almost all of the photographic work, with a professional touch, and superhuman speed. I will always be grateful. For her exceptionally accurate and fast typing, and especially for her amazing efforts toward the end, I warmly thank Doris Haight. Without her help I would never have finished on time.

Above all others, I wish to thank my darling wife, Lorraine, for her help in drafting, typing, and organizing the thesis, and for her patient support of me as a student for these many years. I owe her a debt of gratitude I can never repay; I hope I never stop trying.

I thank Dr. William Schmitz for allowing the data to be analyzed in a way for which it was never intended, and allowing me to use some of his reduced data.

The research reported here, and much of my support as a graduate student, was provided by Office of Naval Research Contract Number N00014-76-C-0197 NR 083-400.

Table of Contents (Contd.)Page No.

Chapter 5.	On the Theory of Internal Wave - Mean Flow Interactions	137
5.1	Introduction	
5.2	The Radiation Balance Equation	
5.3	A Brief Review of the Müller Theory (My View!).	
5.4	Simplified Source Terms	
5.5	Simplified Radiation Balance Equation. - solution and investigation of properties	
5.6	Comparison with Müller Theory	
5.7	Momentum Flux Losses to Critical Layer Absorption.	
5.8	Summary.	
Chapter 6.	Internal Wavefield Current Anisotropy in the Presence of a Low Frequency Flow	188
6.1	Introduction	
6.2	Critical Level Wave Absorption Anisotropy Model.	
6.3	Evaluation of the Integrals	
6.4	Effects of Current Meter Sensor Noise.	
6.5	Summary.	
Chapter 7.	Conclusions	230
Appendix A.	Error Analysis	240
Appendix B.	Interpretive Model for Wavefield	306
Appendix C.	The Relationship Between Action, Momentum and Buoyancy Fluxes	317
References		
Biographical Note.		

Table of Contents

	<u>Page No.</u>
Abstract	2
Acknowledgements	4
List of Figures.	8
Notation	19
Chapter 1. Introduction	21
Chapter 2. Data Analysis	31
2.1 Introduction	
2.2 Decomposition into "Wave" and "Mean" Series	
2.3 The Fourier Transform Procedure	
2.4 Summary of Error Analysis	
2.5 Low-Pass Filter	
Chapter 3. Homogeneity and Isotropy	47
3.1 Low-Frequency Flow	
3.2 Internal Wavefield	
3.3 Rays or Modes?	
Chapter 4. Wavefield-Mean Flow Correlations	60
4.1 Introduction	
4.2 Momentum and Buoyancy Fluxes in Geostrophic Flow	
4.3 Correlations of Wave-induced Reynolds Stress with Mean Flow	
a) Vertical Eddy Viscosity.	
b) Total Band Eddy Viscosity and Horizontal Eddy Diffusivity	
c) Cross-viscosity	
d) Further Investigations of the Momentum Fluxes at the Energetic Moorings.	
4.4 Energy Correlations	
4.5 Summary	

List of Figures

		<u>Page No.</u>
Figure 2.1	Sketch of the Hanning data window and 50% overlap configuration used in the Fourier transform procedure	
Figure 2.2	Coherence between East mean velocity at 600 m and East continuum band stress at 600 m (dashed line) and 1000 m (solid line)	
Figure 2.3	Autospectra of 600 m East mean velocity, shear (600 - 1000 m), continuum band stress at 600 m and 1000 m, from before (solid lines) and after (dashed lines) low-pass filtering	
Figure 3.1	Locations of moorings analyzed	
Figure 3.2	Ellipse parameters for velocity and cross-thermocline shear, and also record average velocity vectors, for moorings 543, 545, 566	
Figure 3.3	Total internal wave kinetic energy from the 1500 m level in the Array II area	
Figure 3.4	Time series of phase between u_1 and u_3 (estimated from temperature) for the continuum band on 566 at 600 m	
Figure 3.5	Coherence between u_1 and u_3 for the continuum band on 566 at 600 m	

List of Figures (Contd.)

		Page <u>No.</u>
Figure 4.1	Time series of $ \text{speed} ^2$ at 600 m and $ \text{shear} ^2$ from the difference of velocities at levels 1 and 3 for moorings 566 (dashed line) and 543 (solid line).	
Figure 4.2	Time series of Horizontal Kinetic Energy, Vertical Kinetic Energy and vertically acting Reynolds stress squared estimated for the continuum band (0.1 - 2 cph) at moorings 566 (dashed line) and 543 (solid line).	
Figure 4.3	Integrands of eq. 4.36 and 4.37 which contribute to actual stress (solid line) and effective stress (dashed line) plotted against frequency.	
Figure 4.4	Low-frequency MODE-region shear profile from Sanford (1975), computed first baroclinic mode, and locations of current meters on moorings analyzed.	
Figure 4.5	Eddy viscosity regression (dots) for mooring 543, 1000 m. The regression line corresponding to Müller's (1976) eddy viscosity estimate is shown for comparison. The maximum stress the wavefield could exert is shown by crosses.	

List of Figures (Contd.)

	<u>Page No.</u>
Figure 4.6 Vertical eddy viscosity regression for continuum band at mooring 566, 1000 m
Figure 4.7 "Cross-viscosity" correlation. Total band North - u_3 Reynolds stress vs. East shear for mooring 545
Figure 4.8 Scatterplots and regressions for con- tinuum band stress at 600 m (upper) and 1000 m (lower) vs. 600 m East velocity
Figure 4.9 Low-pass filtered time series of East shear, East velocity, 600 m, and stresses at 600 m and 1000 m for the continuum band, mooring 566. Corre- lations between pairs of series are shown at right
Figure 4.10 Correlation coefficient of $C_{13}(\omega)$ vs. \bar{u}_{600} for the East direction, mooring 566. Constant width (5 harmonics) frequency bands have been used for the estimates
Figure 4.11 Contribution by frequency to the 600 m stress which is correlated with the 600 m East mean velocity

List of Figures (Contd.)

	<u>Page No.</u>
Figure 4.12 Continuum band stress, 600 m and 1000 m and velocity at 600 m, all 566, East direction. Correlation coefficients for each third of the record are displayed	
Figure 4.13 Time series of momentum flux magnitude squared at 1 km, inertial band, mean speed squared at 500 m, mean shear squared, and horizontal kinetic energy (x2) from the total band, 1000 m, all at mooring 543	
Figure 4.14 Timeseries of mean shear squared, mean speed squared, momentum flux magnitude squared, continuum band at 600 m, and twice the horizontal kinetic energy, continuum band, at 600 m, for mooring 566	
Figure 4.15 HKE and Temperature spectrum from data #5661, computed from two times piece 1 ($\bar{u}_{rms} \approx 25 \text{ cm s}^{-1}$) and piece 2 ($\bar{u}_{rms} \approx 6 \text{ cm s}^{-1}$).	
Figure 4.16 HKE and Temperature spectrum from data #5663. Pieces and times as in figure 4.15	
Figure 4.17 Division of total energy density in the Garrett-Munk (1972, 1975) model internal wave spectrum	

List of Figures (Contd.)

	<u>Page No.</u>
Figure 4.18 Horizontal kinetic energy from mooring 566 at 1 km depth. Inertial band (dashed line) and continuum band (solid line)	
Figure 5.1 Sketch of a typical characteristic for the vertical terms of the Liouville operator, for $\bar{u} = 0$ (solid line) and for finite \bar{u} (dashed line)	
Figure 5.2 Characteristics for waves which encounter a critical level. The waves are coming from the critical layer for $k_3 > 0$, and propagating to the critical layer for $k_3 < 0$. Solid line for $\bar{u} = 0$; dashed line for finite \bar{u}	
Figure 5.3 Frequency behavior of the estimate of momentum flux loss, equation 5.65	
Figure 5.4 Momentum flux lost to critical layer absorption, estimated from GM 75 ⁺ model spectrum	
Figure 6.1 Integration region in (α, ϕ) space for the spectra (6.3) in the presence of mean flow	
Figure 6.2 Anisotropy factor for the GM75 wave model, for $u_M = 1.5 \bar{u}(z)$, $j_* = 6$	

List of Figures (Contd.)

		<u>Page No.</u>
Figure 6.3	G(x), the function involved in the estimate of $P_{11} + P_{22}$ for GM 75 ⁺ . Shown are the small x approximation (solid line), the large x approximation (dashed line), and several numerical estimates (+)	
Figure 6.4	A plot of H(x), involved in the $P_{11} - P_{22}$ integral for GM 75 ⁺	
Figure 6.5	Speed in mm s ⁻¹ and direction in degrees, clockwise from North, from data 5761 (38°30'N., 54°55'W., 4000 m deep) for the month of February, 1976	
Figure 6.6	Power spectra for the East and North velocities at mooring 576 for the month of February, 1976. (50% overlapped Hann, 37 pieces of 36 hours length)	
Figure 6.7	Power spectrum for the North velocity from data 5761 for the period 76-08-25 to 76-09-18, when the mean velocity was less than 5 cm s ⁻¹	
Figure 6.8	Sketch of the geometry for the current meter noise model	

List of Figures (Contd.)

	<u>Page No.</u>
Figure 6.9 Variance of vane angle relative to current meter computed for each 12- sample record, and plotted against the average rotor speed	
Figure 6.10 As figure 6.9, except for compass card angle relative to the current meter	
Figure 6.11 As figure 6.9, for current bearing	
Figure 6.12 As figure 6.9, for rotor speed estimate. .	
Figure 6.13 Anisotropy factor (defined in text) computed by Frankignoul (1974) for data 2204, 2205, 3102 and 3103, taken at Site D using Geodyne 850 current meters. Dashed line is anisotropy factor estimated from the effects of critical layer absorption on the GM76 spectrum. Solid line is the anisotropy factor from the noise model described in section 6.4	
Figure 6.14 Anisotropy factor computed for para- meters shown in table 6.1 (appropriate to the data in figure 6.9). Solid line: $\delta S = .035$, $\delta \theta = 5^\circ$ Dashed line: $\delta S = .05$, $\delta \theta = 7.5^\circ$	

List of Figures (Contd.)Page
No.

- Figure 6.15 Time series of $\bar{u}_2^2 - \bar{u}_1^2$ ($u_2 \equiv v$) averaged over data numbers 4091, 4101 and 4121; wavefield anisotropy relative to a fixed reference frame computed by Frankignoul (1974), and estimated mean flow dilatation

$$\left(\frac{\partial \bar{u}_2}{\partial x_2} - \frac{\partial \bar{u}_1}{\partial x_1} \right) \quad . \quad . \quad . \quad . \quad . \quad . \quad . \quad . \quad . \quad .$$
- Figure 6.16 Power spectra of the East and North velocities from record 5791 taken with a VACM. The coordinate system has been rotated so that the mean velocity was Eastward
- Figure 6.17 Measured anisotropy factor from record 5661. Frequency limits and other parameters are listed in table 6.1. Dashed line is the anisotropy computed from the critical layer absorption model with GM76 dependence (section 5.3). Solid line is the computed anisotropy factor from the current meter noise model (section 5.4), with $\delta S = .011$, $\delta \theta = 1.8^\circ$.
- Figure 7.1 Sketch of a "cats-eye" billow resulting from shear instability. Waves will be radiated when the outer boundary of the closed circulation region extends up into the area where the intrinsic frequency is larger than f

List of Figures (Contd.)

	<u>Page</u> <u>No.</u>
Figure A.1 Sketch of a temperature, density and current shear finestructure step, the measured temperature and velocity signals, and the vertical velocity inferred from temperature	
Figure A.2 Spectrum of velocity difference over 2 m from mooring 551 at 2000 m depth. The ω^{-1} power law used in the estimate of current finestructure contamination is indicated	
Figure A.3 Dots: scatterplot of 2-point estimated vertical temperature gradient vs. central temperature for data in Table A.1. The labelled lines are the temperature gradient relations used in computing $\frac{\partial \bar{T}}{\partial x_3}(\bar{T})$, with the observed temperature excursions indicated by the extent of the line. 600 m relation (10°C - 16°C) shows excursion observed at 566. The 543 and 545 temperature gradient relations were estimated from CTD station numbers Chain 116 #20 (543) and Chain 116 #23 (545).	
Figure A.4 Ratio of rms pressure amplitude divided by rms temperature amplitude, normalized by temperature gradient, vs. frequency for data numbers 5433, 5663. This is an indication of the degree of mooring motion contamination	

List of Figures (Contd.)

	Page <u>No.</u>
Figure A.13 Estimated error spectrum (eq. A.29) vs. harmonic number $n = \frac{\omega}{f}$, for several values of A, where A is the fraction of stalled records
Figure A.14 Estimated error spectrum (A.38) for several values of \bar{A} (defined in text)
Figure A.15 Estimated error spectrum (A.41) for several values of \bar{A}
Figure A.16 Estimated error spectra (A.38 and A.41) superposed on the HKE spectrum for data 5433, with $\bar{A} = 14.6\%$, as observed
Figure A.17 Listing of the subroutine used to compute the confidence intervals of the regression slopes

Notation

\underline{x}	=	(x_1, x_2, x_3)	position
\underline{u}	=	(u_1, u_2, u_3)	velocity
ξ	=	semi-Lagrangian particle position	

$$\frac{\partial \xi}{\partial t} + \underline{u} \cdot \nabla \xi = \underline{u}'; \quad \bar{\xi} = 0$$

$$\epsilon_{ijk} = \begin{cases} +1 & \text{if } i, j, k \text{ is an even cyclic permutation} \\ & \text{of } 1, 2, 3 \\ -1 & \text{if } i, j, k \text{ is an odd cyclic permutation} \\ & \text{of } 1, 2, 3 \\ 0 & \text{otherwise.} \end{cases}$$

c.c.; () * complex conjugate

Ω = functional form of disp. relation

$$= \left(\frac{(k_1^2 + k_2^2) N(z)^2 + k_3^2 f^2}{k_1^2 + k_2^2 + k_3^2} \right)^{1/2} + \underline{k} \cdot \bar{\underline{u}}$$

$$= \Omega_0 + \underline{k} \cdot \bar{\underline{u}}$$

Ω_0 = intrinsic frequency

\underline{V} = $\frac{\partial \Omega}{\partial \underline{k}}$ group velocity

\underline{k} = (k_1, k_2, k_3) = wave vector

s = sign (k_3)

β = $|k_3|$

α = $(k_1^2 + k_2^2)^{1/2}$

$\frac{d}{dt}$ = $\frac{\partial}{\partial t} + \underline{V} \cdot \nabla$ differentiation following group velocity

$$\frac{D}{Dt} = \frac{\partial}{\partial t} + \bar{\mathbf{u}} \cdot \nabla \quad \text{differentiation in an advected frame}$$

= source terms in RBE

= Liouville operator in RBE

F_{ij} wave-induced momentum flux

M_j wave-induced buoyancy flux

$$T_{\alpha j} = F_{\alpha j} - \frac{f}{N^2} \epsilon_{\alpha\beta 3} M_\beta$$

= effective wave momentum flux

$$Q_{\alpha j} = \int d^3k \, k_\alpha \, \eta V_j$$

(Related to $T_{\alpha j}$ - see Appendix C)

Handy Relations

$$\frac{\beta^2}{\alpha^2} = \frac{N^2 - \omega_o^2}{\omega_o^2 - f^2}$$

$$\frac{\beta^2}{\alpha^2 + \beta^2} = \frac{N^2 - \omega_o^2}{N^2 - f^2}$$

$$\frac{\alpha^2}{\alpha^2 + \beta^2} = \frac{\omega_o^2 - f^2}{N^2 - f^2}$$

$$V_{1,2} = \frac{\omega_o^2 - f^2}{\omega_o} \frac{N^2 - \omega_o^2}{\omega_o^2 - f^2} \frac{k_{1,2}}{\alpha^2 + \beta^2}$$

$$V_3 = - \frac{N^2 - \omega_o^2}{N^2 - f^2} \frac{\omega_o^2 - f^2}{\omega_o} \frac{1}{k_3}$$

Chapter 1

INTRODUCTION

Natural internal waves have been observed in water for some time now (cf. Murray, 1892), and even longer in the atmosphere. However, it has only been in recent years that observations have been much more than that; simply observations. Present day internal wave measurements can be interpreted in a common framework, the ω - k oceanic spectral model of Garrett and Munk (1972), now called GM72. (Two updated versions are Garrett and Munk, 1975, called GM75, and GM76, described in Desaubies, 1977, and Cairns and Williams, 1976.) These models bridge the gap between theory and observation, enabling the prospective experimenter to ask in advance of a particular experiment, "Am I likely to see anything that gives new information?" and get an answer. The knowledge of the kinds of information that were missing has prompted the development of many new types of measurement of the internal wavefield (cf. Briscoe, 1975).

The major and surprising result of most of the observations is that the internal wave spectrum appears to be universal to a high degree; no matter where one looks, he will tend to see the same spectral shape and level. Wunsch (1975a) has concluded that the mechanisms which maintain the universal spectrum must be very strong, forcing the spectrum to the prescribed shape within about 10 km horizontally, or 1 km vertically. Recent experiments, reviewed in the "GM"

references above, have tightened up knowledge of the frequency and wavenumber shape of the universal spectrum to a high degree, and allowed inferences to be made about the cause and nature of the mechanisms which shape the spectrum (McComas and Bretherton, 1977).

While major inroads are beginning to be made regarding the internal shaping processes of the spectrum, Wunsch (1975b) has pointed out that there are major gaps in the knowledge of the relative importance of various possible sources and sinks for internal wave energy. One potentially important source (or sink) of energy is interaction with the (usually) larger scale, low-frequency flow, which tends to be more energetic than the internal wavefield, and so at least has a lot of energy to give to the wavefield. Whether the low-frequency flow gives or takes energy on the average, and how rapidly, are the primary questions asked in this work.

Most theoretical studies of propagation of internal waves in the presence of a mean shear current (cf. Garrett, 1968) indicate that an internal wave can propagate through a shear flow with no net exchange of momentum, unless the wave is dissipated. (Considering energy clouds the issue somewhat, cf. Bretherton, 1969b.) At a critical level (references in table 5.1) the wave is slowed down indefinitely, and fails to propagate through the critical level. Presumably, although it has not been demonstrated in the ocean or laboratory, the wave momentum appears in the mean flow. A scenario in which

internal waves are generated at the bottom boundary of the atmosphere by the mean flow over topography, propagate upward and are absorbed at critical levels, is described by Bretherton (1969b). The net effect is a distribution of the drag of the topography over a much greater depth than would be observed without internal waves. A very similar computation for the ocean has been performed by Bell (1975), who estimates that a wave momentum flux of about 0.5 dyne cm^{-2} is generated by a 5 cm s^{-1} bottom current. From considerations of wave energy, Bell estimates that the lee waves induce a vertical mixing coefficient of roughly $10 \text{ cm}^2 \text{ s}^{-1}$. The height to which the waves travel before they give up their momentum to the mean flow is the determining factor for the effective vertical eddy viscosity which the waves induce in this near-bottom region. For a distance of 1 km, the effective vertical eddy viscosity is $10^4 \text{ cm}^2 \text{ s}^{-1}$, a very large value, although the mechanism is limited to the lower kilometer or so of the ocean, where the shear is typically quite weak.

Müller (1974, 1976, 1977) has studied the interaction of a field of internal gravity waves with a large scale mean flow. Using the concept of an equilibrium spectral shape (with that of Garrett and Munk in mind), Müller investigates a balance between the tendency of the mean shear flow to distort the spectrum and the internal relaxation tendencies of the wave-field, which tend to restore the equilibrium shape. Assuming that this equilibrium shape is independent of the mean flow,

Müller finds that the balance of tendencies (distortion and relaxation) lead to asymmetries in the wavefield such that the field exerts a stress which opposes the mean shear. The interaction may, in a local limit, be parameterized by eddy viscosities, both horizontal ($0(10^5)\text{cm}^2\text{ s}^{-1}$) and vertical ($0(10^3)\text{cm}^2\text{ s}^{-1}$). Because of the large aspect ratio of the mean flow, the vertical eddy viscosity is more important than the horizontal to the energy balance of the wavefield.

Observations of internal wave-mean flow interaction are somewhat sparse. Frankignoul (1974, 1976) discovered in internal wave records a tendency for the wave velocities to be more intense in a direction perpendicular to a strong mean current than parallel to it. He tentatively identified critical layer wave absorption as a possible cause for this effect. He also found that the horizontal anisotropy of the currents was related to the large scale mean shears, in a manner consistent with some of the predictions of the Müller theory. However, Frankignoul was only able to verify that horizontal variations in the medium (i.e., the shear flow) will distort the wavefield; this is a propagation effect. Direct estimation of the horizontal eddy viscosity effects predicted by Müller proved impossible with the data at hand, because of the relatively short data length and the high statistical noise level of the horizontally-acting wave stress. Frankignoul found that the internal wavefield energy level and the magnitude squared of the mean vertical shear were

correlated, suggesting an energy exchange; however, the hypothesized energy exchange mechanism (vertical eddy viscosity) was inferred and not directly observed.

Sabinin (1976) has observed packets of high-frequency internal waves which appear to have been generated at the base of a mixed layer by a mean shear which was periodically intensified by inertial oscillations. This is probably the most direct observation of internal wave-mean flow interaction to date, in the sense that exchange of momentum and energy was observed. Perkins (1976) has attributed an observed splitting of the inertial peak in a current spectrum to changes in the effective inertial frequency caused by the vertical component of vorticity associated with an eddy which was observed to have drifted through the observation site. The change in the internal wave passband frequency due to mean shears was predicted theoretically by Magaard (1968), Mooers (1975a,b) and Smith (1973). However, this is just another propagation effect, and actual energy or momentum exchanges were not observed. Holton and Lindzen (reviewed in Lindzen, 1973) were able to use the (theoretical) momentum exchange properties of equatorial internal waves to explain the quasi-biennial cycle of zonal mean winds in the tropical upper atmosphere, in which an alternating (with height) pattern of zonal winds moves slowly downward. It should be mentioned, however, that actual absorption of the momentum of dissipated internal waves by the mean flow has yet to be demonstrated in the laboratory or in situ.

The central point of the observations presented here is a direct test of the vertical eddy viscosity aspect of the (hypothesized) interaction. Using current and temperature data from long-term Polymode Array I and II moorings in the North Atlantic, estimates of wavefield vertically-acting Reynolds stresses and low-frequency vertical shear (often referred to as "mean" because it appears so to the wavefield) were estimated as slowly-varying time series. Statistical correlation analyses were performed to see if the wavefield has any tendency to exert stresses which oppose or reinforce the mean shear, thereby extracting energy from (or giving it up to) the shear. To the extent that Reynolds stresses are accurately estimable using temperature records, the observations of momentum exchange with the shear flow are direct; only energy exchanges are inferred.

Unfortunately, the vertically-acting wave Reynolds stresses cannot be measured directly, since the vertical component of velocity is not measured at current meter moorings. Inferring the internal wave vertical velocity from temperature involves assumptions about the effects of neglected terms in the heat equation used for the estimate. These are discussed in Appendix A.2. A major effect is the advection of temperature by the mean flow, a Doppler effect. If the wave spectrum is not greatly altered from the GM76 spectral form, the Doppler effect is shown in A.2 to be small, inducing only about 10% error into the stress estimates. However, in the introduction

to chapter 4, it is seen that the observed stress of a single wave can be greatly altered from its actual value if the phase speed of the wave, c , is of the order of the advection velocity, even changing in sign accordingly as $\bar{u} \gtrless c$. Most of the waves in the GM76 spectrum have phase speeds greater than 30 cm s^{-1} , and so are relatively unaffected by Doppler effects. However, if the majority of the waves involved in momentum transfer (stress) are relatively short, slow waves the observed stresses can be drastically altered. Accordingly, we propose in chapter 4.1 to interpret the observations in the framework of three simplifying hypotheses; they do not afford a unique interpretation of the observations, but they seem to be the simplest hypotheses which are at all consistent with the observations. They are:

- (1) a local, eddy viscosity type of interaction, in which the wave spectrum is not greatly altered from the GM form, and so Doppler effects are negligible;
- (2) critical layer absorption, involving waves with phase speed of order \bar{u} , and in which case Doppler effects must be accounted for;
- (3) generation of internal waves by the mean shear. These waves will also have phase speeds of order \bar{u} , and so Doppler effects must be considered.

In 4.2, the effect of rotation on the concept of wave momentum flux is discussed, and it is argued that the best estimate of that part of the wave stress which has an effect on the mean flow is obtained by eliminating waves whose

frequency are below twice the inertial frequency from the stress estimates.

Chapter 4.3 contains the main observational work of the thesis. In sections a, b and c, the stress observations are compared with the mean shear in the "eddy viscosity" sense of Hypothesis 1 above. Section (a) describes the estimate of the "effective" eddy viscosity, using the stress estimates described in 4.2. Sections (b) and (c) describe other eddy viscosity estimates, primarily included for completeness. A more general study of the wave momentum fluxes is undertaken in section 4.3-d, without assuming Hypothesis 1. The results are compared to the three hypotheses as the various characteristics of the observed wave stresses are presented. The next section, 4.4, investigates the changes in internal wave energies which occur in concert with the mean flow energy level. Again, the three hypotheses above are compared with the findings. The chapter is summarized in 4.5, and the characteristics of the observed stresses and energy level changes are compared with the hypotheses in table form.

A major finding in chapter 4 is that the wavefield-mean flow interaction must be much weaker than estimated by Müller (1976). In chapter 5, a much-simplified version of the interaction theory is presented. In section 5.2, the radiation balance equation is introduced; in 5.3 a few central points about the Müller theory are discussed, and in 5.4 some simplifications to the full radiation balance equation due to

McComas and Bretherton (1977) are introduced. In 5.5 a very much simplified problem is addressed; that of a wavefield in a steady vertical shear flow. Several points are raised about the solution, the main one being the almost total lack of momentum exchange with the shear flow. This is in contrast to the strong interaction predicted by Müller, and in 5.6 a few opinions on the reason for the difference in interaction strength are given. The only momentum exchange predicted to occur is due to the effects of critical layer absorption, which we discuss in 5.7.

The horizontal anisotropy of internal wave currents is discussed in chapter 6. This is an indirect measure of wavefield interaction, and so is thought to be somewhat less important than the stress and energy level observations. The possibility of anisotropy being caused by critical layer absorption is investigated, and a large part of the chapter is devoted to study of an instrumental noise problem capable of causing the observed anisotropies. No firm conclusions can be drawn, except that the noise problem considered can cause anisotropy of the sign and magnitude observed by Frankignoul (1974, 1976), and thus could be a major contaminant to internal wave measurements.

The early chapters involve preliminaries of a sort. In chapter 2 the initial decomposition of the data and estimation of the stresses is discussed, and a brief summary of Appendix A, which describes error estimates and statistical uncertainties,

is given. In chapter 3, the homogeneity and isotropy of the wave and low-frequency fields in the Western North Atlantic is briefly investigated.

Chapter 2

DATA ANALYSIS

2.1 Introduction

The central theme of this study is the monitoring of time variations of the internal wavefield on timescales associated with the mean (low-frequency) flow. The most efficient way of doing this is to Fast-Fourier Transform short segments of data, then compute and store estimates of auto- and cross-spectra of the velocity components u_1 , u_2 , and u_3 (estimated from temperature) for later comparison with the mean flow. Retaining the spectra in this manner allowed for maximum flexibility in later processing

This method was initially used by McWilliams (1972), and then by Frankignoul and Strait (1972) in investigating energy correspondences within the internal wavefield. While the method is a physically sensible procedure (the spectra are simply related to the stresses exerted by the wavefield), all information about the phase of a wave relative to a fixed time origin is lost. Hence studies of small frequency or phase modulations of waves at inertial (Perkins, 1976) or tidal frequencies (Hendry, 1975) cannot be made with the method used here.

2.2 Decomposition into "Wave" and "Mean" Series

Oceanic energy spectra typically show a peak near the inertial frequency and one at a relatively low frequency,

with a relative gap at intermediate frequencies (Rhines, 1973). The motions at frequencies higher than inertial but lower than the local buoyancy frequency are consistent with internal wave dynamics (Fofonoff, 1969). The low frequency motions are known to obey geostrophic first-order dynamics, and the higher-order dynamical balance is widely thought to be a vorticity balance (the MODE-I Dynamics Group, 1975). Since the dynamical processes of each flow field are so different, and simply because the gap is so distinct, it is natural to treat the two types of motion as separate and distinct. To this end the data were separated according to their frequency content, using the sub-inertial gap as a dividing line in frequency space.

The "mean" time series were obtained by two stages of averaging. A one-hour running mean of each series was first obtained at hourly intervals. This series was then filtered by a finite-width Gaussian filter (J. Maltais, documentation of program "TAPDIS," unpublished Woods Hole Oceanographic Institution report). The approximate amplitude gain of the low-pass filter is given by:

$$G = \exp - (4.5 f^2 T_{1/2}^2)$$

where

$$T_{1/2} = 24 \text{ hours}$$

$$f = \text{frequency in cph.}$$

The phase shift of the filter is zero.

53

From each original value of velocity and temperature, the "mean" value most nearly corresponding in time was subtracted, leaving two sets of series: one "mean" time series set, \bar{u}_1 , \bar{u}_2 , and \bar{T} , composed almost entirely of sub-inertial frequencies, and a set of "wave" time series, u_1' , u_2' , and T' , with almost no sub-inertial content.

2.3 The Fourier Transform Procedure

The "wave" series were broken into 75 hour pieces, with the beginning of each piece 37 hours[†] after the beginning of the preceding one (see fig. 2.1). The piece length, 75 h, was chosen to be close to three whole inertial periods for the "quiet" moorings, four for the energetic moorings, and six semidiurnal tidal periods for all moorings, to minimize spectral leakage from these energetic frequencies. The time series u_1' , u_2' , and T' were Fourier transformed under a Hanning (full cosine arch) data window, which was applied as a convolution filter in the frequency domain. A list of the Fourier transform definitions used is given in Table 2-1.

The data window used in the Fourier transform procedure combines acceptable frequency resolution (a half-power bandwidth of 0.02 cph) with a time resolution of about

[†]Increments of 37 hours rather than 37-1/2 hours were used because the mean velocities and temperatures were available at hourly intervals.

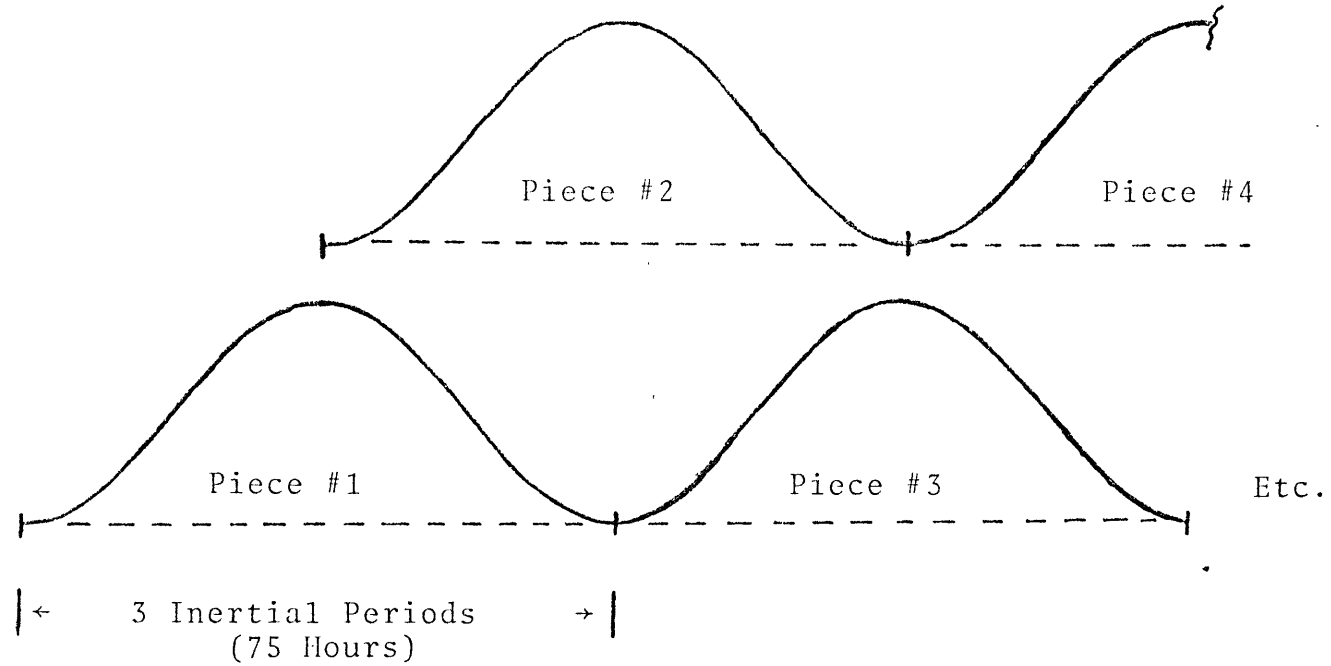


Figure 2.1 Sketch of the Hanning data window and 50% overlap configuration used in the Fourier transform procedure.

The digital Fourier transform of a real time series

$x_j = X(j\Delta t)$ for $0 \leq j \leq N-1$ is denoted by:

$$\hat{X}_k = \frac{1}{N} \sum_{j=0}^{N-1} w_j x_j \exp - i \left(\frac{2\pi j k}{N} \right)$$

The frequency of the k^{th} estimate is $f = \frac{k}{N\Delta t}$ cycles/time.

w_j is the data window, normalized so that $\sum_j w_j^2 = 1$. The

Hanning data window is equivalent to forming a windowed

\hat{X}_{kW} from

$$\hat{X}_{kW} = \left(-\frac{1}{4} \hat{X}_{k-1} + \frac{1}{2} \hat{X}_k - \frac{1}{4} \hat{X}_{k+1} \right) \sqrt{\frac{8}{3}}$$

Allowing $\langle \rangle$ to denote either piece or frequency averages, the spectral estimates are formed as: (* denotes the complex conjugate)

$$C_{xx} = \langle \hat{X}_k^* \hat{X}_k \rangle \quad \text{Power spectrum}$$

Letting y_j, \hat{Y}_k denote a second Fourier transform pair:

$$C_{xy} = \text{Re} \langle \hat{X}_k^* \hat{Y}_k \rangle \quad \text{Cospectrum}$$

$$Q_{xy} = \text{Im} \langle \hat{X}_k^* \hat{Y}_k \rangle \quad \text{Quadrature Spectrum}$$

$$\phi_{xy} = \tan^{-1} \frac{C_{xy}}{Q_{xy}} \quad \text{Phase}$$

$$K_{xy} = \sqrt{\frac{C_{xy}^2 + Q_{xy}^2}{C_{xx} C_{yy}}} \quad \text{Coherence magnitude}$$

Table 2.1. Fourier Transform Definitions

50 hours. The window has an asymptotic decay in the frequency domain rapid enough to prevent high frequency contamination due to the more energetic low frequencies. The net leakage of low-frequency variance into the spectral estimates was estimated to be less than 1%.

The vertical velocity was estimated from the temperature in the frequency domain, prior to summing over frequency, using:

$$\begin{aligned}
 C_{33} &= \left(\frac{\omega}{\Gamma}\right)^2 C_{TT} \\
 C_{13} &= + \frac{\omega}{\Gamma} Q_{1T} \\
 Q_{13} &= - \frac{\omega}{\Gamma} C_{1T} \\
 C_{23} &= + \frac{\omega}{\Gamma} Q_{2T} \\
 Q_{23} &= - \frac{\omega}{\Gamma} C_{2T}
 \end{aligned} \tag{2.2}$$

where:

Γ is the expected value of the mean temperature gradient, estimated as a function of time from the in situ mean temperature.

$\Gamma = +(c_1 + c_2 \bar{T})$, i.e., an exponential fit to the mean temperature profile;

ω = the frequency of the Fourier harmonic.

The assumptions and approximations leading to eq. 2.2 are discussed in Appendix A.

For each of the eighteen frequency bands shown in Table 2.2, the spectral estimates were summed over all Fourier harmonics falling within the band limits. This resulted in eighteen different estimates of the following nine "wave-field" cross-spectra, C_{ij} , Q_{ij} • ($Q_{11} = Q_{22} = Q_{33} = 0$). In addition the three "mean" values $\overline{u_1}$, $\overline{u_2}$, \overline{T} were taken from the time closest to the center of the piece.

This procedure was repeated for each piece (time origin moved along by 37 hours each step), and the resulting data were stored as $9 \times 18 + 3 = 165$ separate time series, each series associated with a unique identifier. This processing was repeated for several of the instruments on each mooring, each set resulting in 165 time series.

The quantities C_{13} , C_{23} , integrated over the continuum band (2f-N) and total band (f-N) will be identified as the continuum band and total band wave Reynolds stresses.

2.4 Summary of Error Analysis

A fairly complete discussion of potential sources of error in estimating the various computed quantities is given in Appendix A. A recounting of the major results follows here.

Vertical Velocity Errors

The vertical velocity was estimated in frequency space from the heat equation:

Band	Low Frequency	Center Frequency	High Frequency	No. Harmonics	$Q(F/\Delta F)$
1 Continuum	0.08667	1.04000	1.99333	143	0.5455
2 Inertial #1	0.03333	0.04000	0.04667	1	3.0000
3 Tidal	0.07333	0.08000	0.08667	1	6.0000
4 } Constant	0.08667	0.11333	0.14000	4	2.1250
5 } "Q"	0.14000	0.17333	0.20667	5	2.6000
6 } "Q"	0.20667	0.26000	0.31333	8	2.4375
7 } "Q"	0.31333	0.38667	0.46000	11	2.6364
8 } "Q"	0.46000	0.56667	0.67333	16	2.6563
9 } "Q"	0.67333	0.82667	0.98000	23	2.6957
10 } "Q"	0.98000	1.19333	1.40667	32	2.7969
11 } "Q"	1.38000	1.68667	1.99333	46	2.7500
12 } Constant	0.35333	0.38667	0.42000	5	5.8000
13 } Width	0.52667	0.56667	0.60667	6	7.0833
14 } Width	0.79333	0.83333	0.87333	6	10.4167
15 } Width	1.15333	1.18667	1.22000	5	17.8000
16 } Width	1.91333	1.95333	1.99333	6	24.4167
17 Total	0.03333	1.01333	1.99333	147	0.5170
18 Inertial #2	0.03333	0.05333	0.07333	3	1.3333

Table 2.2. Set of Frequency Bands Used in Processing.

$$u_3' = - \frac{\frac{\partial T}{\partial t}}{\frac{\partial \bar{T}}{\partial X_3}} \quad (2.3)$$

where the advective and diffusive terms have been neglected. The differentiations are performed in the frequency domain using a "mean" estimate for $\frac{\partial \bar{T}}{\partial X_3}$ (eq. 2.2). The error in estimating $\frac{\partial \bar{T}}{\partial X_3}$ comes from two sources:

- 1) Replacing the instantaneous value with an estimated mean value.

This amounts to neglecting the effects of fine- and microstructure in the temperature field. The current and temperature finestructure fields are probably highly correlated. Contamination of the measurements from these effects could lead to an inferred stress which is negatively correlated with the mean shear. A very rough estimate of these effects (section A.2) suggests that the maximum stress error due to these effects is about $.04 \text{ cm}^2 \text{ s}^{-2}$, or 40% of the observed stress.

- 2) Using the time-varying mean temperature from the center of the data segment to estimate the expected mean temperature gradient.

Based on independent estimates of the gradient from historical data, the error in $\frac{\partial \bar{T}}{\partial X_3}$ from this procedure is estimated to be $\pm 15\%$ for the 1000 m instruments, and $\pm 30\%$ for the upper level instruments (see Appendix A.3).

The effects of the neglected terms in the heat equation (Appendix A.2) on estimates of the Reynolds stresses were found to be negligible at the "quiet" moorings. For mean velocities typical of those at the energetic moorings (30 cm/sec), it was found that the advection terms ($\bar{u} \cdot \nabla T'$) could, in the presence of a wavefield which is vertically asymmetric all the time, cause a false stress to be measured which is proportional to the mean velocity. Assuming a uniform 5% vertical asymmetry (52.5% of the energy going down; 47.5% upward), and based on integrals of the GM 76 model, a positive Reynolds stress would be falsely induced:

$$\overline{u_1' u_3'}_{\text{FALSE}} \approx 3 \times 10^{-4} \text{ cm/sec} \cdot \bar{u}_1.$$

This would constitute 10% of the observed signal at 600 m.

In using the Garrett-Munk model spectrum in the above estimate of the advective effects of the mean flow, and in neglecting Doppler effects on the spectrum, we have implicitly assumed that the wavefield is not strongly modified by the shear flow. In chapter 4, the observations at the energetic moorings are found to be inconsistent with this assumption. If we suppose instead that waves of a particular horizontal phase speed dominate the observed stresses, then the effects of advection on the observed stresses can be directly estimated. These effects are estimated in chapter 4, and the observations at the energetic moorings

41

are found to be consistent with this alternative interpretation.

Mooring Motion

Mooring motion at internal wave frequencies was not severe (less than 1 m) at the "quiet" moorings, and almost nonexistent at frequencies higher than tidal. Mooring motion was greater at the energetic moorings, ranging up to some tens of meters. Since mooring motion was found to be very coherent with depth, it proved possible to correct for the false u_3' signal induced by mooring motion, using the records of pressure from the 800 m level. This was done, and was found to have been unnecessary at the "quiet" moorings. At the energetic moorings, the correction to the Reynolds stress estimates was found to be typically 25% of the estimates summed over the continuum band ($2f - N$) and 40% at the near-inertial frequencies.

Current Measurement Errors

The effects of low measured speeds on the current meter become severe when speeds are as slow as at those found at the quiet moorings. The rotor, or speed sensor, spent 15% of its time stalled. An estimate of the error due to finite stall speed was made, and the noise spectrum was found to affect the internal wave velocity estimates in the range $f - 2f$. The effect is not severe at higher frequencies due to rapid falloff of the noise spectrum.

64

Errors in the speed and direction sensors at high speeds are considered in chapter 6. It is found that small errors in detecting a large mean velocity appear as anisotropic, nearly "white" current noise at internal wave frequencies. At sufficiently high speeds, the errors can dominate the spectra to the extent that a false internal wave current anisotropy is estimated. This effect is strong enough to mask any "real" wavefield anisotropies caused by critical level wave absorption.

Statistical Uncertainties

Uncertainties in computed spectral estimates were estimated following Jenkins and Watts (1969).

Uncertainties for the estimates of correlation coefficients and regression slopes were computed by estimating the fourth moments of the time series involved in the regression. (Formulae and program listings in Appendix A.) This accounts for both the non-normality and non-whiteness of the data. When tested with pseudo-normal random data which had been low-pass filtered, the estimated uncertainties were consistent with those predicted by Wold's (1950) formula. The uncertainty estimates resulting from tests with pseudo-normal independent data were consistent with the usual uncertainty estimate for a bivariate normal process at $\rho_{\text{true}} = 0$.

Summary

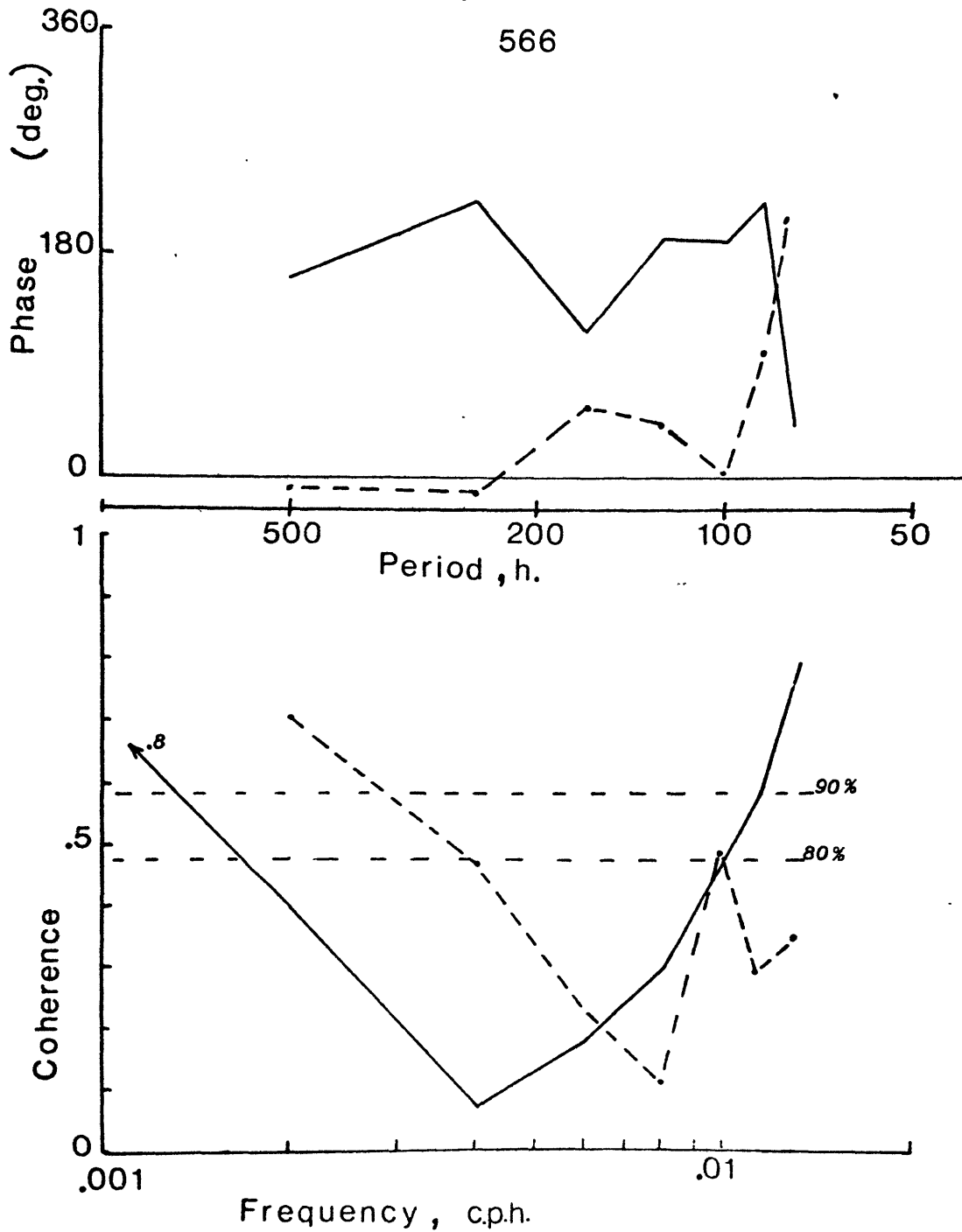
Excepting the problem of finestructure contamination, the most severe errors are worst in the frequency range $f - 2f$. Excluding this range from the computations (continuum band) implies a loss (estimated) of 20% of the Reynolds stress signal, but avoids all the noise problems at moderate velocities. At moorings with high velocities, the most severe problems are mooring motion, which is correctable to some degree, and advection effects in the temperature equation, which are not correctable. The effects of finestructure contamination on the stress estimates are potentially large, but are unknown to a great degree.

2.5 Low-Pass Filter

The 50-hour time resolution of the wavefield spectral estimates was found to be more than adequate for comparison with the mean flow, which varied on time scales longer than ten days. The coherence between the 600 m east mean velocity and the "continuum" band stress is shown in fig. 2.2 (600 m stress, dashed line; 1000 m stress, solid line). Note that, while the phases are relatively stable, the coherence drops to low values at frequencies higher than about .004 cph (10 days), indicating a poor signal-to-noise ratio at the higher frequencies. (Note also that the coherences are not strongly significant, but that the correlation coefficients are, suggesting the correlation estimate is more sensitive

Figure 2.2

Coherence between East mean velocity
at 600 m and East continuum band
stress at 600 m (dashed line) and
1000 m (solid line).



45

than coherence.) Figure 2.3 shows the power spectra (linear axes) of several "slowly-varying" time series from 566. The mean flow has very little variance at the higher frequencies. The wavefield stress time series has considerable variance at high frequencies, but this energy is not coherent with the mean flow. The overall signal-to-noise ratio is greatly improved by the use of a simple, triangular, low-pass convolution filter, with weights $\frac{(1,2,3,2,1)}{9}$. The half-power point of the filter is at 14 days, and the stability of each estimate is enhanced by a factor of $(2)^{1/2}$ by the filter. The spectra of the low-passed series (fig. 2.3, dashed lines) show that the filtered series are much better matched in time scale, overlapping only at the low frequencies, where the coherence is greatest. The mean time series are essentially unchanged. Filtered time series were used in several of the regression estimates in ch. 4. It was found that, when the correlation coefficient was significant, the slope estimate from the regression analysis was not significantly changed by the filtering procedure. The uncertainty of the slope estimate was slightly decreased due to the improved signal-to-noise ratio.

46

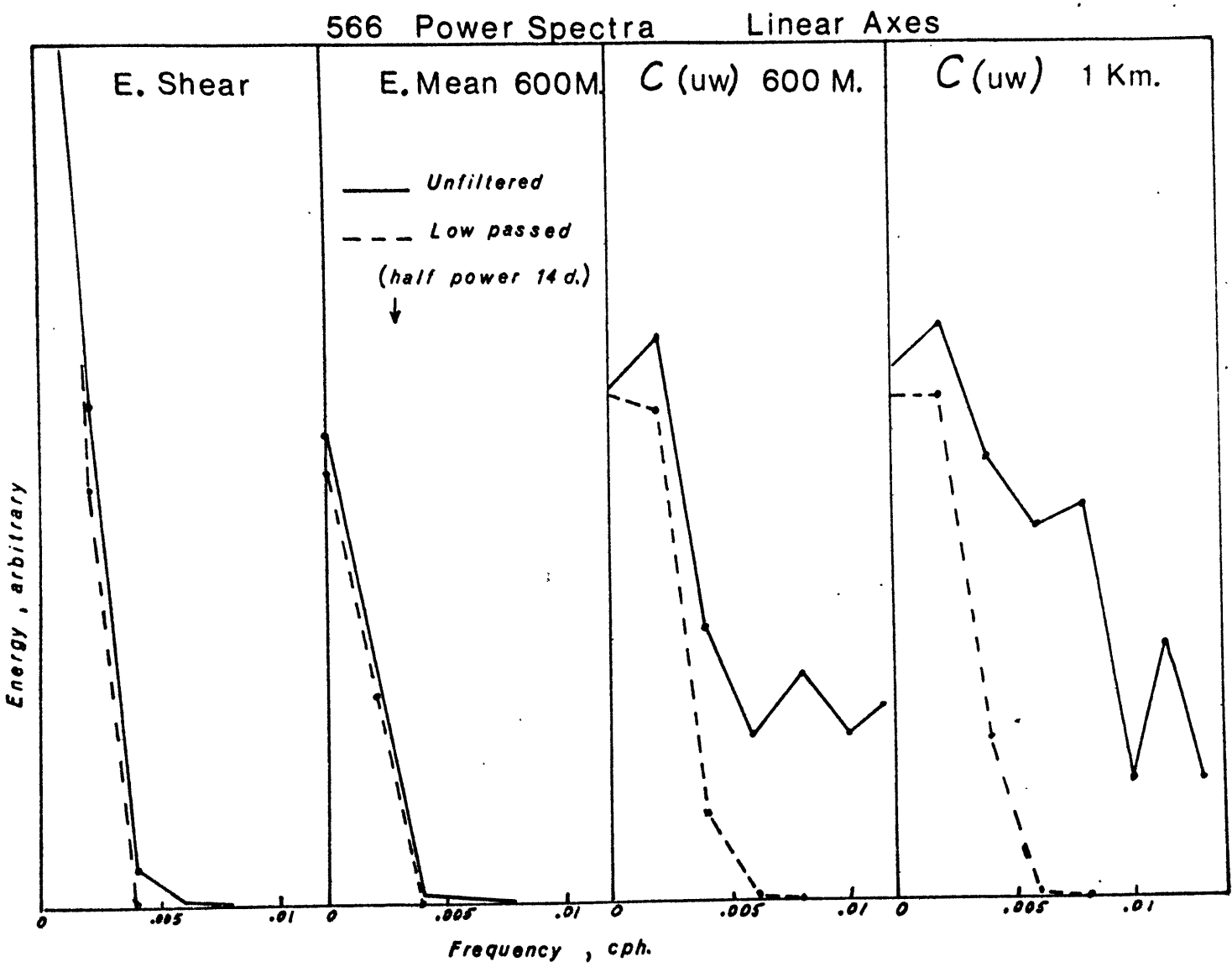


Figure 2.3 Autospectra of 600 m East mean velocity, shear (600 - 1000 m), continuum band stress at 600 m and 1000 m, from before (solid lines) and after (dashed lines) low-pass filtering.

Chapter 3

HOMOGENEITY AND ISOTROPY

3.1. Low-Frequency Flow

Schmitz (1976) has computed stable estimates of the eddy kinetic energy at 4000 m nominal depth in the North Atlantic using combined space-time averages. He has demonstrated that the energy level varies by at least 2 orders of magnitude, the general direction of decrease being somewhat East of South away from the Gulf Stream. From inspection of the Polymode Array I and II data, (the author is very grateful to Dr. Schmitz for allowing the use of the data for these studies), the same general trend of a large-scale gradient of energy increasing towards the North-West is apparent in the upper waters, near the thermocline. However, the records are somewhat short to enable stable estimates to be inferred from averages of individual records.

The locations of the moorings which were analyzed in the present study are shown in figure 3.1. The moorings span a moderate portion of the Western North Atlantic Ocean, and are located in regions of varying low-frequency kinetic energy level. Moorings 565 and 566 are located in the higher energy region.

The low-frequency flow ellipse parameters computed for three of the four moorings shown in figure 3.1 are shown in figure 3.2, along with the record average velocity vectors.

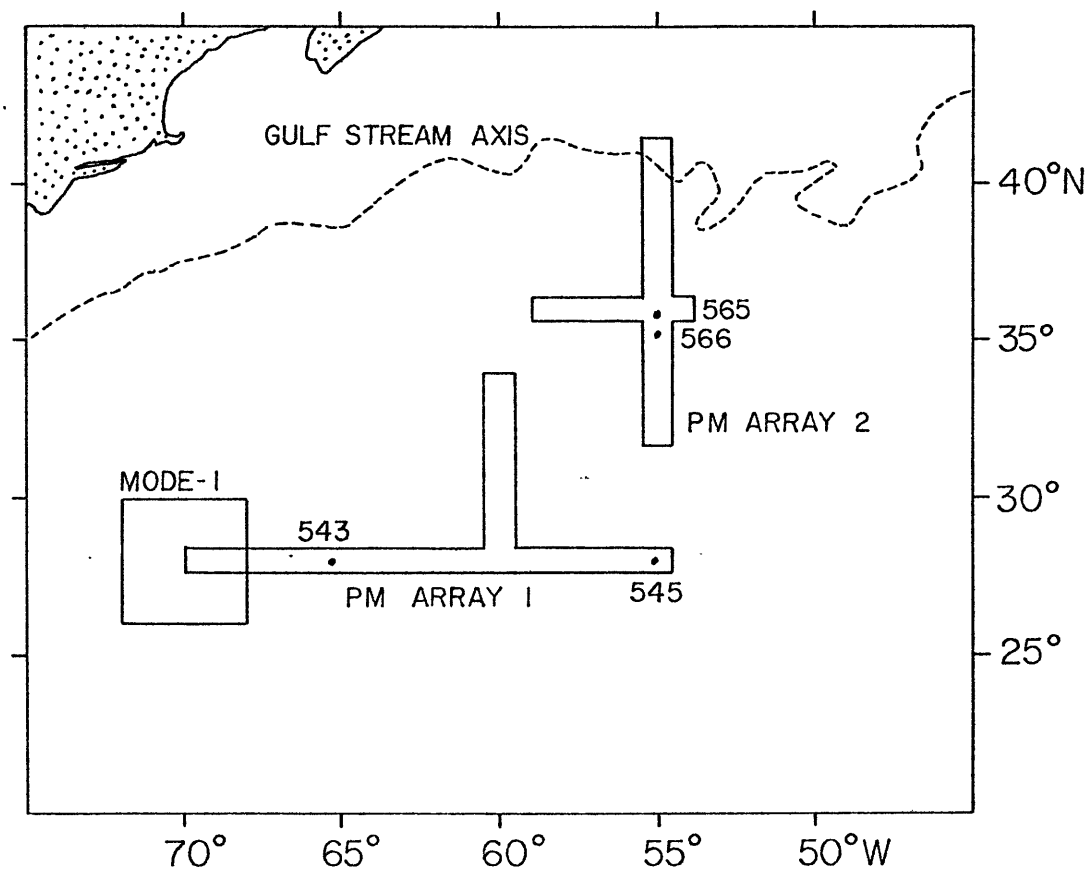


Figure 3.1 Locations of moorings analyzed.

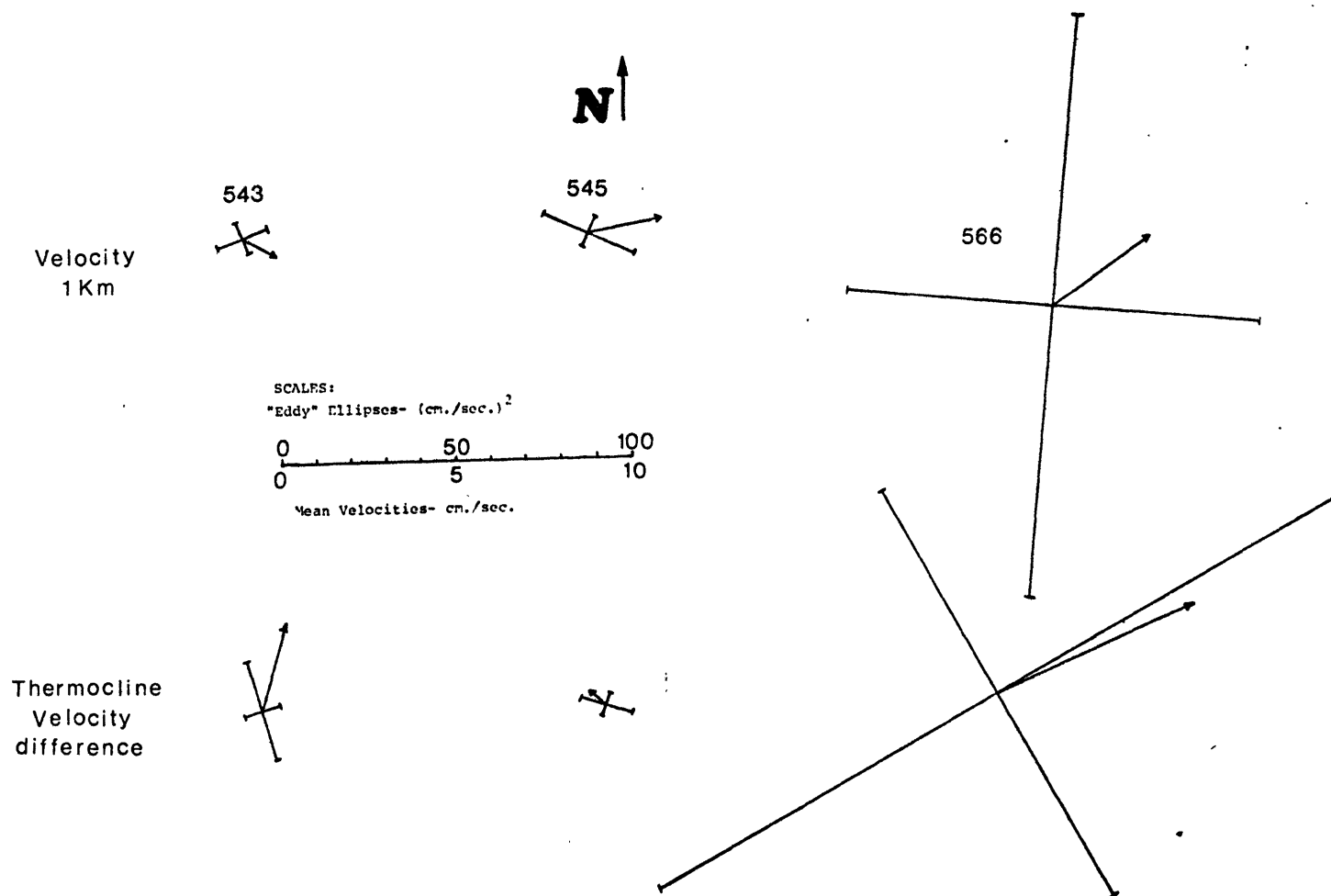


Figure 3.2 Ellipse parameters for velocity and cross-thermocline shear, and also record average velocity vectors, for moorings 543, 545, 566.

The upper set of figures is for the 1000 m velocities; the lower set is for the cross-thermocline velocity difference, computed from the difference between the upper (600 m) and the 1500 m (or 2000 m) velocities. The ellipse parameters are slightly confusing to describe, but they contain a lot of information about the isotropy of the flow (Gonella, 1972). The orientation of the ellipse axes is such that the two velocity components measured in a frame of reference with that orientation will be found to be statistically orthogonal; $\overline{u_1 u_2} = 0$. The maximum anisotropy of the horizontal currents would be observed in this frame of reference. The length of the straight lines is proportional to the mean square velocities measured in the rotated frame of reference. The low-frequency flow is found to be anisotropic if one of the lines (thought of as the major axis of an ellipse, hence the name) is significantly longer than the other, indicating the velocities to be more energetic in that direction. Testing for a ratio of energies (or variances) in this manner uses the F-distribution. The low-frequency flow has a red spectrum, and so up to 50 data days are taken for each degree of freedom in statistical tests such as the F-test. The records are only about 200 days in length, and the F-test is not particularly sensitive. Although some anisotropies are apparent in figure 3.2, they are not statistically significant in the sense that one can predict future anisotropies based on these measurements. We can only say that the mean (frequencies below

inertial) flow was anisotropic to a slight degree at each mooring. The ratio of variances of the major and minor axes of the ellipses was never much larger than two. Note, however, the degree of inhomogeneity: a factor of ten energy difference. This is consistent with Schmitz' (1976) findings.

3.2 Internal Wavefield

Wunsch (1975a) investigated the hypothesis of a universal, horizontally homogeneous and isotropic internal wavefield using current meter data from various locations in the North Atlantic. He found the hypothesis to be true almost everywhere. The wave energy level was relatively constant at all locations except those within 10 km horizontally or 1 km vertically of a topographic feature. He found a weak tendency for wave energies to be higher under the Gulf Stream (a factor of two increase in the wave energy corresponding to a factor of six in the mean flow energy), but could not rule out the possibility of kinematic energy variations due to local time changes in the buoyancy frequency. One of Wunsch's main conclusions was that there must be very powerful mechanisms which maintain the equilibrium energy level and shape of the wavefield, even in the near field of energy sources or sinks.

Schmitz has computed the kinetic energy of motions at internal wave frequencies from Polymode Array I and Array II data, and has kindly consented to allow a subset of the data

to be plotted here. In figure 3.3, the total internal wave kinetic energy levels from the 1500 m level are plotted against location. Also shown by an "x" are any topographic features which extend up to shallower than 2500 m (taken from Uchupi, 1971). It can be seen that there are no anomalously high energies associated with topographic features, suggesting that little wave energy is present in the area of study which is propagating up from below. This is in keeping with the findings of Wunsch (1975).

The wave energy shows an apparent large-scale gradient, decreasing from North to South by a factor of two over the 6° extent of the array. While kinematic effects of stratification cannot be ruled out, an energy gradient was observed at all levels. The factor of two change in wave energy corresponds to a factor of ten in eddy kinetic energy found by Schmitz (1976), in the same general direction, and furthermore, the changes correspond in comparative levels (2:10) in temporal changes in energy levels discussed in chapter 4.4 of this work. Also Wunsch (1975a) found a factor of two wave energy increase in the vicinity of the Gulf Stream, but was unable to rule out temporal changes in buoyancy frequency as a possible cause. The energy changes are very suggestive, but more work involving very careful normalization using an average buoyancy frequency profile needs to be done before definite conclusions can be drawn. Unfortunately, the data necessary to compute an average buoyancy profile are sparse,

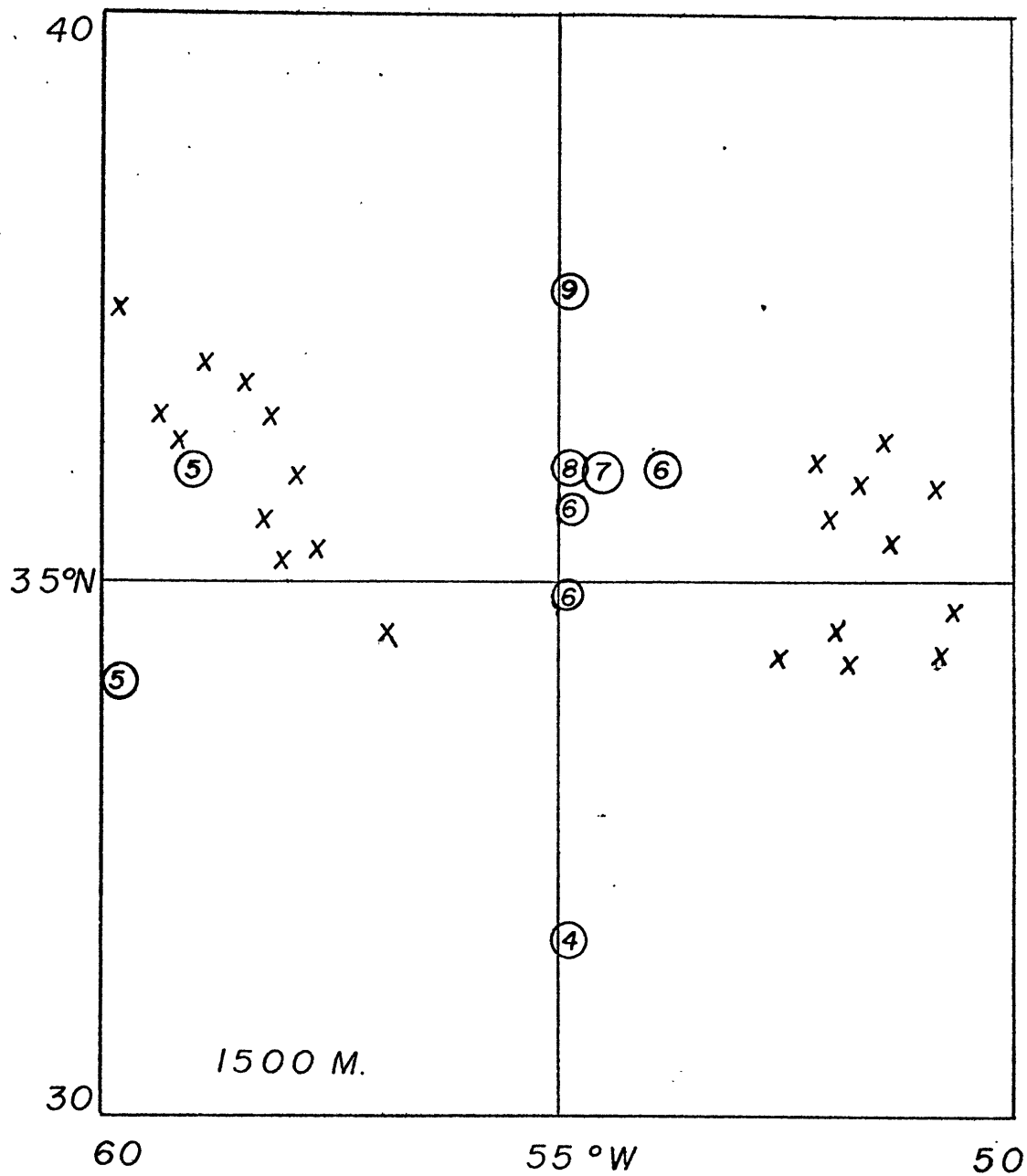


Figure 3.3 Total internal wave kinetic energy from the 1500 m level in the Array II area.

and the problem is compounded by the extremely large (about 200 m) excursions of the main thermocline.

A necessary condition for isotropy in the wavefield is that the East and North velocity spectra be equal. Another is that the East-North cospectrum be equal to zero. If both of these conditions are satisfied, then the current ellipse described in section 3.1 is a circle, and the wavefield is isotropic. The current auto- and co-spectra for the continuum band are listed for the 1000 m level at each mooring analyzed. The 600 m level was not used to avoid contamination by high mean velocities. The largest ratio of East and North auto-spectra is 1.14, and the largest cospectrum is 7% of the auto-spectrum. The rms currents in any direction are different in strength from those in any other direction by less than 10%. Hence, even though the low-frequency flow field is inhomogeneous on the large scale, the internal wavefield is isotropic to a high degree.

3.3 Rays or Modes?

Because the processed data are stored in the form of short-piece estimates of internal wave spectra, it is possible to observe changes in the spectra on an "event" timescale. Conceivably, it is possible to monitor short-term phase variations between u_1 and u_3 , and interpret the variations in terms of the vertical phase-locking of the wavefield. A potential error is the possibility of finestructure contami-

TABLE 3.1

Record average spectra of horizontal current
from 1000 m level. Units are $\text{cm}^2 \text{s}^{-2}$.

DATA	C_{11}	C_{22}	C_{12}
5663	3.89	3.42	-.005
5653	3.45	3.43	.18
5453	2.65	3.01	-.133
5433	2.06	2.16	.053

Continuum Band

nation (Appendix A.2), but we will ignore this possibility.

We consider a wavefield on the timescale of wave packets; hopefully this timescale is not greatly different from the approximately 50 hour time resolution of the Fourier transform window we have used. On this short timescale, we expect to be able to observe deviations of the wave spectrum from isotropy and vertical symmetry, although it may not be possible to distinguish them individually from statistical fluctuations in the usual sense. From Appendix B, if the dominant asymmetry is caused by a vertically propagating wave packet, the phase between u_1 and u_3 (for $\omega^2 \gg f^2$) will be either 0° or 180° depending on propagation directions. However, if the dominant asymmetry is mode-like, composed of an up- and a downgoing ray which are locally phase locked for a large number of wave periods, the phase between u_1 and u_3 will be $\pm 90^\circ$, depending on the horizontal propagation direction, and on the sign of the factor $\sin(k_3 \cdot x_3)$ from the modal amplitude factors in Appendix B. Hence, by examining the short-term phase between u_1 and u_3 , a qualitative estimate of the phase locking of up- and downgoing waves can be made.

A time series of the phase between u_1 and u_3 for the continuum band from mooring 566 at 600 m is shown in figure 3.4. The data points which fall more closely to the "ray" phases 0° , 180° have been circled, and the times when more than one such point occurs has been marked on the time base with hatch-marks. Only 15% of the points represent rays

dominating; the other 85% indicate a high degree of phase-locking of up- and downgoing waves. The coherence estimated between u_1 and u_3 is shown in figure 3.5. The "ray" times have been indicated on the time base as before. There is no obvious tendency for the coherence to be higher than usual at these times; it may even be lower, although it is hard to tell. Apparently, the wavefield has a strong tendency towards vertical symmetry, with phase-locking of up- and downgoing components. McComas and Bretherton (1977) suggest a mechanism which could cause this, called elastic scattering. We describe this in chapter 5.4. The effect of this mechanism is to hinder vertical propagation of wave energy and momentum through reflection about the vertical.

A similar discrimination between ray and mode tendencies was made by computing the variances of the u_1 - u_3 co- and quadrature spectra, which indicate rays (momentum flux) and modes, respectively. In all cases computed, the ratio of variances was found to either be one to within statistical uncertainty, or to indicate a dominance of modes. In no case were rays found to dominate. A similar result was found from the analysis of the Internal Wave Experiment (Müller, Olbers and Willebrand, 1977). Since we will be looking for Reynolds stress (ray) effects in chapter 4, we expect that the observed stresses will be relatively small.

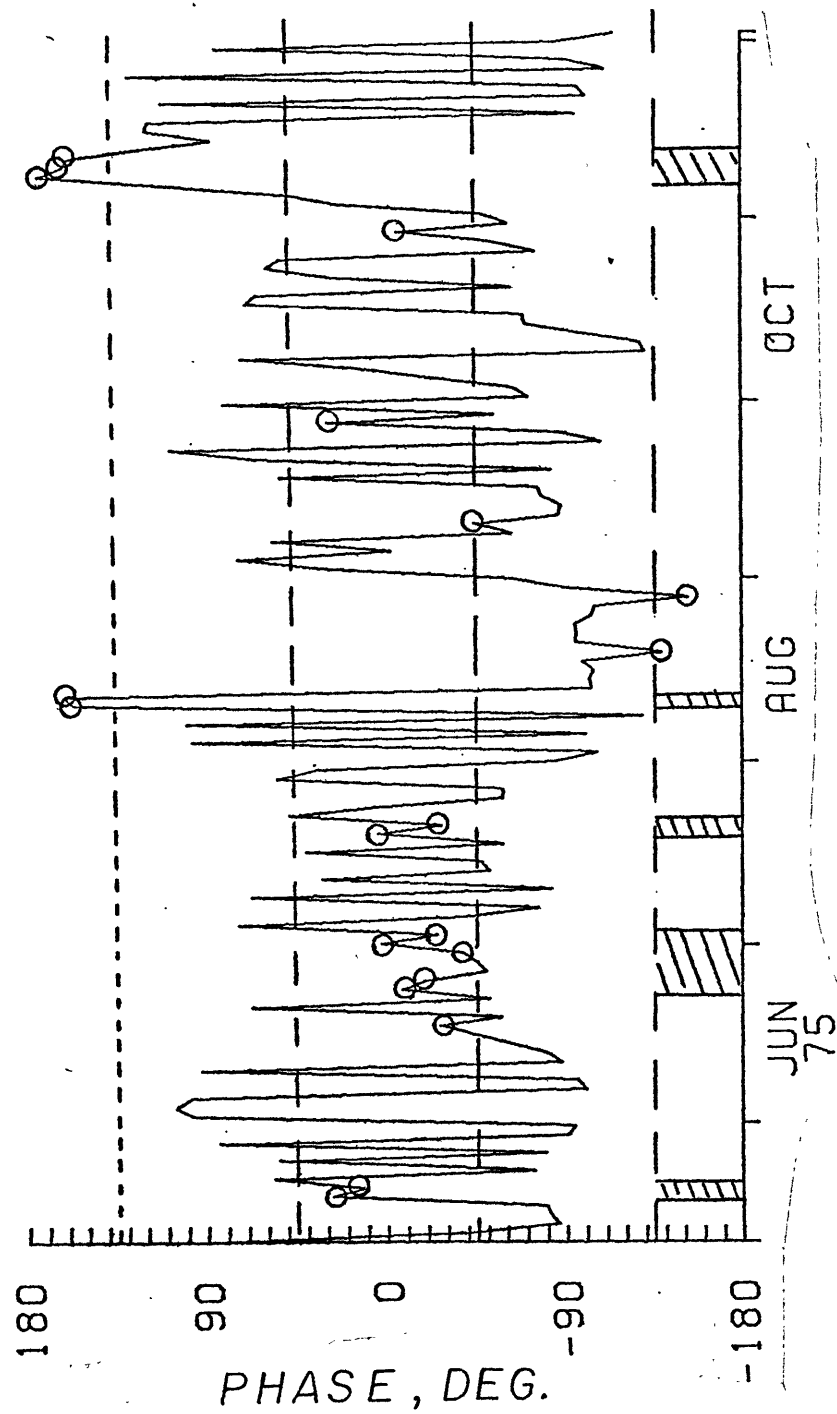


Figure 3.4 Time series of phase between u_1 and u_3 (estimated from temperature) for the continuum band on 566 at 600 m.

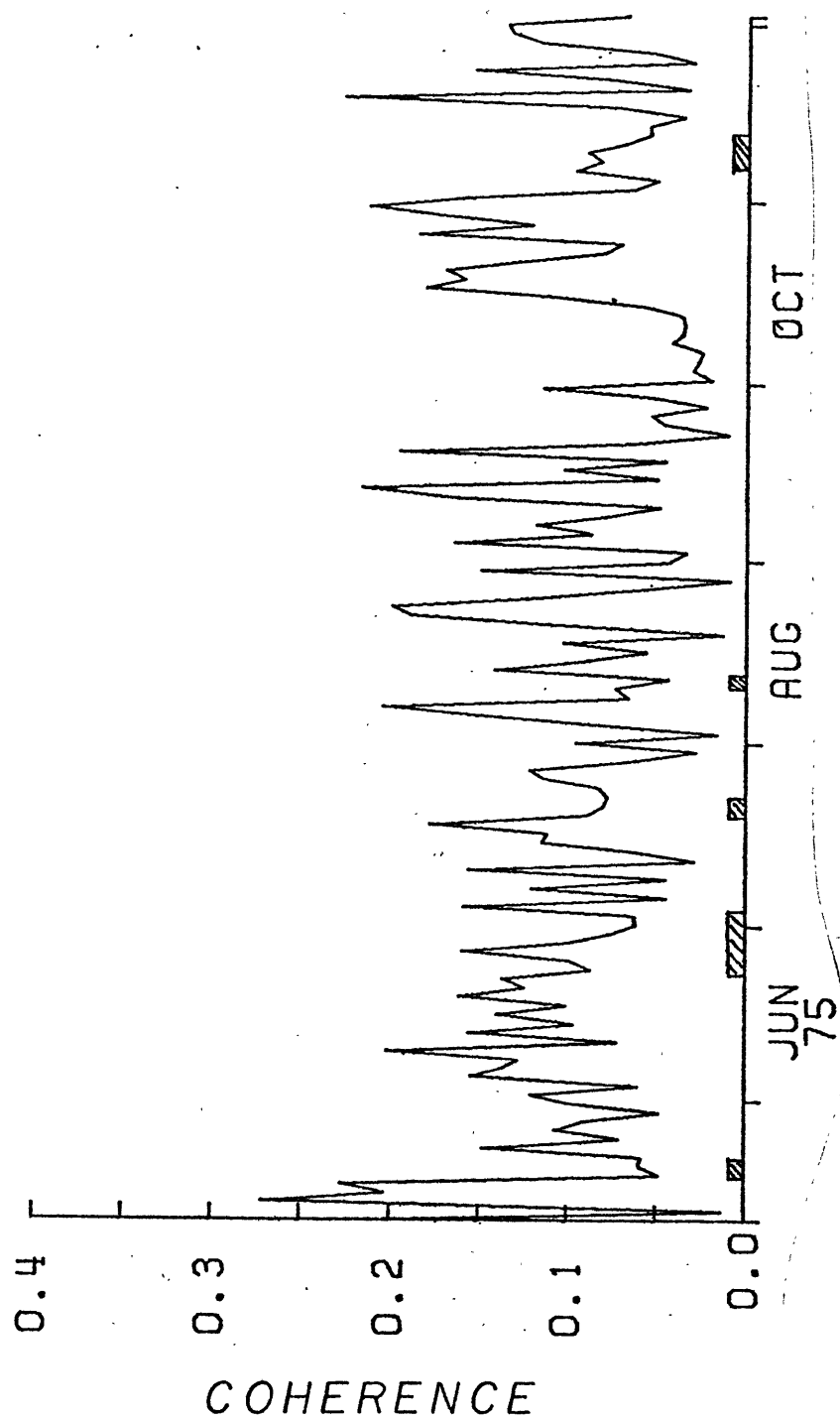


Figure 3.5 Coherence between u_1 and u_3 for the continuum band on 566 at 600 m.

Chapter 4

WAVEFIELD-MEAN FLOW CORRELATIONS

4.1 Introduction

Müller (1976) has analyzed theoretically the interaction between the wavefield and a shear flow, and suggested that the main effect might be that the shear flow induces anisotropies in the wavefield such that the wavefield will exert stresses that oppose the shear and thus extract energy from the mean flow. He estimates that the stress-shear relation may be parameterized by horizontal and vertical eddy viscosities. Because of the small aspect ratio of the mean flow, the most important effect is the vertical eddy viscosity, whereby the $(\overline{u_\alpha u_3})$ wave stress is predicted to be proportional to the (negative) shear, $-\frac{\partial \overline{u}}{\partial x_3}$. Müller estimates a constant of proportionality $\nu_v = 5 \times 10^3 \text{ cm}^2 \text{ s}^{-1}$. Much of this chapter involves estimating this parameter from observations of wave stress and mean shear.

The energetically less important aspect of the Müller interaction is the horizontal eddy viscosity. This implies the horizontally-acting wave stresses $(u_\alpha u'_\beta)$ where $\alpha, \beta = 1, 2$, measured from the horizontal currents, are proportional to the horizontal gradients of the mean flow. This effect cannot be observed from single moorings, since the horizontal gradients cannot be estimated. Frankignoul (1976) has

61

attempted to estimate horizontal eddy viscosities directly from the MODE-1 Array data, but found that the uncertainties were far larger than the value predicted by Müller.

Frankignoul (1974) also detected a tendency for the internal wave currents to be stronger in a direction perpendicular to the mean flow than parallel to it. This effect is unrelated to horizontal or vertical eddy viscosity effects, and so is investigated separately in chapter 6. Measurements of physical quantities such as current ellipses (Gonella, 1972) from horizontal current spectra have a $\pm 180^\circ$ ambiguity, while the vertically-acting stresses do not. This difference demands that the two types of quantities be interpreted in a somewhat different manner, and justifies the separate treatment.

As an aid to interpretation of the observations, we will need to make use of a few simple rules relating the actual and measured (from temperature) momentum fluxes, and the direction of the vertical flux of wave energy. In Appendix A, the effects of estimating u_3 from the temperature perturbations are all estimated and found to be small, except for (potentially) the effects of finestructure contamination, which we must ignore here, and the horizontal advection, or doppler shift term. Denoting:

$$u_3^M = - \frac{\partial T'}{\partial t} \left(\frac{\partial \bar{T}}{\partial x_3} \right)^{-1} \quad (4.1)$$

$$u_3^T = \text{the actual value of } u_3'$$

we have, from the heat equation:

$$u_3^M \approx u_3^T + \bar{u} \cdot \nabla T' \left(\frac{\partial \bar{T}}{\partial x_3} \right)^{-1}. \quad (4.2)$$

For an individual wave, with dependence:

$$\begin{aligned} u(\underline{x}, t) &= \text{Re}\{U(\underline{z}) e^{-i(k_1 x_1 + k_2 x_2 - \omega t)}\} \\ (\overline{u_1' u_3'})^M &= (\overline{u_1' u_3'}) \frac{\omega}{\omega_0} \\ &= \frac{(\overline{u_1' u_3'})^T}{\left(1 - \frac{\underline{k} \cdot \bar{\underline{u}}}{\omega}\right)}. \end{aligned} \quad (4.3)$$

Hence the sign of the observed stress is changed from the true value according to $\bar{u} > c$, where c is the component of horizontal phase speed in the direction of \bar{u} . For $c > \bar{u}$, or if c opposes \bar{u} , the sign is not changed.

Jones (1967) investigated the propagation of horizontally plane waves in a geostrophic vertical shear flow. From his equations (his \underline{k} is minus our \underline{k}) it is easy to show:

$$\overline{p' u_3'} = \frac{\omega_0}{k_\alpha} [\overline{u_\alpha' u_3'} + \epsilon_{\beta\alpha 3} \xi_\beta \overline{u_3'}] \quad (4.4)$$

(No α summation; $\alpha = \text{either } 1 \text{ or } 2$)

where ξ_β is defined by eq. 4.28 as a Lagrangian particle displacement. Using eqs. 4.32 and 4.33 we have

$$\overline{p' u_3'} = \frac{\omega_0}{k_\alpha} (\overline{u_\alpha' u_3'})^T \left(1 - \frac{f^2}{\omega^2}\right) \quad (4.5)$$

where $\omega = \omega_0 - \mathbf{k} \cdot \bar{\mathbf{u}}$, the intrinsic frequency.

Identifying $\overline{p'u_3}$ as the vertical flux of wave energy, we can see that the sign of the stress exerted by a wave traveling upward will change with that of ω_0/k_α . Combining the last two results, we obtain:

$$(\overline{u_\alpha'u_3'})^M = \frac{k_\alpha \omega}{\omega_0^2 - f^2} \overline{u_3'p'}. \quad (4.6)$$

Hence the observed stress for a single wave depends only on the direction of the α component of the horizontal phase speed (in an absolute or non-advected reference frame) and the sign of the vertical energy flux. The sign of the phase speed relative to $\bar{\mathbf{u}}$ does not affect the relation. Note that this relation may not hold for a spectrum of such waves if they have different phase speeds. A field of waves with both upward and downward propagating waves can give rise to a Reynolds stress of either sign, with the net energy flux and measured Reynolds stress not simply related. For this reason, any interpretation of the data based on these relations is not unique. It is possible to find more than one interpretation that is consistent with the observations. We shall look at the simplest one.

We now put forth three working hypotheses to which we will compare the observations.

Hypothesis #1: Local eddy viscosity interaction

We assume that the wavefield interaction we are observing involves primarily the part of the wavefield which is allowed to propagate vertically through the entire water column, those waves with $N > (\omega - \mathbf{k} \cdot \mathbf{u}(z)) > f$ at all depths. (Any other waves will be absorbed at critical levels, and so we might expect little wave energy to be at those wavenumbers and frequencies.) Then any local interaction, such as that suggested by Müller (1976), will lead to a wave stress which depends on the shear, and to a vertical eddy viscosity which may vary in magnitude parametrically with $N(z)$, but should not change sign with depth. For waves satisfying the above "passband" condition, the horizontal phase speed of the waves is greater than the water velocity at all depths, and from eq. 4.3 we see that the Doppler term for such waves cannot change the sign of the Reynolds stress as estimated from the temperature field. From the model spectrum[†] we estimate in

[†] The initials GM are used to denote a class of kinematic internal wave spectral models. The models referred to in shorthand are:

GM 72 - Garrett and Munk (1972), in which the frequency dependence was modelled, but no attempt was made to include detailed horizontal wavenumber dependence. Rather, a uniform excitation of the first 20 modes was assumed.

GM 75 - Garrett and Munk (1975). The wavenumber dependence was modelled, in the light of new information on horizontal scales.

GM 76 - Cairns and Williams (1976), also Desaubies (1977). Very similar to GM 75, but a much more analytically convenient form.

Formulae for GM 75 and GM 76 are given in chapter 6.

Appendix A that it should have only a 10% effect. We shall find that the observed stresses do change sign with depth, suggesting that either the local eddy viscosity changes sign with depth, or the observed stresses are dominated by waves whose phase speeds are $O(\bar{u})$ or less.

The second and third hypotheses are based on the assumption that the waves which cause the observed stresses have a horizontal phase speed of the order of \bar{u} , so that the Doppler term in the heat equation is capable of actually changing the sign of the observed stresses from the sign of the actual stresses exerted by the wave. These hypotheses must necessarily involve waves much shorter than the typical wavelength associated with waves in the Garrett-Munk spectra.

Since the sign of the observed stress of a single wave depends only on the sign of the vertical group velocity, we can rule out immediately any mechanisms involving waves propagating through the shear region. Any simple mechanisms giving rise to opposing measured stresses on either side of the shear region must be due to a net flux of energy either into or out of the shear zone.

For waves whose phase speed opposes the mean flow velocity, the only simple interaction with the mean flow occurs when $\omega - \mathbf{k} \cdot \mathbf{u}(z) = N(z)$. At this depth, vertical reflection occurs (Bretherton, 1966), causing the waves to change direction. We expect no net vertical energy flux, and from 4.6 expect that the observed stresses of opposite sign are not due to reflection of this sort.

Waves with a phase speed in the direction of the mean flow are the basis for our two alternate hypotheses.

Hypothesis #2: Critical level wave absorption

Waves with a component of horizontal phase speed in the direction of \bar{u} and of the correct magnitude can encounter critical levels (Bretherton, 1966; Jones, 1967) in their vertical travels. Theoretical investigation of the wave-mean flow interaction problem (chapter 5) suggests that this might be the dominant interactive mechanism. Waves which encounter critical layers in the region of maximum shear (600 - 1000 m) must have

$$\bar{u}_{1000} < c < \bar{u}_{600} \quad (4.7)$$

and from 4.6, we expect to observe a positive (negative) inferred stress at the 1000 m (600 m) level, consistent with propagation of energy into, but not out of, the shear zone.

Hypothesis #3: Wave generation at the shear zone

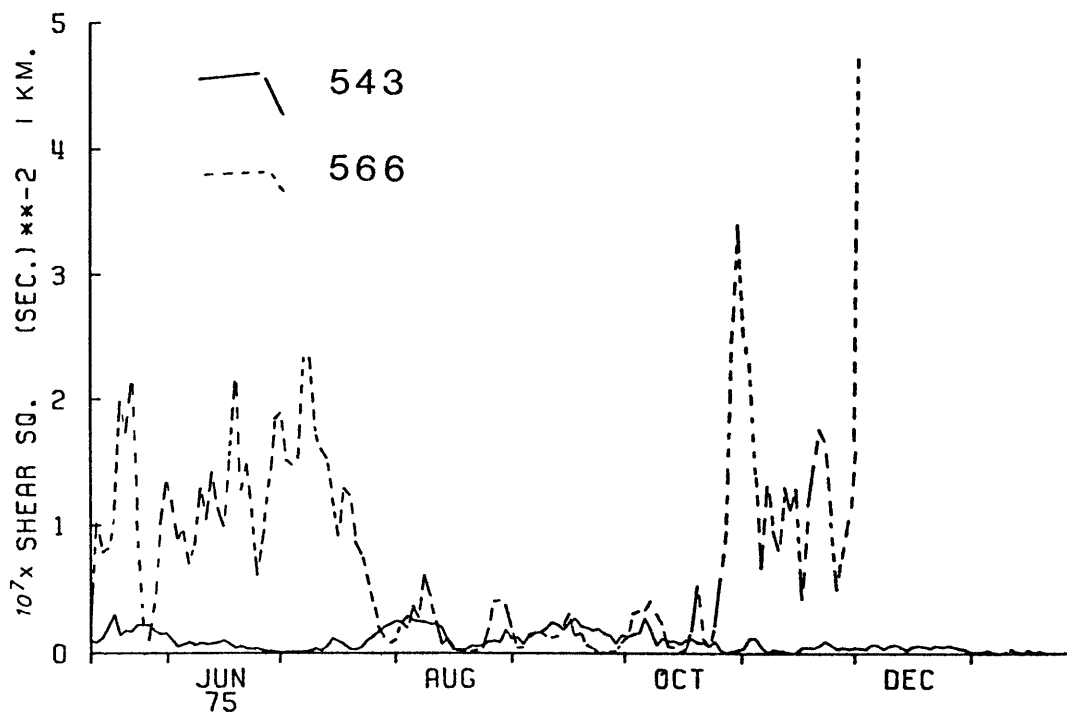
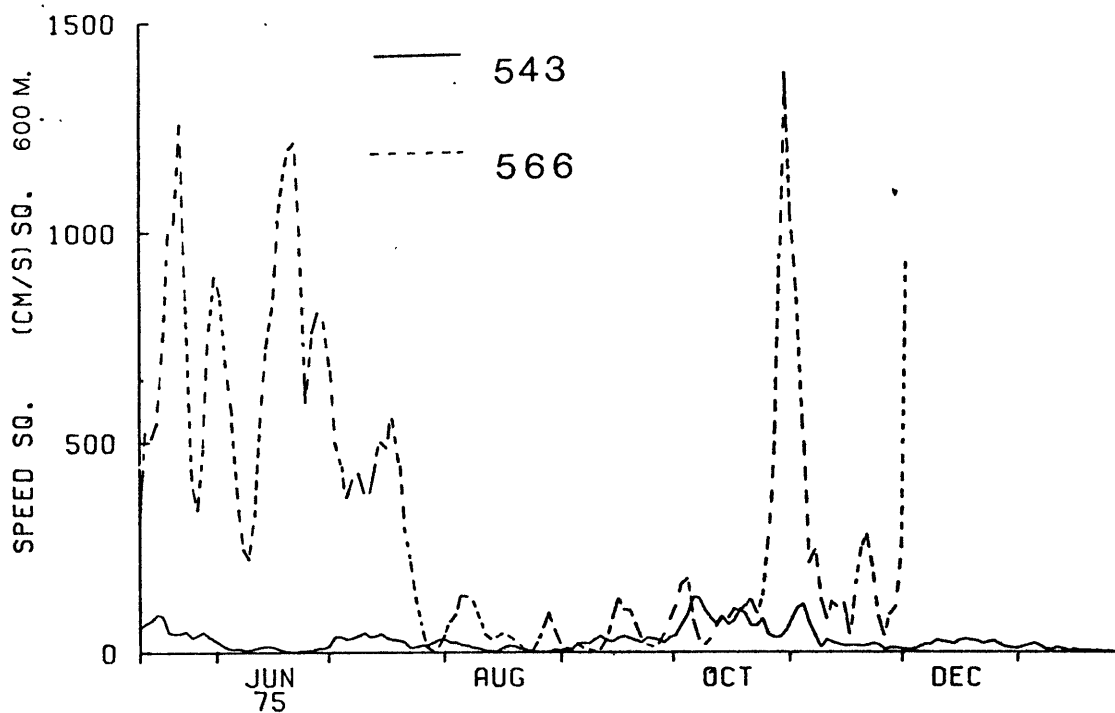
Waves generated in the region of maximum shear are most likely to be due to advected non-wave disturbances, such as billows or patches of turbulence. The relative flow over and under these disturbances can generate lee waves in the same manner as flow over a bumpy bottom. These generated waves will have a horizontal phase speed equal to the advection velocity at the level of the original disturbance. There will be a net outward energy flux, and so from equation 4.6,

we expect a positive (negative) inferred stress at the 600 m (1000 m) levels.

The moorings have been classed as "quiet" (543, 545) or "energetic" (565, 566) based on the intensity of the low-frequency flow. Figure 4.1 shows time series of $(\bar{u})^2 + (\bar{v})^2$ at the uppermost level and estimates of $|\text{shear}|^2$ from moorings 566 (dashed line) and 543 (solid line) plotted on the time base for 566. Note first the difference in strength of the velocity and shear between the moorings; a factor of ten. Note also that the mean flow at mooring 566 became "quiet" for a period during the middle of the record. Certain wave-field quantities from the same two moorings are shown in fig. 4.2. Although the vertical kinetic energy is considerably higher at mooring 566, the total kinetic energy doesn't differ from that of 543 by more than a factor of two. The energy levels and the wave stress magnitude from moorings 566 and 565 vary with the strength of the mean flow, and are very different in the quiet and energetic segments of the record. These modulations are investigated in detail in §4.4.

In §4.2 the effect of the Coriolis force on the relation between wave stress and buoyancy flux in a geostrophic shear flow is investigated. It is shown that the momentum and buoyancy flux effects partially cancel, so that an effective stress can be defined as $(1 - f^2/\omega_o^2)$ times the actual stress. This is the stress which affects the mean shear.

Figure 4.1 Time series of $|\text{speed}|^2$ at 600 m and $|\text{shear}|^2$ from the difference of velocities at levels 1 and 3 for moorings 566 (dashed line) and 543 (solid line).



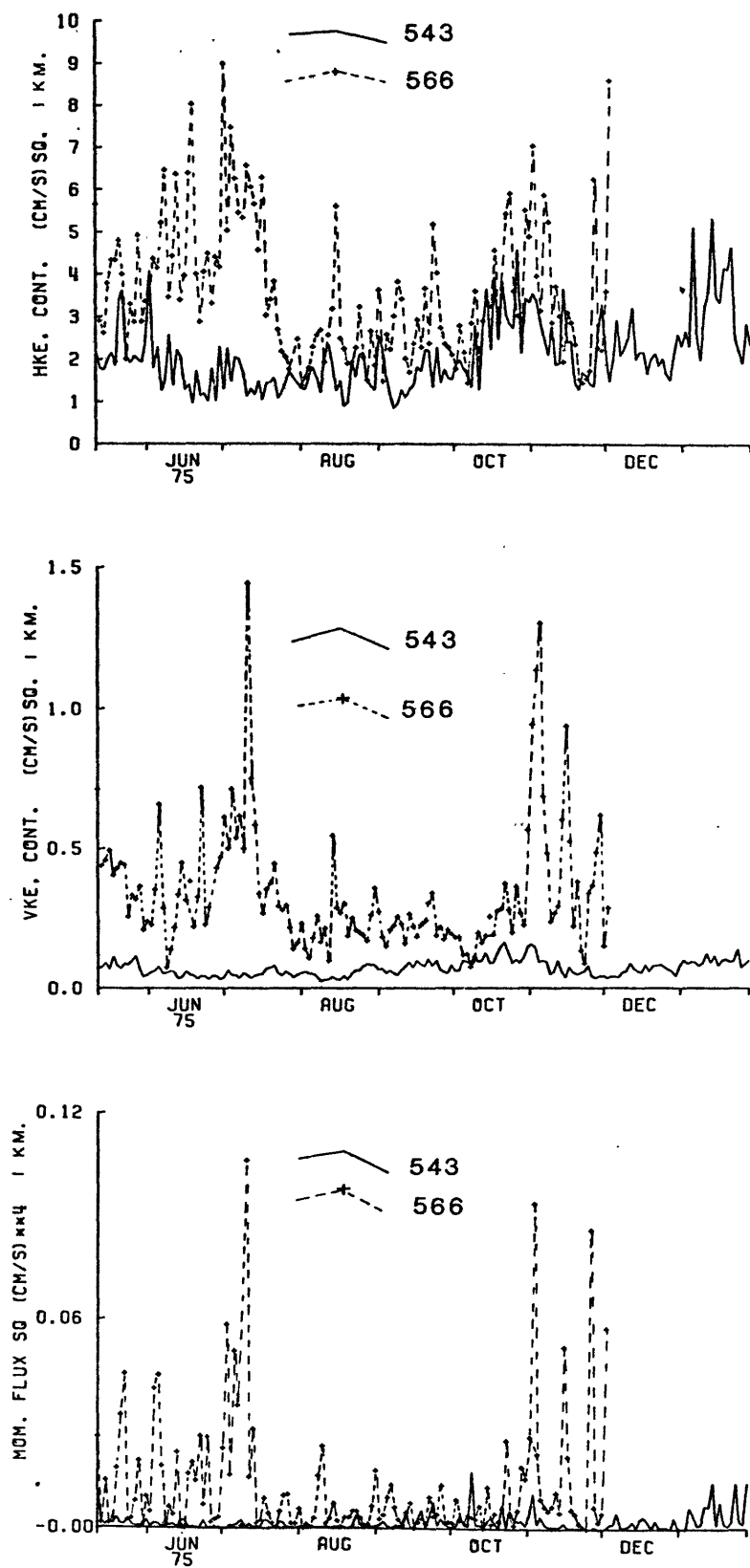


Figure 4.2 Time series of Horizontal Kinetic Energy, Vertical Kinetic Energy and vertically acting Reynolds stress squared estimated for the continuum band (0.1 - 2 cph) at moorings 566 (dashed line) and 543 (solid line).

The continuum band ($2f-N$) stress is shown to be an accurate estimate of this stress.

In §4.3 are examined correlations of the wave stresses and buoyancy fluxes with properties of the mean flow. Estimates of the effective vertical eddy viscosity (under Hypothesis #1) are made using the continuum band stresses. Estimates of a "total" vertical eddy viscosity and horizontal diffusivity were attempted, with much larger uncertainties. The observed eddy viscosity estimates were found to change sign with depth, which is inconsistent with Hypothesis #1. In section 4.3d, the behavior of the continuum band stresses was examined more closely in time, depth, and frequency, without making the assumption of a local, eddy-viscosity type of interaction.

4.2 Momentum and Buoyancy Fluxes in Geostrophic Flow

The effect of internal waves on mean flow is measured by the divergence of the momentum and buoyancy flux tensors which the wave field sets up. In this section we will show that, in the presence of rotation, the momentum and buoyancy fluxes of the wavefield are related, and effectively combine to form a single "effective" stress tensor. This stress tensor can be rather simply related to the actual stress tensor, and turns out to be easier to estimate accurately than the actual stress.

Hasselmann (1971) obtained equations describing a wave-field in the presence of a mean flow by decomposing the Eulerian velocities, u , and the pressure (p) and buoyancy (b) fields, into wave and mean contributions. He used the Reynolds decomposition to obtain separate equations for the wave and mean flow fields: For internal waves in the ocean, a sensible and unique decomposition is made on the basis of the widely separated timescales of the wavefield and lower-frequency flows (Rhines, 1973):

$$\begin{aligned} u_i &\rightarrow \bar{u}_i + u_i' \\ b &\rightarrow \bar{b} + b' \\ p &\rightarrow \bar{p} + \bar{p}_w + p_w' \end{aligned} \tag{4.8}$$

where

- an overbar indicates a time average on timescales of a few inertial periods
- primes indicate wavefield quantities ($\overline{x'} = 0$)
- \bar{p}_w indicates the mean wave-induced pressure field

The fine points of the decomposition of pressure into three fields are discussed in Müller (1974). The mean wave induced pressure is balanced by slight mean vertical displacements (Bretherton, 1969a), and has no dynamic effect on the mean flow field. It may safely be ignored for our purposes.

The density field has been broken up in the following manner:

1) An equilibrium stratification $\rho_e(x_3)$, has been defined as the density field in the absence of motion. (Iso-pleths have been flattened to match gravitational potentials; diffusive effects due to density gradients not being normal to the boundaries were ignored.)

2) The Boussinesq approximation has been made, and $N^2(x_3)$ has been defined:

$$N^2(x_3) = - \frac{g}{\rho_0} \frac{\partial \rho_e}{\partial x_3} . \quad (4.9)$$

3) The buoyancy field, b , is defined as (minus) the density perturbation:

$$b = - \frac{g}{\rho_0} (\rho(\tilde{x}, t) - \rho_e(x_3)) . \quad (4.10)$$

4) The buoyancy field is decomposed into "wave" and "mean" parts.

In this case (note that the WKB approximation is not necessary here) the equations take the form (Müller, 1976):

$$(\frac{\partial}{\partial t} + \bar{\mathbf{u}} \cdot \nabla) \bar{u}_i + \epsilon_{ijk} \bar{u}_k - \bar{b} \delta_{i3} + \frac{1}{\rho_0} \frac{\partial \bar{P}}{\partial x_i} = - \frac{\partial}{\partial x_j} F_{ij} \quad (4.11)$$

$$(\frac{\partial}{\partial t} + \bar{\mathbf{u}} \cdot \nabla) \bar{b} + N^2 \bar{u}_3 = - \frac{\partial}{\partial x_j} M_j \quad (4.12)$$

$$(\frac{\partial}{\partial t} + \bar{\mathbf{u}} \cdot \nabla) \bar{\xi} - \bar{u}_3 = - \frac{\partial}{\partial x_\alpha} D_\alpha^S \quad \text{at} \quad x_3 = \bar{\xi} \quad (4.13)$$

where

$$F_{ij} = \overline{u_i' u_j'} + \bar{p}_w \quad (\text{mean wave momentum flux})$$

$$M_j = \overline{u_j' b'} \quad (\text{mean wave buoyancy flux})$$

$$D_\alpha^s = \overline{\int_{\xi}^{\xi+\xi'} u_\alpha dx_3} \quad (\text{mean wave induced surface mass flux})$$

The effects of the wavefield on the mean flow field enter in through the divergence of the Reynolds stress tensor, $\frac{\partial}{\partial x_j} (\overline{u_i' u_j'})$, and the divergence of the wave buoyancy fluxes, $\nabla \cdot \tilde{M} = \frac{\partial}{\partial x_j} (\overline{u_j' b'})$. Under the Boussinesq approximation, the "rigid-lid" surface boundary conditions are valid for internal wave motions, and so the internal wave-induced surface mass flux is negligible. If the WKB approximation is valid in the horizontal direction, $M_3 = 0$.

It is well established (the MODE-I Dynamics Group, 1975) that the low-frequency flow is, to a first approximation, in hydrostatic and geostrophic balance:

$$\bar{u}_\alpha = - \frac{\epsilon_{\alpha\beta 3}}{f\rho_0} \frac{\partial \bar{p}}{\partial x_\beta} \quad (4.14)$$

$$\bar{u}_3 = 0 \quad (4.15)$$

$$\frac{\partial \bar{p}}{\partial x_3} = \rho_0 \bar{b} \quad (4.16)$$

This is a degenerate balance; the dynamics are hidden in the vorticity balance, which is obtained by taking the vertical component of the curl of the mean momentum equations:

$$\frac{\partial}{\partial t} \left(\frac{\partial^2}{\partial x_1^2} + \frac{\partial^2}{\partial x_2^2} + \frac{\partial}{\partial x_3} \frac{f^2}{N^2} \frac{\partial}{\partial x_3} \right) \frac{\bar{p}}{f\rho_0} + \dots = - \epsilon_{\alpha\beta 3} \frac{\partial}{\partial x_\alpha} \left(\frac{\partial}{\partial x_\beta} T_{\beta j} \right) \quad (4.17)$$

where:

$$T_{\alpha j} = \overline{u_\alpha u_j} - \frac{f}{N^2} \epsilon_{\alpha\beta 3} \overline{u_\beta b}.$$

We define $T_{\alpha j}$ as the effective wave stress.

Since $\epsilon_{\alpha\beta 3} \frac{\partial}{\partial x_\alpha} (x_\beta) = (\text{curl } \underline{x})_3$ we can recognize

$\epsilon_{\alpha\beta 3} \frac{\partial}{\partial x_\beta} \frac{\partial}{\partial x_j} T_{\beta j}$ as either the divergence of a wave vorticity flux, or as the 3-component of the curl of an effective wave momentum flux divergence, $\frac{\partial}{\partial x_j} T_{\beta j}$. The effective wave momentum flux differs from the actual flux only for $j = 3$, in which case each momentum flux is linked to a buoyancy flux.

For diagnostic purposes, it is helpful to return to the horizontal momentum equations for the mean flow, re-writing the effects of the wave-field as the divergence of the effective wave stress;

$$\left(\frac{\partial}{\partial t} + \underline{\bar{u}} \cdot \nabla \right) \bar{u}_\alpha + f \epsilon_{\alpha 3 \beta} \bar{u}_\beta + \frac{1}{\rho_0} \frac{\partial \bar{p}}{\partial x_\alpha} = - \frac{\partial}{\partial x_j} T_{\alpha j} \quad (4.18)$$

$$\frac{\partial \bar{p}}{\partial x_3} = \rho_0 \bar{b} \quad (4.19)$$

$$\left(\frac{\partial}{\partial t} + \underline{\bar{u}} \cdot \nabla \right) \bar{b} = 0, \quad (4.20)$$

The effective stress only appears in the horizontal momentum equations; and the geostrophic balance is implicitly recognized due to the long timescales of the flow. When the

vorticity equation is (re-) computed, the previous equation results. We shall show that, since the momentum and buoyancy components of the effective stress tensor are related, combining the two effects into an effective stress makes it easier to understand the total effects of the wavefield on a quasigeostrophic flow.

A useful technique for investigating wave-mean flow interactions is to check for phenomenological relations between the wavefield fluxes and mean-flow gradients which may be parameterized as eddy viscosities or eddy diffusivities:

$$\overline{u_{\alpha}' u_3'} = - \nu_v \frac{\partial \bar{u}_{\alpha}}{\partial x_3} \quad (4.21)$$

$$\overline{u_{\alpha}' u_{\beta}'} = - \nu_H \frac{\partial \bar{u}_{\alpha}}{\partial x_{\beta}} \quad (4.22)$$

$$\overline{u_{\alpha}' b'} = D_H \frac{\partial \bar{b}}{\partial x_{\alpha}} \quad (4.23)$$

Substitution into eq. 4.11-4.13 shows the viscous and diffusive effects of the wavefield on the mean flow, in the event that such relationships are found.

An alternative characterization of the wavefield is in terms of the effective stresses. This takes into account the combining of the vertically acting stresses and the buoyancy fluxes:

$$T_{\alpha 3} = \nu_v^E \frac{\partial \bar{u}_{\alpha}}{\partial x_3} \quad (4.24)$$

$$T_{\alpha\beta} = v_H^E \frac{\partial \bar{u}_\alpha}{\partial x_\beta} \quad (4.25)$$

where:

$$v_v^E = v_v + \frac{f^2}{N^2} D_H .$$

Since no buoyancy fluxes are involved in the horizontally-acting stresses, $v_H^E = v_H$. (It is shown in Appendix C that $\overline{u_\alpha u_\beta}$ differs from $\int d^3k \tilde{k}_\alpha \eta v_\beta$ by a quantity whose divergence has no curl, so that some caution is necessary in interpreting the relationship between v_H and action flux divergence.)

So, in terms of their effect on a geostrophic mean flow, the 1,3 momentum flux and 3 buoyancy flux appear together, in an effective stress. Under the WKB approximation in the horizontal, it will now be shown that the momentum and buoyancy fluxes of a vertically-propagating wave are linked because of the Coriolis force, and that we can write the effective stress in terms of the measured, or actual stress. The advantage of this is that the effective stress turns out to be a far less error-prone quantity to estimate from moored measurements than either the actual stress or the buoyancy flux.

The equations of motion for the fluctuating field are obtained by subtracting the mean flow equations from the un-averaged equations (Müller, 1976):

$$\begin{aligned} \frac{Du_i'}{Dt} + f\epsilon_{i3k} u_k' - b'\delta_{i3} + \frac{1}{\rho_0} \frac{\partial p'}{\partial x_i} \\ + u_j' \frac{\partial}{\partial x_j} \bar{u}_i = - \frac{\partial}{\partial x_j} (u_i' u_j' - \overline{u_i' u_j'}) \end{aligned} \quad (4.26)$$

$$\frac{Db'}{Dt} + N^2 u_3' + u_j' \frac{\partial \bar{b}}{\partial x_j} = - \frac{\partial}{\partial x_j} (u_j' b' - \overline{u_j' b'}) \quad (4.27)$$

where

$$\frac{D}{Dt} = \frac{\partial}{\partial t} + \bar{\mathbf{u}} \cdot \nabla$$

The terms on the right-hand side of 4.26 and 4.27 represent the finite-frequency source terms due to nonlinear interactions, discussed in chapter 5.3. We ignore these effects here, assuming them to be "weak in the mean."

We define quasi-Lagrangian horizontal particle displacements, ξ_α , by:

$$\frac{D\xi_\alpha'}{Dt} = u_\alpha'; \quad \overline{\xi_\alpha'} = 0. \quad (4.28)$$

Now, since the horizontal scales of the mean velocity field (~ 100 km) are much larger than the horizontal scales of the internal waves (~ 10 km), the concept of a wave which is locally plane in the horizontal is valid (WKB in the horizontal, to lowest order. Note that no assumptions about vertical scales are necessary). Since the equations are on a f -plane, we can rotate the coordinate system so the x_1 axis is aligned with the horizontal wavenumber of a single Fourier

component of the field ($\cos(k_1 x_1 - \omega t)$ dependence). The equation for the cross-wavenumber velocity is: (the x_2 gradients vanish)

$$\frac{Du_2'}{Dt} + f u_1' = 0 . \quad (4.29)$$

Hence:

$$\xi_2' = \frac{f}{\omega_0} u_1' . \quad (4.30)$$

Each wave is accompanied by a cross-wavenumber displacement, due to the Coriolis force, which is in phase with the along-wavenumber velocity. Jones (1967) found the quantity $\overline{u_\alpha' u_3'} - f \epsilon_{\alpha\beta 3} \overline{\xi_\beta' u_3'}$ to be conserved by a wave in its vertical travels, and identified the quantity as being proportional to the vertical flux of angular momentum. A similar, but interestingly different interpretation is given by Bretherton (1969b).

Since the largest part of the density perturbation is due to the vertical wave velocities, the "extra term" in Jones's expression can be related to the buoyancy flux.

Using 4.27:

$$\frac{Db'}{Dt} + N^2 u_3' + u_j' \frac{\partial \bar{b}}{\partial x_j} = 0 \quad (4.31)$$

and so

$$\begin{aligned} \frac{f}{N^2} u_2' b' &= f \overline{\xi_2' u_3'} + \frac{f}{N^2} \overline{(u_1')^2} \frac{\partial \bar{b}}{\partial x_1} \\ &= \frac{f^2}{\omega_0^2} [\overline{u_1' u_3'} + \overline{(u_1')^2} \frac{\partial \bar{b}}{\partial x_1} N^{-2}] \end{aligned} \quad (4.32)$$

(Similarly for $\overline{u_1' b'}$)

The term arising from the horizontal gradient is $O(R_i^{-1/2})$ compared to the first term. Its actual size was checked in connection with estimates of wave stress errors from the density equation (Appendix A), and found to be small, which it must be for the WKB approximation to be consistent.

Hence, as long as the mean flow Richardson number is moderately large, a buoyancy (and heat) flux accompanies the vertically acting momentum flux, and lies to the left of the momentum flux. It is due to the Coriolis force causing cross-wave velocities which are in phase with the buoyancy perturbations. The buoyancy flux can be thought of as the ability to tilt the isopleths of the mean field, and, through the thermal wind equation, affect the shear in the direction of the Reynolds stress. The effective stress due to each component is, in terms of the actual stress:

$$\begin{aligned} T_{\alpha 3} &= \overline{u_\alpha' u_3'} - \frac{f}{N^2} \epsilon_{\alpha \beta 3} \overline{u_\beta' b'} \\ &= \overline{u_\alpha' u_3'} \left(1 - \frac{f^2}{\omega_0^2} \right) \end{aligned} \quad (4.33)$$

Hence the buoyancy flux terms are of order $\frac{f^2}{\omega_o^2}$ smaller than the stress, affect the mean shear in the opposite sense as the stress, and actually cancel it as $\omega_o \rightarrow f$.

Defining spectral densities of the cross-spectra as in Appendix B, we find that the above relationships (4.33) exist among the spectral elements:

$$\overline{u_i u_j} = \int_f^N C_{ij}(\omega) d\omega \quad (4.34)$$

$$\epsilon_{\alpha\beta} C_{\beta b}(\omega) = C_{\alpha 3}(\omega) \cdot \frac{f^2}{\omega^2} \quad (4.35)$$

(Doppler effects have been neglected here.)

The buoyancy flux terms contribute comparatively little to the effective stress except at intrinsic frequencies below $2f$. For example, the effective stress obtained from the Garrett-Munk spectrum is (computed assuming $k_1 > 0$ $v_3 > 0$)

$$\begin{aligned} T_{13} &\approx \int_f^N C_{13}(\omega) \left(1 - \frac{f^2}{\omega^2}\right) d\omega \\ &= \frac{2E_o f}{\pi^2 N_o} \int_f^N \frac{d\omega}{\omega} \left(1 - \frac{f^2}{\omega^2}\right) \\ &\approx \frac{2E_o f}{\pi^2 N_o} \left[\ln \frac{N(z)}{f} - \frac{1}{2}\right] \end{aligned} \quad (4.36)$$

while the directly-computed actual stress is:

$$\begin{aligned}\overline{u_1' u_3'} &= \frac{2\tilde{E}_o f}{\pi^2 N_o} \int_f^N \frac{d\omega}{\omega} \\ &= \frac{2E_o f}{\pi^2 N_o} \ln \frac{N(z)}{f}\end{aligned}$$

$$\text{where } E_o = 30 \text{ cm}^2 \text{ s}^{-2}.$$

The two integrands are shown in fig. 4.3; they differ by a factor of $1 - \frac{f^2}{\omega^2}$, which is only important near the inertial frequency. We note also that, for $\frac{N(z)}{f} \sim 50$:

Reynolds stress	$\int_f^N \frac{d\omega}{\omega} \approx 3.91$	$\int_{2f}^N \frac{d\omega}{\omega} \approx 3.22$
Effective stress	$\int_f^N \frac{d\omega}{\omega} (1 - \frac{f^2}{\omega^2}) \approx 3.41$	$\int_{2f}^N \frac{d\omega}{\omega} (1 - \frac{f^2}{\omega^2}) \approx 3.1$

(4.38)

Hence, by estimating the actual Reynolds stress with a lower integration limit of $2f$, we eliminate the most troublesome frequencies in terms of noise, and also eliminate the frequencies at which the actual momentum flux is partially cancelled by the perpendicular buoyancy flux. The physical stress estimated with a lower bound of $2f$ should be about 20% lower than the total actual stress, but only 7% lower than the total effective stress.

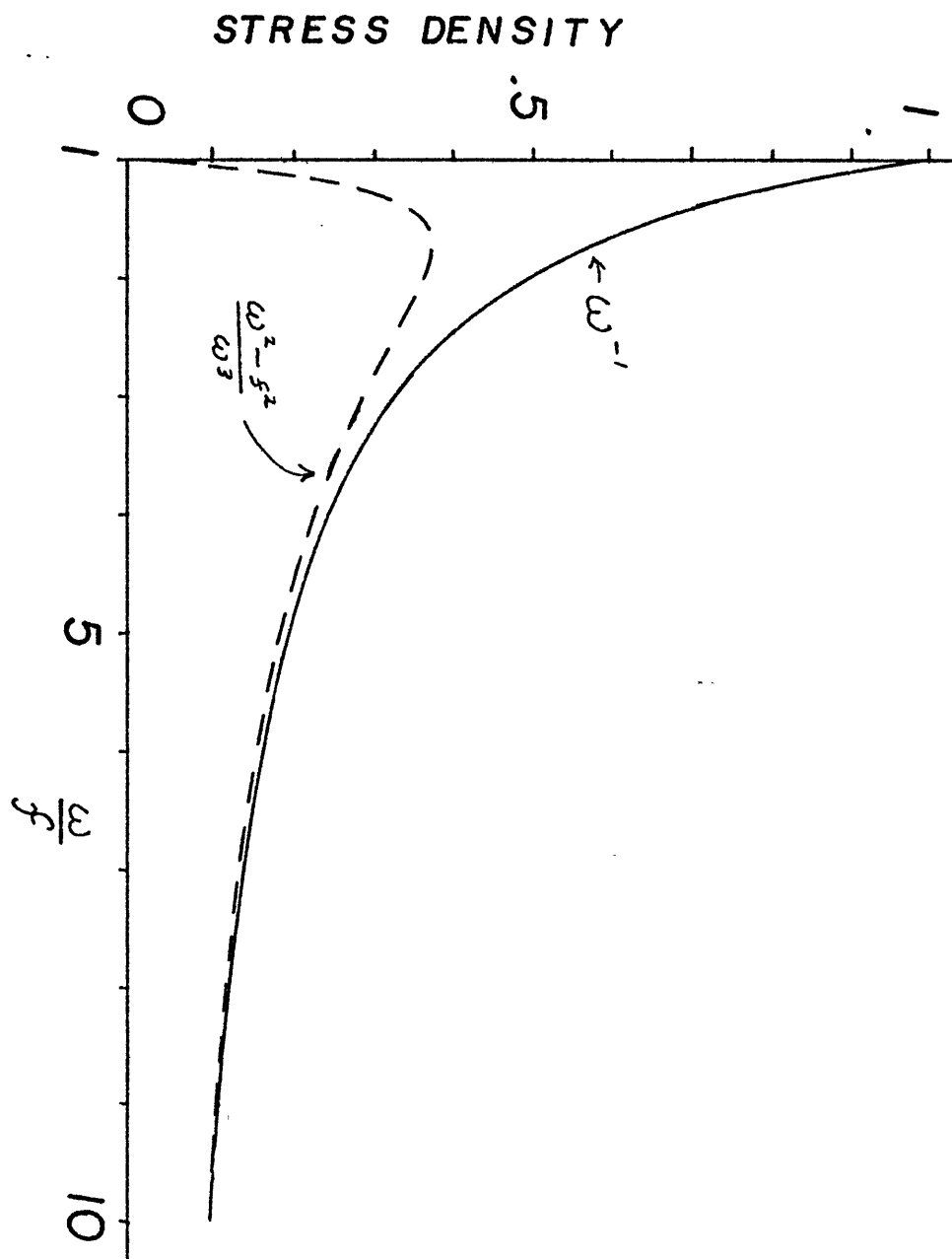


Figure 4.3 Integrands of eq. 4.36 and 4.37 which contribute to actual stress (solid line) and effective stress (dashed line) plotted against frequency.

The terms "momentum flux" and Reynolds stress will be used to indicate the physical quantities, while the term "effective momentum flux" will be used to indicate the quantity associated with wave action fluxes ($T_{\alpha j}$).

4.3 Correlations of Wave-induced Reynolds Stress with Mean Flow

a) Vertical Eddy Viscosity

The main purpose of this section is to investigate Hypothesis #1; the possibility that the wavefield has any tendency to exert vertically acting stresses which vary consistently with the mean flow, and in so doing cause a net energy exchange.

One way to do this, as mentioned in 4.2, is to check for eddy viscosity correlations:

$$\overline{u_{\alpha} u_3} = -v_v \frac{\partial \bar{u}_{\alpha}}{\partial x_3} \quad (4.39)$$

This is suggested by the results of a theory of internal wave-mean flow interaction by Müller (1976). Under the assumption that the interaction is local (meaning that the waves are affected primarily by the local value of the shear), Müller predicts that a vertical eddy viscosity of $v_v \sim 4000 \text{ cm s}^{-2}$ should be observed.

Sanford (1975) has obtained a realization of the low-frequency velocity shear from the MODE-1 region, reproduced in Fig. 4.4. Recent computations (Sanford, personal communication, 1976) on this profile and an independent

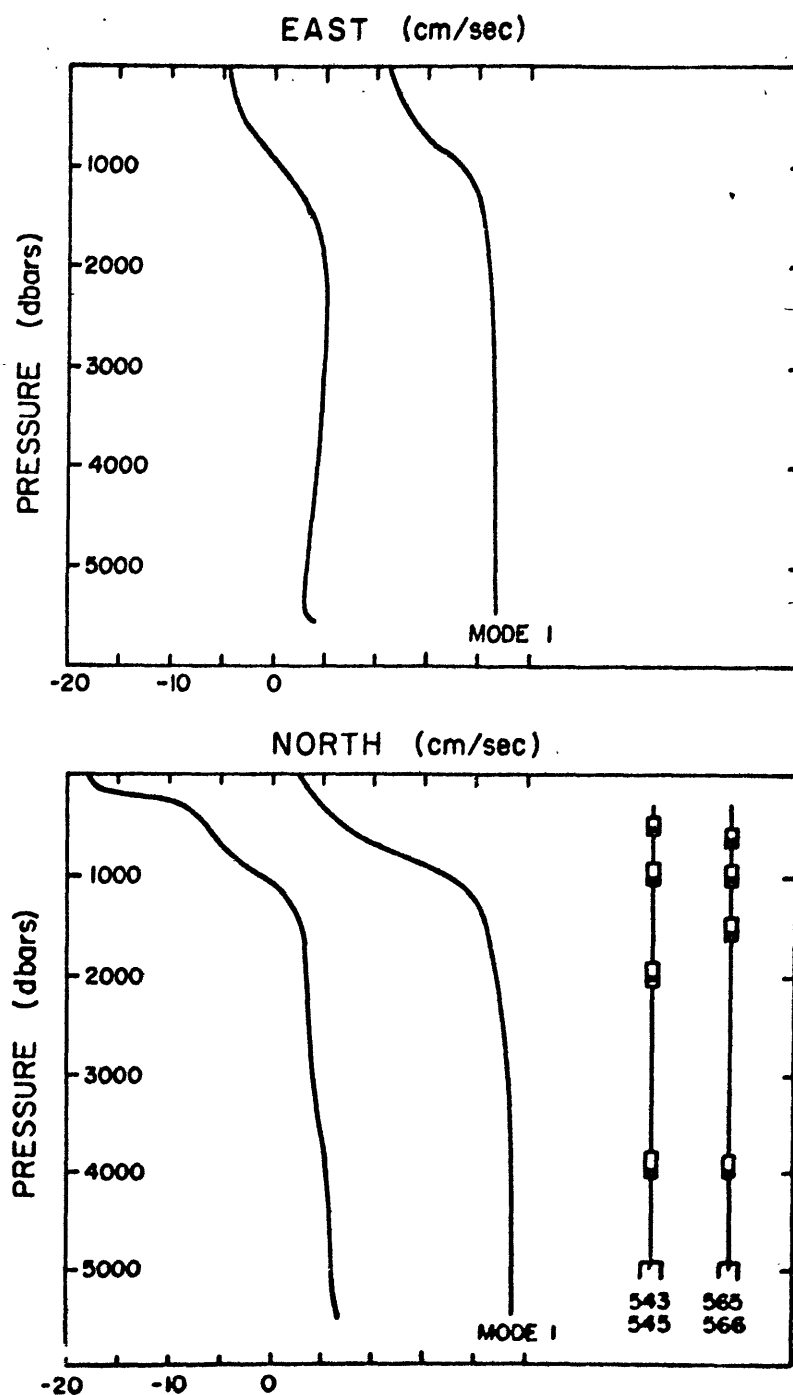


Figure 4.4 Low-frequency MODE-region shear profile from Sanford (1975), computed first baroclinic mode, and locations of current meters on moorings analyzed.

realization indicate that a very high percentage (about 95%) of the baroclinic variation is in the first baroclinic Rossby wave mode. Richman (1976) found a similar behavior from analysis of current meter records. Fig. 4.4 also shows the first baroclinic mode for the MODE-1 region, and the current meter locations. The best estimate of the shear, given the instrument locations available, is from a first-difference of the 500 m (or 600 m at the Array 2 moorings) and 1000 m velocities. Assuming a local wave-mean flow interaction, the largest local shear, and hence the largest stress signal, should be observed at the 1000 m instrument. The "best-estimate" of the wavefield eddy viscosity is thus afforded by estimating the shear as a one-sided difference, and comparing to the stresses at 1000 m. An alternative shear estimate, corresponding to a more "non-local" interaction (averaged over a greater depth interval) was provided by differencing the 500 (600) and 2000 (1500) m velocities. Note that the shear estimates used are an average over a finite depth interval. The shear estimated from the upper two levels will tend to underestimate the maximum (as a function of depth) shear by a factor of 1.5-2. The large vertical scale average will tend to underestimate the maximum shear by a factor of 4-6. This will increase the eddy viscosity estimates over what might be estimated at the level of maximum shear.

Two different frequency bands were used in the eddy viscosity computations. The "total" band, with integration

limits from inertial frequency (.04 cph) to the Nyquist frequency, yielded an estimate of the "total" wave stress, including the near-inertial frequencies. As explained in Appendix A, the near-inertial frequencies have many error problems. In 4.2 it was shown that the effects of stresses at these frequencies on a quasigeostrophic mean flow are partially cancelled by the accompanying buoyancy flux. A better measure of the effect of the wavefield is afforded by the "effective" stress (introduced in chapter 4.2):

$$(\overline{u_1' u_3'})^E \approx \int_f^N d\omega C_{13}(\omega) \left(1 - \frac{f^2}{\omega_o^2}\right). \quad (4.40)$$

The continuum band provides an accurate an noise-free estimate of 95% of this stress. Since the lower summation limit of the continuum band is .1 cph, the effects of the semidiurnal tides are also excluded from this estimate. Being the most noise-free and accurate estimate of the "effective" wavestress, the continuum band stress estimates were the most useful ones. Müller (1976) states that if waves in the frequency range $f - 2f$ were excluded from consideration in his theory, the resulting eddy viscosity estimate would be essentially unchanged.

The model assumed for the least-squares regression of the stress time-series on the shear time series is:

$$\overline{u_\alpha' u_3'} = -v_v \frac{\partial \overline{u}_\alpha}{\partial x_3} + c + (\text{noise}) . \quad (4.41)$$

So that, denoting:

$$y_i = \overline{u_\alpha u_3} (t)$$

$$x_i = \frac{\partial \bar{u}_\alpha}{\partial x_3} (t)$$

at time $i\Delta t$

we have:

$$v_v = \rho_{xy}(\tau) \sigma_y / \sigma_x \quad (4.42)$$

where

$$\rho_{xy}(\tau) = \frac{\sum_{t=r}^s (x_t - \bar{x})(y_t - \bar{y})}{(n - |\tau|) \sigma_x \sigma_y}$$

$$\bar{x} = \frac{1}{n} \sum_{t=r}^s x_t \quad (\text{similarly for } y)$$

$$\sigma_x = \frac{1}{n - (\tau)} \sum_{t=r}^s (x_t - \bar{x})^2$$

$$r = \begin{cases} 1 & \tau \geq 0 \\ |\tau| & \tau < 0 \end{cases} \quad (4.43)$$

$$s = \begin{cases} n - \tau & \tau \geq 0 \\ n & \tau < 0 \end{cases}$$

τ is chosen to maximize ρ_{xy} at small positive lags to allow for wave propagation delays.

38

Since the statistical variations of the stress estimates dominate the errors in shear estimation, the regression model assumes all the "noise" is in the "y" (stress) variable. Most uncertainty computations for regressions assume that the two series are independent, random sample pairs drawn from a joint-normal distribution. These uncertainty estimates are generally far too optimistic if the time series involved are not "white" or if either or both series does not have a Gaussian distribution. Accordingly, the higher moments of both series were estimated directly, and (twice) the expected variance of the slope estimate was computed according to the method described in Appendix A. This was taken as a 95% confidence interval for the slope estimate, which accounted for the non-whiteness and non-normality of the data.

Figure 4.5 shows a scatterplot (dots) of continuum band stress at 1 km (y-axis) versus estimated shear (x-axis) for mooring 543, one of the quiet moorings. The computed regression line (solid line) corresponding to the effective eddy viscosity estimate, $\nu_v = 29.2 \pm 112 \text{ cm}^2 \text{ s}^{-1}$, and the 95% confidence limits (dashed lines) are shown also. The regression line which should result from $\nu_v = 3680 \text{ cm}^2 \text{ s}^{-1}$ (80% of the Müller estimate, corresponding to the continuum band) is shown as a heavy solid line. From the relatively small scatter of the observed stresses on this diagram, it is apparent that the small estimated eddy viscosity cannot be

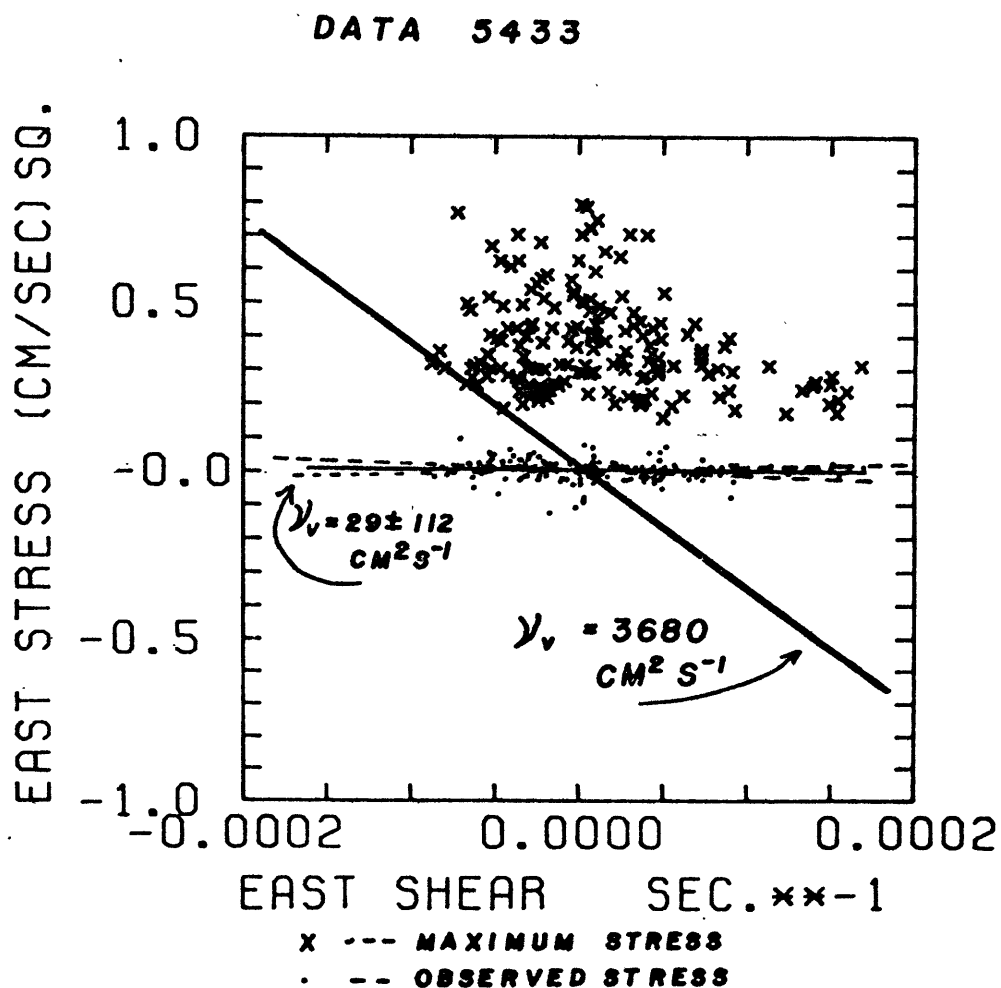


Figure 4.5 Eddy viscosity regression (dots) for mooring 543, 1000 m. The regression line corresponding to Müller's (1976) eddy viscosity estimate is shown for comparison. The maximum stress the wavefield could exert is shown by crosses.

a statistical fluctuation due to a noise problem; the stresses are an order of magnitude smaller than they would be according to the estimates of Müller. If the scatter of the data were as observed, only about the indicated $v_v = 3680 \text{ cm}^2 \text{ s}^{-1}$ slope, the correlation coefficient (an indication of the signal-to-noise ratio) would be 0.99.

Also shown in figure 4.5, as crosses, are the continuum band estimates of $(C_{11}, C_{33})^{1/2}$, the lower half of the 1,3 coherence. This is the absolute maximum stress that the wavefield can exert. It is readily seen that there is enough energy in the wavefield (if it were made asymmetric by the Müller interaction) to enable the wavefield to exert the stresses predicted by the Müller theory. Only for shears in excess of about 10^{-4} s^{-1} would the wavefield find it impossible to exert the predicted stresses without becoming more energetic.

Estimates of the effective eddy viscosity using the continuum band stress estimates at 1000 m depth are shown in table 4.1. The upper pair of rows list the average and standard deviations (σ) of the stress estimates. The second block of rows refers to a regression against a shear estimated as the difference between the upper and 1000 m levels, assuming a fairly local interaction. The average and standard deviation of the shear, the correlation coefficient, and the estimated eddy viscosity are listed here. At the bottom of this block are also listed the expected stress

Table 4.1
VERTICAL EDDY VISCOSITY ESTIMATES
Continuum Band

	543		545		566		565	
	East	North	East	North	East	North	East	North
1000 m (Level 2)								
Mean C_{uw} , cm^2/s^2	0	3.25×10^{-3}	-7.2×10^{-3}	.012	-.0219	.0087	.000	-.008
σ , "	.0314	.0277	.0466	.0446	.0774	.0718	.085	.097
Difference (Level 1-2)								
Mean Shear, s^{-1}	1.07×10^{-5}	4.72×10^{-5}	2.98×10^{-5}	1.05×10^{-5}	1.257×10^{-4}	4.2×10^{-5}	3.3×10^{-5}	2.39×10^{-5}
σ , " , s^{-1}	5.46×10^{-5}	5.97×10^{-5}	3.996×10^{-5}	3.613×10^{-5}	1.634×10^{-4}	1.885×10^{-4}	1.8×10^{-4}	2.53×10^{-4}
Correlation coeff.	-.052 \pm .2	-.055 \pm .2	.030 \pm .2	.053 \pm .3	-.332 \pm .2	-.116 \pm .15	-.230 \pm .22	-.215 \pm .23
Eddy viscosity, cm^2/s	<u>29.1\pm112</u>	<u>26\pm90</u>	<u>-35\pm221</u>	<u>-66\pm347</u>	<u>157\pm105</u>	<u>44\pm57</u>	<u>103\pm97</u>	<u>82\pm86</u>
σ , C_{uw} } $\frac{\text{if } v_v}{= 3680 \text{ cm}^2/\text{s}}$		0.22		0.14		.62		.73
Correlation		.99		.95		.99		.99
Difference (Level 1-3)							NOT COMPUTED	
Mean Shear, s^{-1}	4.91×10^{-6}	1.67×10^{-5}	-3.38×10^{-6}	2.4×10^{-6}	5.78×10^{-5}	2.2×10^{-5}		
σ , " , s^{-1}	16.7×10^{-6}	2.46×10^{-5}	1.81×10^{-5}	1.24×10^{-5}	8.61×10^{-5}	1.017×10^{-4}		
Correlation Coeff.	.008 \pm .2	-.041 \pm .2	.073 \pm .2	-.003 \pm .2	-.308 \pm .2	-.174 \pm .18		
Eddy viscosity, cm^2/s	- 15 \pm 375	47 \pm 230	-189 \pm 518	12 \pm 800	315 \pm 205	128 \pm 132		

standard deviation if the eddy viscosity were $3680 \text{ cm}^2 \text{ s}^{-1}$ (v_v times the shear standard deviation) and the correlation coefficient that we would expect to observe if the eddy viscosity were that large (using the original scatter as an estimate of the noise level).

It is readily seen that the eddy viscosity estimates at the two quiet moorings (545 and 543) are consistent with zero eddy viscosity, with confidence limits an order of magnitude smaller than the eddy viscosity predicted by the Müller theory. At these moorings, the shear is weak enough to meet the conditions for validity of the Müller theory, and yet strong enough to induce a stress signal which would have been clearly observable. Any interaction between the wave-field and the mean flow is much weaker than predicted by Müller, and is too weak to observe by these methods at locations where the mean flow is as weak as at these moorings.

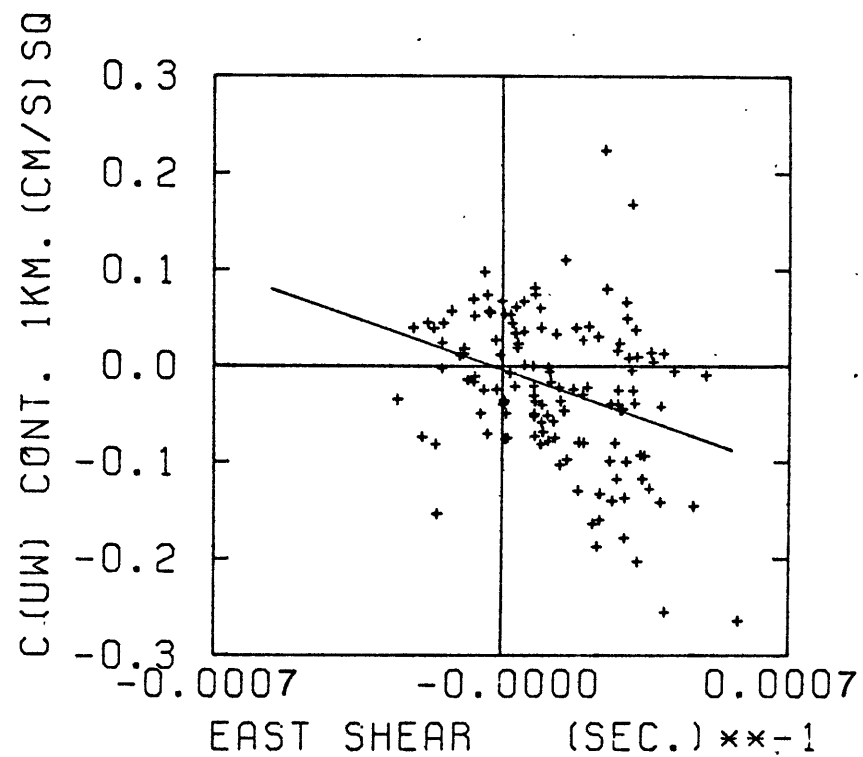
The bottom block of rows lists the eddy viscosity estimates using the shear estimated from the difference of the upper (600 or 500 m) and intermediate (1500 or 2000 m) levels, assuming a far less local interaction, and effectively averaging over a large vertical scale to obtain the shear estimate. The estimated shears are very much weaker because of the large depth interval used for the average, and correspondingly the eddy viscosity confidence limits are much larger. However, the estimates are consistent with zero vertical eddy viscosity.

C (UW) IS LAGGED BY 74 HOURS

$$R = -.33$$

$$\nu_v = (157 \pm 105) \text{ cm./s.}^2$$

5663



21:53 NOV 02, '76

Figure 4.6 Vertical eddy viscosity regression for continuum band at mooring 566, 1000 m.

99

Statistically meaningful, but small, eddy viscosities were estimated at the two energetic moorings, 565 and 566. For example, a scatterplot of 1000 m continuum band stress vs. East shear (600 - 1000 m difference) and the computed regression line are shown in fig. 4.6 for data 5663. This regression corresponds to $v_v = 157 \pm 105 \text{ cm s}^{-2}$. However, the estimates were of opposing sign on either side of the thermocline. The geometric mean (East and North) "average" eddy viscosity estimate from the energetic moorings was (based on the shear estimates from 600-1000 m):

$$\begin{array}{ll} 600 \text{ m} & v_v = (-100 \pm 85) \text{ cm s}^{-2} \\ 1000 \text{ m} & v_v = (+100 \pm 75) \text{ cm s}^{-2} \end{array} \quad (4.44)$$

Of the possible errors in estimating the stress and shear which were considered in Appendix A, all were negligible for $\omega > 2f$ as long as the local velocity was less than about 15 cm s^{-1} . The errors considered included mooring motion, various neglected terms in the buoyancy equation used to estimate u_3' , and the effects of finite rotor stall speed. The possibility of finestructure in current and temperature combining to induce false stresses was investigated with inconclusive results.

The high (25 cm s^{-1}) mean velocities at the energetic moorings caused slight problems with the Reynolds stress estimates at 600 m, due to the neglected Doppler shift term in the heat equation used to estimate u_3' . The dominant

error in the stress measurements was found in Appendix A to be:

$$\overline{u_{\alpha} u_3}_{\text{measured}} = \overline{u_{\alpha} u_3}_{\text{true}} + \frac{\bar{u}_{\alpha}}{\frac{\partial \bar{T}}{\partial x_3}} \overline{u_{\alpha} \frac{\partial T}{\partial x_{\alpha}}} \quad (4.45)$$

The error term was estimated from the Garrett-Munk (1975) model spectrum, and was found to change sign with the sign of the vertical asymmetry of the wavefield. For \bar{u} positive, and an asymmetry of:

$$\frac{\epsilon(v_3 > 0) - \epsilon(v_3 < 0)}{\epsilon(v_3 > 0) + \epsilon(v_3 < 0)} = \pm .05 \quad (4.46)$$

(This is a reasonable maximum value suggested by Briscoe, 1977, personal communication.) The contribution to the stress signal was $\pm 10\%$ of the observed (positive) signal. This uncertainty was considered in the 600 m eddy viscosity estimate. However, by using the Garrett-Munk spectrum for the estimate, we have assumed that the wave spectrum is now altered much by the shear flow. This assumption will be questioned shortly.

In addition to "eddy viscosity" regressions, the average (500 m plus 1000 m) Reynolds stresses and the stress divergences (500 m minus 1000 m) were checked against estimates of the shear, with the same results. The stress divergence from mooring 543 (total band) was marginally significant in the North direction, but not in the East. This was ascribed to statistical fluctuation, consistent with uncorrelated data.

A similar vertical eddy viscosity estimate from 40 days of data on the Trimooored Internal Wave Experiment (T. Joyce, personal communication) yielded estimates of $v_v = 0(-10^3)$ $\text{cm}^2 \text{s}^{-1}$ for the continuum band, and $v_v = 0(-3 \times 10^3)$ $\text{cm}^2 \text{s}^{-1}$ for the total band. However, the statistical uncertainty of this estimate is quite large due to the short data length. Examination of the time series shows that, effectively, one eddy event was observed. The data from mooring 543 were broken up into ten 40-day realizations of stress and shear time series, and the eddy viscosity was estimated for each of these pieces. One piece gave an estimate of $v_v = 3800$ $\text{cm}^2 \text{s}^{-1}$, with a correlation coefficient of 0.6 for the total band, and other pieces yielded estimates of $0(-10^3 \text{ cm}^2 \text{s}^{-1})$. Hence the large v_v estimated from IWEX seems to be consistent with statistical fluctuations of the estimate due to the relatively short data length.

b) Total Band Eddy Viscosity and Horizontal Eddy Diffusivity

To check for unexpectedly strong involvement of near-inertial oscillations in organized momentum and buoyancy transfer, cross-spectra were estimated in the total frequency band (f-N). Vertical eddy viscosity and horizontal diffusivity estimates were made with wavefield quantities derived from the total band.

In computing the regressions using the stress estimated from the "total" band it was found that the significant eddy

viscosity estimates increased by about 25% over the continuum band estimates. Assuming the stress distribution from GM 75 would lead us to expect a 20% increase. However, most of this increase is probably offset by buoyancy flux effects. It was also found that the stress variance for the total band increased by a factor of two, decreasing the signal-to-noise ratio and the observed correlation coefficients correspondingly. The result is that the eddy viscosity estimates using the "total" band are slightly increased, but the confidence limits on the estimates are increased by a factor of about two. The results are essentially unchanged from the continuum band estimate; just much "noisier." It is strongly felt that the continuum band yields the most accurate eddy viscosity estimate.

The horizontal eddy diffusivity was estimated by first computing heat flux time series, summed over the total internal wave band. This was only attempted for the quiet moorings, and no correction was made for mooring motion. If a geostrophic balance is assumed for the mean flow, then an estimate of the horizontal eddy diffusivity is provided by a regression of the northward heat flux on the east mean shear, derived from the 500 m-1000 m velocity difference:

$$\overline{u_2' T'} = D_H \left(\frac{\bar{T}_z f}{N^2} \right) \frac{\partial \bar{u}_1}{\partial x_3} \quad (4.47)$$

$$\overline{u_1' T'} = -D_H \left(\frac{\bar{T}_z f}{N^2} \right) \frac{\partial \bar{u}_2}{\partial x_3} \quad (4.48)$$

where:

\bar{T}_z = mean vertical temperature gradient

$$= [.012^\circ \text{ C m}^{-1}]$$

$$N = [2 \text{ cph}]$$

$$f = [.04 \text{ cph}] .$$

This was suggested by H. Bryden (personal communication, 1976). No statistically significant correlations of the above type were found; however, the heat flux variance was so large that the 95% confidence limits on D_H are very large. We estimate:

$$D_H = 0 \pm 5.8 \times 10^5 \text{ cm}^2 \text{ s}^{-1} . \quad (4.49)$$

The confidence limits are an order of magnitude larger than the theoretical eddy diffusivity of $-4.6 \times 10^4 \text{ cm}^2 \text{ s}^{-1}$ predicted by Müller. Hence the surprisingly large error bounds on the diffusivity estimates allow no practical evaluation of the strength of this effect.

c) Cross-viscosity

The quiet moorings exhibited a tendency for the total band wave momentum flux to lie to the left of the shear estimates:

$$\overline{u_1' u_3'} = -a \frac{\partial u_2}{\partial x_3} \quad (4.50)$$

$$\overline{u_2' u_3'} = a \frac{\partial u_1}{\partial x_3} \quad (4.51)$$

where $\frac{\partial u_1}{\partial x_3}$ is the velocity shear estimated between 500 and 2000 m. The effect was most noticeable at mooring 545, which had the weakest shear, and was not observable at 566 which had the strongest. An example of the strongest correlation is shown in fig. 4.7, which shows a scatter plot of $\overline{u_2' u_3'}$ vs. $\frac{\partial \bar{u}_1}{\partial x_3}$ for mooring 545. Although the computed regression slope is statistically meaningful, with a correlation coefficient of +.48 in this case, the contribution to this effect comes almost entirely from the near-inertial frequencies, where estimation of wave stresses tends to be most error-prone. Therefore we cannot be certain that the effect is real, and not just related to a problem in stress estimation. (It should be noted, however, that the u_2' , u_3' quadrature component (similar to $\overline{u_2' b'}$), shows no such correlation.)

The estimated magnitudes of the coefficient a , computed as the mean of the East and North regressions, are:

$$\left. \begin{array}{ll} 545 & a \approx 200 \text{ cm}^2 \text{ s}^{-1} \\ 543 & a \approx 100 \text{ cm}^2 \text{ s}^{-1} \\ 566 & a \approx 0 \text{ cm}^2 \text{ s}^{-1} \end{array} \right\} \pm 200 \text{ cm}^2 \text{ s}^{-1} \quad (4.52)$$

Since the stresses are perpendicular to the shears, no energy exchange occurs. The stresses merely try to force the

545LOWPASSED

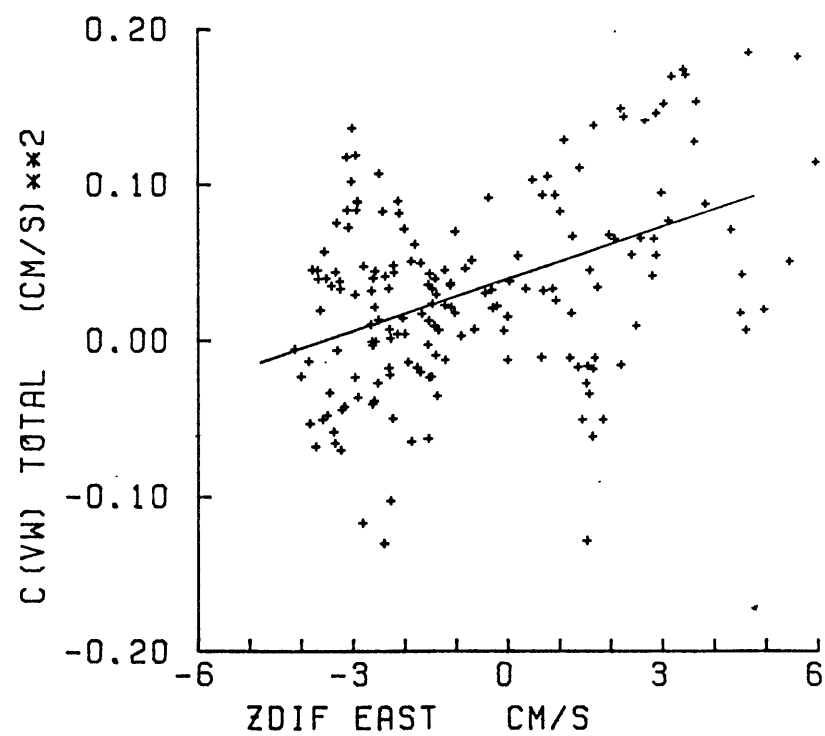


Figure 4.7 "Cross-viscosity" correlation. Total band North - u_3 Reynolds stress vs. East shear for mooring 545.

mean shear to rotate slowly to the left, at an angular velocity corresponding to 400 day (or longer) periods. This effect is analogous to the effects of the Coriolis force in causing inertial oscillations. The Coriolis force can do no work, since it acts at right angles to the velocities. The shear data show no convincing evidence of anticlockwise rotation at low frequencies.

The effect of these stresses on the vorticity balance of a quasi-geostrophic mean flow can be easily computed by substituting expressions 4-42, 43 into the horizontal momentum equations and computing the curl. The stress terms come out to be:

$$-a \frac{\partial}{\partial x_3} (\nabla_H \cdot \bar{u}) . \quad (4.53)$$

Since the mean flow is, to a good approximation, horizontally non-divergent, these stresses have no effect on the mean flow vorticity balance. In addition, since the contribution to these stresses is from the inertial frequencies, the effects are probably cancelled by opposing buoyancy flux effects. (We can't estimate these because of the noise.)

d) Further Investigations of the Momentum Fluxes at the Energetic Moorings

In 4.3(a-c) we have investigated the wavefield-mean flow interaction within the framework of Hypothesis #1, the hypothesis of a local, eddy viscosity type of interaction. We now look more closely at the behavior of the

stresses at the energetic moorings, and compare the observations to the alternative hypotheses discussed in the introduction to this chapter.

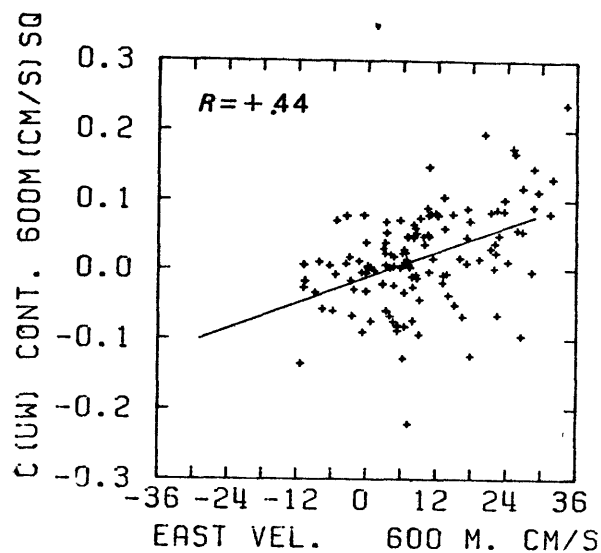
Figure 4.8 shows scatterplots of the continuum band C_{13} stress estimates at 600 m (upper plot) and 1000 m (lower plot), plotted against the East mean velocity from 600 m. The regressions on the 600 m velocity tended to yield larger correlation coefficients than against the shear estimates. As can be seen, associated with a positive velocity is a positive estimated stress at 600 m and a negative estimated stress of similar magnitude at 1000 m. Under the local interaction hypothesis, we would estimate a strong momentum flux divergence in the vicinity of the thermocline. Dividing the water column into three layers, with the 600 m and 1000 m levels as boundaries, we see that, if the stresses are as observed, there is a mean transfer of momentum out of the shear region. This would tend to accelerate the upper and lower layers at the expense of the central layer, resulting in a very odd effect.

To better estimate the correlation coefficients in all regressions that follow in this section, the low-pass filter described in chapter 2 was used to improve the signal-to-noise ratio of the wave stresses by a factor of about 2.

Time series (filtered) of the continuum band stresses at 600 and 1000 m, the 600 m velocity, and the shear across the thermocline are displayed in fig. 4.9 along with the

C(UW) IS LAGGED BY 37 HOURS

5663



C(UW) IS LAGGED BY 74 HOURS

5663

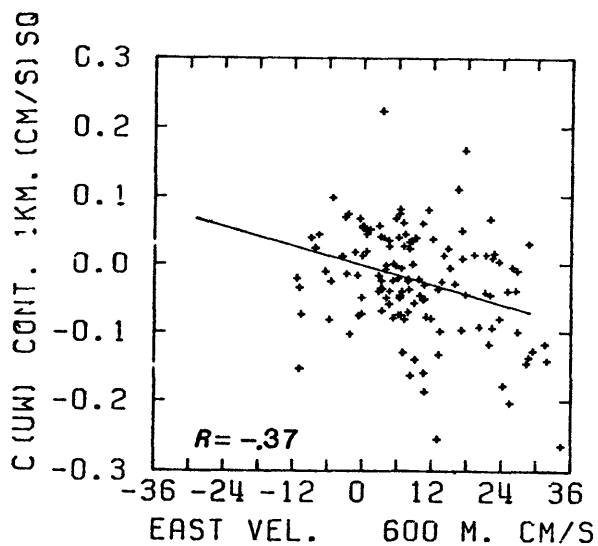


Figure 4.8 Scatterplots and regressions for continuum band stress at 600 m (upper) and 1000 m (lower) vs. 600 m East velocity.

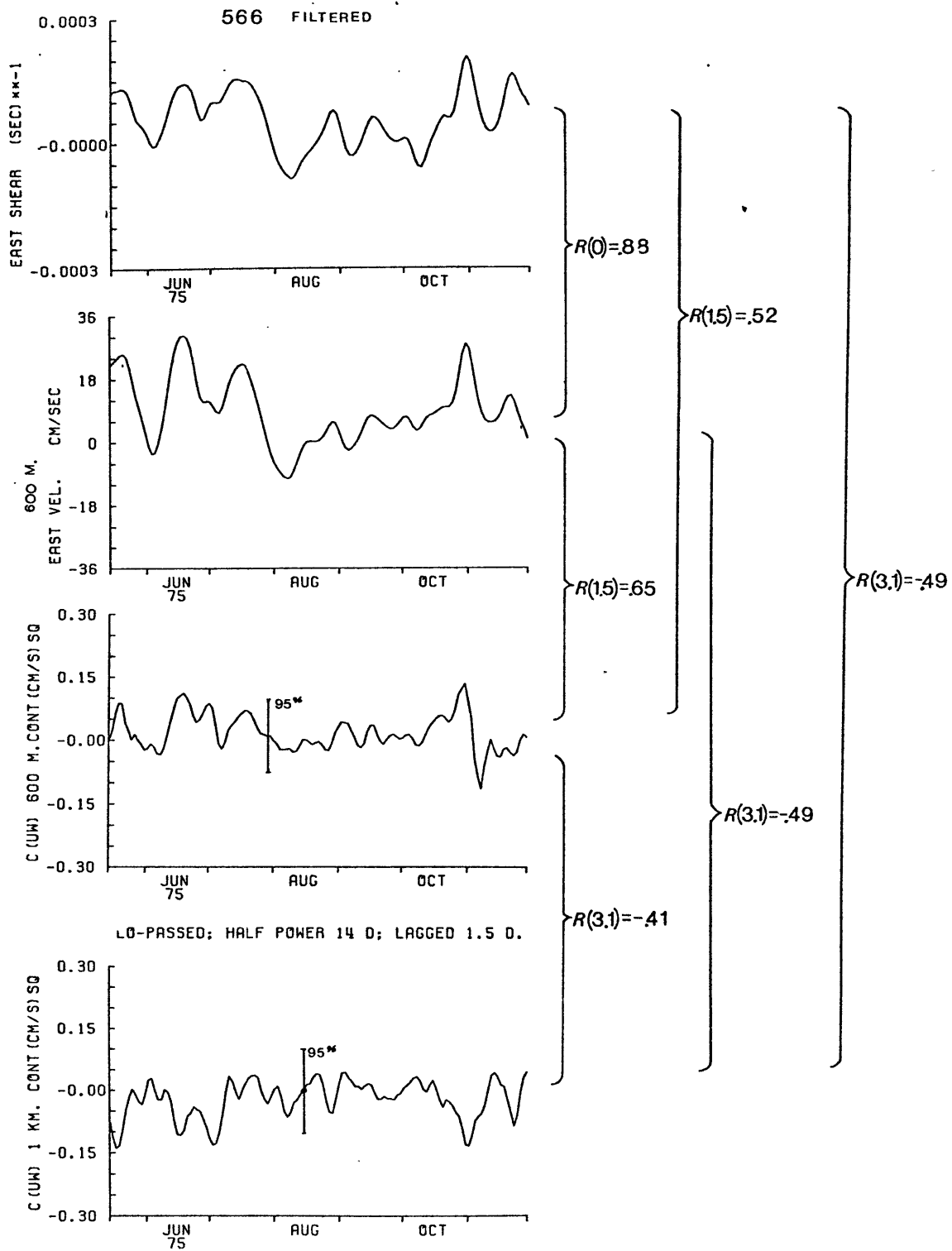


Figure 4.9 Low-pass filtered time series of East shear, East velocity, 600 m, and stresses at 600 m and 1000 m for the continuum band, mooring 566. Correlations between pairs of series are shown at right.

correlation coefficients for each pair of series. The East direction for mooring 566 is shown. Corresponding correlations for the North direction are significant but weaker. The difference seems to be associated with a slightly more intense mean-square velocity at 600 m, and not a difference in shear intensity.

Note first that the correlation between the shear and the 600 m velocity is very high, mainly because the dominant part of the shear estimate is the 600 m velocity, which is generally about twice as large as the 1000 m velocity. Since the two time-series are so well related, it is not easy to tell them apart in a statistical sense. The 600 m stress is better correlated with the 600 m velocity than the 600 m-1000 m shear.

The 600 m and 1000 m stresses appear to be about equally intense, as we have seen from figure 4.8. The shear estimates are not as well correlated with each other as with the velocity or shear. The 95% confidence limits shown were computed following Jenkins and Watts (1969), assuming a white spectrum across the entire continuum band. This is obviously untrue, and as discussed in Appendix A, one effect of the non-whiteness (non-overlap of the two autospectra in frequency space) would tend to decrease the confidence limits, while the other (a reduction of the effective amount of averaging because of the 'Q' of the spectrum) would tend to increase the confidence limits. Judging from the level of white

noise in the spectra of the stress time series, and from the signal-to-noise ratio indicated by the correlation coefficients in figure 4.9, the confidence limits shown are conservative by 25% or so.

Table 4.2 lists the maximum lagged correlation coefficients and the lag in hours (positive lag corresponds to the stress being delayed) for several mean flow variables versus wavefield stress variables. The upper set is from mooring 566 (East) and the lower set is from mooring 565 (North). Note that the stresses are not observable at the 1500 m level (or 4000 m); they are only significant near the high-shear region. Also, it is virtually impossible to distinguish between the correlations involving the 600 m stress and the estimated divergence. Similarly, the wave variables tend to be better correlated with the 600 m velocity than with the shear estimated by differencing the 600 and 1000 m velocities.

Under Hypothesis #1, the wavefield is only slightly modified from the Garrett-Munk spectral shape, and so Doppler shift effects would be negligible. Any stresses, observed and real, should be better related to the shear than the velocity. We do not expect the stresses to be of opposing sign under this hypothesis. The observed stresses are of the opposite sign from what we expect if the stresses are related to critical layer absorption (Hypothesis #2). The observations are, however, consistent with Hypothesis #3,

Table 4.2

A. 566 REYNOLDS STRESS CORRELATIONS. EAST
DIRECTION ONLY: LOW PASS FILTERED

Reynolds Stress	\bar{u} 600 m	\bar{u} 1000 m	$\Delta\bar{u}$ 600-1000	$\Sigma\bar{u}$ 600+1000
Stress divergence, 600-1000 m [Lag in hours]	.661 +37	.55 +37	.56 +37	.65 +37
Stress, 600 m	.65 +37	.55 +37	.52 +37	.63 +37
Stress, 1000 m	-.49 +74	-.37 +74	-.49 +74	-.46 +74
Stress, 1500 m	0	0	0	0

B. 565 REYNOLDS STRESS CORRELATIONS. NORTH
DIRECTION ONLY: LOW PASS FILTERED

	\bar{u}_{600}	$\Delta\bar{u}_{6-10}$
Stress divergence	.671 0	.530 -37
Stress 600 m	.733 +37	.529 -37
Stress 1000 m	-.417 -37	-.317 -37

generation of internal waves at the level of maximum shear, such that the generated waves travel upward and downward from the region, with horizontal phase speed equal to the velocity at the generation zone. Denoting \bar{u}_g as the phase speed of the waves (we are assuming a unidirectional mean flow for simplicity), \bar{u}_6 as the mean velocity at 600 m, and \bar{u}_{10} as the mean velocity at 1000 m, we obtain, from equation 4.3:

$$T_6 = - \frac{T_g}{1 - \frac{\bar{u}_6}{\bar{u}_g}} \quad (4.54)$$

$$T_{10} = - \frac{T_g}{1 - \frac{\bar{u}_{10}}{\bar{u}_g}} \quad (4.55)$$

where:

T_g is the actual stress exerted by the generated waves (approximately conserved with depth)

T_6, T_{10} are the observed stresses at the 600 m and 1000 m levels, respectively.

Making use of the fact that the observed stresses at each level were about equal and opposite, we find:

$$\bar{u}_g = \frac{\bar{u}_6 + \bar{u}_{10}}{2} \quad (4.56)$$

$$\begin{aligned}
 T_6 &= - T_{10} \\
 &= \frac{\bar{u}_6 + \bar{u}_{10}}{\bar{u}_6 - \bar{u}_{10}} T_g .
 \end{aligned}
 \tag{4.57}$$

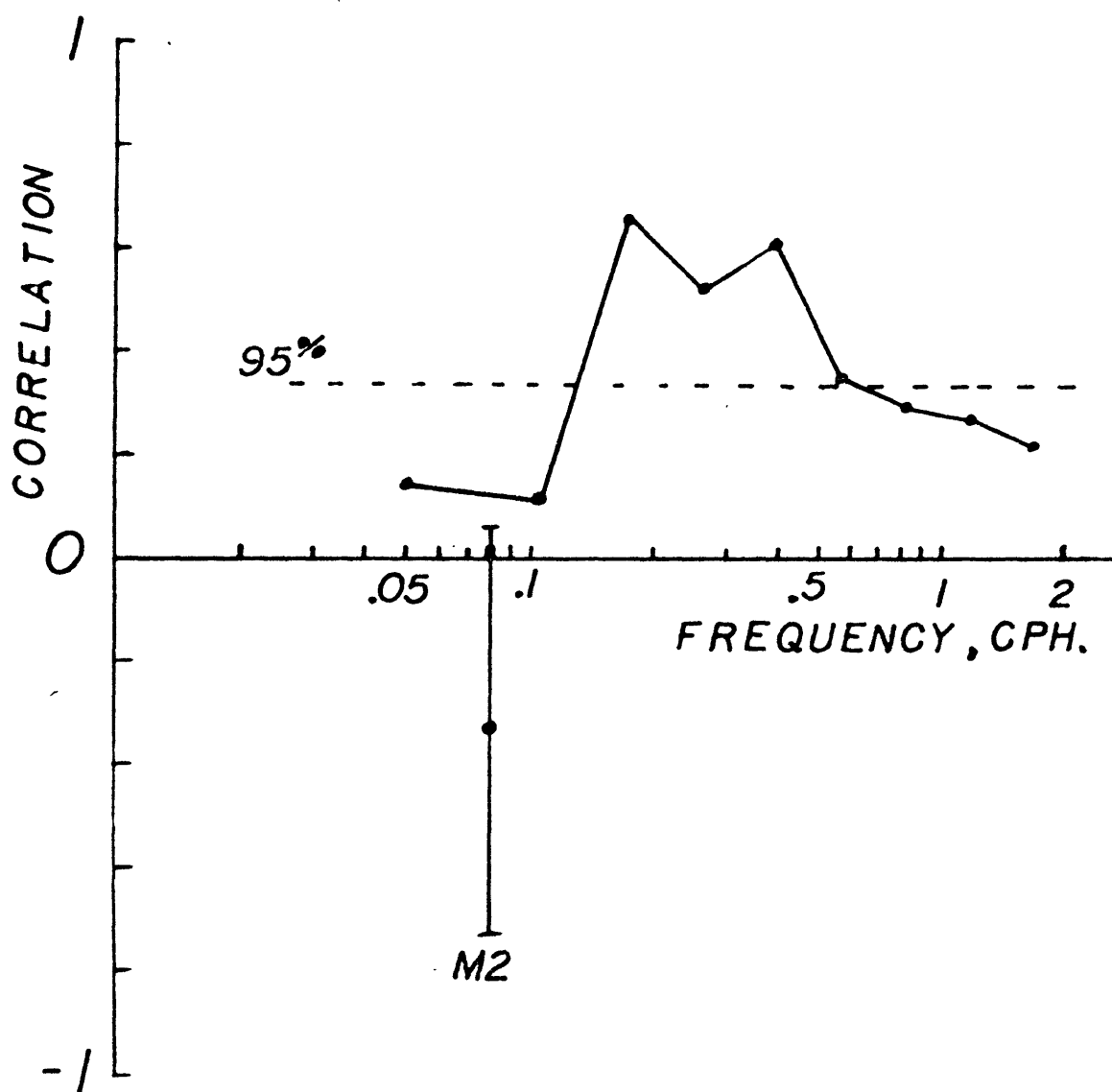
The larger velocity is \bar{u}_6 , and so the observed stresses might be expected to be better correlated with \bar{u}_6 and $\bar{u}_6 + \bar{u}_{10}$ than the shear, which is proportional to $\bar{u}_6 - \bar{u}_{10}$, as we find in table 4.2. The observed stresses are consistent with the hypothesis of wave generation.

To try and isolate the frequency dependence of the wave stresses which contribute to the correlation with the 600 m velocity, the stresses were estimated in several narrow, constant-width frequency bands covering the internal wave range, and the stress-velocity regression was performed for each band, including the inertial and tidal frequencies. The correlation coefficient as a function of frequency is shown in fig. 4.10. This is a signal-to-noise ratio estimate, indicating the relative fraction of the wavefield at each frequency involved in transferring momentum coherently with the mean velocity. The largest fraction is in the middle frequencies, periods ranging from 1-8 hours. The stresses associated with tidal frequencies behave in a manner opposite to the rest of the wavefield, with weak negative correlations.

An estimate of the relative contribution to the coherent stresses, by frequency, is shown in fig. 4.11. This is obtained from the slope of the regressions in fig. 4.10,

110]

Figure 4.10 Correlation coefficient of $C_{13}(\omega)$ vs. \bar{u}_{600} for the East direction, mooring 566. Constant width (5 harmonics) frequency bands have been used for the estimates.



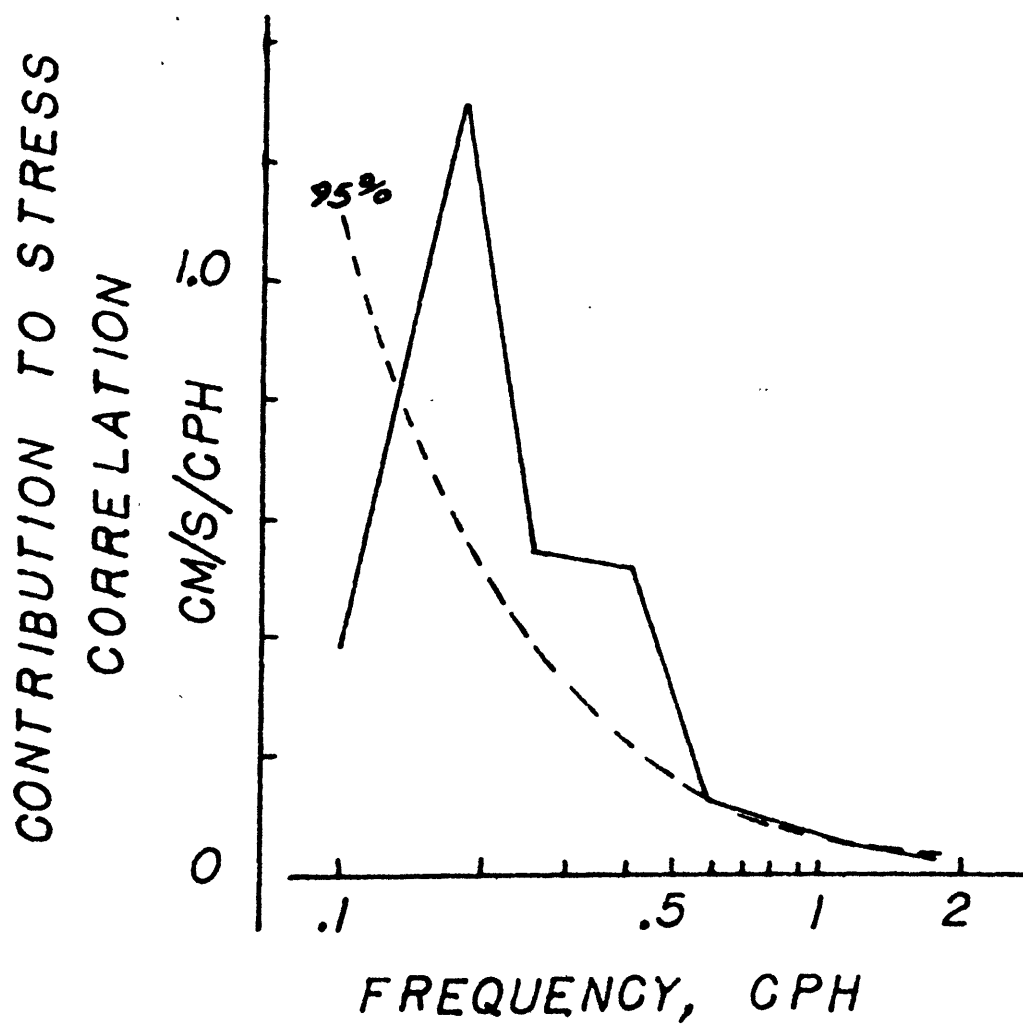


Figure 4.11 Contribution by frequency to the 600 m stress which is correlated with the 600 m East mean velocity.

normalized by the width of the frequency band. The uncertainty estimates become so large at frequencies below 0.1 cph that it is not possible to tell if the relative density peaks at intermediate frequencies.

Taking a typical \bar{u} (800 m) = 15 cm s^{-1} , we can estimate the length scales of the generated waves. For dominant periods from 1-8 hours, we find:

$$60 \text{ m} < \lambda < 500 \text{ m}$$

where λ is the wave length.

Figure 4.12 shows the filtered time series of 600 m continuum band East Reynolds stress, 600 m East velocity, and the 1000 m stress. The series have been broken into 69-day pieces (1/3 of the record) and the correlations are displayed for each piece. The 95% uncertainty of the correlation coefficients is about ± 0.35 . While the 600 m stress is positively correlated with the velocity at all times, the 1000 m stress is anti-correlated with the velocity during pieces 1 and 3 (while the velocities are strong), and is positively correlated during the center period when the velocities and shears are weak.

As described earlier, the behavior during the energetic periods is consistent with the hypothesis of wave generation at the level of maximum shear. The behavior of the stresses during the quiet center period is not consistent with Hypotheses 2 or 3 (critical layer absorption or

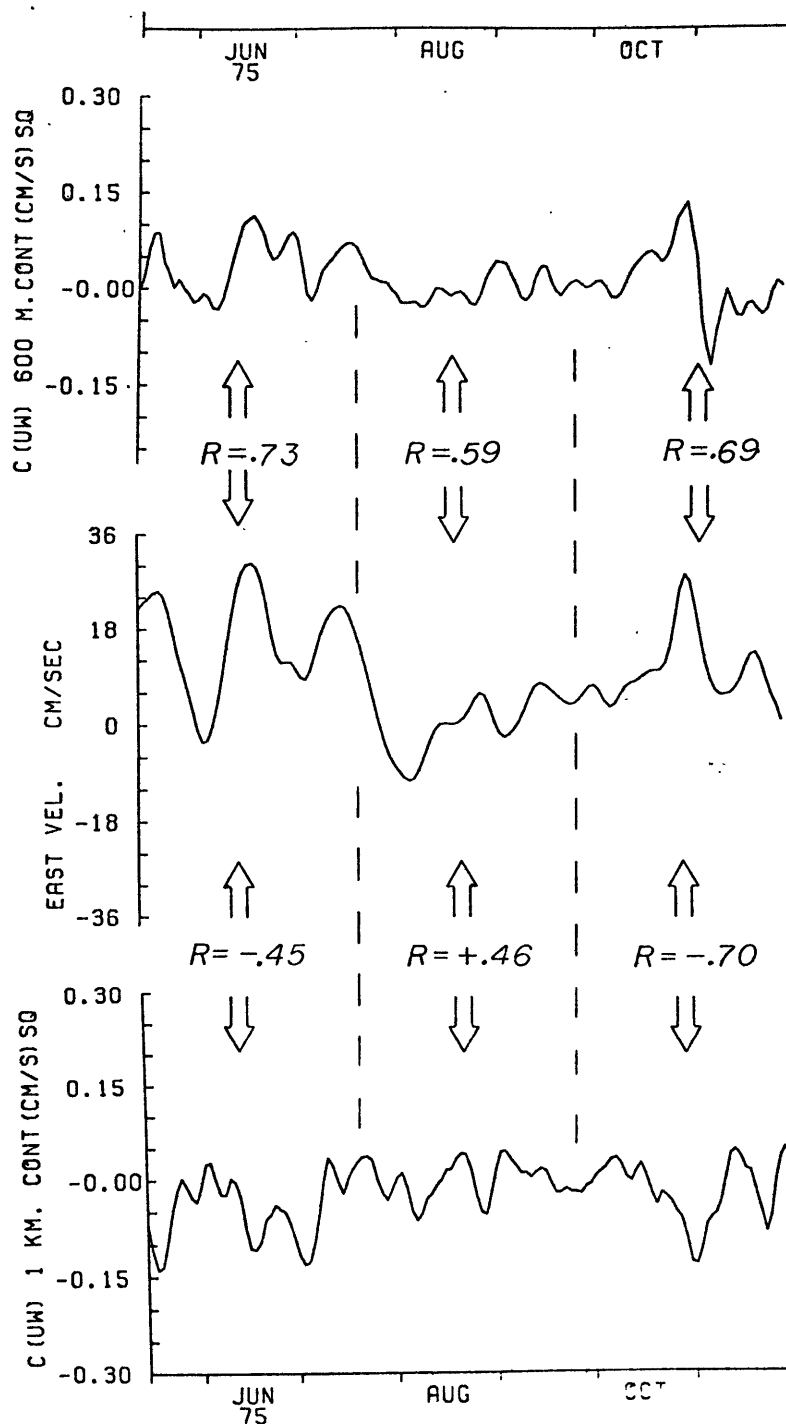


Figure 4.12 Continuum band stress, 600 m and 1000 m and velocity at 600 m, all 566, East direction. Correlation coefficients for each third of the record are displayed.

generation) and is only consistent with local interaction if the eddy viscosity is negative.

4.4 Energy Correlations

The wavefield energy can change with the mean flow for (primarily) two reasons. If the wavefield systematically exerts a Reynolds stress against (or with) the horizontal or vertical shear (i.e., a horizontal or vertical eddy viscosity), energy exchange occurs between the wavefield and mean flow. For vertical eddy viscosity effects, the rate of work (per unit mass) of the mean flow on the wavefield is

$$v_v \left[\left(\frac{\partial \bar{u}_1}{\partial x_3} \right)^2 + \left(\frac{\partial \bar{u}_2}{\partial x_3} \right)^2 \right] .$$

The other cause for wavefield energy level correlations is a change in the rate of wave generation associated with the mean flow, such as Doppler effects on the surface generation processes, generation by shear instability at the thermocline, or bottom generation (lee waves). (A kinematic change in apparent energy due to local time variations in $N(z)$ can occur, but since $N \sim \left(\frac{\partial T}{\partial z} \right)^{1/2}$, these changes are only about $\pm 15\%$.)

Figure 4.13 shows unfiltered timeseries of "Momentum flux squared" $(\overline{u_1' u_3'})^2 + \overline{u_2' u_3'}^2$ for the inertial band, "speed squared" $\bar{u}_1^2 + \bar{u}_2^2$, "shear squared" $\left(\frac{\partial \bar{u}_1}{\partial x_3} \right)^2 + \left(\frac{\partial \bar{u}_2}{\partial x_3} \right)^2$, and horizontal kinetic energy from the internal wave total band at 1000 m depth for a quiet mooring, 543, and shows the

115.]

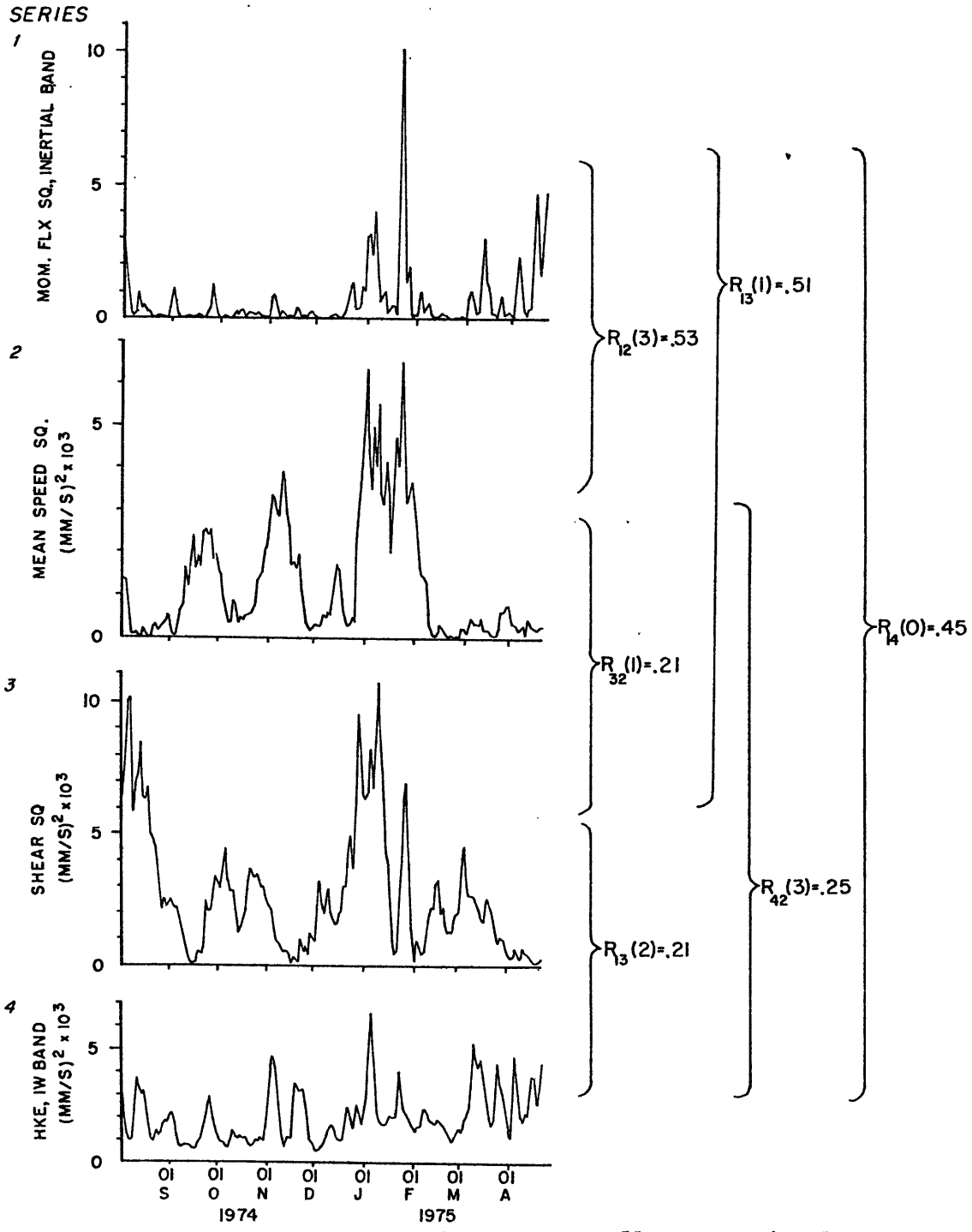


Figure 4.13 Time series of momentum flux magnitude squared at 1 km, inertial band, mean speed squared at 500 m, mean shear squared, and horizontal kinetic energy (x2) from the total band, 1000 m, all at mooring 543.

correlation coefficients between the pairs of time series on the right. Due to the non-normal distribution of the quantities (they are all positive definite), the correlation significance levels tend to be higher, about 0.35. The magnitude of the vertically acting stress is significantly correlated with the shear squared. This is because of the "cross-viscosity" discussed in 4.3c, a tendency for the wave stress to lie to the left of the shear. Because the forces are perpendicular to the displacements, no energy exchange occurs and correspondingly the total horizontal kinetic energy is not significantly correlated with the mean flow. No horizontal kinetic energy versus mean flow correlations in the tidal, inertial, continuum, or total frequency bands were observed at either of the quiet moorings. The anisotropy of the tidal currents was found to be weakly correlated with the mean flow, but this is attributed to a simple Doppler shift effect - a shift of the intrinsic frequency of the tidal motions causing a change in the aspect ratio, $\frac{f}{\omega_0}$, of the current ellipse.

At the energetic moorings, statistically significant energy correlations were observed at all frequencies except tidal. Figure 4.14 shows, for the continuum band at mooring 566, time series of mean shear squared, estimated from 600 and 1000 m velocities, mean speed squared at 600 m, momentum flux magnitude, and horizontal kinetic energy (both from the continuum band, 600 m) along with the correlation coefficients between pairs of time series on the right. All pairs

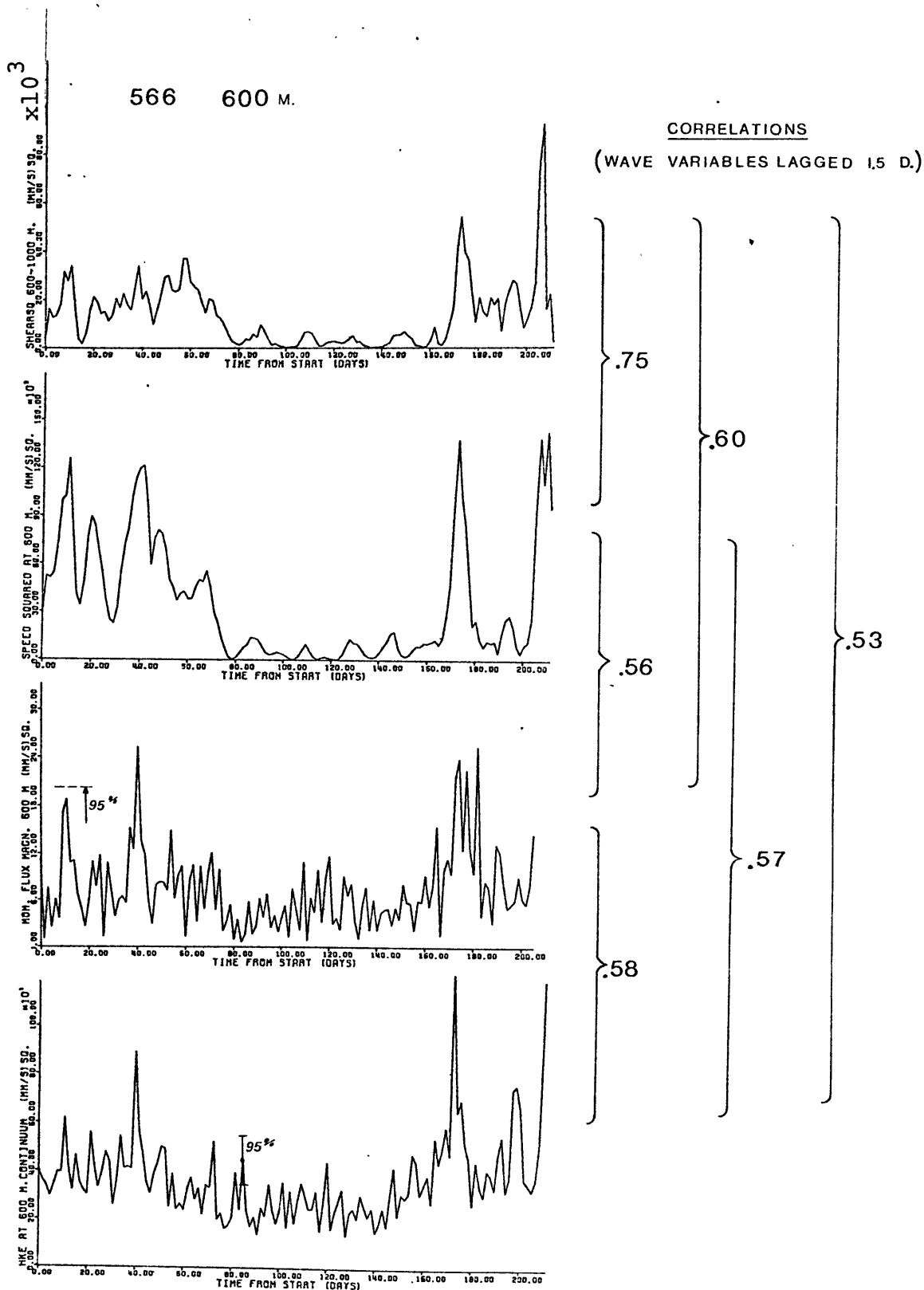


Figure 4.14 Time series of mean shear squared, mean speed squared, momentum flux magnitude, continuum band at 600 m, and twice the horizontal kinetic energy, continuum band, at 600 m, for mooring 566.

AUTOSPECTRA, DATA 5661

--- PIECE 1 - 75-05-09 TO 75-07-24

— PIECE 2 - 75-07-23 TO 75-10-02

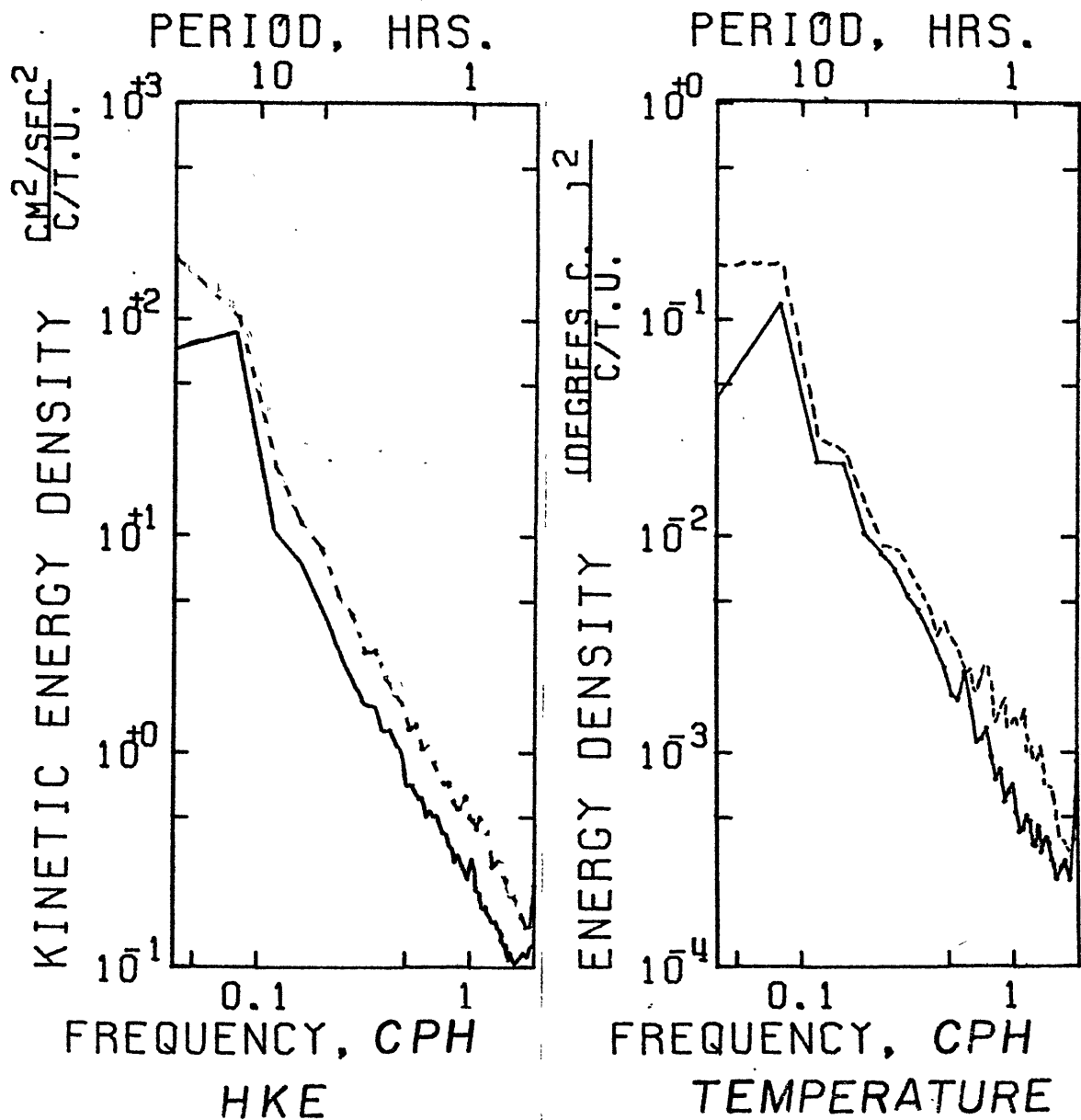


Figure 4.15 HKE and Temperature spectrum from data #5661, computed from two times, piece 1 ($\bar{u}_{\text{rms}} \approx 25 \text{ cm s}^{-1}$) and piece 2 ($\bar{u}_{\text{rms}} \approx 6 \text{ cm s}^{-1}$).

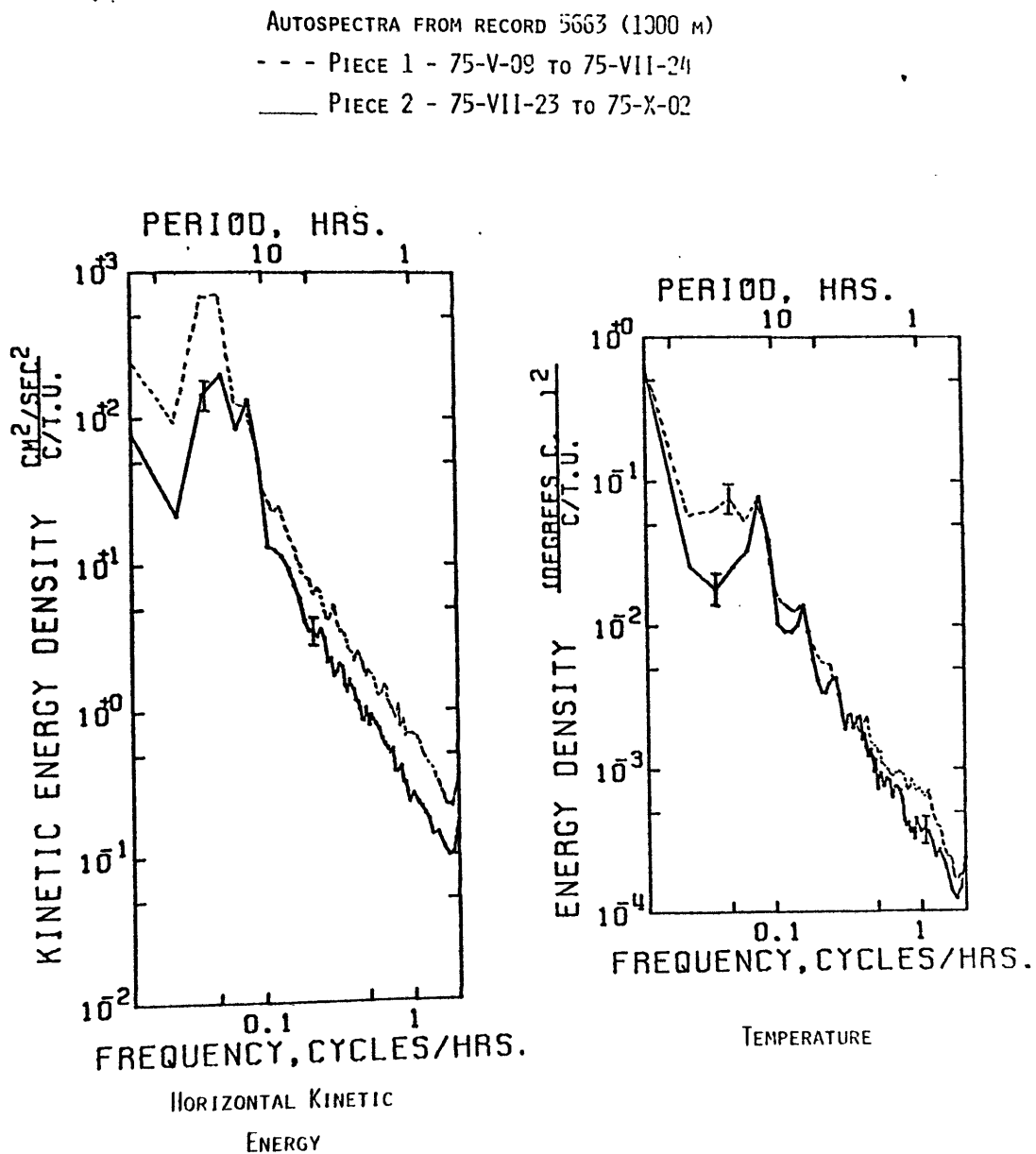


Figure 4.16 HKE and Temperature spectrum from data #5663.
 Pieces and times as in figure 4.15.

Table 4.3

RELATIVE KINETIC ENERGY LEVELS AT MOORING 566 FROM
ENERGETIC (PIECE 1) AND QUIET (PIECE 2) PERIODS

	Total Band 1 Km (cm ² s ⁻²)	Continuum Band 1 Km (cm ² s ⁻²)	Mean Flow HKE at 600 m (cm ² s ⁻²)
Garrett & Munk (1972) N = 2.3 cph	17.3	5.8	0
5663 Piece 1	27.3	5.2	600
5663 Piece 2	4.0	2.0	60
ΔE (Piece 1 - Piece 2)	23.3	3.2	540
Average $\frac{1}{2}$ (Piece 1 + Piece 2)	15.7	4.2	330

$$\text{Total } \Delta E \approx \text{Inertial } \Delta E + 2 * \text{Continuum } \Delta E$$

$$= 20 + 6.4$$

$$= 26$$

of time series are positively correlated, and once again it is impossible to decide if the correlations are related to the shear or the 600 m velocity.

Some idea of the frequency dependence of the observed energy level changes was obtained by computing the horizontal kinetic energy and temperature power spectra for records 5661, 600 m and 5663, 1000 m. The basic records were divided into piece 1, the first third of the record, corresponding to a relatively energetic low-frequency flow, ($\bar{u}_{rms} \sim 25 \text{ cm s}^{-1}$) and piece 2, the center third, corresponding to a relatively weak mean flow ($\bar{u}_{rms} \sim 7 \text{ cm s}^{-1}$). Figures 4.15 and 4.16 show the spectra from pieces 1 (dashed line) and 2 (solid line), for the 600 and 1000 meter levels. A significant energy increase is noted at all internal wave frequencies except that of the M_2 tide. The stability of the tidal estimates suggests that the observed changes are real, and not induced by the instrument. The velocity spectra increase uniformly throughout the internal wave frequency range, but in the temperature spectra, the greatest increase is in the mid-frequencies, from about 0.5-1.5 cph, corresponding to the frequencies of the largest stress--mean velocity correlations (fig. 4.10). In addition, an enormous increase in kinetic energy at near-inertial frequencies was observed in piece 1, although the inertial band HKE--mean speed correlations were weak at 600 m, and insignificant at 1000 m. Table 4.3 lists the average kinetic energy from pieces 1 and 2 of record 5663, and for comparison, the

expected energies from the Garrett-Munk (1972) model, and the mean flow kinetic energies from pieces 1 and 2. The division of energies from the Garrett-Munk model is shown in fig. 4.17. Accompanying the factor of 10 increase in mean flow energy is a factor of $2^{-1/2}$ increase throughout the continuum band, and a factor of 7 increase in total energy, mainly due to the f-2f contribution. The ratio of energies in the two frequency bands ($\frac{\text{total}}{\text{continuum}}$) shifts from 2:1 in the quiet period to 5:1 in the energetic period. (The expected ratio from Garrett-Munk is 3:1.) Since the bulk of the energy dissipation of the wavefield is believed to be due to shear instability, which is primarily contributed to by near-inertial waves (Garrett and Munk, 1972b), this shift in the frequency dependence may represent an attempt by the wavefield to greatly increase its dissipation rate.

The question arises as to possible sources of this extra wave energy. We now borrow a simplifying model from Frankignoul (1976) in an attempt to decide if the increase can be due to the energy exchange associated with the shear stresses.

Frankignoul (1976) has observed time correlations between the internal wave horizontal kinetic energy and the quantity $(\frac{\partial \bar{u}_1}{\partial x_3})^2 + (\frac{\partial \bar{u}_2}{\partial x_3})^2$ in current meter data taken during MODE-1. He attributes the increases in wave energy level to interaction of the wavefield with the vertical shear in the manner suggested by Müller (1976). Assuming a relaxation

Breakdown of energy in Garrett-Munk (1972, 1975) spectrum.

HKE, $f - 2f$ (excluding inertial cusp) 25%	HKE, $2f - N$ (continuum band) 25%
HKE, inertial cusp 25%	Potential Energy 25% $+ O(\frac{f}{N})$ V.K.E.



$$30 \text{ ergs cm}^{-3} \cdot \frac{N(z)}{N_0}$$

Figure 4.17 Division of total energy density in the Garrett-Munk (1972, 1975) model internal wave spectrum.

time of 3-5 days (estimated separately), he indirectly estimates a vertical eddy viscosity of $0 (10^3) \text{ cm}^2 \text{ s}^{-1}$. A slightly refined version of Frankignoul's wave energy model, which we will now derive, leads to:

$$E - E_0 \approx \nu_v \tau \left[\left(\frac{\partial \bar{u}_1}{\partial x_3} \right)^2 + \left(\frac{\partial \bar{u}_2}{\partial x_3} \right)^2 \right] \quad (4.58)$$

where:

E = the wave energy;

E_0 = the wave energy in the absence of shear;
 $= 30 \text{ cm}^2 \text{ s}^{-2}$ for the Garrett-Munk model

τ = a characteristic "relaxation" time for the wavefield, discussed in chapter 5;

ν_v = vertical eddy viscosity.

The physical assumptions leading to this equation are that in the absence of shear, the wavefield is maintained by a balance of statistically steady source terms, \mathcal{S}_0 and irreversible transfer and relaxation processes, parameterized as $-\tau E$. The wavefield energy equation is then:

$$\frac{dE}{dt} = \mathcal{S}_0 - \tau^{-1} E \quad (4.59)$$

with a steady state characterized by:

$$E_0 = \mathcal{S}_0 \tau^{-1} . \quad (4.60)$$

In the presence of shear, the dissipation and transfer processes act on the new energy applied by the working of the wave stresses against the shear. In a quasi-steady state, we expect a balance of the two energy source terms with the relaxation (dissipation) term:

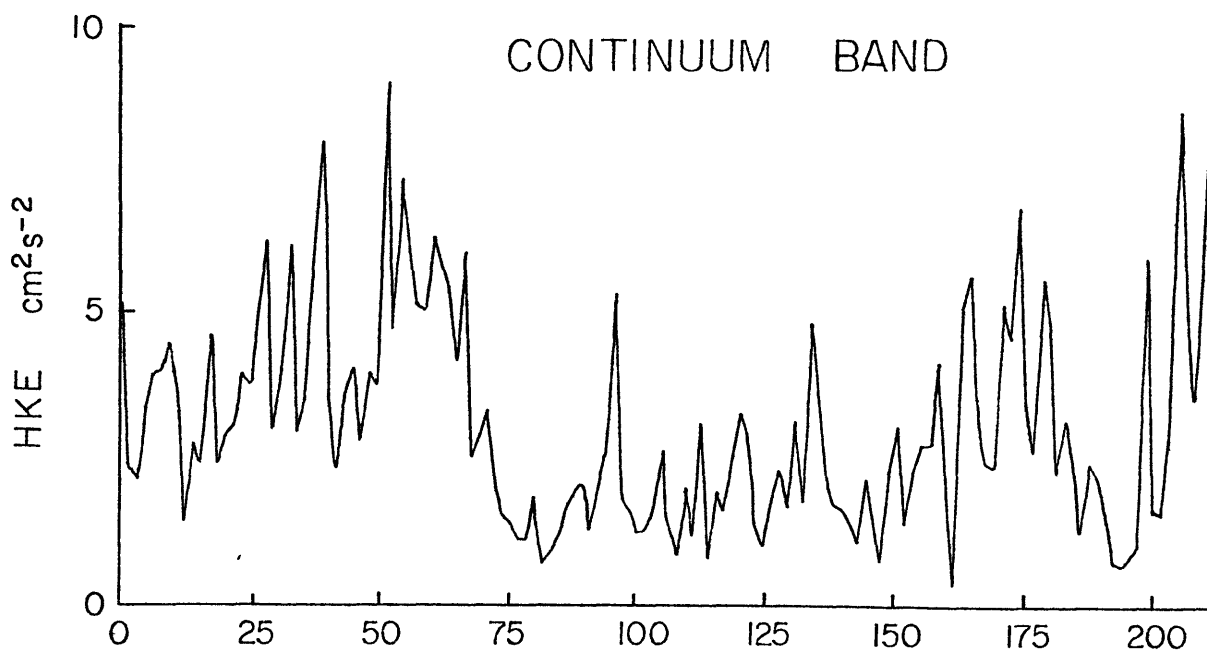
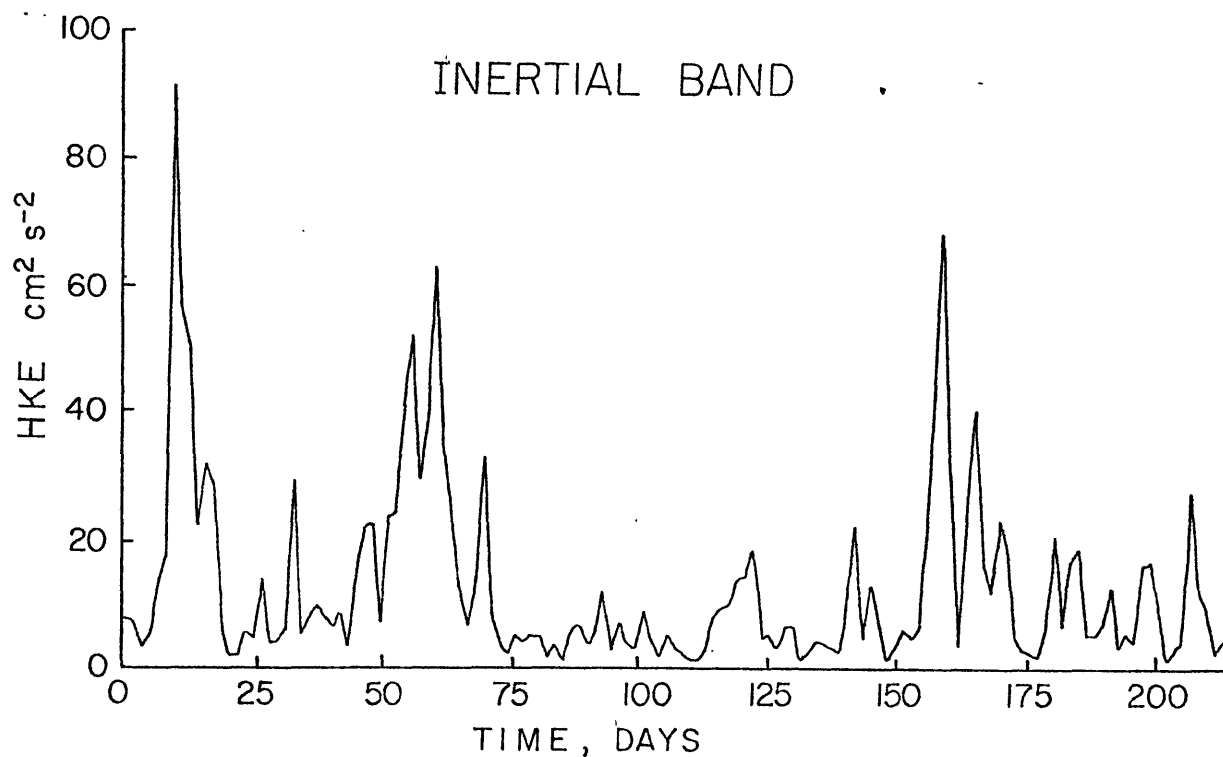
$$\begin{aligned} \frac{dE}{dt} &= \nu_v \left| \frac{\partial \bar{u}}{\partial x_3} \right|^2 - \tau^{-1} E + \mathcal{S}_0 \\ &= \nu_v \left| \frac{\partial \bar{u}}{\partial x_3} \right|^2 - \tau^{-1} (E - E_0) = 0 . \end{aligned} \tag{4.61}$$

Frankignoul (1976) neglected the E_0 term in deriving the above, so that the wavefield would have zero energy in the absence of shear, according to his equation. It is shown in chapter 5 that the concept of a basic state, E_0 , which is maintained in shape and level independent of the mean flow by irreversible processes, is probably not valid; the wave spectrum is able to be altered by the shear and still be close to equilibrium. However, the general concept of relaxation processes is probably valid, and so the relaxation time arguments characterize the response of the equilibrium wavefield to a general energy input. Since we have estimates of ν_v , we can estimate the energy input directly, and so we are guessing only at the rate of dissipation of this new energy. (Note that τ characterizes the initial rate of decay of the entire wavefield energy if the energy sources, \mathcal{S}_0 , were suddenly turned off.)

Thorpe (1975) suggests $\tau \sim 9d$ from Garrett and Munk's (1972b) estimate of the rate of energy dissipation by breaking internal waves. However, since the mechanism is an inherently nonlinear one (a critical Richardson number argument), the estimate is very sensitive to the wavefield intensity, the form of the spectrum, and the statistical nature of the process. The estimate is only a rough one at best, and their work suggests that the linearization of the relaxation term $-\tau^{-1} E$ is open to serious doubt since the effect of dissipation may be to clamp the energy at a fixed level. Frankignoul (1976) estimates $\tau \sim 5$ days from measurements of internal wave current anisotropy in the presence of a mean flow, but it is shown in chapter 6 that current anisotropy measurements of this type may be error prone.

Figure 4.18 shows the horizontal kinetic energy at 1 km depth on mooring 566 for the inertial band (dashed line) and the continuum band (solid line). We see that the continuum band has a basic energy level, E_0 , which modulates with the mean flow, and upon which is superposed energy "events." These events are from 2-6 days in duration, are random, and do not appear to be associated with the mean flow. E_0 varies with the mean flow on timescales at least as short as 20 days (more precise estimates are obscured by the energy events), suggesting that $\tau \sim 20$ days. The inertial band has no such basic energy level ($E_0 \approx 0$; related to the χ^2 distribution of spectral estimates for a small number of degrees of freedom

Figure 4.18 Horizontal kinetic energy from mooring 566 at 1 km depth. Inertial band (dashed line) and continuum band (solid line).



appropriate to a narrow band, but random, process). The energy "events" completely obscure the estimation of τ for the inertial band, and presumably are responsible for degrading the correlation of the inertial energy with the shear.

For $v_v = 100 \text{ cm}^2 \text{ s}^{-1}$; $\left| \frac{\partial \bar{u}}{\partial x_3} \right|^2 = 10^{-7} \text{ s}^{-1}$, and $\tau = 10 \text{ d}$, we compute:

$$\begin{aligned} \Delta E &= \left| \frac{\partial \bar{u}}{\partial x_3} \right|^2 v_v \tau \\ &= 9 \text{ cm}^2 \text{ s}^{-2} . \end{aligned} \tag{4.62}$$

This is large enough in magnitude to explain the energy increases in the continuum band, since ΔE for that band is about $2 \cdot \text{HKE} = 6 \text{ cm}^2 \text{ s}^{-2}$. However, the negative eddy viscosity at 600 m depth estimated under Hypothesis #1 would lead to expectation of an energy decrease at that level, while an increase is observed at both levels. The increase is inconsistent with the first hypothesis, that of a local, Müller-type interaction involving long waves for which Doppler shift is negligible. The increases are also inconsistent with the second hypothesis, of critical layer wave absorption, which would lead us to expect an energy decrease at both levels. Energy increases at both levels are consistent with the third hypothesis, that of wave generation at a shear region, since the actual stresses exerted by the generated waves oppose the shear, effectively resulting in a negative

eddy viscosity at the shear zone. (The 600 m stresses as inferred from temperature have their sign changed by Doppler shift effects, as discussed in the introduction to this chapter.)

Another way of looking at this energy exchange is to consider that the generated waves propagate away from the shear zone conserving their action (at least approximately). Both the upgoing and downgoing waves undergo an increase in intrinsic frequency magnitude from inertial near the generation zone to a higher frequency at some distance from the region. Then, since action is the energy divided by the intrinsic frequency, the energy of the waves increases as the intrinsic frequency through working of the wave stress on the shear:

$$\begin{aligned}\epsilon &= (\omega - \vec{k} \cdot \vec{u}) A \\ &= \omega_0 A\end{aligned}\tag{4.63}$$

The downgoing waves start out at $\omega_0 = +f$, and are considered to have a positive action (we adopt the convention of a positive energy for the waves). They propagate downward into a region of decreasing velocity, and so $\omega_0 = \omega - \vec{k} \cdot \vec{u}$ increases, and so does the energy. The upgoing waves start out at $\omega_0 = -f$, and so to keep the energy positive must be considered to have negative action, as though they were carrying a momentum deficit. (This also predicts a negative stress, $k_\alpha A v_3$). They travel up into increasing velocity, and so

$\omega_0 = \omega - \mathbf{k} \cdot \bar{\mathbf{u}}$ decreases from $-f$, increasing in absolute value. Since the action is negative, the energy increases for these waves also.

The estimated total energy increase of $26 \text{ cm}^2 \text{ s}^{-2}$ is primarily due to the large increase of near-inertial energy. A change of this magnitude is only consistent with our wave generation hypothesis if either:

- the relaxation time for near-inertial waves is considerably longer than our estimate of 10 days, say $\tau = 30$ days, or;
- if we have underestimated the effective vertical eddy viscosity by a factor of 3. From our estimate in 4.3d the current meter locations are about 200 m above and below the source region. The wave stresses are not visible at 1500 m, or 700 m from the source. It is possible (indeed, plausible according to McComas and Bretherton, 1977) that the vertically propagating waves are strongly attenuated by the time they have reached the levels of our observations.

Comparing the mean flow and wavefield kinetic energy densities in Table 4.3, it would appear that the wavefield would have little effect on the mean flow. Indeed, considering the rate of energy exchange:

$$\frac{dE}{dt} = \nu_v \left| \frac{\partial \bar{\mathbf{u}}}{\partial x_3} \right|^2 \quad (4.64)$$

leads to a decay timescale for the mean flow of about 800 days, based on the kinetic energy. Consideration of the potential energy of the mean flow (Müller, 1974) increases this estimate further. Clearly, the energy exchange is of little importance to the mean flow.

4.5 Summary

In the introduction to this chapter, we derived two simple rules relating the observed and actual stresses exerted by waves for which Doppler effects are important. Anticipating the results, we suggested three working hypotheses to which we compared the observations. Number one was the hypothesis of a local, eddy viscosity sort of interaction, in which the wavefield is not strongly modified from its basic state in the absence of shear flow. Then the majority of the wavefield is not strongly affected by Doppler effects, and we expect the inferred (from temperature) and actual stresses to be of the same sign.

Our second hypothesis was suggested in the chapter on theory of the interaction (or rather, non-interaction), Chapter 5. It was suggested there that critical layer absorption might be the dominant form of interaction. Doppler effects are important in this case, and we expect the inferred and actual stresses to be of opposite sign at the upper level. The signature of this interaction would be a negative stress-shear correlation above the thermocline, and a positive correlation below.

The third hypothesis is that of generation of internal waves by the shear, most likely at the thermocline. The signature of this would be the reverse of the absorption signature, a positive stress-shear correlation at 600 m, and a negative one at 1000 m.

In section 4.2 it was shown that the vertically-acting Reynolds stress exerted by a wave is accompanied by a buoyancy flux 90° to the left, due to the influence of the Coriolis force on the horizontal wave velocities. The Reynolds stress represents a vertical transfer of horizontal mean momentum, and the buoyancy flux represents the ability to tilt the isopycnals of the quasigeostrophic mean flow. The two effects tend to cancel each other, coming more and more into equal and opposite balance as $\omega_0 \rightarrow f$. As long as the mean flow is quasigeostrophic, one can define an effective stress which combines the momentum and buoyancy flux effects:

$$(\overline{u_1' u_3'})^E = (\overline{u_1' u_3'}) - \frac{f}{N^2} \overline{u_2' b'} \quad (4.65)$$

$$(\overline{u_2' u_3'})^E = (\overline{u_2' u_3'}) + \frac{f}{N^2} \overline{u_1' b'} \quad (4.66)$$

The buoyancy field, b' , is $-\frac{g}{\rho_0}$ times the wavefield density perturbation. Using the WKB approximation in the horizontal directions, it was shown:

$$(\overline{u_\alpha' u_3'})^E = \overline{u_\alpha' u_3'} \left(1 - \frac{f^2}{\omega_0^2}\right) \quad (4.67)$$

The continuum band, with limits of $2f-N$, includes 95% of that portion of the wave stress which is not cancelled by buoyancy flux effects, while excluding the semidiurnal tidal frequency and the most troublesome frequency band ($2-2f$) in terms of error in the stress estimates.

In 4.3a the vertical eddy viscosity was estimated (in terms of Hypothesis #1) from the regression of the continuum band stresses at 1000 m, on the shear estimated by differencing the 500 (or 600) m and 1000 m velocities. At moorings 545 and 543, where the conditions for validity of the Müller theory are satisfied, and the errors for the stress estimates were estimated to be negligible, the eddy viscosity estimates were found to be consistent with $\nu_v = 0 \pm 200 \text{ cm}^2 \text{ s}^{-1}$. This is an order of magnitude smaller than estimated by the Müller theory. Although Müller states that considering waves whose frequency is greater than $2f$ does not appreciably affect his eddy viscosity estimate, the eddy viscosity regressions were performed using the total (f - Nyquist) internal wave band, with no change to the results, except that the uncertainties were increased by a factor of two. It is shown in chapter 5 that a dynamical balance can exist in the wavefield which allows the wavefield to "bend" with the shear flow, and, except for the effects of critical layers, not exchange momentum with the mean flow. The above observational evidence suggests that this may be the case. However, no evidence suggesting critical layer absorption was found.

Estimates of vertical eddy viscosity coefficients at moorings 565 and 566 (characterized by much more energetic low-frequency motions) suggest:

$$v_v = \begin{cases} - 100 \pm 85 \text{ cm}^2 \text{ s}^{-1} & 600 \text{ m} \\ + 100 \pm 75 \text{ cm}^2 \text{ s}^{-1} & 1000 \text{ m} \end{cases} \quad (4.68)$$

The change of sign of the eddy viscosity with depth is inconsistent with our first hypothesis, that of a local interaction. After some further eddy viscosity investigations (done for completeness) in 4.3b and 4.3c, the behavior of the significant stresses at moorings 565 and 566 was investigated in 4.3d, without assuming a local interaction. In 4.4, the changes in energy level of the wavefield were investigated. The observed characteristics of the interaction are listed in Table 4.4, and compared for consistency with the three hypotheses just mentioned (#1, local interaction, #2, critical layer absorption, and #3, wave generation).

To summarize - the observed stresses are inconsistent with ideas of a strictly local eddy viscosity and are instead consistent with generation of short internal waves by local shear instability in the region of the main thermocline. The stress was found to be proportional to the shear at sufficiently high shear, leading to an effective vertical eddy viscosity (near the thermocline) of $+100 \text{ cm}^2 \text{ s}^{-1}$. The word effective is stressed because of the highly non-local nature of the interaction. The momentum flux is proportional to

the maximum shear, and represents a transfer of mean momentum from the upper layer to the lower one. Since the stresses are not observable at 1500 m, the exchange of momentum is confined to within 500 m of the shear zone (600-1000 m). No evidence suggesting critical layer absorption was found.

The local wave energy level changes observed are consistent with the rate of work done by the stresses against the shear, but do not account for the large, long-term energy increase in the near-inertial frequencies.

36
Table 4.4

Summary of Results; and Comparison with Hypotheses

	#1	#2	#3
Signs of observed stress correlations at 500, 1000 m	N	N	Y
Stress better correlated with \bar{u} at 600 than shear	N	Y	Y
Behavior of stress correlation during quiet period of 566	Y	N	N
Energy changes with shear	N	N	Y

Hypothesis:

- #1 Local, eddy viscosity type of interaction.
- #2 Critical layer absorption.
- #3 Wave generation at thermocline.

Chapter 5

ON THE THEORY OF INTERNAL WAVE-MEAN FLOW INTERACTIONS

5.1 Introduction

The Müller internal wave-mean flow interaction theory suggests that the effect of a mean shear on an isotropic, vertically symmetric wave spectrum is to introduce a combined vertical-horizontal asymmetry, resulting in a wave Reynolds stress which strongly opposes the shear. The small aspect ratio of the wave and mean fields indicates that the strongest effect may be approximated, in the "local interaction" limit of a short relaxation time τ (compared to the time a typical wave takes to propagate a reasonable vertical distance, τ_p), by a vertical eddy viscosity:

$$v_v \approx E_0 \frac{f}{N_0 \pi} \frac{\tau}{1 + \left(\frac{\tau}{\tau_p}\right)^2} \quad (5.1)$$

where E_0 is the average energy density of the wavefield.

Based on $\tau = 20$ h, Müller estimates a vertical eddy viscosity of $v_v = 5 \times 10^3 \text{ cm}^2 \text{ s}^{-1}$. Assuming a short τ and local interaction, I estimate an observed value of $v_v = 0 \pm 200 \text{ cm}^2 \text{ s}^{-1}$ from the two quiet moorings (545, 543). If the interaction is assumed to be less local, so that the effective shear is averaged over a 1500 m depth interval, rather than 500 m, the estimate becomes $v_v = 0 \pm 600 \text{ cm}^2 \text{ s}^{-1}$. Both are far short of the predicted value. The mean flow velocities at both these moorings were slow enough that mooring motion and

Doppler contamination of the vertical velocity estimates were negligible.

At the two more energetic moorings, I estimate a vertical eddy viscosity of $+(100 \pm 75) \text{ cm}^2 \text{ s}^{-1}$ at a depth of 1000 m, and $-(100 \pm 75) \text{ cm}^2 \text{ s}^{-1}$ at a depth of 600 m. This change of sign with depth, and the fact that the stresses are better correlated with the 600 m velocity than with the shear estimate, are incompatible with the predictions of the Müller theory.

According to the Müller model, the combined horizontal-vertical asymmetry increases with the shear to yield a wave stress. The asymmetry can only increase within limits, however. If all the wave momentum flux in the direction of the shear were organized so as to oppose it (waves with $\tilde{k} \cdot \frac{\partial \bar{u}}{\partial z} > 0$ traveling downward, those with $\tilde{k} \cdot \frac{\partial \bar{u}}{\partial z} < 0$ traveling upward), the maximum possible reynolds stress would be, from GM 76 (see Chapter 5.7)[†]

[†]The initials GM are used to denote a class of kinematic internal wave spectral models. The models referred to in shorthand are:

GM 72 - Garrett and Munk (1972), in which the frequency dependence was modelled, but no attempt was made to include detailed horizontal wavenumber dependence. Rather, a uniform excitation of the first 20 modes was assumed.

GM 75 - Garrett and Munk (1975). The wavenumber dependence was modelled, in the light of new information on horizontal scales.

GM 76 - Cairns and Williams (1976), also Desaubies (1976). Very similar to GM 75, but a much more analytically convenient form.

Formulae for GM 75 and GM 76 are given in Chapter 6.

$$\begin{aligned}\overline{u'w'}_{\max} &= E_0 \frac{4}{\pi} \frac{f}{N_0} \ln\left(\frac{N(z)}{f}\right) \\ &\approx 0.62 \text{ cm}^2 \text{ s}^{-2}\end{aligned}\quad (5.2)$$

using

$$N_0 = 3 \text{ cph}$$

$$N(z) = 2 \text{ cph}$$

$$f = .04 \text{ cph}$$

$$E_0 = 30 \text{ cm}^2 \text{ s}^{-2}.$$

With an eddy viscosity of $5 \times 10^3 \text{ cm}^2 \text{ s}^{-1}$, this maximum stress should occur at a shear of $\sim 10^{-4} \text{ s}^{-1}$, or a velocity difference of about 4 cm s^{-1} across the 400 m thick main thermocline. At this shear strength, or somewhat below, the stresses are no longer a perturbation to the wavefield, and the Müller mechanism must cease to be strictly valid. However, the expected stress induced by a shear corresponding to a 1 cm/sec velocity difference (2 cm s^{-1} was typical at the quiet moorings) is only $0.15 \text{ cm}^2 \text{ s}^{-2}$. While this represents a small perturbation to the wavefield, it should have been easily observable above the $0.05 \text{ cm}^2 \text{ s}^{-2}$ noise level.

Thus, under conditions in which the Müller theory should be valid, and the predicted stress signal should have been observable, the expected wave stress correlations were not observed. Under conditions of shear so intense that a correlated stress signal is observed, the observations are inconsistent with the Müller theory. Whatever interaction exists

between the internal wavefield and the low-frequency vertical shear is both different in nature and weaker than the interaction predicted by Müller.

In the following sections of this chapter, a much-simplified version of the Müller theory is examined. The particular problem addressed is that of a wavefield in the presence of a steady vertical shear flow. Some theoretical results of McComas and Bretherton (1977) on the effects of resonant interactions on the wave spectrum are used to simplify the radiation balance equation. For the part of the wavefield most strongly influenced by the simplified source terms, an "equilibrium" wave spectrum is found (Chapter 5.5) in which the effects of the nonlinear interactions cancel in such a way that the spectrum does not evolve in time. This equilibrium spectrum can exist in the presence of a shear, is actually distorted by the shear, and except for the effects of critical layer absorption, does not exchange momentum with the shear. For zero mean velocity, the spectrum reduces to the equilibrium state found by McComas and Bretherton (1976), which is consistent with the high wavenumber region of the GM'75 wave model.

The Müller theory effectively assumes that the equilibrium wavefield is independent of the mean shear, so that all waves view the refraction due to the shear as a perturbation from the equilibrium wavefield, and are forced to "relax" back to the original ($\bar{u} = 0$) spectral shape. This relaxation leads to a large predicted eddy viscosity. The simplified

solution demonstrates that it is conceivable for the "equilibrium" wavefield to depend on the shear flow through the dispersion relation, so that all random perturbations will tend toward the shear-distorted equilibrium. This rather subtle difference drastically alters the strength (and sense) of the predicted momentum exchange, leading to a zero or slightly negative vertical eddy viscosity.

5.2 The Radiation Balance Equation

The evolution of the wave action density spectrum $\eta(\underline{x}, \underline{k}, t)$ is determined by the radiation balance equation, or RBE:

$$\mathcal{L}(\eta) = \frac{D\eta}{Dt} = \frac{\partial \eta}{\partial t} + \dot{\underline{x}} \cdot \frac{\partial \eta}{\partial \underline{x}} + \dot{\underline{k}} \cdot \frac{\partial \eta}{\partial \underline{k}} = \mathcal{S} \quad (5.3)$$

where

$$\begin{aligned} \dot{\underline{x}} &= \frac{\partial \Omega}{\partial \underline{k}} \equiv \underline{V} && \text{(group velocity)} \\ \dot{\underline{k}} &= - \frac{\partial \Omega}{\partial \underline{x}} && \text{(rate of refraction)} \\ \underline{k} &= (k_1, k_2, k_3) && (5.4) \\ \Omega &= \frac{N^2(k_1^2 + k_2^2) + f^2 k_3^2}{k_1^2 + k_2^2 + k_3^2} + \underline{k} \cdot \underline{\bar{u}} \\ &= \Omega_0 + \underline{k} \cdot \underline{u} \end{aligned}$$

$\Omega(\underline{k}, \underline{x}, t)$ is the functional form of the dispersion relation $\omega = \Omega$. The functional form is denoted by Ω ; the value taken

by a given wave is denoted by ω . The intrinsic frequency, $\omega_0 = \omega - \underline{k} \cdot \underline{u}$, is similarly denoted. The equation describes the time rate of change of the spectral density in a Lagrangian sense, $\frac{D}{Dt}$, following a hypothetical wave group at $(\underline{x}, \underline{k}, t)$ as it travels through a 6-dimensional phase space $(\underline{x}, \underline{k})$ with a 6-dimensional velocity $(\dot{\underline{x}}, \dot{\underline{k}})$. The source term, \mathcal{S} , represents, in a statistical sense, the Lagrangian rate of increase or decrease in wave action density due to interactions with waves at other wavenumbers, interaction with external fields, etc. \mathcal{S} is a catch-all for all the non-conservative processes that affect the wave in its travels.

A predecessor of the RBE was developed to describe surface wavefields in terms of energy density (not action) by Hasselman (1968). For the energy transfer equation to be valid in the presence of a mean flow, an explicit source term describing the work done by the waves in propagating through a shear must be included (Phillips, 1966, p. 50). This term was greatly simplified by Garrett (1968) for internal waves in particular, and, more generally (Bretherton and Garrett, 1968), for systems whose equations of motion may be derived from a variational principle (Whitham, 1965). For a slowly-varying wavetrain propagating through a moving medium whose properties are allowed to vary slowly, the equation for the energy density, ϵ , of the wave was shown to be:

$$\frac{d\epsilon}{dt} + \epsilon \nabla \cdot \underline{v} = \frac{\epsilon}{\omega_0} \frac{d\omega_0}{dt} \quad (5.5)$$

where

$$\frac{d}{dt} = \frac{\partial}{\partial t} + \tilde{v} \cdot \nabla$$

The quantity $\omega_o = \omega - \tilde{k} \cdot \tilde{u}$ is the intrinsic frequency of the wave--the frequency of the wave as would be measured by an observer moving with the local velocity of the medium. The term on the right is identified with (and was shown to be, in several cases) the rate of working of the wave stress tensor against the mean shear. Rearranging the equation:

$$\frac{d}{dt} \left(\frac{\epsilon}{\omega_o} \right) + \frac{\epsilon}{\omega_o} \nabla \cdot \tilde{v} = 0 \quad (5.6)$$

or

$$\frac{\partial}{\partial t} \left(\frac{\epsilon}{\omega_o} \right) + \nabla \cdot \left(\tilde{v} \frac{\epsilon}{\omega_o} \right) = 0 \quad (5.7)$$

We immediately recognize that the quantity $a = \frac{\epsilon}{\omega_o}$, called wave action density, is conserved as the wave propagates through the moving medium, since the integral form of Eq. 4 is:

$$\frac{d}{dt} \iiint_{Vol} \frac{\epsilon}{\omega_o} d^3 \tilde{x} = 0 \quad (5.8)$$

where Vol is any volume whose surface moves with the local group velocity.

There is, then a complete wave-particle analogy; wave groups conserve their integrated action $A = \int a d^3 \tilde{x}$ in their

travels. If the quantities $\tilde{x} \cdot \tilde{k}$ are regarded as generalized coordinates for the wave packet, the wave packet itself moves in (\tilde{x}, \tilde{k}) space as though it were a particle under the influence of a Hamiltonian $\Omega(\tilde{k}, \tilde{x}, t)$:

$$\frac{d\tilde{k}}{dt} = - \frac{\partial \Omega}{\partial \tilde{x}} \quad (5.9)$$

$$\frac{d\tilde{x}}{dt} = \frac{\partial \Omega}{\partial \tilde{k}} .$$

The concept of an ensemble of such packets moving in the phase space (\tilde{k}, \tilde{x}) could now be introduced, and a conservation law for the action density of the ensemble of wave groups could be derived. This derivation is completely parallel to the derivation of Liouville's theorem, which is the conservation law for the number density of an ensemble of non-interacting particles moving under the influence of a Hamiltonian (see, for example, Marion, 1970). It seems possible, however, to ignore the wave-particle analogy and return to the differential form of the law of wave action conservation. The concept of a wave action density spectrum can be introduced and a conservation law for the spectrum can be derived, allowing the wave groups to be as large as the scale of the medium.

Consider a volume Vol in 6-dimensional phase space (\tilde{x}, \tilde{k}) . We define the action density spectrum as the ensemble averaged action of all waves within the box,

normalized by Vol, in the limit as $\text{Vol} \rightarrow 0$:

$$\eta(\underline{k}, \underline{x}, t) = \lim_{\text{Vol} \rightarrow 0} \left\langle \frac{A}{\text{Vol}} \right\rangle \quad (5.10)$$

where A is the integrated action of all waves or parts of wave trains whose position and wavenumber falls within Vol. Obviously, a sort of "continuum hypothesis" must be made - the scale of Vol must be simultaneously:

- (a) small enough so that η varies little over the volume,
- (b) large enough so that the concept of a slowly-varying (in \underline{x} and \underline{k}) wave packet is valid.

The brackets $\langle \rangle$ indicate an ensemble average, so it is not necessary for the volume Vol to contain a large number of wave packets. In fact, since the action of each packet locally obeys a fluid-like conservation law, it is not even necessary for Vol to contain entire wavegroups. As long as (b) is valid, the physical size of the wavegroups is immaterial, since the concept of a local flux of wave action in physical space is well-defined through the law of action conservation. (Flux in wavenumber space is already well defined due to a well defined local \underline{k} and $\dot{\underline{k}}$.)

To derive Liouville's theorem for the action density spectrum, we allow Vol to be an infinitesimal 6-D cube of volume $d^3 \underline{x} d^3 \underline{k}$ for which (a) and (b) are valid. The center of the cube is at $\underline{x}, \underline{k}$. Computing the rate of change of the total action in the box, we find it must be equal to the sum

146

of the action fluxes through all twelve faces. The fluxes in phase space are due both to the flux in physical space, $\dot{\eta} \underline{x}$, and the flux in wavenumber space, $\dot{\eta} \underline{k}$. In a manner completely analogous to the derivation of the conservation of mass in fluid mechanics, or the divergence theorem in calculus, we relate the fluxes on opposing faces of the cube by expanding in a Taylor series. For example, we consider the face at $(\underline{x}, \underline{k} - \frac{d\underline{k}_1}{2})$ and its counterpart $(\underline{x}, \underline{k} + \frac{d\underline{k}_1}{2})$. The faces are aligned so that \underline{x} is constant. Thus we need only consider the flux in wavenumber space for these faces:

$$\begin{aligned}
 & (\text{Flux \#1} + \text{Flux \#2}) \cdot (\text{Surface area of faces 1, 2}) \\
 &= (\dot{\eta} \underline{k}_1 \Big|_{\underline{x}, \underline{k} - \frac{1}{2} d\underline{k}_1} - \dot{\eta} \underline{k}_1 \Big|_{\underline{x}, \underline{k} + \frac{1}{2} d\underline{k}_1}) (d\underline{k}_2 d\underline{k}_3 d^3 \underline{x}) \quad (5.11) \\
 &= - \frac{\partial}{\partial k_1} (\dot{\eta} \underline{k}_1) d\underline{k}_1 d\underline{k}_2 d\underline{k}_3 d^3 \underline{x} + \text{higher order terms.}
 \end{aligned}$$

Summing up the fluxes, we find that only the divergences enter the conservation equation for η :

$$\begin{aligned}
 \frac{\partial \eta}{\partial t} \cdot d^3 \underline{x} d^3 \underline{k} &= \sum (\text{surface fluxes}) \\
 &= - \left[\frac{\partial}{\partial k_i} (\dot{\eta} \underline{k}_i) + \frac{\partial}{\partial x_i} (\dot{\eta} \underline{x}_i) \right] d^3 \underline{k} d^3 \underline{x} \quad (5.12)
 \end{aligned}$$

Therefore

$$\left[\frac{\partial \eta}{\partial t} + \frac{\partial}{\partial x_i} (\dot{\eta} \underline{x}_i) + \frac{\partial}{\partial k_i} (\dot{\eta} \underline{k}_i) \right] d^3 \underline{k} d^3 \underline{x} = 0 \quad (5.13)$$

Since the volume $d^3\mathbf{k} d^3\mathbf{x}$ is arbitrary, the quantity in brackets must be zero. Using the propagation equations (5.4) we find:

$$\begin{aligned} \frac{\partial \eta}{\partial t} &= \frac{\partial \Omega}{\partial k_i} \frac{\partial \eta}{\partial x_i} + \eta \frac{\partial}{\partial x_i} \left(\frac{\partial \Omega}{\partial k_i} \right) + \\ &\quad - \frac{\partial \Omega}{\partial x_i} \frac{\partial \eta}{\partial k_i} - \eta \frac{\partial}{\partial k_i} \left(\frac{\partial \Omega}{\partial x_i} \right) = 0 . \end{aligned} \quad (5.14)$$

Since $\frac{\partial}{\partial x_i} \left(\frac{\partial \Omega}{\partial k_i} \right) = \frac{\partial}{\partial k_i} \left(\frac{\partial \Omega}{\partial x_i} \right)$ except at $k_3 = 0$, the turning point, we have

$$\frac{\partial \eta}{\partial t} + \dot{x}_i \frac{\partial \eta}{\partial x_i} + \dot{k}_i \frac{\partial \eta}{\partial k_i} = 0 . \quad (5.15)$$

This is Liouville's theorem, expressing conservation of action density for an ensemble of wave groups propagating freely in phase space. It states that an observer moving in phase space at velocity $\dot{\mathbf{k}}(\mathbf{x}, \mathbf{k}), \dot{\mathbf{x}}(\mathbf{x}, \mathbf{k})$ sees a constant action density.

Liouville's theorem describes free propagation of waves under the WKB approximation. The effects of all processes which can alter the action of a wave have been ignored. Bretherton (1969c) has been able to include the effects of weak resonant interactions within the wavefield, and found that the Liouville conservation law took the form of the Boltzmann equation:

$$\frac{\partial \eta}{\partial t} + \frac{\partial \Omega}{\partial k_i} \frac{\partial \eta}{\partial x_i} - \frac{\partial \Omega}{\partial x_i} \frac{\partial \eta}{\partial k_i} = \quad (5.16)$$

$$\int d^3 \underline{k}_1 \int d^3 \underline{k}_2 \{ \eta(\underline{k}_1) \eta(\underline{k}_2) - \eta(\underline{k}) \eta(\underline{k}_1) - \eta(\underline{k}) \eta(\underline{k}_2) \} D$$

The terms on the right-hand side of (16) express changes in action density due to weakly nonlinear resonant triad interactions among the internal waves. D is an extremely complicated coupling coefficient, a function of \underline{k} , \underline{k}_1 , and \underline{k}_2 , which is zero unless:

$$\underline{k} + \underline{k}_1 + \underline{k}_2 = 0 \quad (5.17)$$

$$\Omega(\underline{k}) + \Omega(\underline{k}_1) + \Omega(\underline{k}_2) = 0 .$$

These are termed the resonance conditions for interaction.

Details of the effects of the resonant interaction terms were investigated numerically, for the GM 72 and GM 75 spectra, by Olbers (1976). He also introduced an extremely valuable concept to the internal wave literature: the average spectral shape of the wavefield is determined by these, and other, statistically irreversible processes, and that perturbations from this "equilibrium" state will decay irreversibly toward equilibrium at a rate predetermined by the details of the process. His estimates of the initial rate of change of the model spectrum provided a first rough estimate of this time-scale under the assumption that weak resonant processes are the dominant ones.

107

McComas and Bretherton (1977, hereafter denoted MB) performed a similar numerical investigation of these source terms for a refined (GM'75, GM'76) internal wave model. More importantly, they discovered that a few classes of interaction dominated the spectrum in different regions. Each class has a clear-cut physical interpretation, and simplifying expressions for the source terms due to each interaction were found. These simplifications have paved the way for a detailed understanding of the equilibrium wavefield, with knowledge of some of its action source, transfer, and sink mechanisms. While the equilibrium wavefield may present the external appearance of "nothing going on," with its apparent isotropy, homogeneity and vertical symmetry, that appearance is due to a set of internal balances. An understanding of those balances in ever-increasing detail is probably the best way to understand the wavefield as a whole, including its deviations from equilibrium.

Müller and Olbers (1975) introduced the radiation balance equation and the appropriate boundary conditions to the internal wave literature. They give a rather complete accounting of the source terms due to various forcing, interaction, and dissipation processes, and estimate the size of some of them. However, we lack detailed knowledge of several potentially important processes, especially in the areas of near-surface forcing through and interaction with the oceanic boundary layer, and the details of turbulent dissipation.

5.3 A Brief Review of the Müller Theory (My View!)

Müller (1976) attacked the interaction problem by expanding the RBE in a small parameter which estimates the refraction effects of the mean flow on a wave:

$$\varepsilon = \frac{\delta\omega}{\omega}$$

or equivalently, (5.18)

$$= \frac{|c_p|}{|\bar{u}|} .$$

The expansion breaks down near a critical level, where $\varepsilon = 1$.
The ordered problems so obtained are:

$$\text{Zeroth Order: } \mathcal{L}_0(\eta_0) = \mathcal{S}(\eta_0) \quad (5.19)$$

$$\text{Order } (\varepsilon): \quad \mathcal{L}_0(\delta\eta) + \delta\mathcal{L}(\eta_0) = \delta\mathcal{S} \quad (5.20)$$

where: Subscript 0 indicates zeroth order quantities, δ indicates an order ε perturbation.

$$\delta\eta = \eta - \eta_0 \quad (5.21)$$

$$\delta\mathcal{L} = \bar{u}_i \frac{\partial}{\partial x_i} - \frac{\partial}{\partial x_i} (k_j \bar{u}_j) \frac{\partial}{\partial k_i} \quad (5.22)$$

$$\delta\mathcal{S} = \mathcal{S} - \mathcal{S}(\eta_0) .$$

The zeroth order problem is taken as solved, and the Garrett-Munk spectrum is taken ^{as} ~~to~~ the solution. Müller then expands \mathcal{S} in a Taylor series about the equilibrium state to obtain:

$$\mathcal{S} = \mathcal{S}(\eta_0) + \left. \frac{\partial \mathcal{S}}{\partial \eta} \right|_{\eta_0} \delta \eta \quad (5.23)$$

$$\approx \mathcal{S}(\eta_0) - \frac{\delta \eta}{\tau} \quad (5.24)$$

where τ is the characteristic timescale of the irreversible transfer and dissipation processes in the source term $\mathcal{S}(\eta)$.

This characterization of \mathcal{S} closes the problem at order ϵ , and the perturbations to the spectrum due to the shear can be estimated. Müller finds that the relaxation effects due to the spectrum attempting to regain its old shape (η_0), enter into a tug-of-war with the perturbations to the propagation terms, which leads to asymmetries in the wavefield. This leads to a Reynolds stress that is exerted by the wavefield and which opposes the mean shear, and thus extracts energy from it.

It is important to realize that the characterization of the source terms plays a dominant role in the net effect of wave-mean flow interactions. In expanding \mathcal{S} , Müller has implicitly assumed that \mathcal{S} and the basic state are independent of the mean velocity. This becomes obvious when we substitute for $\delta \eta$:

$$\mathcal{S} \approx \mathcal{S}(\eta_0) + \frac{\eta_0(k; z) - \eta}{\tau} . \quad (5.25)$$

By examining a particular form for \mathcal{S} , which McComas and Bretherton (1977) have indicated to be dominant over a considerable portion of the wavefield, we hope to show by example that it is conceivable for the basic state (solution to the order 1 problem) to be dependent on the velocity field, through the dispersion relation, in such a manner that the shear is able to distort the equilibrium wavefield and yet there is no back interaction on the mean flow.

5.4 Simplified Source Terms

Detailed numerical analysis of the effects of weak resonant interactions was undertaken by MB on the GM 75 and GM 76 model internal wave spectra. They successfully isolated three types of resonant interaction, each of which dominates in some portion of the wavefield. Moreover, they derive simplified expressions for the source terms which make the net effect of these interactions easier to understand and which explain some of the general features of the observed internal wave spectrum. We will focus on two of these mechanisms that are dominant in the high modenumber, non-inertial (frequencies significantly higher than inertial) region of the spectrum, denoted by MB as elastic scattering and induced diffusion. The sum of these two approximate source terms is a good approximation to those in (16) for $\omega \gtrsim 2f$.

Elastic scattering is relatively simple to understand. The near inertial motions appear to higher frequency waves to be a nearly steady pattern of horizontal shear flow, periodic in the vertical direction. In the weak resonant interaction formalism the incident wave (k_1, k_2, k_3) is back-scattered into its counter part $(k_1, k_2, -k_3)$ by the shear components of wavenumber (approximately) $(0, 0, 2k_3)$. The net effect can be approximated by a source term that reflects a tendency for the wavefield to be vertically symmetric:

$$S_1 \approx Q(2\beta) [\eta(\alpha, \beta) - \eta(\alpha, -\beta)] \quad (5.26)$$

where: $Q(2\beta)$ is related to the spectral density of low frequency shear at wavenumber 2β .

$$\beta = |k_3|.$$

Q was evaluated by MB and found to be surprisingly large, indicating a tendency for the wavefield to become completely symmetric within a few vertical wavelengths.

Obviously, if the wavefield is symmetric, there is no net vertical transfer of energy or momentum, and so this term is one possible explanation for a small observed eddy viscosity. However, we will temporarily defer questions of wavefield symmetry and concentrate on the effects of the induced diffusion source term, keeping in mind that this

neglected term will only tend to decrease the vertical flux of the wave momentum.

Induced diffusion is the name given to the class of interactions involving one wave of very low frequency and small wavenumber (low modenumber, large scale near-inertial oscillations) and two waves of higher frequency, smaller scale, and, because of the resonance conditions, nearly equal wavenumber. Denoting the low modenumber wave by 1, and the other two by 2,3, the resonance conditions are:

$$\begin{aligned}\omega_1 &= \omega_2 - \omega_3 \\ \tilde{k}_1 &= \tilde{k}_2 - \tilde{k}_3\end{aligned}\tag{5.27}$$

or;

$$\left. \frac{\Delta\omega}{\Delta\tilde{k}} \right|_{2,3} = \frac{\omega_1}{\tilde{k}_1}$$

In other words, the wave packets 2,3 travel at a group velocity that exactly matches the phase speed of the large scale wave, and hence continually see the same shear. This allows the effect on waves 2,3 to be cumulative.

It is shown by MB that the source term for this interaction reduces to an equation describing diffusion in wavenumber space:

$$\mathcal{S}_2 = \frac{\partial}{\partial k_i} (a_{ij} \frac{\partial \eta}{\partial k_j})\tag{5.28}$$

where a_{ij} is a diffusion tensor. Through scale arguments ($k_3 \gg k_1, k_2$ for oceanic internal waves) they determine that the dominant term is the a_{33} term, representing diffusion in vertical wavenumber.

An equivalent picture of this mechanism is obtained by considering the low frequency waves to be a random, large-scale shear field. A small-scale wave packet travelling through this field has its wavenumber perturbed randomly, according to:

$$\dot{k}_i = - \frac{\partial \Omega}{\partial x_i} = -k_j \frac{\partial \bar{u}_j}{\partial x_i} \quad (5.29)$$

The expected value of the wavenumber remains constant, but its mean-square perturbation increases with time; the position of the packet in wavenumber space becomes indistinct and diffuse. Following the classic arguments by Taylor (1921), MB compute the rate of change of the mean-square wavenumber perturbation:

$$\begin{aligned} \left\langle \frac{d}{dt} (k_i k_j) \right\rangle &= \langle \dot{k}_i k_j + k_i \dot{k}_j \rangle \\ &= \int_0^t d\tau \langle \dot{k}_i(t) \dot{k}_j(t+\tau) + \dot{k}_i(t+\tau) \dot{k}_j(t) \rangle \end{aligned} \quad (5.30)$$

RAY

where $\langle \rangle$ denotes the ensemble average, taken over the shear ensemble. By substituting from the ray equations for \dot{k} , and taking the limit of time large compared to the correlation time, an alternative formula for a_{ij} is found:

$$a_{ij} = \int_{-\infty}^{\infty} d\tau \, k_m k_n \frac{\partial \bar{u}_m}{\partial x_j} (\underline{x} + \underline{V}\tau, t+\tau) \frac{\partial \bar{u}_n}{\partial x_i} (\underline{x}, \tau) \quad (5.31)$$

where \underline{V} is the group velocity vector. For a_{33} due to horizontal (near inertial) shear, this reduces to:

$$a_{33} = \int_{-\infty}^{\infty} d\tau \, k_i \frac{\partial \bar{u}_i}{\partial z} (z + V_3 \tau, t+\tau) \cdot k_j \frac{\partial \bar{u}_j}{\partial t} (z, t) \quad (5.32)$$

From this form, it is obvious that a_{33} can be a function only of $k_i \cdot \frac{\partial \bar{u}_i}{\partial z}$ and the vertical group velocity. Through transformation to a spatial correlation, rather than temporal; $\zeta = V_3 \tau$, the form:

$$a_{33} = \frac{B(k_H, \bar{u}_z)}{V_3} \quad (5.33)$$

(where V_3 is the vertical group velocity) is suggested. This is the form found by MB for a_{33} through the resonant interaction formalism for the GM 75 model:

$$\begin{aligned} a_{33} &\approx (2 \times 10^{-5}) s^{-1} \cdot \frac{\omega \beta^3}{f \beta_*} \\ &\approx (2 \times 10^{-5}) s^{-1} \cdot \frac{N \alpha}{f \beta_*} V_3^{-1} \end{aligned} \quad (5.34)$$

where:

$$\alpha^2 = k_1^2 + k_2^2$$

$$\beta = |k_3|$$

$$\beta_* = j\pi \frac{b N(z)}{N_0}$$

$$j_* = 3, \quad b = 1.3 \text{ km}, \quad N_0 = 3 \text{ cph}$$

valid in the range:

$$\beta \gtrsim \beta_*$$

$$f^2 \ll \omega^2$$

which is the region of the spectrum in which this mechanism dominates the resonant interaction source term. The term is so large that a diffusion timescale is $O(1)$ period for vertical wavelengths of 100 m.

5.5 Simplified Radiation Balance Equation

In the presence of a steady vertical shear flow, $\bar{u}(z)$ the RBE reduces to (Müller and Olbers, 1975):

$$\frac{\partial \Omega}{\partial \beta} \frac{\partial \eta}{\partial z} - \frac{\partial \Omega}{\partial z} \frac{\partial \eta}{\partial \beta} = \mathcal{S}(\eta) \quad (5.35)$$

where: $\eta(k, z)$ is the action density spectrum.

$\omega = \Omega(k, z)$ is the dispersion relation

$$= \Omega_0(k, z) + \tilde{k} \cdot \tilde{\bar{u}}$$

$$\Omega_0^2 = \frac{\alpha^2 N^2(z) + f^2 \beta^2}{\alpha^2 + \beta^2} \quad (5.36)$$

$$\alpha^2 = k_1^2 + k_2^2$$

$$\beta = |k_3|.$$

To further simplify the problem, we consider the region of the spectrum $\omega \gtrsim 2f$, $\beta \gtrsim \beta_*$ (notation follows that of Garrett and

Munk, 1975), where the "induced diffusion" source term dominates:

$$\approx \frac{\partial}{\partial \beta} \left(\frac{B(\alpha)}{|V_3|} \frac{\partial \eta}{\partial \beta} \right) \quad (5.37)$$

where:

$$V_3 = \frac{-\partial \Omega}{\partial \beta} \cdot s = \text{vertical group velocity,}$$

$$s = \text{sgn}(k_3).$$

A particular solution to the simplified equation, for this particular source term, is:

$$\eta_p(\alpha, \beta, z) = C(\alpha, s) \Omega(\beta, z) + D(\alpha, s). \quad (5.38)$$

This is a linear superposition of two terms; the first represents a spectrum with a non-divergent flux of action out to higher and higher vertical wavenumbers. The second term is simply a spectrum which is white in β ; $\frac{\partial \eta}{\partial \beta} = 0$ for this term, and there is no flux of action.

There are several points to be made about this solution:

--It is consistent with observations of the equilibrium state for $\bar{u} = 0$.

In the absence of shear, the above solution is:

$$\eta_p = \frac{C'(\alpha, s)}{\beta} + D'(\alpha, s). \quad (5.39)$$

157

This is the solution found by MB as the equilibrium form for the induced diffusion source term. They also point out that, in the region of concern, $\omega \gtrsim 2f$, $\beta \gtrsim \beta_*$, the GM 75 spectrum may be written:

$$\eta_{GM} = \frac{\varepsilon(\alpha, \beta)}{\omega(\alpha, \beta)} \approx \text{const.} \times \frac{\beta^2 A(\frac{\beta}{\beta_*})}{N^2 \alpha^2 + f^2 \beta^2} \quad (5.40)$$

Now: A is proportional to $(1 + \frac{\beta}{\beta_*})^{-q}$;

and

$$\frac{f^2 \beta^2}{N^2 \alpha^2} \ll 1 \quad \text{for} \quad \frac{\omega^2}{f^2} \gg 1.$$

Therefore:

$$\eta_{GM} \sim \beta^{(2-q)} \quad (5.41)$$

The value of $q = 2.5$ was chosen in GM 75, midway between the two equilibrium values of $q = 2$, $q = 3$. GM 76 is equivalent to $q = 2$, in exact equilibrium. Recent observations (Müller, Olbers, and Willebrand, 1977) of the high wavenumber slope are consistent with $2 \leq q \leq 3$, indicating that the oceanic internal wave spectrum is close to equilibrium under the diffusion mechanism.

--The solution (5.38) is consistent with a WKB balance in the vertical.

Because the spectrum is a special case of the form $\eta_D = f(\alpha, \Omega(\beta, z), s)$ the Liouville operator (for steady state,

$\frac{\partial}{\partial t} = 0$) is identically satisfied:

$$\mathcal{L}(\eta_p) = \frac{\partial \Omega}{\partial \beta} \left(\frac{\partial \eta_p}{\partial \Omega} \frac{\partial \Omega}{\partial z} \right) - \frac{\partial \Omega}{\partial z} \left(\frac{\partial \eta_p}{\partial \Omega} \frac{\partial \Omega}{\partial \beta} \right) = 0 . \quad (5.42)$$

Since the Liouville theorem is derived by considering an ensemble of freely propagating wave groups (for which WKB is valid), the spectrum is consistent with a spectrum composed of waves propagating freely in the vertical under WKB variation. This can be verified by computing the energy density as a function of α, ω ;

$$\epsilon_p(\alpha, \beta, s; z) = f(\alpha, \Omega(\beta, z), s) \cdot (\Omega - \mathbf{k} \cdot \bar{\mathbf{u}}) \quad (5.43)$$

$$\begin{aligned} \epsilon_p(\alpha, \omega, s; z) &= \frac{f(\alpha, \omega, s) \cdot \omega_0}{|V_3|} \\ &= \frac{f(\alpha, \omega, s) \cdot \omega_0^2 \cdot \alpha \cdot N(z)}{(\omega_0^2 - f^2)^{3/2}} \end{aligned} \quad (5.44)$$

where:

$$f(\alpha, \Omega, s) = C(\alpha, s)\Omega + D(\alpha, s)$$

$$\omega_0 = \omega - \mathbf{k} \cdot \bar{\mathbf{u}} .$$

This has the familiar $N(z)$ variation with depth obtained from applying the WKB approximation, and observed in moored current spectra (Briscoe, 1975) even though the bulk of the spectral energy is at low mode numbers which might not be expected to have this variation. The length scales also change with depth á la WKB since β is obtained from the dispersion relation:

164

$$\beta = \frac{N(z)\alpha}{\sqrt{\omega_o^2 - f^2}} \quad (5.45)$$

This change of scale with depth has been verified by Leaman (1976) for waves of near-inertial frequency; however, it has not been done for higher frequency waves.

This balance is not unlike the equilibrium balance in the Boltzmann equation of kinetic theory, which leads to the Maxwell distribution of particle energies. In that case, the equilibrium state is steady, and there is a separate balance between the propagation terms (Liouville operator) and the terms which describe the effects of molecular collisions (analogous to the wave interaction source terms). While there may be collisions (interactions), they are symmetric in such a way that there is no net change of number density (action density) along a six-dimensional particle (ray) trajectory. Hence, for both the particle and wave field equations, the equilibrium state can be one which allows quasi-free propagation of particles (waves).

--The equilibrium balance exists in the presence of the mean shear.

For any value of $\bar{u}(z)$ the basic balance of the RBE for this solution is:

$$\begin{aligned} \mathcal{L}(\eta_D) &= 0 \\ S(\eta_D) &= 0 \end{aligned} \quad \text{separately (c.f. eq. 5.42)} \quad (5.46)$$

For $\bar{u} = 0$, perturbations of the wavefield from the equilibrium condition approach the equilibrium solution irreversibly. In the presence of shear, the equilibrium state is distorted, through alteration of the dispersion relation:

$$\Omega_0 \rightarrow \Omega_0 + \mathbf{k} \cdot \bar{\mathbf{u}}(z) . \quad (5.47)$$

All perturbations now approach this new equilibrium state, rather than the state which existed in the absence of shear. This is the essential difference from the Müller theory, which assumed that the equilibrium state is independent of the shear flow, and that all perturbations, including those induced by the shear, would tend to relax back to the old equilibrium state.

--There is very little momentum exchange with the shear flow.

The effect of the wavefield on the vertical shear flow is measured by the quantity:

$$\frac{d}{dz} \int d^3 \mathbf{k} \, k_i \eta(\mathbf{k}, \mathbf{x}) V_3 \quad i = 1, 2 \quad (5.48)$$

As discussed more fully in 5.6, this is approximately equal to the divergence of the wavefield Reynolds stress, a physical quantity that is both easy to understand and helpful in interpreting the wavefield-mean flow interaction. Since the wavefield is propagating freely in the vertical direction the momentum flux (really the action flux) is non-divergent. This is very similar to the mechanism discussed by Rhines (1973) as a simple explanation of the inertial peak; a spectrum of free waves forced at a boundary tends, at long time, to one in which fluxes of conserved quantities are nondivergent. This comes about in our solution because, when written with $\underline{k} = (k_1, k_2, k_3)$ as independent variables, the spectrum has the form $\eta(k_1, k_2, \Omega(k_3, z), s)$. Upon transformation to (k_1, k_2, ω, s) as independent variables, the Jacobian cancels the group velocity in the expression

$$k_i \eta_{,3} V_3 . \quad (5.49)$$

The only z -dependence comes in at the boundaries of the integration region, representing a loss of wave momentum through critical level absorption:

$$\begin{aligned}
\frac{d}{dx_3} (\overline{u_1}, \overline{u_3}) &\approx \frac{d}{dz} \int d^3k \, k_1 \, v_3 \, \eta_D(k_1, k_2, \Omega(k, x_3), s) \\
&= \frac{d}{dx_3} \int_{-\infty}^{\infty} dk_1 \int_{-\infty}^{\infty} dk_2 \int_{f+k \cdot \underline{\tilde{u}}}^{N+k \cdot \underline{\tilde{u}}} d\omega \sum_s \frac{k_1 \frac{\partial \Omega}{\partial k_3} \eta_D(k_1, k_2, \omega, s)}{\left| \frac{\partial \Omega}{\partial k_3} \right|} \\
&= \frac{d}{dx_3} \int_{-\infty}^{\infty} dk_1 \int_{-\infty}^{\infty} dk_2 \int_{f+k \cdot \underline{\tilde{u}}}^{N+k \cdot \underline{\tilde{u}}} d\omega \sum_s k_1 s \, \eta_D(k_1, k_2, \omega, s) \\
&\approx - \int_{-\infty}^{\infty} dk_1 \int_{-\infty}^{\infty} dk_2 \, k_1 \, \eta_D(k_1, k_2, f+k \cdot \underline{\tilde{u}}, +1) k \cdot \frac{\partial \underline{\tilde{u}}}{\partial x_3}
\end{aligned}
\tag{5.50}$$

We have assumed perfect reflection (a vertically symmetric spectrum) near $\omega_0 = N$ (Bretherton, 1967), and total momentum absorption at $\omega_0 = f$, leading to vertical symmetry. The stress divergence caused by this critical layer absorption is estimated in section (5.7).

For a velocity difference of 2 cm s^{-1} across the thermocline, a cross-thermocline stress difference of $.006 \text{ cm}^2 \text{ s}^{-1}$ is estimated. This is much weaker than that predicted by Müller (too small to measure, in fact) and of a sense so as to reinforce the shear, rather than oppose it. The stress magnitude estimated for a velocity difference of 30 cm s^{-1} , typical of that found at the energetic moorings, is about $.1 \text{ cm}^2 \text{ s}^{-2}$. This is typical of the observed stress magnitude. We discuss this further in section (5.7).

--The solution (38) is valid for realistic shear magnitudes.

Since no perturbation expansion has been used, the solution is valid for large shears. The main restriction is that the effects of critical layers, where $\Omega_0 = \pm f$, must be properly taken into account. In practice this is not easily done, and some physically plausible mechanism, such as viscous or nonlinear dissipation, must be used to remove the singularities caused by critical layers.

--The solution (38) cannot be valid over the entire spectrum.

The β^{-1} behavior at low wavenumbers and β^0 behavior at high wavenumbers (eq. 39) leads to $\int d\beta \eta_D = \infty$. The addition of high wavenumber dissipation removes the "white" non-integrability, and a low-wavenumber source of action would remove the β^{-1} singularity.

--The solution (38) suggest there is an infinite strength inertial cusp.

From (44) we see that the energy density goes as $(\omega_0^2 - f^2)^{-3/2}$. This is of the same form as predicted by Rhines (1973) because the RBE balance is one of quasi-free propagation. Recently, Bell (1976) has estimated the frequency dependence of the internal wavefield by means of the angle ($\arcsin \beta/\alpha$) dependence in horizontal-vertical temperature tow spectra. He concluded that the inertial cusp is very strong:

$$\varepsilon(\omega) \sim (\omega^2 - f^2)^{-m/2} \quad (5,51)$$

where:

$$2 \leq m \leq 3.$$

--There is a potential for local energy increase with \bar{u} at near-inertial frequencies.

Since $\varepsilon_D \sim [(\omega_0 - \underline{k} \cdot \underline{\bar{u}})^2 - f^2]^{-3/2}$ (eq. 44) the local energy density of the wavefield can increase with \bar{u} , especially near the inertial frequencies. This is due to the V_3^{-1} which appears in the representation of $\varepsilon(\alpha, \omega)$. This is a kinematic effect and does not imply interaction with the mean shear.

The equilibrium state is one of constant action flux and free vertical propagation. This can be visualized as a beam of wave packets traveling vertically. If they are equispaced in time, the distance between packets is inversely proportional to their rate of travel. Where V_3 is small, the packets tend to bunch up, creating a locally high action (and energy) density. However, the product $\eta \cdot V_3$, which equals the action flux, is constant.

This effect should be most visible near the inertial frequency. However, it is not clear that the equilibrium spectrum at these frequencies is one of free vertical propagation, as required for this effect to occur. (MB found another class of interaction not considered here to be important for $\omega \leq 2f$.)

Assuming that the above free propagation condition holds at all frequencies, the effect of vertical shear on the wavefield was estimated by matching the form $\eta(\alpha, \Omega(\beta, z))$ to the GM 75 model spectrum (chapter 6). Numerical integrations indicate that the bunching effect is more than cancelled by the effects of critical layer absorption, leading to relatively minor ($\sim 10\%$) changes in energy level with \bar{u} . The largest increase in energy was at $\frac{\omega}{f} = 3$, where a 10 percent increase occurred at $\bar{u} = 2.5$ cm/s. As \bar{u} was increased beyond this, however, the energy level dropped, reaching 50% of its initial value at $\bar{u} = 40$ cm/s. This result is only approximate, however, since the bunching effect was weakened to $(\omega_o^2 - f^2)^{-1/2}$ in order to avoid numerical problems.

5.6 Comparison with Müller Theory

In order to understand the difference between the two versions of simplified source terms for the RBE, it is helpful to refer to a characteristic diagram, on the (β, z) plane. The characteristics of the Liouville operator are simply lines of constant frequency--lines in (k, x) space along which a single wave packet would traverse under the WKB approximation. We consider a horizontally homogeneous and isotropic medium.

A sample Liouville operator characteristic for $\bar{u} = 0$ is sketched in Fig. 1. As z decreases, $N(z)$ typically decreases, and k_z also decreases. As long as the action density

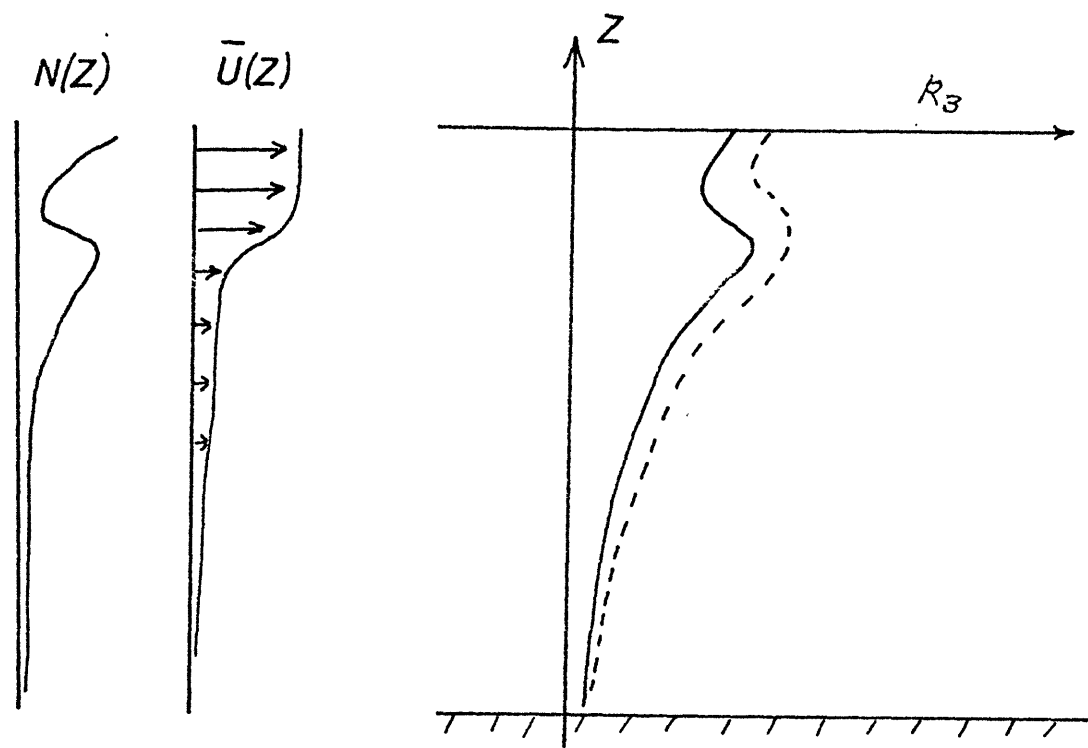


Figure 5.1 Sketch of a typical characteristic for the vertical terms of the Liouville operator, for $\bar{u} = 0$ (solid line) and for finite \bar{u} (dashed line).

is constant along each characteristic, $\eta(\alpha, \Omega(\beta, z))$, the Liouville operator is satisfied. The relaxation terms adjust the relationship of action density among the characteristics so that, in the relaxed state, the source terms are also zero. This corresponds to free propagation.

When a vertical shear alters \mathcal{L} , the characteristics are perturbed in the k_3 direction by the amount:

$$\delta k_3 = \frac{\delta \omega}{\left(\frac{\partial \Omega}{\partial k_3}\right)} = \frac{\tilde{k} \cdot \tilde{u}}{V_3} \quad (5.52)$$

The same characteristic in the presence of shear is indicated by a dashed line.

The solution desired by the Liouville operator is of the form $\eta(\alpha, \Omega)$; it wants the original action to stay constant along the new characteristic. However, Müller has approximated the source term by:

$$\mathcal{S} \approx \mathcal{S}(\eta_0) + \frac{\eta_0(\tilde{k}; z) - \eta}{\tau} \quad (5.53)$$

Müller and Olbers (1975) suggest that the basic state balance is characterized by $\mathcal{S}(\eta_0) = 0$, a consequence of free vertical propagation in the basic state. Note that η_0 is explicitly independent of \tilde{u} indicating that when the characteristics are perturbed by the shear, the wavefield senses the perturbation; $\eta_0 - \eta = \frac{\partial \eta_0}{\partial \Omega} \delta \omega = + \frac{\partial \eta_0}{\partial \Omega} \tilde{k} \cdot \tilde{u}$. With this form for \mathcal{S} , the relaxation effects attempt to balance the shear-induced

perturbations. It is this balance between refraction and relaxation that leads to net momentum exchange with the mean flow.

In contrast, the diffusive equilibrium solution can be distorted by the shear so that η_D is constant along the perturbed characteristics. This means $\mathcal{L}(\eta_D) = 0$. In addition, the perturbed wavefield is still in diffusive equilibrium, so that $\mathcal{S} = 0$. The wavefield makes no attempt to relax back to its original state, and so suffers no exchange of momentum with mean flow.

For the white, or β_0 , term of the solution, eq. 39, it is easy to see that the wavefield has no reference marks in the k_3 direction, and so doesn't know when it is perturbed. The perturbed state looks just like the unperturbed one. The same is true of the β^{-1} term, although it is not quite so obvious.

It would appear that the main difference between the present theory and that of Müller is in the characterization of the source terms. Müller effectively assumes that \mathcal{S} is independent of \bar{u} , whereas we chose a form for \mathcal{S} (the diffusion form) which is partially dependent on \bar{u} through the dispersion relation. This allows the equilibrium state to be altered by the shear without altering the balance from the equilibrium condition. The end result of this difference in source terms is the presence or absence of a very strong interaction, the signature of which is not observed in oceanic data.

The idea of a basic state which is not independent of the shear flow can be argued from the fact that the wave spectrum appears to behave in the WKB-prescribed manner for any stratification, $N(z)$. Consider first $\bar{u} = 0$. Since WKB variation implies a separate $\mathcal{L}(\eta_0) = 0 = \mathcal{S}(\eta_0)$ balance, the source terms must vanish for any η_0 satisfying:

$$\eta_0 = f(\alpha, \Omega_0) \quad (5.54)$$

where f is prescribed by \mathcal{S} . This is the general solution of the Liouville operator. In other words, \mathcal{S} depends on z only through the dispersion relation.

The presence of a mean shear modifies only the dispersion relation. This change can be conceptually viewed as a change in the stratification, indicating that the basic state balance:

$$\mathcal{L} = 0 = \mathcal{S} \quad (5.55)$$

still will hold for this "new" stratification, and the shear-distorted basic state is simply:

$$\eta(\alpha, \beta, z) = f(\alpha, \Omega(\beta, z)) \quad (5.56)$$

An example of a basic state of this form is given by the diffusive equilibrium solution, eq. 38 where

$$\Omega = \Omega_0 + \underline{k} \cdot \underline{\bar{u}} . \quad (5.57)$$

This suggests a more reasonable characterization of the source terms might be one which allows the equilibrium state to "bend" with the shear:

$$S \approx \frac{\eta_0(\alpha, \Omega(\beta, z)) - \eta(\underline{k}; z)}{\tau} . \quad (5.58)$$

Note that the possibility of a non-equilibrium state being induced by horizontal shear still exists, and that the aspects of the Müller mechanism leading to horizontal eddy viscosity effects are probably still valid.

Another way of viewing this "non-interaction" is to note that, in the limit of weak Doppler shift effects, one might regard the shear as a statistical, rather than deterministic, quantity. The source term for wavefield-shear interaction reduces to a diffusion term of exactly the same form as was obtained for wave-wave interactions (see Müller, 1977, M B, 1977). It follows that, if the wavefield is in diffusive equilibrium with regard to its internal interactions, it is also in diffusive equilibrium with respect to external interactions with a random external field. Hence, the equilibrium wavefield is not expected to interact with the random field of shear flow.

In addition to the different characterizations of the RBE source terms, there is one other difference between the Müller theory and that presented here. Müller expands the RBE in a small parameter which characterizes the weakness of the refraction by the mean flow; $\epsilon \approx \frac{\delta\omega}{\omega}$. We have used the small aspect ratio of the wavefield and the mean flow to argue that the vertical propagation terms in the Liouville operator dominate the horizontal and time derivative terms, leading to the simplified RBE (section 5.5) as the zeroth order problem. Based on a vertical scale of 500 m and a vertical group velocity scale of 0.7 cm s^{-1} (internal wave scales are taken from Müller, 1974, table 1)), we find that the vertical RBE terms have a timescale of about 1 day. The horizontal timescale is about 25 days, based on 100 km length scales and horizontal velocity scales ($\bar{u} + \bar{v}$) of 20 cm s^{-1} . The time derivative term is expected to be of the same order as the timescale of the mean flow, about 15 days. The relaxation terms are still largely unknown, but MB estimate very short relaxation times for some of their simplified mechanisms; certainly less than 1 day. Hence the dominant terms are those included in the simplified RBE, and a suitable small parameter for expansion of the RBE is the ratio of timescales of the two sets of terms; $\epsilon = 0$ (1 day/15 days). This expansion has the advantage that the lowest order solution is valid for strong refraction, and can include the effects of critical layer absorption, a potentially strong effect.

5.7 Momentum Flux Losses to Critical Layer Absorption

It is shown in Appendix C that the measure of the "effective" vertical flux of horizontal momentum (insofar as its effect on a quasigeostrophic mean flow is considered) is related to the action flux:

$$(\overline{u_\alpha u_3})_{\text{EFF.}} \equiv \int d^3k \, k_\alpha \eta V_3. \quad (5.59)$$

Far away from the inertial peak and critical levels, this quantity reduces to the measured Reynolds stress, $\overline{u_\alpha u_3}$. Considering the Reynolds stress rather than the effective stress introduces only about 12% error for the ω^{-1} frequency distribution of stress typical of the oceanic internal wavefield. Hence, in considering the effects of critical level wave absorption, we will consider the "observed", rather than "effective", momentum fluxes.

The solution for a wavefield in the presence of a shear flow (section 5.5) indicates that an equilibrium state is possible in which the waves undergo free vertical propagation, exchanging no momentum with the mean flow. The momentum flux (or more accurately, the action flux), due to a spectrum of such waves is non-divergent. This is probably not true, however, for those waves which encounter critical levels in their vertical travels, for which $\omega - \mathbf{k} \cdot \overline{\mathbf{u}}(z) = \pm f$. According to all the studies listed in

table 5.1, those waves are absorbed if the shear Richardson number is larger than about one. Thus the momentum flux of each wave goes to nearly zero rather suddenly if the wave encounters a critical level. On a characteristic diagram such as fig. 5.2, this is equivalent to some of the characteristics extending out to $k_3 = \pm\infty$, where the appropriate boundary condition is $\eta = 0$. We will simply account for the momentum flux lost by noting, as a function of \bar{u} , which characteristics are "lost" due to critical layers.

The effects of the "elastic scattering" source terms are to force the spectrum towards vertical symmetry, inhibiting vertical fluxes of wave momentum into the critical regions. Not enough is known about the behaviour of the source term coefficients at short length scales to enable explicit inclusion of these effects in an analytic model. We will thus ignore these effects and assume a perfectly asymmetric spectrum (no wave action propagating out from a critical level) in the vicinity of a critical level. We are, in effect, estimating the maximum possible transfer of momentum to the mean flow due to critical layer absorption.

The detailed structure of the solution $\eta_0(\mathbf{k}) = F(k_1, k_2, \Omega(\mathbf{k}, z), s)$ is determined by the forcing at the surface and by the relaxation effects of the source terms in the RBE. Without detailed knowledge of these processes it

Table 5.1

CRITICAL LAYER STUDIES

	Was WKB approx. made?	Vertical component of f	Horizontal component of f	Dissipation	Non- linearity
Bretherton (1966)	Y	N	N	N	N
Booker & Bretherton (1967)	N	N	N	Rayleigh Friction	N
Hazel (1967)	N	N	N	Y	N
Frankignoul (1970)	N	Y	N	N	N
Jones (1967)	N	Y	N	Rayleigh Friction	N
Grimshaw (1975)	N	Y	Y	Rayleigh Friction	N
Breeding (1971)	N	N	N	Y	Y

1776

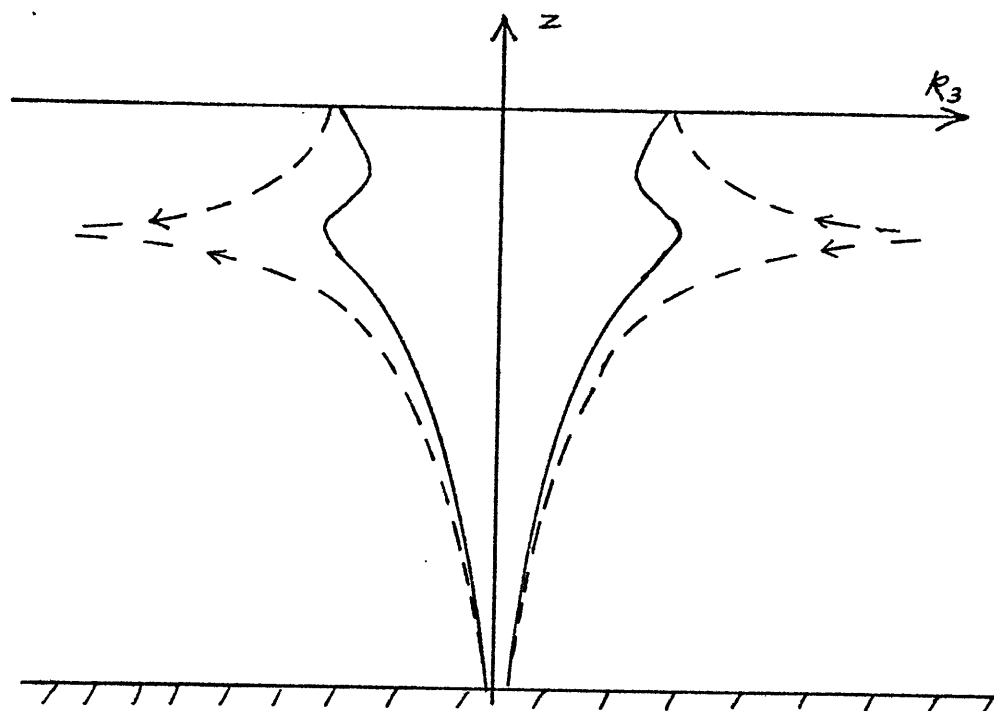


Figure 5.2 Characteristics for waves which encounter a critical level. The waves are coming from the critical layer for $k_3 > 0$, and propagating to the critical layer for $k_3 < 0$. Solid line for $\bar{u} = 0$; dashed line for finite \bar{u} .

178

is not possible to judge the effect that a finite mean velocity at the surface has on the generation processes, and hence on the wave field. Since the phase speeds of most generating fields, such as storms, are typically much larger than horizontal phase and group speeds of oceanic internal waves, one is tempted to suppose that the surface flow merely changes the relative velocity between the disturbance and the medium by a small fraction. This would change the angle subtended by the internal wave "wake" left by the disturbance a small amount, without appreciably affecting the energy input. One might thus expect the "usual" wave spectrum to be generated although it is unclear whether this would be in a non-moving frame of reference, or in a frame moving with the surface water. We choose the first alternative, corresponding to a field of waves with an unaltered distribution of horizontal phase speeds. The form of the solution is then determined by matching the energy spectrum to the GM 75 model spectrum at a level of no mean motion. For a match in the frame moving with the surface velocity, we simply replace \bar{u} with $\bar{u} - \bar{u}_{\text{surface}}$ in all the results.

Since the momentum flux of our action spectrum and the GM 76 wave model are independent of depth (except for critical layer losses), the momentum fluxes will be the same after matching at a common depth. In matching to the Garrett-Munk spectrum at a level of no motion, we are

179

implicitly assuming that the balance of generation and transfer processes which maintain the equilibrium state are unaffected by critical level absorption some distance away. This appears to be true for the diffusion process, but might not be true in general.

We now compute the effective momentum flux, assuming 100% vertical asymmetry, from the match of the action spectrum to the Gm 76 model in chapter 6.2:

$$\begin{aligned} \overline{u_1' u_3'} \Big|_E &= \int d^3k \, k_1 V_3 \, n_0 \\ &= \int d\omega \int \alpha d\alpha \int \frac{d\phi}{2\pi} \frac{2E_0 f}{\pi N_0 \alpha} \frac{\omega^2 - f^2}{\omega^3} A\left(\frac{\alpha}{\alpha_*}\right) \alpha_*^{-1} \quad (5.60) \end{aligned}$$

where:

$$\begin{aligned} E_0 &= 30 \text{ cm}^2 \text{ s}^{-2} \\ \alpha_*(\omega) &= \frac{j_* \pi}{N_0 b} \sqrt{\omega^2 - f^2} \\ j_* &= 3 \\ N_0 &= 3 \text{ cph} \\ b &= 1.3 \text{ km} . \end{aligned}$$

(The Jacobian $\frac{\partial \beta}{\partial \omega}$ cancels the V_3 term.) For $\omega \gtrsim 2f$ we recover the momentum flux which would be computed directly from GM 76 if the u_3' phase in their model were altered by 90° :

$$\overline{u_1 u_3} \approx \frac{E_o f}{\pi^2 N_o} \int d\omega \int d\alpha \int d\phi \omega^{-1} A\left(\frac{\alpha}{\alpha_*}\right) \alpha_*^{-1} \cos \phi \quad (5.61)$$

For GM 76:

$$A\left(\frac{\alpha}{\alpha_*}\right) = \frac{2}{\pi} \left(1 + \frac{\alpha}{\alpha_*}\right)^{-2} \quad (5.62)$$

The stress which is eliminated by critical layer absorption, for which $\omega - \underline{k} \cdot \underline{\bar{u}} \leq f$, is the portion of the \underline{k} -plane (figure 6.1) which is beyond the right-hand boundary. (This sounds like a complicated way to estimate the stress loss, but it actually simplifies the computation over the apparently direct integration in equation 5.50.) The momentum flux loss is:

$$\overline{u_1 u_3} \Big|_{\text{LOST}} \equiv \frac{2 E_o f}{\pi^2 N_o} \int_f^N \frac{d\omega}{\omega} \frac{2}{\pi} \int_{\frac{\omega-f}{\bar{u}_1}}^{\infty} \frac{d\alpha}{\alpha_* \left(1 + \frac{\alpha^2}{\alpha_*^2}\right)} \int_0^{\cos^{-1}\left(\frac{\omega-f}{\bar{u}_1 \alpha}\right)} d\phi \cos \phi \quad (5.63)$$

We define

$$u_* = \frac{N_o b}{j_* \pi} = 72.2 \text{ cm s}^{-1}$$

$$U = \bar{u}_1 / u_* \quad (5.64)$$

$$W = \frac{\omega}{f} .$$

Then the integral becomes:

$$\overline{u_1 u_3} \Big|_{\text{LOST}} = \frac{2 E_O f}{\pi^2 N_O} \frac{1}{U} \int_1^{\frac{N}{f}} \frac{dW}{W} \left\{ \left[\left(\frac{W-1}{\sqrt{W^2-1}} \right)^2 + U^2 \right]^{\frac{1}{2}} - \left[\frac{W-1}{\sqrt{W^2-1}} \right] \right\} \quad (5.65)$$

We stop at this point and look at the frequency behavior of the critical layer stresses (fig. 5.3). The integrand is always 1 at $W = 1$, and decreases to $\frac{\sqrt{1+U^2}-1}{U} \cdot W^{-1}$ at large W . The inertial cusp is always integrable, and becomes less and less important as U becomes small. Except for a slight increase near $\omega = f$, the momentum flux loss occurs in proportion to the total momentum flux at each frequency. Evaluating the frequency integral we find:

$$\overline{u_1 u_3} \Big|_{\text{LOST}} = \frac{2 E_O f}{\pi^2 N_O U} \left[\begin{aligned} & 2 \sqrt{1-U^2} \left(\arctan \sqrt{\frac{U^2}{1-U^2}} - \arctan \sqrt{\frac{Y^2+U^2}{1-U^2}} \right) \\ & + \sqrt{1+U^2} \left(\ln \frac{1 + \sqrt{\frac{Y^2+U^2}{1+U^2}}}{1 - \sqrt{\frac{Y^2+U^2}{1+U^2}}} - \ln \frac{1 + \sqrt{\frac{U^2}{1+U^2}}}{1 - \sqrt{\frac{U^2}{1+U^2}}} \right) \\ & + 2 \arctan Y - \ln \frac{1+Y}{1-Y} \end{aligned} \right] \quad (5.66)$$

for $U < 1$, and

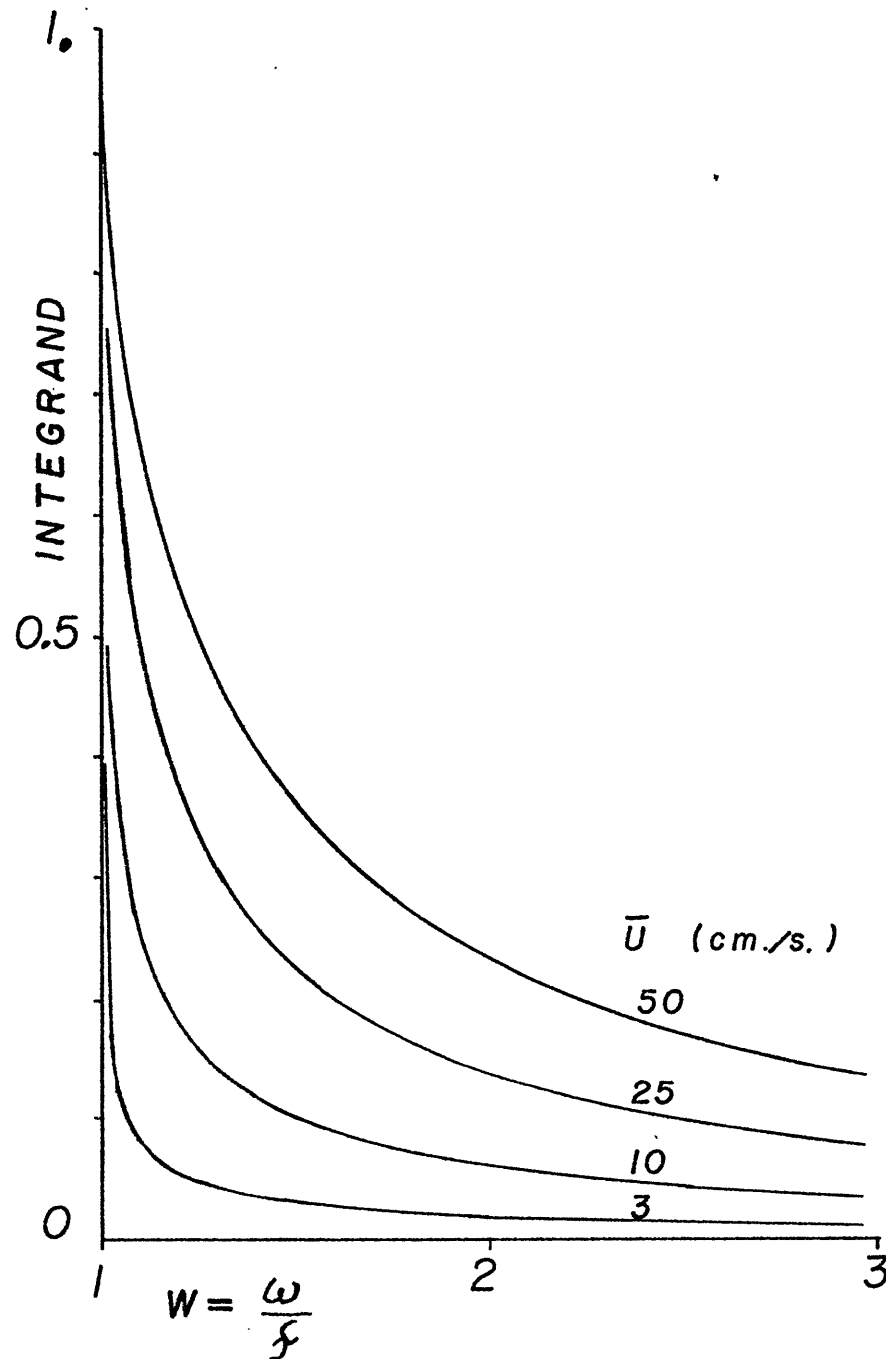


Figure 5.3 Frequency behavior of the estimate of momentum flux loss, equation 5.65.

$$\overline{u_1' u_3'} \Big|_{\text{LOST}} = \frac{2E_o f}{\pi^2 N_o U} \left[\begin{aligned} & \sqrt{U^2-1} \left\{ \ln \frac{1 + \sqrt{\frac{Y^2+U^2}{U^2-1}}}{1 - \sqrt{\frac{Y^2+U^2}{U^2-1}}} - \ln \frac{1 + \sqrt{\frac{U^2}{U^2-1}}}{1 - \sqrt{\frac{U^2}{U^2-1}}} \right\} \\ & + \sqrt{U^2+1} \left\{ \ln \frac{1 + \sqrt{\frac{Y^2+U^2}{U^2+1}}}{1 - \sqrt{\frac{Y^2+U^2}{U^2+1}}} - \ln \frac{1 + \sqrt{\frac{U^2}{U^2+1}}}{1 - \sqrt{\frac{U^2}{U^2+1}}} \right\} \\ & + 2 \arctan Y - \ln \frac{1+Y}{1-Y} \end{aligned} \right] \quad (5.67)$$

for $U > 1$.

For both representations above,

$$Y = \frac{1 - \frac{f}{N(z)}}{\sqrt{1 - \frac{f^2}{N^2(z)}}} \quad (5.68)$$

As $\bar{u}_1 \rightarrow \infty$ the integral becomes:

$$\overline{u_1' u_3'}_{\text{MAX}} = \frac{2E_o f}{\pi^2 N_o} \ln\left(\frac{N(z)}{f}\right). \quad (5.69)$$

This is the maximum momentum flux available (in any given direction) from the GM 76 spectrum. The depth dependence $N(z)$ is due to waves which encountered a vertical turning

184

point at $\omega_0 = N(z)$. Those waves are absent from the spectrum at depths below their turning point. For $N(z) = N_0 = 3$ cph, $f = .04$ cph, this maximum stress is $0.35 \text{ cm}^2 \text{ s}^{-1}$. ($= .35 \text{ dyne cm}^{-2}$). At a level where $N(z) = 2$ cph, the maximum available is $0.32 \text{ cm}^2 \text{ s}$.

The \bar{u} behavior of the absorbed momentum flux is surprisingly well-behaved, considering its apparent complexity. A plot of this stress vs \bar{u} for various values of $N(z)f$ is shown in fig. 5.4 for $N_0 = 3$ cph, $f = 0.04$ cph. The wave momentum flux lost is almost directly proportional to the velocity, for moderate \bar{u} , with a constant of proportionality, \tilde{V} , of 0.0028 cm s^{-1} in the thermocline. Since an arbitrary, nondivergent wave momentum flux can be superimposed on this picture, we can only estimate stress divergences:

$$\frac{\partial}{\partial z}(\bar{u}_1 \bar{u}_3) \approx -\tilde{V} \frac{\partial \bar{u}_1}{\partial z} \quad (5.70)$$

Neglecting all the other terms in the mean flow equation, we have an extremely simple solution for the time evolution of an initial velocity profile, $\bar{u}_1(z, t_0) = g(z)$: (c.f., Jones and Houghton, 1971)

$$\frac{\partial \bar{u}_1}{\partial t} - \tilde{V} \frac{\partial \bar{u}_1}{\partial z} = 0 \Rightarrow \bar{u}(z, t) = g(z + \tilde{V}t) \quad (5.71)$$

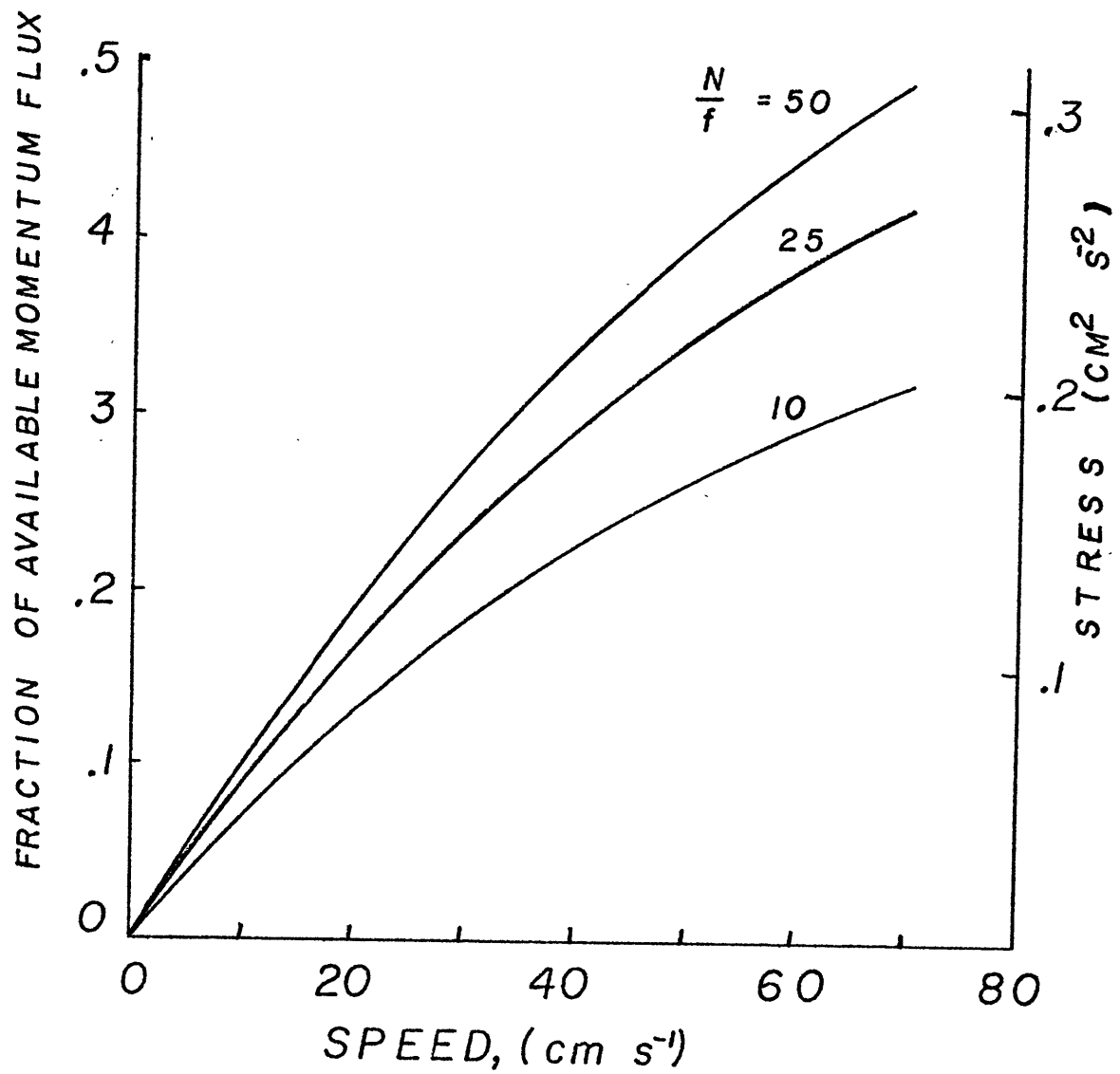


Figure 5.4 Momentum flux lost to critical layer absorption, estimated from GM 75⁺ model spectrum.

Since the wave momentum absorption by the mean velocity is almost proportional to the local shear, regions of high shear trap more wave momentum and feel greater acceleration. An initial shear profile will tend to move downward, preserving its shape, at velocity $\tilde{V} \sim 2.4$ m/day. This effect is so weak as to be unobservable. No stress correlations consistent with critical layer absorption were observed, although stress correlations indicating critical level wave generation were observed.

5.8 Summary

The solution to the radiation balance equation (RBE) with a particular source term demonstrates that it is possible to have an equilibrium solution to the RBE which:

- is consistent with present models and observations of the internal wave field,
- is consistent with free vertical propagation of individual waves and the associated WKB characteristics that have been observed,
- exists in the presence of a vertical shear without attempting to "relax" back to the state that existed before the shear.

The only momentum exchange with the mean flow comes in through critical layer effects, either absorption or generation. The expected stresses due to absorption are

quite weak; based on a 400 m thick thermocline, the maximum expected magnitudes correspond to a vertical eddy viscosity of $\sim 112 \text{ cm}^2 \text{ s}^{-1}$.

The essential difference between the present theory and that of Müller lies in the characterization of the source terms. Müller assumes the source terms (and equilibrium state) to be independent of the shear. We have demonstrated that some realistic source terms allow the equilibrium state to be a function of \bar{u} through the dispersion relation. The wavefield can thus move with the Liouville characteristics and remain in equilibrium.

Chapter 6

INTERNAL WAVEFIELD CURRENT ANISOTROPY IN THE PRESENCE OF A LOW FREQUENCY FLOW.

6.1. Introduction

Frankignoul (1974) discovered in data taken from Site D a strong tendency for internal wave velocities to be stronger in a direction normal to the low-frequency current than parallel to it. He defined an "anisotropy factor"; $A.F. = \frac{P_{uu} - P_{vv}}{P_{uu} + P_{vv}}$ where P_{uu} and P_{vv} are the spectra of velocity components in directions parallel and normal, respectively, to the low frequency velocity. He then plotted scatter diagrams of A.F. vs. $|\bar{u}|$ which demonstrated a tendency for the A.F. to be negative and large during times of large (greater than 10 cm/sec) mean current. He also found that the effect was strongest at higher internal wave frequencies.

Frankignoul investigated several possible causes for this effect, including the effect of Doppler shifting an isotropic (in the advected reference frame) wavefield. He concluded that none of the investigated mechanisms could be responsible for the large observed anisotropy, and estimated that the effects of critical level wave absorption might account for the observed anisotropy.

The proposed "basic state" R,B.E. solution offers an opportunity to investigate Frankignoul's suggestion by allowing us to compute the wavefield anisotropy in the presence of a mean velocity, assumed unidirectional for simplicity. The

detailed functional form of the spectrum was estimated by matching the spectrum to the Garrett-Munk (1975) model spectrum at a level of no mean motion. The action density spectrum for an arbitrary velocity was used to estimate the theoretical velocity spectra, and hence the theoretical anisotropy factor, as a function of the local $\bar{u}(z)$ (which determines the amount of Doppler shift) and the maximum $\bar{u}(z)$ in depth, which determines the fraction of the wavefield presumed to be lost to critical level absorption.

It was found in section 6.2 that, while critical level absorption, and (especially) reflection at a level where $\omega - k \cdot \bar{u} = N_{\text{LOC}}$ could induce anisotropies of 0(-0.15) in the wavefield, the mechanism could not explain the large (-.5) negative A.F. observed by Frankignoul (figure 6.13) and myself (figure 6.17). However, an extremely simple model which assumes random speed and direction errors in estimating the mean flow, satisfactorily accounts for the anisotropy in measurements taken with Geodyne 850 current meters. The VACM (Vector Averaging Current Meter) samples direction and speed in such a way that a large number of samples are taken in a moderate current. The meter appears to do enough averaging that the noise becomes insignificant.

6.2 Critical Level Wave Absorption Anisotropy Model

We start with the general R.B.E. "solution" (simply a balance of the vertical propagation terms) as a function of

$\alpha = (k_1^2 + k_2^2)^{1/2}$, ϕ = angle, measured from $\bar{u}(z)$, and ω , corresponding to an action density spectrum in which the vertical flux of action is depth independent (see chapter 5)

$$\eta(\alpha, \phi, \omega; z) = \frac{F(\alpha, \phi, \omega)}{V_3(\alpha, \phi, \omega; z)} \quad (6.1)$$

$V_3^{-1} = (\frac{\partial \omega}{\partial k_3})^{-1}$ is the Jacobian of the transformation from k_3 to ω . (We may neglect the vertical asymmetry of the spectrum for the moment, since it doesn't affect the horizontal velocities.) This spectrum, consistent with a balance of the vertical propagation terms in the RBE, is that of a field of internal waves which propagate freely in the vertical except for reflection and critical layer absorption at $\omega - \underline{k} \cdot \bar{u} = N, f$ respectively. The physics of the model are essentially those suggested by Frankignoul (1974).

The detailed structure of F is determined by the forcing at the surface and by the relaxation effects of the source terms. We have argued in 5.7 that the dominant wave generation processes should not be strongly affected by the mean flow, and hence that we expect something much like the equilibrium spectrum to be forced. It is unclear whether this would be in an advected or non-advected frame of reference. In the absence of further information on the effects of Doppler shifting on internal wave generation, we will determine F by matching the spectrum to the GM 75 and GM 76 model spectra at a level of no mean motion. To change the results to those for a spectrum which is forced in an

advection frame, we simply replace \bar{u} by $\bar{u} - \bar{u}_{\text{surface}}$ in the results.

Performing the match, we find, using the notation of Garrett and Munk (1975):

$$\eta(\alpha, \phi, \omega; z) = \frac{E_0 2N(z) f(\omega^2 - f^2)}{N_0 \pi \omega^3} \frac{A(\frac{\alpha}{\alpha_*}) \omega_0}{\alpha_* (\omega_0^2 - f^2)^{3/2}} \quad (6.2)$$

where:

$A(x)$ = wavenumber dependence (2 forms used)

$$\omega_0 = \omega - \alpha \bar{u}(z) \cos \phi$$

$$\alpha_*(\omega_0) = j_* \pi / N_0 b \quad \omega_0^2 - f^2$$

$$E_0 = 30 \text{ cm}^2 \text{ s}^{-2}$$

$$N_0 = 2\pi \times 3 \text{ h}^{-1}$$

$$b = 1.3 \text{ km}$$

$$j_* = \text{mode no. bandwidth}$$

The horizontal velocity spectra are given by (From B-3):

$$P_{uu}(\omega) = \int_0^{2\pi} d\phi \int_0^{\alpha_M} d\alpha U^2 \eta \omega_0$$

$$P_{vv}(\omega) = \int_0^{2\pi} d\phi \int_0^{\alpha_M} d\alpha V^2 \eta \omega_0 \quad (6.3)$$

where:

$$\alpha_M = \begin{cases} \frac{\omega - f}{u_M \cos \phi} & \cos \phi > 0 \\ \frac{\omega - N}{u_M \cos \phi} & \cos \phi < 0 \end{cases}$$

$$U^2 = \frac{N^2 - \omega_o^2}{N^2 - f^2} \left[\cos^2 \phi + \frac{f^2}{\omega_o^2} \sin^2 \phi \right]$$

$$V^2 = \frac{N^2 - \omega_o^2}{N^2 - f^2} \left[\frac{f^2}{\omega_o^2} \cos^2 \phi + \sin^2 \phi \right]$$

$$\bar{u}_M = \text{Max. in } z \text{ of } \bar{u}(z) .$$

A sketch of the integration region is given in fig. 6.1.

The integration boundaries are the inner pair of vertical lines, which approach the outer lines as $u(z) \rightarrow u_M$.

The $N^2 - \omega_o^2$ and $N^2 - f^2$ in the wave functions U^2, V^2 can be replaced by N^2 consistent with the GM 75 and GM 76 models. In practice, it made virtually no difference whether this approximation was made, since the horizontal currents are minimal at high frequencies.

The integrals have a complicated topography near the outer boundary when $\bar{u}(z) = \bar{u}_M$ (the outer boundaries on figure 6.1). There is a non-integrable cusp in horizontal kinetic energy at this boundary, due to the v_3^{-1} behavior of the spectrum. The waves in this region have a near-inertial intrinsic frequency, and so are highly isotropic. To avoid problems in the numerical integration for GM 75 (section 4.3), the action density spectrum was multiplied by a factor $(\omega_o^2 - f^2)/(\omega^2 - f^2)$. This reduced the strength of the cusp to finite energy. Since we have reduced the strength of the isotropic part of the field, we expect this approximation will increase the estimate of the anisotropy factor over its actual value.

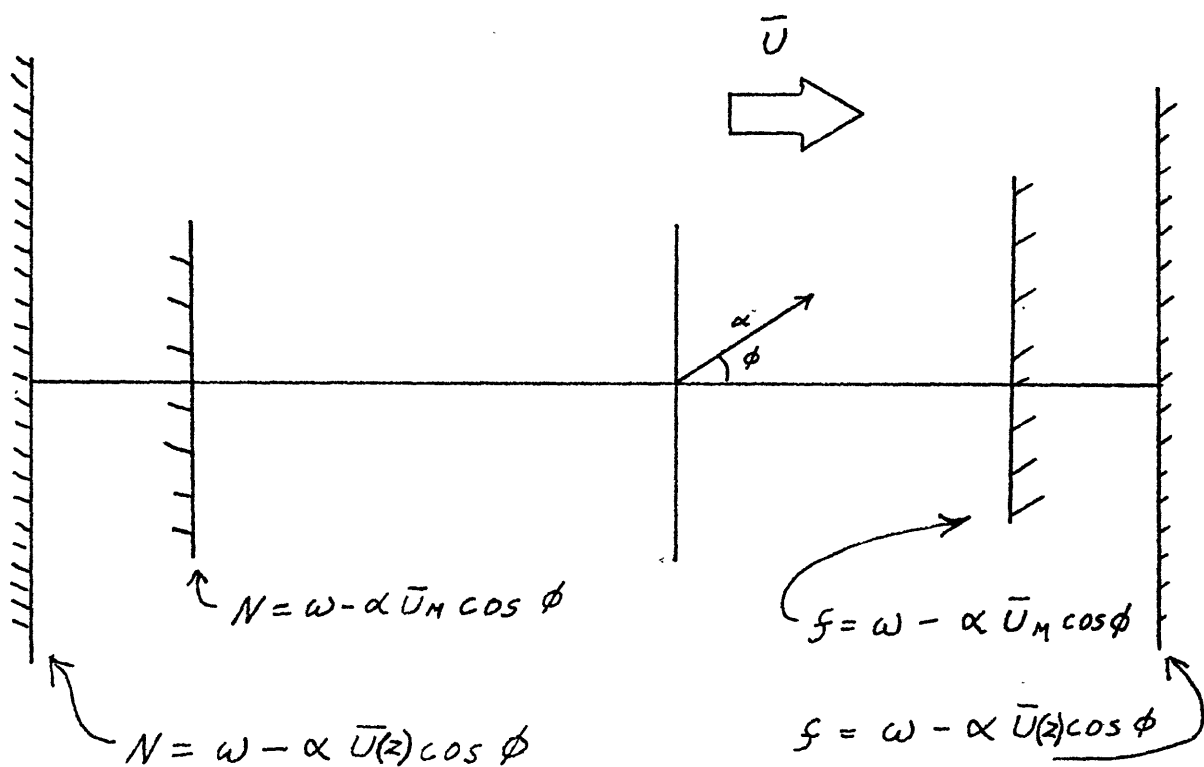


Figure 6.1 Integration region in (α, ϕ) space for the spectra (6.3) in the presence of mean flow.

6.3 Evaluation of the Integrals

For the GM 75 model, we have:

$$A(x) = \frac{1.5}{(1+x)^{2.5}} \cdot \quad (6.4)$$

This form for the wavenumber spectrum is analytically inconvenient; the inner integral (in any coordinate system) is elliptic, and so the outer integral is analytically intractable. Therefore, the integrals were estimated numerically for several values of \bar{u}_M and $\bar{u}(z)$ = (local value). The computed anisotropy factor for this model versus \bar{u} (local) is shown in figure 6.2 for several frequencies corresponding to those used by Frankignoul (1974). (Maximum \bar{u} is 1.5 times local \bar{u} ; $j_* = 6$.) The measurements of A.F. vs. \bar{u} by Frankignoul are shown in figure 6.13 for comparison. It is seen that the computed A.F. are of the observed sign and order of magnitude. However, anisotropies of (-.4) are not reached unless unrealistically large values for \bar{u}_M are assumed. Hence, the anisotropy does not seem to be accounted for by critical level absorption.

The anisotropy factor was computed for several values of $\bar{u}(z)$ and \bar{u}_M , and it was found that, when $\bar{u}_M \geq 1.5 \bar{u}(z)$, the anisotropy was roughly independent of $u(z)$, depending only on u_M . This indicates that the Doppler shift terms in the integrands are negligible where the action density is large, and that we may approximate $\omega - \alpha \cdot \bar{u} \cos \phi$ with ω in equations 6.3, keeping the boundaries $\omega - \alpha u_M \cos \phi = f, N$ in the same place. This approximation was made for integrands

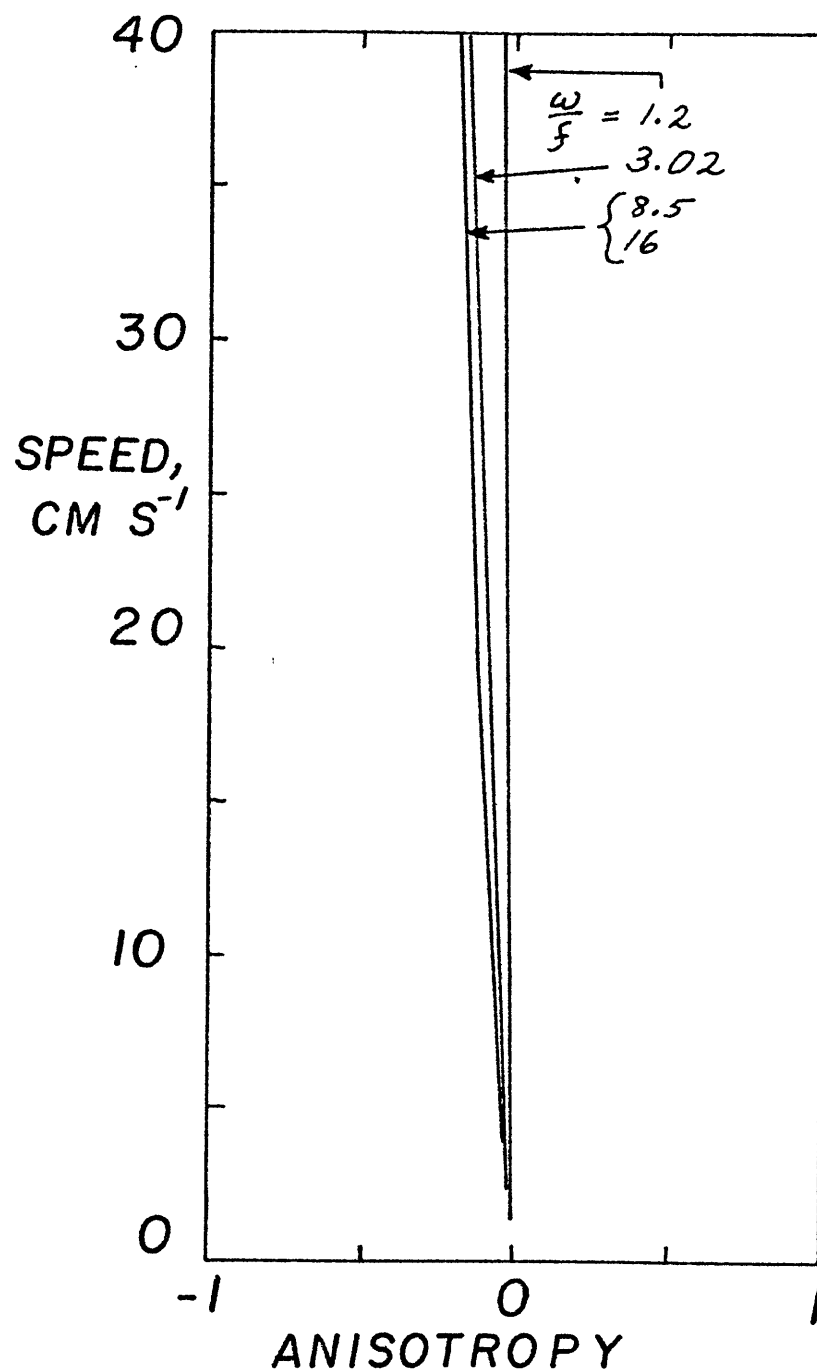


Figure 6.2 Anisotropy factor for the GM75 wave model, for $u_M = 1.5 \bar{u}(z)$, $j_* = 6$.

involving a "new, improved" version of the spectrum (Cairns and William, 1976), designated GM 76:

$$A(x) = \frac{\pi}{2} \frac{1}{1+x^2} \quad j_* = 3 \quad (6.5)$$

This form of wavenumber dependence is very convenient analytically, and it was possible to obtain analytic expressions for the integrals. This was done in the hope that the more accurate spectral representation of GM 76 might lead to larger estimates of the anisotropy factor than those from GM 75.

The integrals obtained for GM 76 were, neglecting Doppler shift effects:

$$P_{uu} - P_{vv} \approx -2k(\omega) \left[H\left(\frac{\omega - f}{u_M \alpha_*}\right) + H\left(\frac{N - \omega}{u_M \alpha_*}\right) \right] \quad (6.6)$$

$$P_{uu} + P_{vv} \approx \frac{\omega^2 + f^2}{\omega^2 - f^2} k(\omega) \left[G\left(\frac{\omega - f}{u_M \alpha_*}\right) + G\left(\frac{N - \omega}{u_M \alpha_*}\right) \right] \quad (6.7)$$

where:

$$H(x) = (x \sqrt{1+x^2} \cdot \ln\left(\frac{\sqrt{1+x^2} + 1}{x}\right)) - x$$

$$G(x) = \frac{\pi^2}{2} - 2x \int_0^{\pi/2} \frac{u \sin u \, du}{\cos^2 u + x^2}$$

$$K(\omega) = \pi \frac{1.5 E_O N(z) f \cdot \bar{u} \alpha_*}{4\omega (N^2 - f^2)}$$

$G(x)$ could not be evaluated analytically. However, approximations for large and small x were found which were accurate

197

to better than 5% in their respective ranges $x \gtrsim 2$. For large x :

$$\begin{aligned} G(x) &\approx \frac{\pi^2}{2} - \frac{2}{x} \int_0^{\pi/2} u \sin u \, du \\ &\approx \frac{\pi^2}{2} - \frac{2}{x} \end{aligned} \quad (6.8)$$

For small x , we re-write the integral in Cartesian coordinates, (k, l) rather than (α, ϕ) . The original integral becomes:

$$\begin{aligned} P_{uu} + P_{vv} &= \frac{\omega^2 + f^2}{\omega^2 - f^2} k(\omega) \cdot 2 \int_{-\left(\frac{N-\omega}{u_M \alpha_*}\right)}^{\left(\frac{\omega-f}{u_M \alpha_*}\right)} dk \int_0^\infty dl \frac{1}{(k^2 + l^2)^{1/2} (1 + k^2 + l^2)} \\ &= \frac{\omega^2 + f^2}{\omega^2 - f^2} k(\omega) \left[G'\left(\frac{\omega-f}{u_M \alpha_*}\right) + G'\left(\frac{N-\omega}{u_M \alpha_*}\right) \right] \end{aligned} \quad (6.9)$$

where:

$$G'(x) = \int_0^x dk \frac{1}{(1+k^2)^{1/2}} \ln \frac{(1+k^2)^{1/2} + 1}{(1+k^2)^{1/2} - 1}.$$

Comparison with 6.7 shows that $G' = G$.

Now, for small x (and therefore k), we expand all the terms $(1+k^2)^{\pm 1/2}$ in a binomial expansion, and keep the lowest order terms:

$$\begin{aligned} G(x) &\approx \int_0^x dk (1 + 0(k^2)) \ln \left(\frac{4}{k^2} + \dots \right) \\ &= 2x - x \ln \left(\frac{x^2}{4} \right). \end{aligned} \quad (1.10)$$

We shall see that the above approximations cross at about $x = 2$, and are each accurate in their respective ranges:

$$G(x) \approx \begin{cases} \frac{\pi^2}{2} - \frac{2}{x} & x \geq 2 \\ 2x(1 - \ln \frac{x}{2}) & x \leq 2 \end{cases} \quad (6.11)$$

Plots of the small and large x approximations for $G(x)$ and numerical estimates are plotted in figure 3 for a 4-decade range of x . The approximations are surprisingly good; better than 5% over their respective ranges. A plot of $H(x)$ is shown in figure 6.4, on linear axes, to illustrate the behavior of the integral $(P_{uu} - P_{vv})$.

In view of the behavior of the integrals it was found that:

1. A large anisotropy cannot be caused by critical level absorption because of the factor $\frac{\omega^2 - f^2}{\omega^2 + f^2}$ appearing in the ratio $(P_{uu} - P_{vv})/(P_{uu} + P_{vv})$.
2. It was found that the largest anisotropy for a given value of u_M can be produced by allowing ω to approach N . This occurs at $\frac{N-\omega}{u_M \alpha_*} \sim 0.4$, where $H(.4) \sim 0.3$. However, this means that $\omega - f \sim N - f$ is large, so that the anisotropy factor is approximately:

$$\begin{aligned} \text{A.F.} &\approx \frac{\omega^2 - f^2}{\omega^2 + f^2} \frac{-2(H(.4) - H(\infty))}{G(.4) + G(\infty)} \\ &\approx -0.12 \end{aligned} \quad (6.12)$$

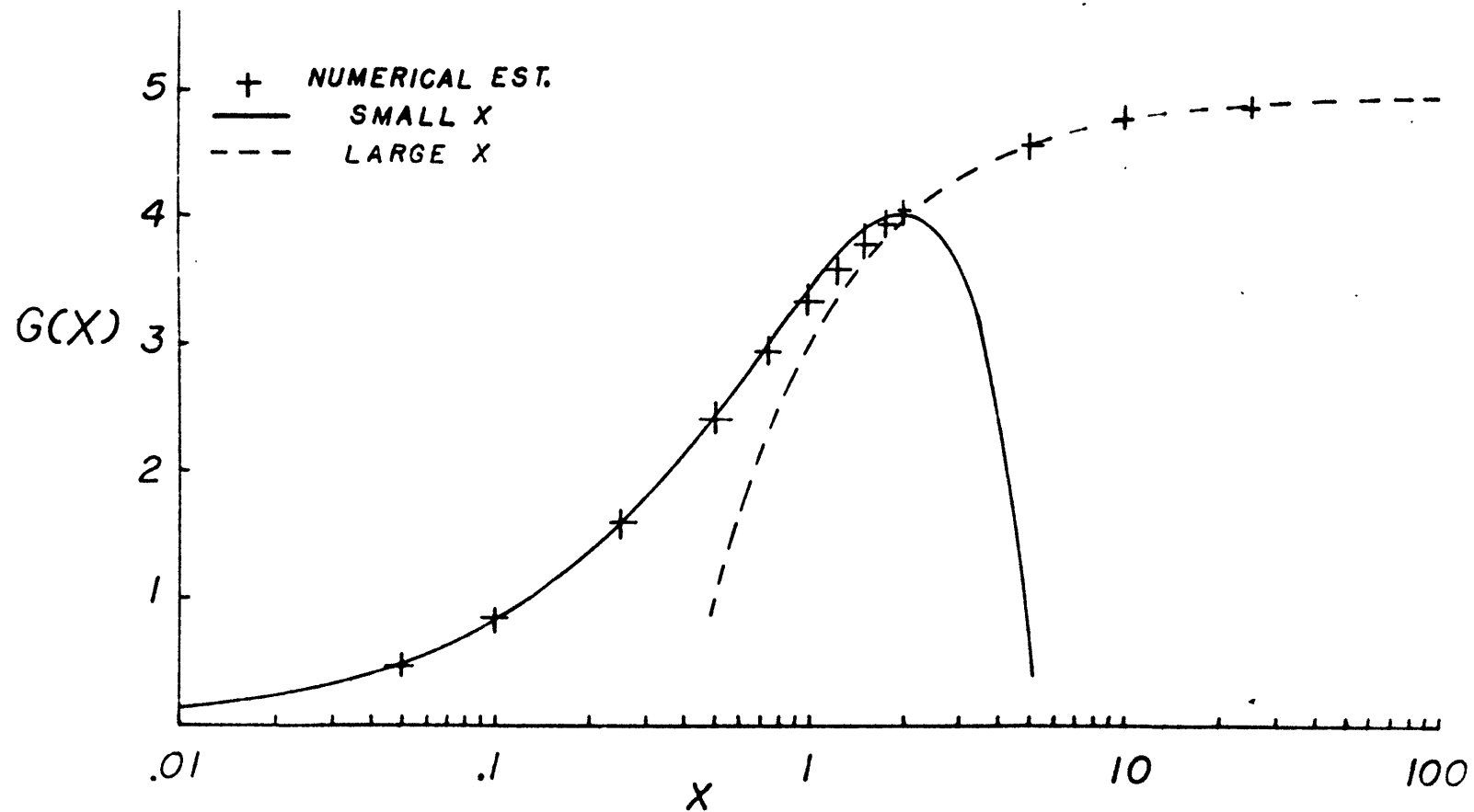


Figure 6.3 $G(x)$, the function involved in the estimate of $P_{11} + P_{22}$ for GM 75⁺. Shown are the small x approximation (solid line), the large x approximation (dashed line), and several numerical estimates (+).

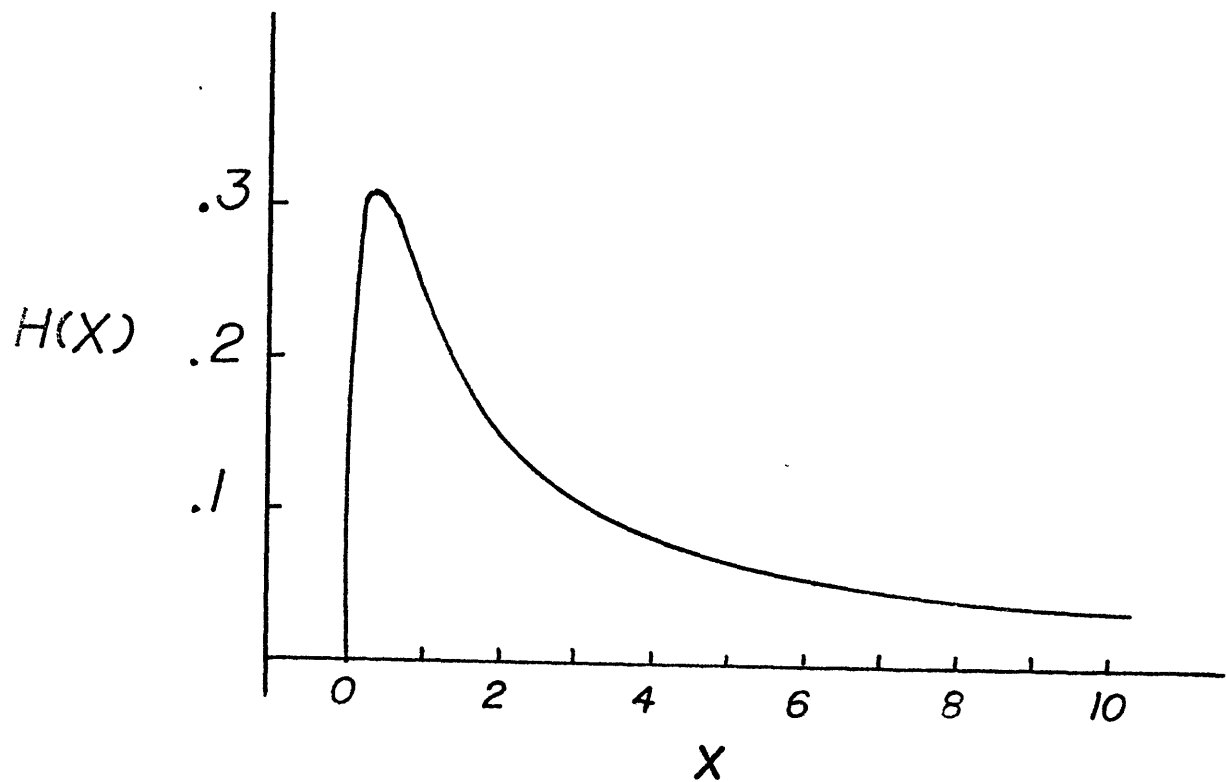


Figure 6.4 A plot of $H(x)$, involved in the $P_{11} - P_{22}$ integral for GM 75^+ .

The anisotropy was found to increase only slowly with \bar{u}_M beyond this value, due to the decrease in $H(x)$.

Plots of the GM 76 estimated anisotropy factor for parameters representative of the measurement conditions for data 5661 and Frankignoul's (1974) Site D data are shown in the following section.

6.4 Effects of Current Meter Sensor Noise

Since the effects of critical layer absorption do not account for the observed current anisotropy, nor do the effects of Doppler distortion of the measured currents (Frankignoul, 1974), we now investigate the possibility of instrumental effects.

Mooring 576 is a subsurface POLYMODE Array II mooring at a comparatively northern latitude ($38^\circ 30' \text{ N}$, $54^\circ 55' \text{ W}$), with a single 850 current meter at 4000 m nominal depth. During the month of February 1976, the instrument recorded high speeds, $20\text{--}30 \text{ cm s}^{-1}$. The indicated direction, measured clockwise from north, held fairly steadily at 180° , or due south (see figure 6.5).

The power spectra of the east and north velocities are shown in figure 6.6. Both are dominated by a white spectrum at medium-to-high internal wave frequencies, but the level is almost a decade higher for the east direction, perpendicular to the mean flow, than for the north. Current

702

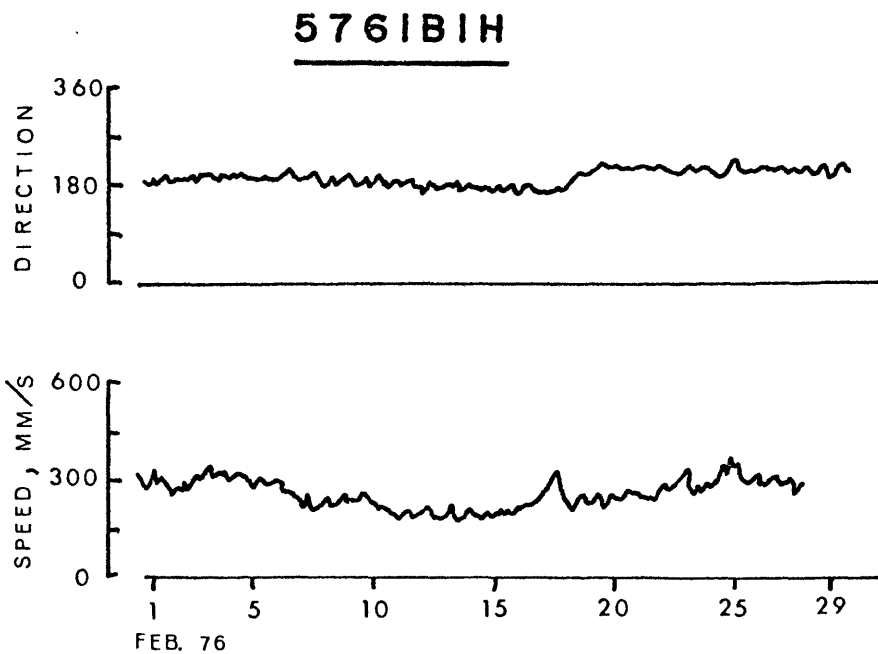


Figure 6.5 Speed in mm s^{-1} and direction in degrees, clockwise from North, from data 5761 ($38^{\circ}30'\text{N.}$, $54^{\circ}55'\text{W.}$, 4000 m deep) for the month of February, 1976.

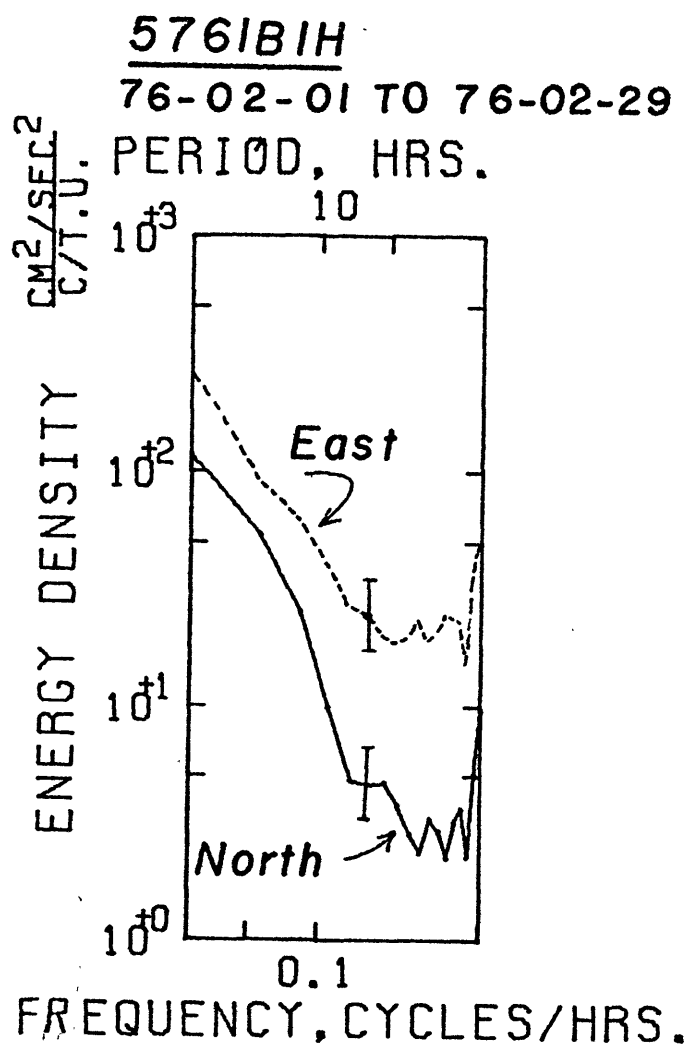


Figure 6.6 Power spectra for the East and North velocities at mooring 576 for the month of February, 1976. (50% overlapped Hann, 37 pieces of 36 hours length.)

fine-structure is similar in origin to temperature fine-structure contamination, and presumably produces a non-white noise spectrum as in Joyce and Desaubies (1977). The float for the mooring is at 4 km, well removed from surface wave effects. Presumably, then, this noise is instrumental in origin, as its white spectrum would suggest.

Figure 6.7 shows the energy spectrum for the north velocity, computed in the same manner as for figure 6.6, from a segment of the record when the mean velocity was much slower, typically 5 cm s^{-1} . (The East and North spectra were equal to within statistical uncertainties.) Note that there is no obviously white portion of the spectrum, and that the spectrum continues downward at high frequencies as is usual for internal wave spectra. (The energy density scale for figure 6.7 is a full decade lower than for figure 6.6.) Obviously the white noise is strongly anisotropic in the sense observed by Frankignoul, and is related to the mean velocity. The most reasonable explanation for this noise is the effect of small errors in the measurement of the direction and speed of the current. We will presently attempt to model this.

Current meters used at Woods Hole Oceanographic Institution measure current speed and direction, each with some error. This error is reduced to an extent by an averaging procedure which varies with the type of instrument.

205

5761BIH

76-08-25 TO 76-09-18

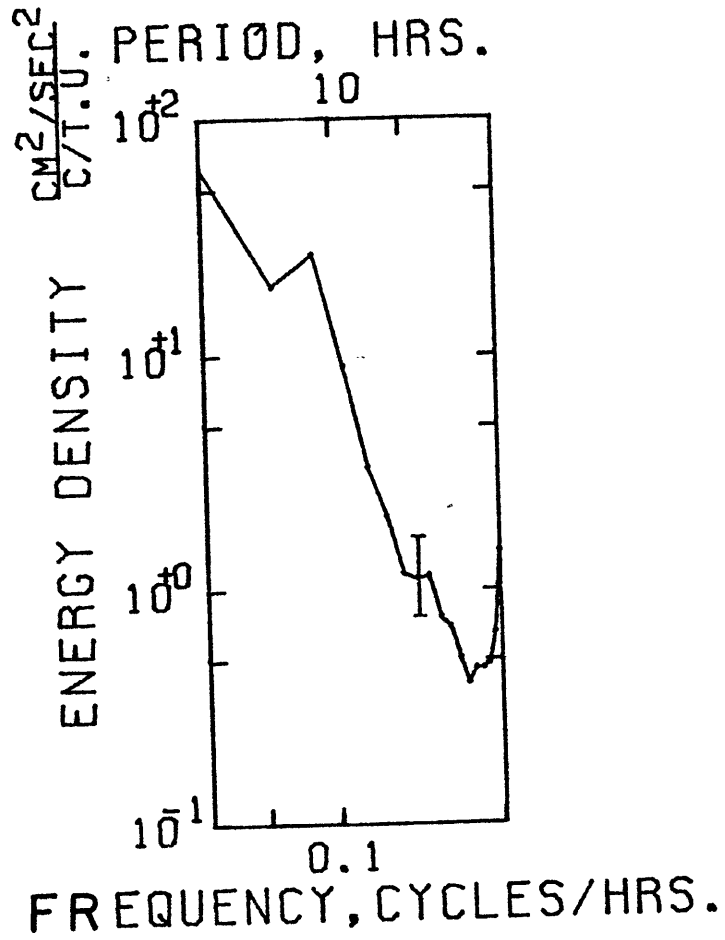


Figure 6.7 Power spectrum for the North velocity from data 5761 for the period 76-08-25 to 76-09-18, when the mean velocity was less than 5 cm s⁻¹.

The Geodyne 850 current meter obtains a single measurement by "burst-sampling." In a single recording interval, several samples of direction and speed are recorded, and later vector-averaged to yield a single velocity estimate. Typically, from 12 to 62 samples are taken at intervals of 5.27 seconds to form a single estimate. The VACM (Vector-averaging current meter, model 605, American Machine and Foundry, Alexandria, VA 22314) samples direction and speed every 1/8 rotor turn, or about 4.7 cm of water displacement. These samples are summed within the instrument to form one current velocity estimate, effectively averaged over the sample interval. While a fixed number of estimates per record is taken with the 850 current meter, the number of estimates taken by the VACM varies dramatically with the speed. Since the measurement is spread out over the record sampling interval, the averaging is likely to be more effective. (The burst sampling scheme was designed for a different purpose--to remove relatively high frequency surface wave noise from the measurements.)

Consider an isotropic internal wave field in the presence of a relatively large mean current $\bar{u} \gtrsim 5 \text{ cm s}^{-1}$. We assume that the rms direction error in a given record is $\delta\theta$, assumed to be independent of the speed. We will assume the rms speed error to be of the form:

$$\text{rms speed error} \approx \bar{u} \cdot \delta S + \Delta \quad (6.13)$$

so that the speed error is, at large mean speed, linearly proportional to the speed, with fractional error ΔS . Δ represents a velocity-independent error in the speed measurement, which is a catch-all for systematic speed offsets, stall speed errors, etc. The effect of stall speed error was considered in the "error estimates" appendix, and found to be non-white in nature, and unimportant for $\bar{u} \geq 5$ cm/sec. We will assume that the order of magnitude of Δ is small, perhaps less than 1/4 cm/sec. At low mean speeds (less than 5 cm/sec), when Δ is important, the internal wave field alters the direction of the total current vector to such an extent that the resulting errors are uniformly distributed in direction. Thus at low speeds we expect no anisotropy to be induced by measurement error. At high speeds the effect of Δ is expected to be unimportant compared to δS .

In a coordinate system rotated so that the x-axis is in the direction of the mean current, the cartesian velocities measured are:

$$\begin{aligned} u &= S \cos \theta \\ v &= S \sin \theta \end{aligned} \tag{6.14}$$

where S, θ are the true speed and direction.

For $\bar{u} > 5 - 10$ cm s⁻¹ and for small direction and speed errors, the cartesian velocity errors are, approximately:

$$\begin{aligned} \delta u &\approx \delta S \bar{u} + \Delta + O(\delta \theta^2) \\ \delta v &\approx \delta \theta \bar{u} \end{aligned} \tag{6.15}$$

Note that, for $\delta\theta$ (radians) larger than δS , the tip of the velocity vector is most likely to fall within an ellipse whose major axis is oriented normal to the flow (see figure 6.8). This anisotropic noise is introduced into the measurements of the internal wave field, causing high estimates of the wavefield anisotropy factor at high frequencies.

A plausible cause for large direction errors has been suggested by Payne (1977, personal communication), who has found evidence that on some moorings, current meters undergo large amplitude (90°), high-frequency (1/60 to 1 Hertz) torsional oscillations. Payne suggests that the current meter is acting as the mass in a torsional pendulum, with the mooring line under tension acting as the spring. Excitation is provided by vortex-shedding from non-cylindrical parts of the mooring hardware, such as flotation "hard-hats." He finds the frequency and amplitude behavior of the oscillations to vary dramatically from mooring to mooring, depending on the design.

Figures 6.9-6.12 are scatterplots of the variance of a basic quantity computed from the original twelve samples comprising a record, plotted against the average rotor speed for that record. The quantities for which variance scatterplots were computed are:

figure 6.9 vane angle relative to the instrument

figure 6.10 compass card angle relative to the
instrument

FIG. 6.8

209

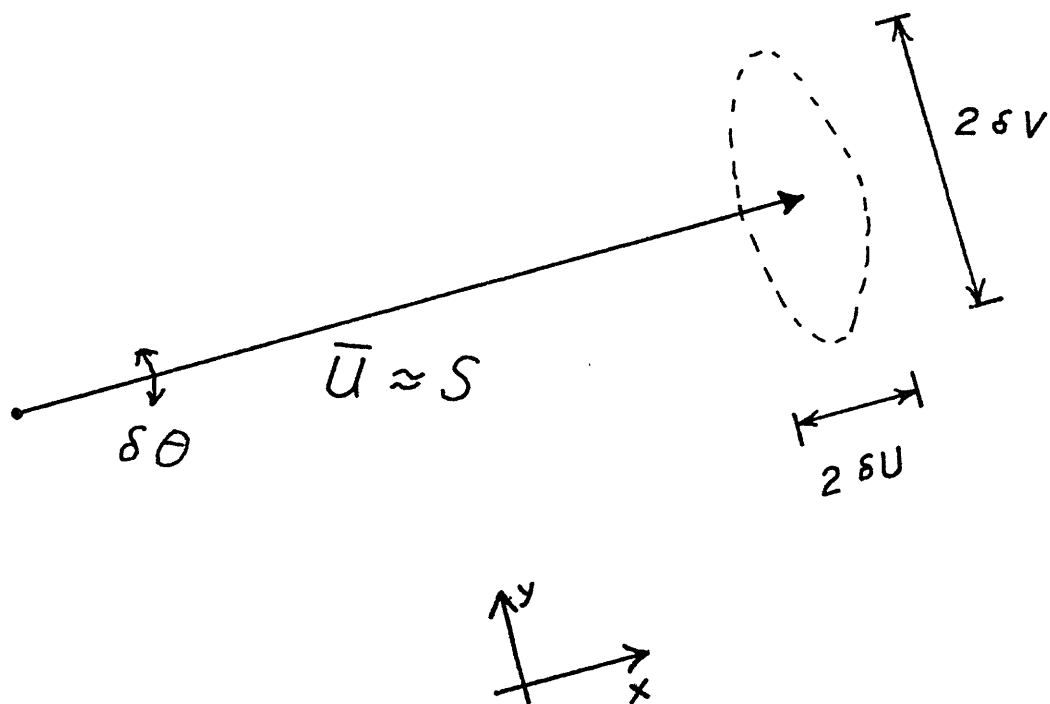


Figure 6.8 Sketch of the geometry for the current meter noise model.

figure 6.11 current bearing estimated from the vane
and compass

figure 6.12 rotor speed variance .

The quantities are displayed for data number 5761, our previous example.

Figure 6.9, the vane angle variance, gives an idea of the amplitude of the torsional oscillations as a function of speed. (The vane doesn't turn while the meter does.) The rms amplitude starts at about 20° at low speeds, and increases to about 30° (85° , peak-to-peak) at 14 cm s^{-1} , remaining roughly constant at higher speeds. There is an odd "drop-out" speed (24 cm s^{-1}) but we will ignore this. The compass variance decreases with increasing speed, even though the amplitude of the oscillation is roughly constant. Since the compass mechanism is damped, this indicates that the oscillation frequency is increasing with speed. The pendulum frequency should increase with the tension in the mooring line, and so with the speed, if we are observing torsional pendulum effects.

Figure 6.11 shows the variance of the current bearing versus rotor speed. The error is due to failure of the vane and compass to track the direction changes rapidly enough. The variance is roughly constant at high (greater than 15 cm s^{-1}) speed, corresponding to an rms error in the record average of 2.9 degrees, assuming all 12 samples to be statistically independent.

Figure 6.9 Variance of vane angle relative to current meter computed for each 12-sample record, and plotted against the average rotor speed.

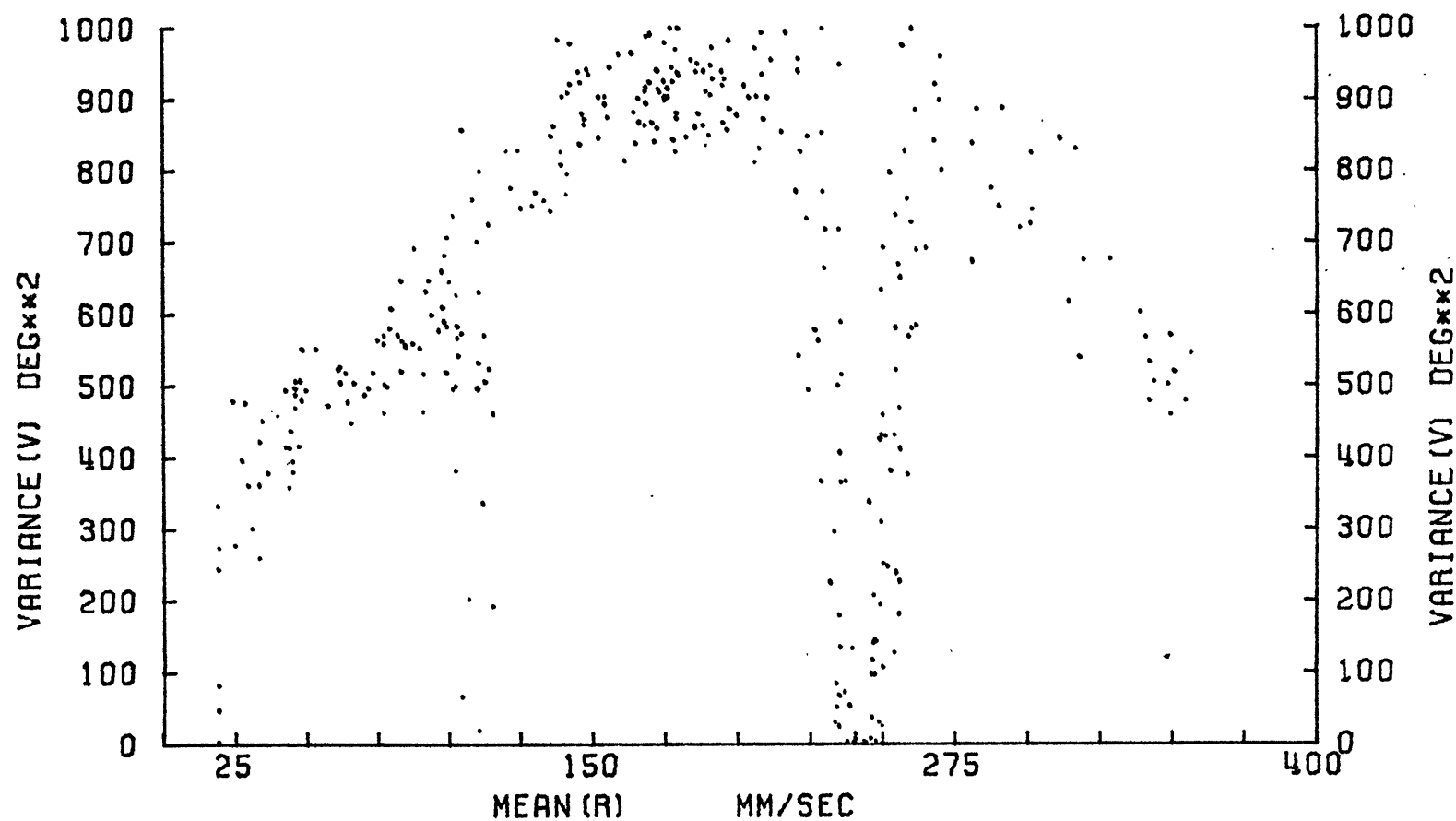


Figure 6.10 As figure 6.9, except for compass card angle relative to the current meter.

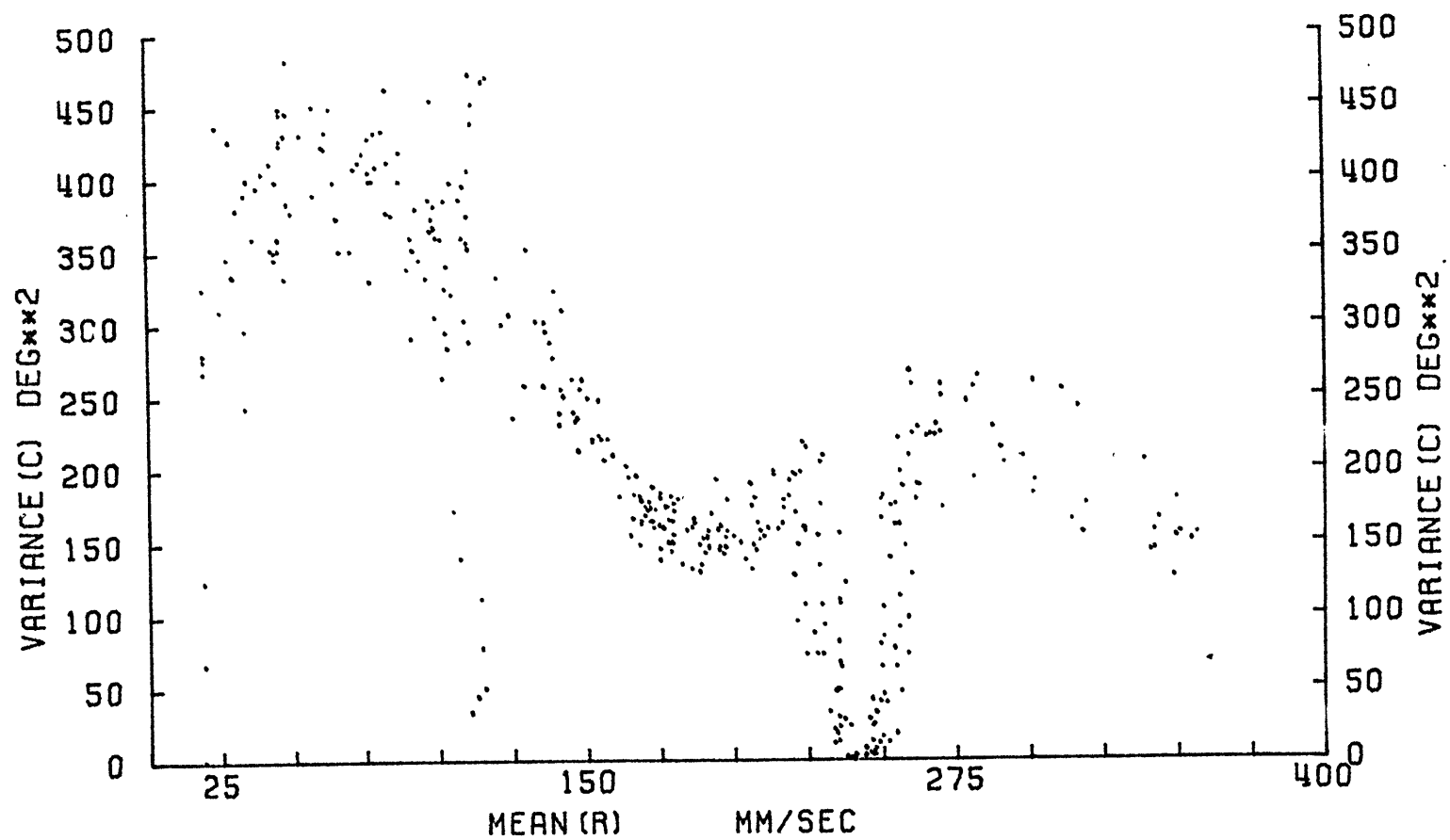


Figure 6.11 As figure 6.9, for current bearing.

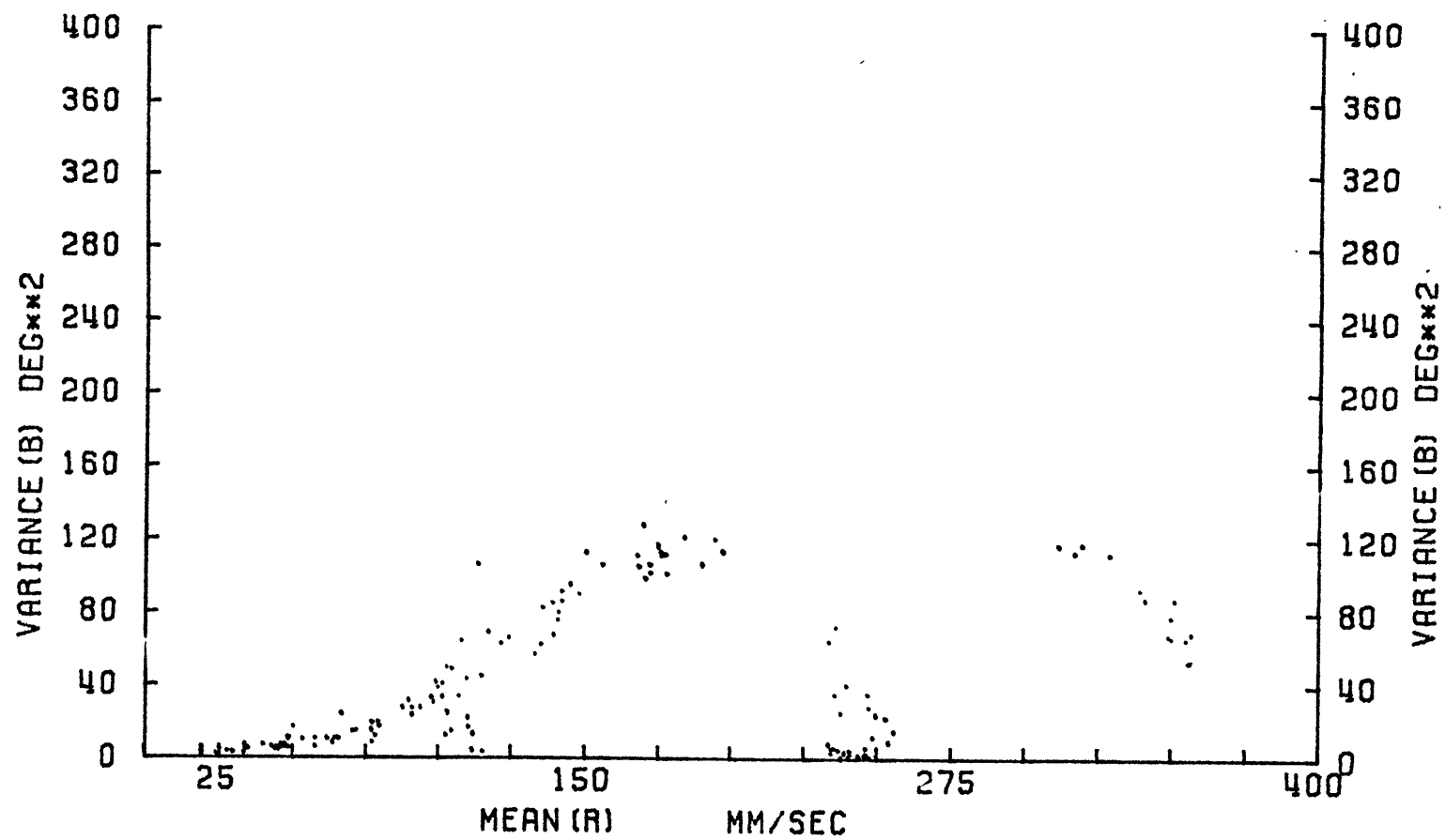


Figure 6.12 As figure 6.9, for rotor speed estimate.

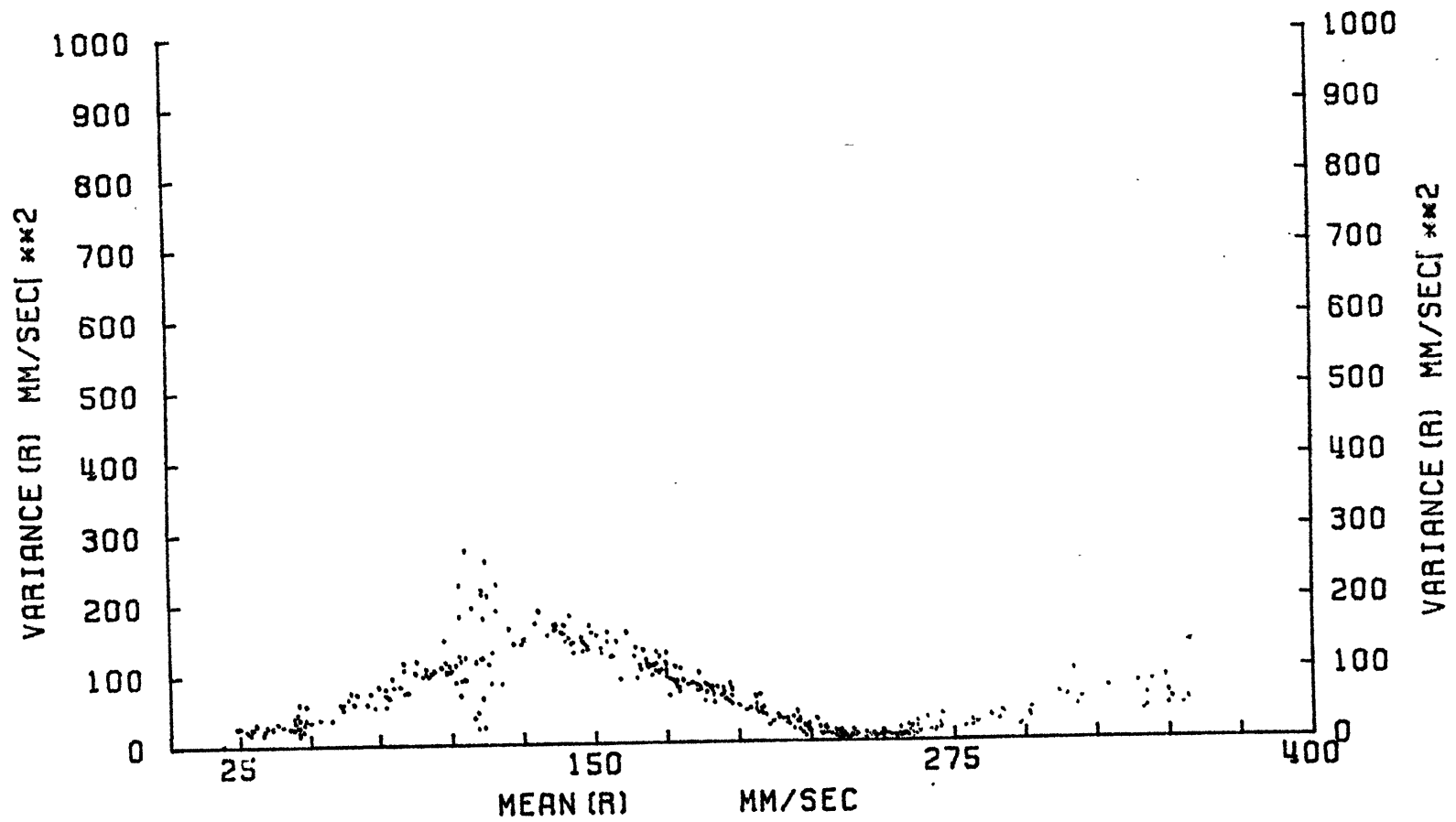


Figure 6.12 shows the variance of the rotor speed versus the average rotor speed. It behaves very oddly with speed, increasing and decreasing and then increasing again. A typical speed error in an averaged record (again, assuming all twelve samples to be independent) is 1 cm s^{-1} .

The bearing and rotor speed variances vary very oddly with speed, and since the oscillation frequency varies, the degree of independence between samples is hard to estimate. In modelling the speed dependence of the errors in direction and speed, we will simply assume $\delta\theta = \text{constant}$ and assume that the speed error is proportional to the speed. This second assumption is not strictly true, but gives a better form for the anisotropy factor. A constant speed error would predict a small positive anisotropy factor at low speeds, which is not observed, probably because the true current direction changes due to inertial oscillations at low speeds. So to give the observed anisotropy behavior at low speeds, we set $\Delta = 0$.

Assuming that the measurement errors δu , δv are uncorrelated at adjacent sample times (i.e., white noise), we estimate the measured velocity spectra (denoted by superscript M):

$$P_{uu}^M = P_{uu} + (\delta S^2 \bar{u}^2 + \delta S \Delta \bar{u} + \Delta^2) \quad (6.16)$$

$$P_{vv}^M = P_{vv} + \delta\theta^2 \bar{u}^2 \Delta\omega \quad (6.17)$$

where:

P_{uu}, P_{vv} are the true velocity spectra, integrated over a frequency range of ω_{MIN} to ω_{MAX}

$$\Delta\omega = (\omega_{\text{MAX}} - \omega_{\text{MIN}}) \cdot 2\Delta t$$

= Bandwidth of the frequency band in Nyquists

Δt = Sampling interval.

Assuming no wavefield anisotropy and setting $\Delta = 0$, we compute the anisotropy factor:

$$\text{A.F.} = \frac{A_{\infty}}{1 + \left(\frac{u_0}{\bar{u}}\right)^2} \quad (6.18)$$

where:

$$A_{\infty} = - \frac{\delta\theta^2 - \delta S^2}{\delta\theta^2 + \delta S^2}$$

$$u_0 = \frac{P_{uu} + P_{vv}}{(\delta S^2 + \delta\theta^2) \Delta\omega}$$

As \bar{u} increases, the A.F. increases from zero to $\frac{1}{2} A_{\infty}$ at $\bar{u} = u_0$, and then on to A_{∞} at $\bar{u} = \infty$.

Integrating over the white portion of the power spectra in figure 6.6, from .194 cph to .444 cph, we find the total noise variance perpendicular to the current is $11.3 \text{ cm}^2 \text{ s}^{-2}$ and that parallel with the current is $1.7 \text{ cm}^2 \text{ s}^{-2}$, where each value is uncertain by $\pm 14\%$. The rms mean speed,

computed from the piece mean velocities, was 25.6 cm s^{-1} .

Therefore, from the noise model, neglecting the effects of Δ :

$$\delta S = \left(\frac{1.7 \text{ cm}^2 \text{ s}^{-2}}{\bar{u}^2} \right)^{1/2} \quad (6.19)$$

$$= .05$$

$$\delta \theta = \left(\frac{11.3 \text{ cm}^2 \text{ s}^{-2}}{\bar{u}^2} \right)^{1/2} \quad (6.20)$$

$$= 7.5^\circ$$

Probable uncertainties for these estimates, allowing for the $\pm 20\%$ mean speed variation and 20° direction variation over the record, are about 15%. These are larger than our estimates of the direction and speed errors (speed error converted to cm s^{-1} estimated from figures 6.11 and 6.12, indicating that the samples are not independent at 5 second intervals.

Figure 6.13 is taken from Frankignoul (1974). The author is extremely grateful to Dr. Frankignoul for allowing him to reproduce this and figure 6.15 here for comparison purposes.) The figure shows scatter plots of short-piece estimates of anisotropy factor:

$$\text{A.F.} = \frac{P_{u_1 u_1} - P_{u_2 u_2}}{P_{u_1 u_1} + P_{u_2 u_2}} \quad (6.21)$$

defined with respect to the mean velocity direction for each data segment, versus the mean speed for the data segment.

The data are from records 2204, 2205, 3102, and 3103, taken at Site D by Geodyne 850 current meters. The frequency bands,

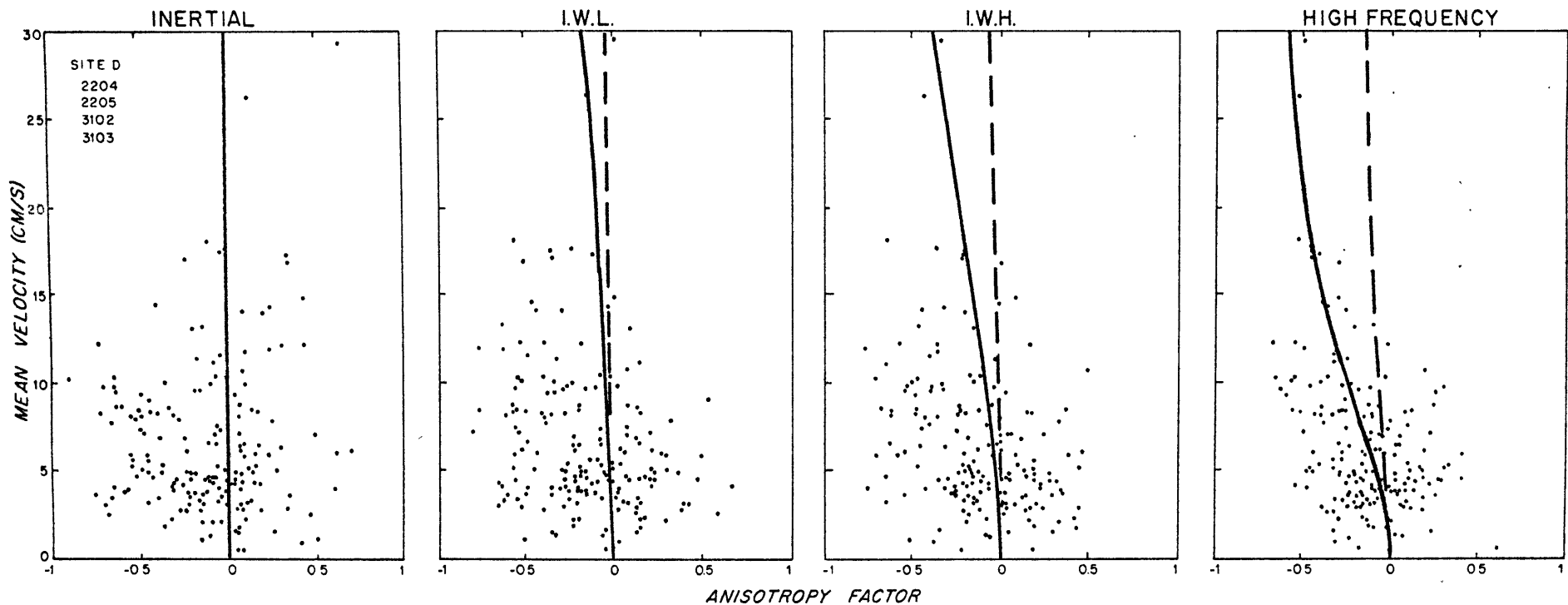


Figure 6.13 Anisotropy factor (defined in text) computed by Frankignoul (1974) for data 2204, 2205, 3102 and 3103, taken at Site D using Geodyne 850 current meters. Dashed line is anisotropy factor estimated from the effects of critical layer absorption on the GM76 spectrum. Solid line is the anisotropy factor from the noise model described in section 6.4.

as defined by Frankignoul, are listed in Table 6.1 along with the record-average power spectra integrated over the bands. (These were computed only for data 2204 and taken as representative.)

The dashed line is the anisotropy estimated from the GM 75+ critical level absorption model, for the parameters ω/f , N/f listed in Table 6.1. Apparently critical layer absorption cannot cause current anisotropy as large as observed.

The solid line is the anisotropy factor from the noise model, with:

$$\delta S = .035 \quad (6.22)$$

$$\delta \theta = 5^\circ \quad (6.23)$$

These observations were taken with 31 samples per record, as opposed to 12 for data 5761. If we assume the noise is reduced by taking more samples (the noise contribution must be white to periods shorter than one minute), from the parameters computed using figure 6.6:

$$\delta S = \frac{12}{31} \times .05 = .031 \quad (6.24)$$

$$\delta \theta = \frac{12}{31} \times 7.5 = 4.7^\circ \quad (6.25)$$

A match this close may just be luck; the data in figure 6.13 may be fit by a surprising variety of $\delta S, \delta \theta$ due to the scatter. For example, figure 6.14 shows the computed

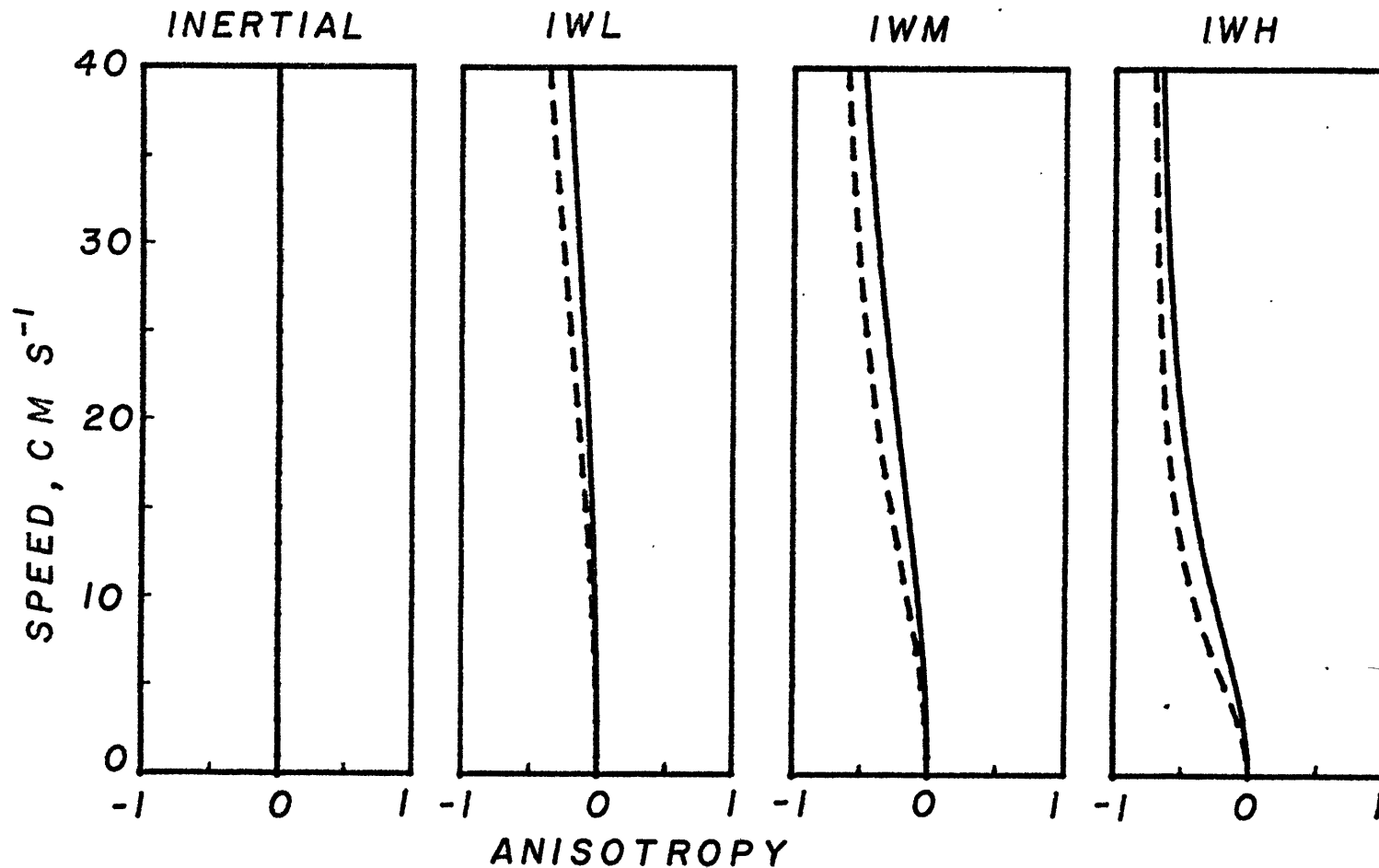
Table 6.1. Parameters used for anisotropy computations

Data	Band	Max. Period Hours	Min. Period Hours	$\Delta\omega$ Nyquists	$P_{uu} + P_{vv}$ cm^2/sec^2	ω/f	N/f
2204	Inertial	19.0	19.00	0.004	31.8	1.1	18.75
2204	IWL	7.5	3.4	0.0804	2.66	3.5	18.75
2204	IWM	3.0	1.3	0.228	1.70	8.5	18.75
2204	IWH	1.3	0.5	0.615	0.98	16.0	18.75
5561	7	3.2	2.2	0.0734	0.622	8.23	50
5661	9	1.5	1.0	0.153	0.362	17.6	50
5661	10	1.0	0.71	0.215	0.286	25.4	50
5661	11	0.72	0.5	0.310	0.204	35.5	50

Figure 6.14 Anisotropy factor computed for parameters shown in table 6.1 (appropriate to the data in figure 6.9).

Solid line: $\delta S = .035$, $\delta \theta = 5^\circ$

Dashed line: $\delta S = .05$, $\delta \theta = 7.5^\circ$



2.2

anisotropy for the figure 6.13 parameters, with $\delta S = .035$, $\delta\theta = 5^\circ$ (solid line), and $\delta S = .05$, $\delta\theta = 7.5^\circ$ (dashed line). The former is assuming the noise is reduced by the extra averaging, the latter is assuming it is not. While one gets the subjective impression that the data are better fit with the reduced noise values, there is some room for uncertainty. Hence it appears that the noise is reduced somewhat by the extra averaging, but quantitative estimates of the reduction are uncertain.

The simple noise model might also account for the apparent correlation of the quantities

$$\frac{P_{u_1 u_1} - P_{u_2 u_2}}{P_{u_1 u_1} + P_{u_2 u_2}} \text{ (fixed frame)} \quad \text{and} \quad -\left(\frac{\partial \bar{u}_1}{\partial x_1} - \frac{\partial \bar{u}_2}{\partial x_2}\right) \quad (6.26)$$

found by Frankignoul (1974) in support of the Müller (1976) theory of internal wave-mean flow interaction. Transforming the current (and noise) measurements to a fixed frame and assuming the wave field is isotropic, we find (since $\overline{\delta S \delta\theta} = 0$):

$$\frac{P_{u_1 u_1}^M - P_{u_2 u_2}^M}{P_{u_1 u_1}^M + P_{u_2 u_2}^M} = \frac{\Delta\omega(\bar{u}_1^2 - \bar{u}_2^2)}{P_{u_1 u_1} + P_{u_2 u_2} + (\delta S^2 + \delta\theta^2)\Delta\omega(\bar{u}_1^2 + \bar{u}_2^2)} \quad (6.27)$$

For a sufficiently low speed ($\bar{u} \lesssim u_0$) we may neglect the noise contribution to the denominator. Then:

$$\frac{P_{u_1 u_1}^M - P_{u_2 u_2}^M}{P_{u_1 u_1}^M + P_{u_2 u_2}^M} \sim - \frac{\delta \theta^2 - \delta S^2}{P_{u_1 u_1} + P_{u_2 u_2}} \Delta \omega (\bar{u}_1^2 - \bar{u}_2^2). \quad (6.28)$$

The quantity $\bar{u}_1^2 - \bar{u}_2^2$ can look surprisingly like $\frac{\partial \bar{u}_1}{\partial x_1} - \frac{\partial \bar{u}_2}{\partial x_2}$. Figure 6.15 shows a plot of $\bar{u}_2^2 - \bar{u}_1^2$ averaged over the three records 4091, 4101, 4121. The lower half is a comparison of the average wavefield anisotropy and estimates of $\frac{\bar{u}_2}{x_2} - \frac{\bar{u}_1}{x_1}$ from the same three moorings. (The instruments were 850 current meters.) It is debatable which mean quantity is better correlated with the anisotropy, but the noise would appear to be, at the least, a very strong contaminant to these measurements.

So far, we have only discussed the noise effects in the 850 current meter. The VACM has practically the same direction and speed sensors as the 850, and so an individual sample should have much the same noise problems, assuming the noise has a physical origin such as vortex-shedding from the cage bars. However, the sampling scheme for the VACM is radically different from that of the 850. One sample is taken every 1/8 rotor turn, or 4.7 cm of water displacement, and added vectorially into the average for the sampling interval. In a 20 cm s⁻¹ current, over 3600 samples are taken in a fifteen minute interval. The samples are probably not independent on this four per second spacing, but obviously the noise level will be greatly reduced in comparison to the 850 sampling scheme.

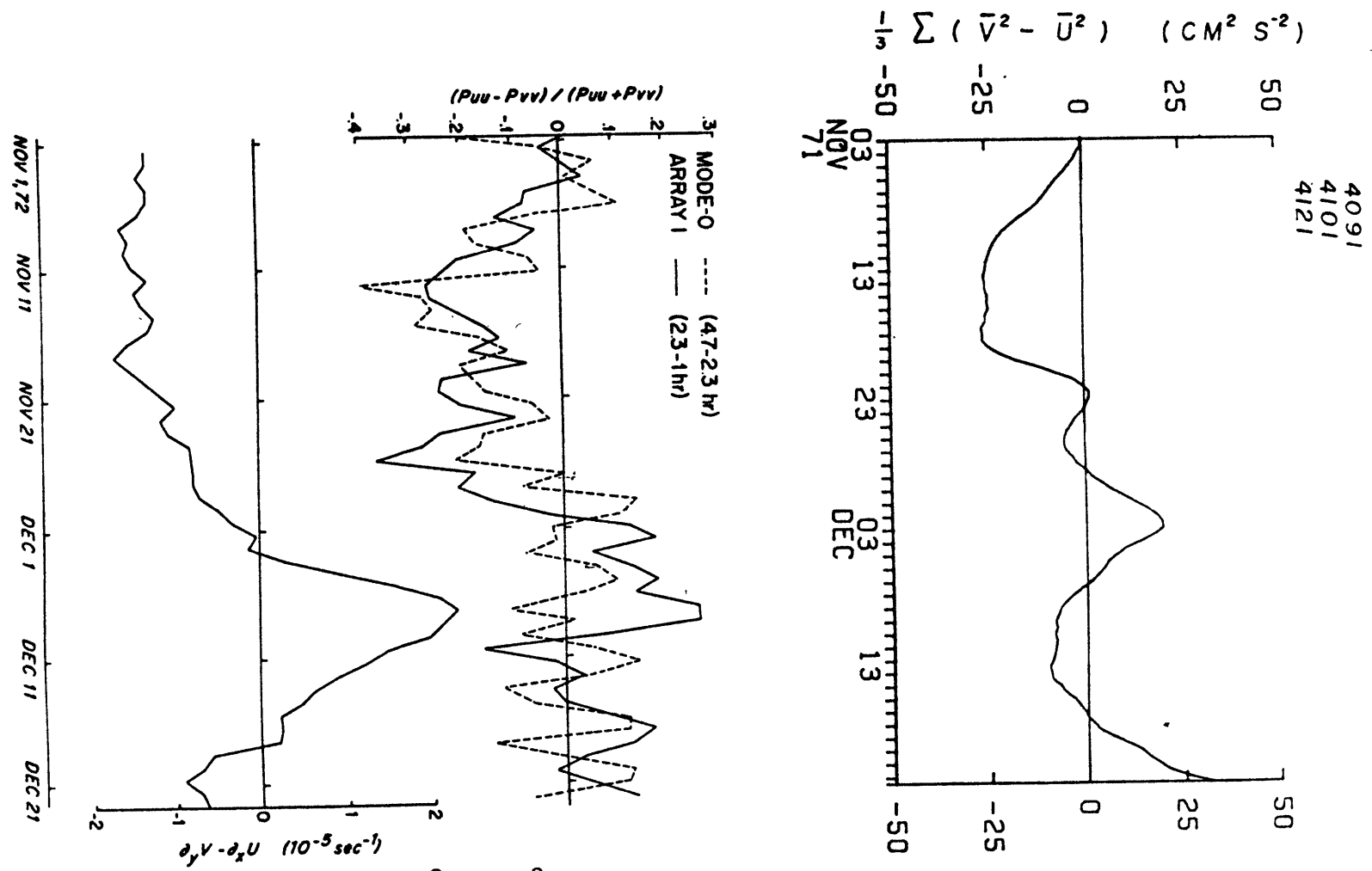


Figure 6.15 Time series of $\bar{u}_2^2 - \bar{u}_1^2$ ($u_2 \equiv v$) averaged over data numbers 4091, 4101 and 4121; wavefield anisotropy relative to a fixed reference frame computed by Frankignoul (1974), and estimated mean flow dilatation $(\frac{\partial u_2}{\partial x_2} - \frac{\partial u_1}{\partial x_1})$.

Figure 6.16 shows the east and north power spectra from record number 5791. The mean velocity was about 40 cm s^{-1} (eastward in a rotated coordinate system). The data were taken with a VACM, and so about eight samples per second were taken. There is no hint of any white noise in the spectrum, indicating that the noise level has dropped considerably. This could be because of the large amount of averaging, or else the mooring may not have oscillated. As mentioned previously, the oscillation behavior is highly variable.

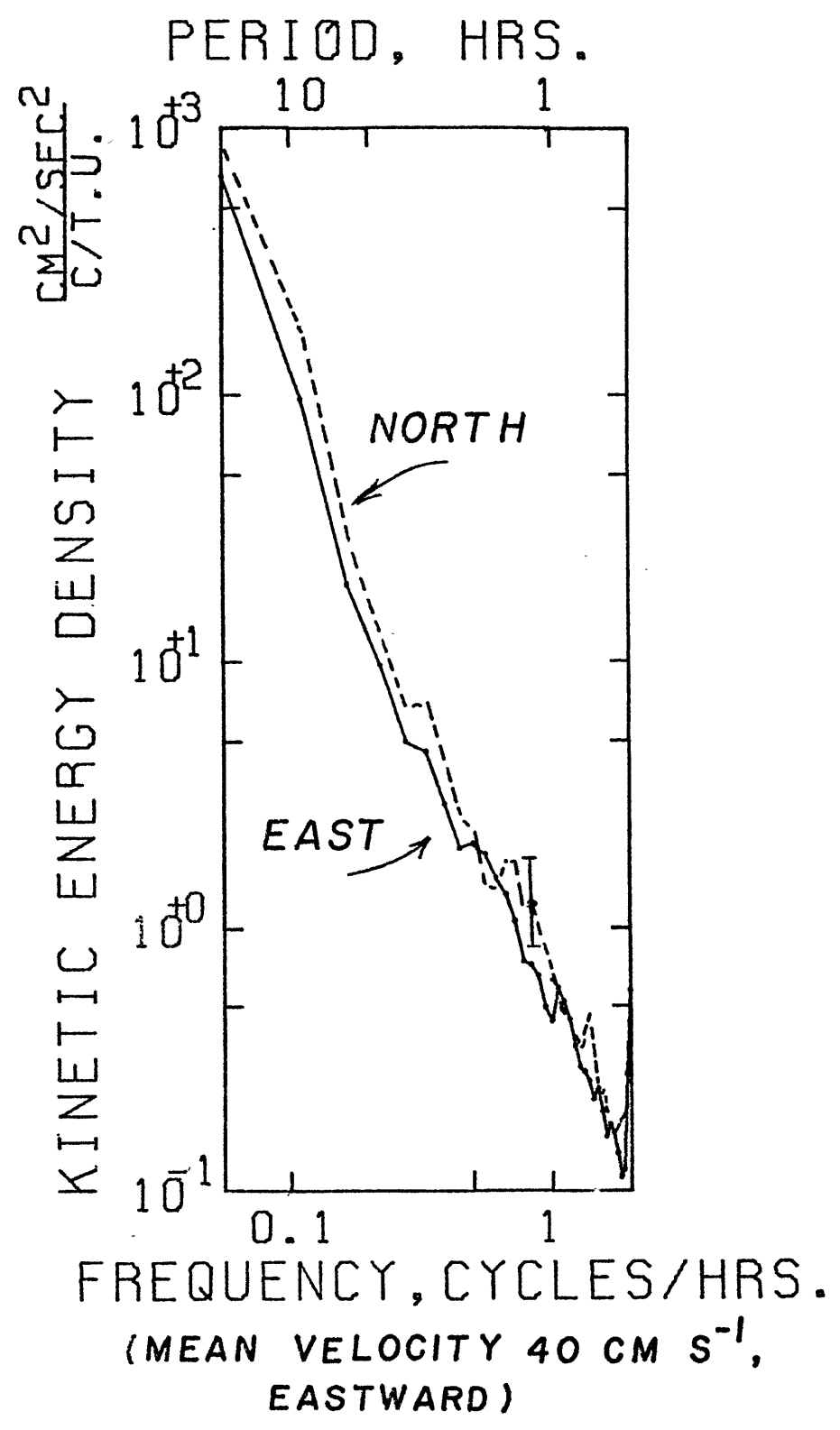
One interesting feature of figure 6.16 is the fact that there is a factor of about 1.4 increase in the cross-current velocity energy, which closely follows the -2 slope expected from internal wave spectra. This corresponds to an anisotropy of about -0.17, roughly independent of frequency. This effect may indeed be real, and so correspondingly may anisotropy measurements from short-piece spectral estimates from a VACM on mooring 566, to be presented next. This possibility is given additional weight by the fact that the total HKE in the tidal frequency band retains a constant level in the face of an order of magnitude change in the mean flow energy (figures 4.16 and 4.17).

Figure 6.17 shows scatterplots of anisotropy factor (rotated into the mean velocity) versus speed for four high-frequency bands from data 5661 at 600 m depth. The frequency band limits and other parameters are listed in Table 6.1. Comparison of the frequency limits with those from

226

DATA 5791
76-02-15 TO 76-02-29

Figure 6.16 Power spectra of the East and North velocities from record 5791 taken with a VACM. The coordinate system has been rotated so that the mean velocity was Eastward.



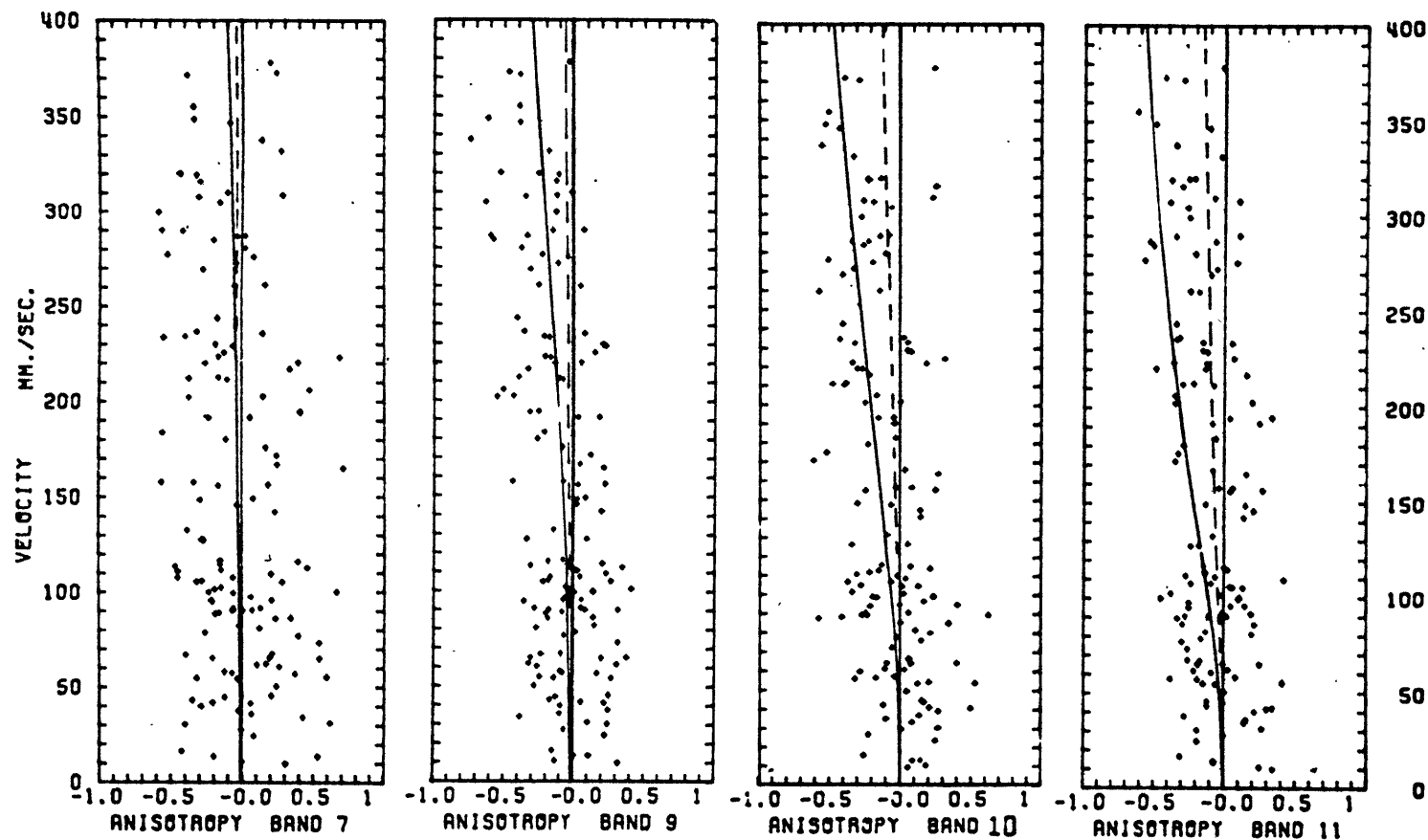


Figure 6.17 Measured anisotropy factor from record 5661. Frequency limits and other parameters are listed in table 6.1. Dashed line is the anisotropy computed from the critical layer absorption model with GM76 dependence (section 5.3). Solid line is the computed anisotropy factor from the current meter noise model (section 5.4), with $\delta S = .011$, $\delta \theta = 1.8^\circ$.

Frankignoul (1974) in the same table shows that the anisotropy from these VACM measurements is much weaker, and occurs most strongly (least weakly?) in the mid-frequency band, #9, with 1-1/4 hour periods.

The dashed line is the estimated anisotropy due to critical layer absorption, from the GM 75+ model, indicating that this mechanism cannot account for even these relatively weak anisotropies. The solid line is a fit of the "white noise" model to these observations, with $\delta S = 0.011$, $\delta \theta = 1.8^\circ$. The frequency behavior of the anisotropy is inconsistent with the white noise model, as the anisotropy is smaller than predicted at high frequencies.

6.5 Summary

The discovery by Frankignoul (1974) of a strong tendency for internal wave velocities to be larger in a direction normal to the mean current than parallel to it was re-investigated. The effect of critical layer absorption on an isotropic spectrum in producing current anisotropies was investigated using numerical integrals involving the Garrett-Munk (1975) model internal wave spectrum, and analytically using the GM 76 (Cairns and Williams, 1976) version of the spectrum. It was found that critical level absorption cannot account for the observed current anisotropies.

The anisotropy measurements made with Geodyne 850 current meters were satisfactorily accounted for by a simple

noise model. It was found that small errors in sensing the direction and speed of the current vector contaminate the internal wave spectra with anisotropic white noise. The noise appears to be due to the current meter undergoing large amplitude torsional oscillations, driven by vortex shedding from the mooring hardware. The frequency and amplitude behavior of the oscillation is highly variable from mooring to mooring. While it appears that the noise is satisfactorily averaged out by the sampling scheme of the VACM (although not by 850 current meters), the variability of the phenomenon makes hard and fast conclusions concerning the VACM anisotropy measurements impossible. They may or may not be real.

Chapter 7

CONCLUSIONS

The primary conclusion to come out of this work is a negative one, that the interaction between the internal wavefield and the mean vertical shear flow is very weak, a factor of about 30 weaker than the theoretical prediction of Müller (1976). The estimated wavefield Reynolds stresses at all four moorings analyzed indicated that the vertical eddy viscosity was less than $200 \text{ cm}^2 \text{ s}^{-1}$ in magnitude. At two of these moorings, the conditions for validity of the Müller theory were satisfied, and the wave stresses should have been clearly observable and error-free under the conditions of measurement. The stresses were much smaller than predicted, however, and not correlated with the mean shear. The observed changes in energy level were consistent with the findings of a very weak interaction.

Theoretical investigation of the interaction of the internal wavefield with a steady vertical shear flow demonstrated that it is possible for the wavefield to have an equilibrium, steady state which is consistent with free vertical propagation of the waves, and so gives many of the WKB characteristics (strong inertial peak, change in energy level with $N(z)$) which have been observed. This equilibrium state is free to bend with the wavefield characteristics, and except for critical layer effects, does not exchange momentum with the shear. This is in contrast to the equilibrium state

pictured in the Müller theory, in which the wavefield attempts to return to its old, non-shear, state, and in so doing, exchanges momentum very strongly with the mean flow. The only interaction of our equilibrium state with the mean shear comes in through the effects of critical layer absorption. The maximum expected strength of this effect was estimated, and found to be (for a 400 m thick thermocline) roughly equivalent to a vertical eddy viscosity of $-100 \text{ cm}^2 \text{ s}^{-1}$. No evidence to support the hypothesis of critical layer absorption was found in the observations.

No conclusions could be drawn about the horizontal eddy viscosity aspects of the Müller theory; the mechanisms which shape the spectrum are probably different in the horizontal and vertical wavenumber directions, and so the nature of the crucial relaxation processes is likely to be different. Another difference between the horizontal and vertical directions is that, to a large degree, the wavefield is forced at the top or bottom boundary in a horizontally homogeneous fashion, and the propagation effects most strongly felt by the wavefield are in the vertical direction.

Our investigations of internal wave horizontal current anisotropy have indicated that current measurements taken with Geodyne 850 current meters can, in the presence of a large mean current, induce false current anisotropy in the internal wave measurements. The vector averaging current meter takes several thousand samples per record in a moderate current, and

so may reduce the error to negligible levels. However, no firm conclusions were drawn regarding the VACM. The majority of the measurements of horizontal current anisotropy taken by Frankignoul (1976) were with VACM's, and so may actually indicate distortion of the internal wave spectrum associated with horizontal gradients of the mean current. This could be simply a propagation effect (the Liouville terms in the radiation balance equation); direct estimates of horizontal eddy viscosity did not prove possible.

At the two moorings with more energetic low-frequency fields, significant correlations of the wave stresses and energy levels with the mean flow were observed. These were inconsistent with ideas of a strictly local "eddy viscosity" type of interaction, involving primarily waves from the equilibrium (Garrett and Munk, sort of) spectrum. The correlations of energy and stress were instead consistent with generation of short internal waves by intense shear in the region of the main thermocline, at about 800 m. The generation seems to "turn on" at a shear of roughly $2 \times 10^{-4} \text{ s}^{-1}$, or a velocity difference of 10 cm s^{-1} across the thermocline. When the shear is above this value, the observed stresses are proportional to the shear, resulting in an inferred vertical eddy viscosity of about $100 \text{ cm}^2 \text{ s}^{-1}$. This value for the eddy viscosity may be underestimated by up to a factor of two because of error in the shear estimation, and the tendency for the wavefield to become vertically symmetric (McComas and

Bretherton, 1977) not considered here. (Any vertical fluxes of wave momentum should be vertically reflected in a continuous manner and be almost invisible a short distance from the source region. Hence the stresses may be much stronger closer to the source region.)

So we may conclude that, on the average, the mean flow is a source for internal wave energy, but a relatively minor one. From a vertical eddy viscosity of $-4 \times 10^2 \text{ cm}^2 \text{ s}^{-1}$, and a shear of $2 \cdot 10^{-4} \text{ s}^{-1}$ over the 400 m of the main thermocline, I estimate a depth-integrated energy input to the internal wavefield of $.16 \text{ erg cm}^{-2} \text{ s}^{-1}$, or about 16% of the tidal energy input estimated by Bell (1975). The dominant source (if there is one) has not been discovered. Experiments will have to gravitate to more likely source sites, such as the top, bottom and edges of the waveguide.

Little can be deduced about the mechanism of generation from these measurements. According to the Miles - Howard theorem (Miles, 1961, Howard, 1961), shear instability should not occur unless the Richardson number,

$$R_i = N^2 \cdot \left| \frac{\partial \bar{u}}{\partial x_3} \right|^2 \quad (7.1)$$

is less than 1/4. We estimate a minimum Richardson number from the large-scale shear and stratification of 50. There are three ways the ocean can overcome this problem and transfer energy from the shear into internal waves, and they may all be important, together or separately, at some time.

First, Stewart (1969) and Scorer (1969) argue that the shear tends to be concentrated at regions of high density gradient, to such an extent that the local Richardson number is smaller than the large-scale Richardson number. Hence the large scale Richardson number is not a good indicator of the stability of a shear flow, if the gradients are nonuniform, as in the oceanic thermocline. Scorer goes on to describe how the step-layer structure can be self-sustained by the interaction of the shear and the fine-structure.

Second, the shear is greatly enhanced by the (intermittent) presence of inertial oscillations. Fig. 4.18 shows the horizontal kinetic energy at 1 km depth on mooring 566 for the inertial band (dashed line) and the continuum band (solid line). There is a tendency for the short-time energy events to occur simultaneously during the times of high shear (first and last third of the record). This could indicate enhanced wave generation during the presence of an inertial oscillation at 800 m depth. Additional current measurements at 800 m depth would have resolved this question.

The third possible wave generation mechanism (and this is speculation) is afforded by Maslowe (1973), who has demonstrated that there exist nonlinear neutral modes in a shear flow. These are essentially billows, advected with the mean velocity, with a closed-streamline circulation maintained by the shear. They might be initially generated by breaking internal waves, and then remain as a semi-permanent feature.

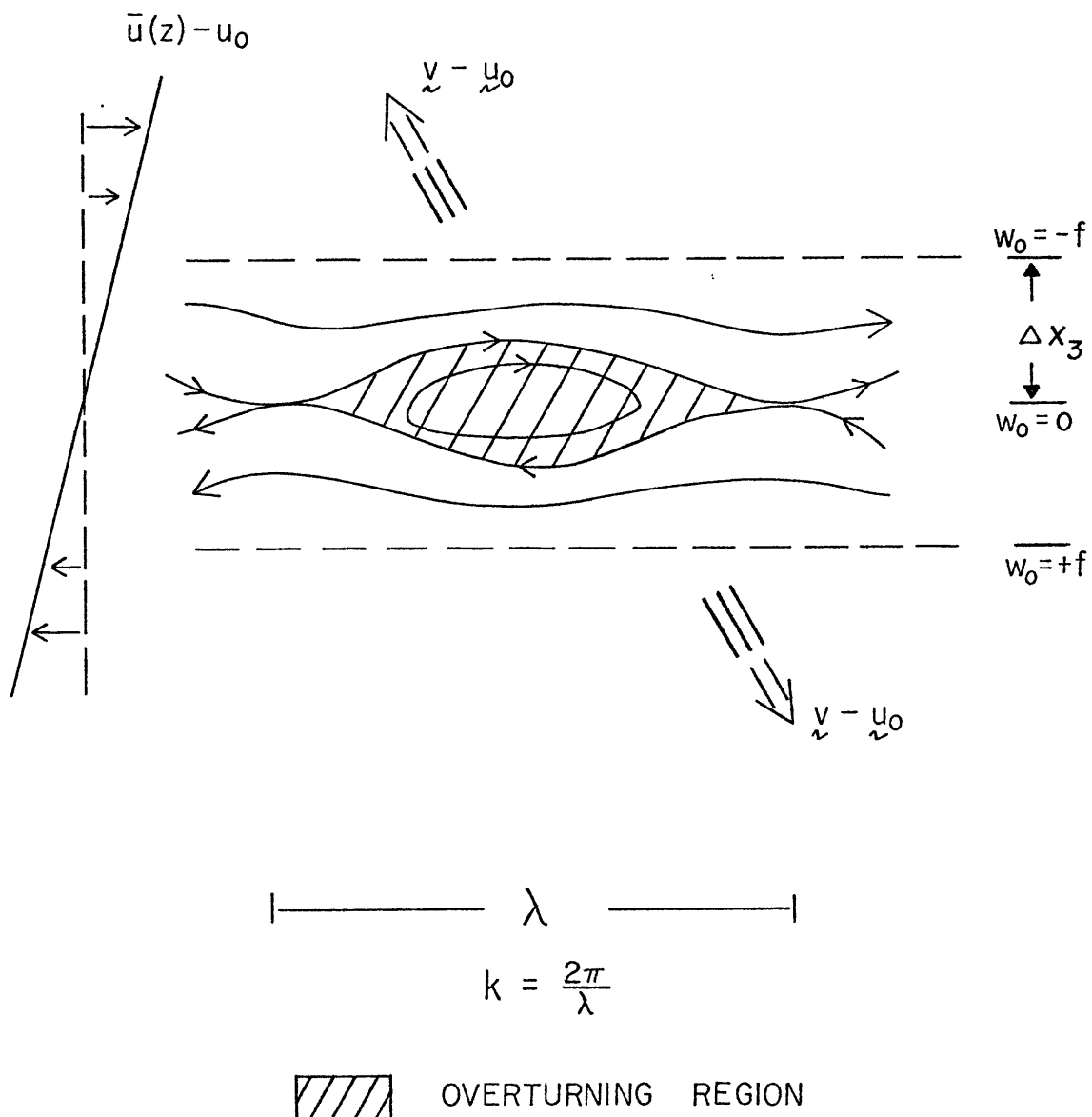
Fig. 7.1 shows a sketch of one of these rolls, with all quantities defined relative to the advection velocity of the rolls. The frequency of the disturbance is ω as seen by an observer, and $\omega - \tilde{k} \cdot \tilde{u}_0 = 0$ in the advected frame. Δx_3 is the distance from the center of the billow, where $\omega_0 = \omega - \tilde{k} \cdot \tilde{u}(z) = 0$, to the generation site, where $\omega_0 = \pm f$. The streamlines above and below the rolls must go up and down as if over a wavy bottom, and if the wavy streamline region extends up (and down) into the region where $(\omega_0)^2 > f^2$, (i.e., if the billow height approaches or exceeds Δx_3), we expect waves to be generated, as shown, giving the observed Reynolds stresses. Note that the actual stresses are negative on either side, so that the radiated waves transfer mean momentum from the upper side to the lower side of the rolls, trying to decrease the shear. This is consistent with the observed energy level increase observed at the 600 and 1000 m levels. Patches of turbulence left by breaking waves could also generate waves in this manner.

The distance, Δx_3 , from the center of the billow is:

$$\Delta x_3 = \frac{f}{k \frac{\partial \bar{u}}{\partial x_3}} \sim \frac{10^{-5} \text{ s}^{-1}}{\frac{\partial \bar{u}}{\partial x_3}} \cdot \lambda \quad (7.2)$$

Thus, the distance from the billow center to the wave generation region, $\omega_0 = \pm f$, is proportional to the billow length, λ . This is also the wavelength of the generated

Figure 7.1 Sketch of a "cats-eye" billow resulting from shear instability. Waves will be radiated when the outer boundary of the closed circulation region extends up into the area where the intrinsic frequency is larger than f .



waves.. For a shear of 10^{-4} s^{-1} , we find:

$$\Delta x_3 = \frac{\lambda}{10} \quad (7.3)$$

As the shear decreases, the wave generation region moves away from the billow, decreasing the effectiveness.

Taking a typical $\bar{u}_0 = \bar{u}$ (800) of 15 cm s^{-1} we can estimate the length scales of the generated waves and billows. The dominant wave periods were found to be about 1-8 hours, leading to:

$$60 \text{ m} < \lambda < 500 \text{ m} \quad (7.4)$$

and a vertical scale of:

$$6 \text{ m} < \Delta x_3 < 50 \text{ m} \quad (7.5)$$

Presumably a dominant length scale of billows could occur and give rise to a set of frequencies of generated waves due to the variation in advection ($\bar{u}(800)$) speeds. Note also that, at $\bar{u}(800) = 15 \text{ cm s}^{-1}$, we are excluding shear-generated waves of wavelength longer than 4 km by using the continuum frequency band. It seems unlikely that wave-generating billows of this length exist, however.

The particular questions raised by the observations of wave generation, which were not answered, are:

- (1) What is the generation mechanism of these waves? Is it one of the three above?
- (2) How intense are the wave stresses near the generation zone, and how rapid is the decay as one moves away from the shear zone?

(3) Can vertical phase propagation be observed?

Because of severe Doppler shift effects, the above questions cannot be answered unambiguously from a fixed mooring. The small nonlinearities of mechanical current meter sensors also throw suspicion on these "higher order" wave measurements (the wave stress-shear correlations are a form of bispectrum, which is a tool used to detect nonlinearities). Extensive error analysis is necessary, but not always sufficient (witness the anisotropy measurements) to rule out the possibility of unwanted effects creeping into the observations. These problems could be remedied through the use of a free-floating mooring which would drift with the mean current at thermocline level. An array of line temperature sensors would unambiguously measure vertical displacements due to internal waves, and pairs of temperature difference measurements could monitor finestructure activity.

Appendix A

ERROR ANALYSIS

A.1. Introduction

In this appendix several potential sources of error are investigated and their magnitudes estimated.

The estimated wave stresses were affected by three effects, discussed in A.2 - A.4. The contribution to the wave stress estimates due to the terms in the temperature equation which were neglected is investigated in A.2. The procedure used for estimating the mean temperature gradient, and the estimated error, is described in A.3. The corrections for mooring motion at internal wave frequencies is described in A.4.

The effect of a finite current sensor threshold speed on the internal wave velocities is estimated in A.5.

In A.6 the scheme used to estimate regression uncertainties is discussed, and in A.7 the formulae used to estimate the variance reduction properties of the spectral estimates are derived.

In A.8 the errors in estimating the low-frequency velocity and shear from VACM observations are quoted.

A.2 The Heat Equation

The relations used to estimate the cross-spectra involving u_3' in Chapter 2.3 are derived from a much-simplified heat equation, which expresses approximate balance between the terms:

$$\frac{\partial T}{\partial t} + u_3' \Gamma \sim 0 \quad (\text{A.1})$$

where $\Gamma = \frac{\partial \bar{T}}{\partial x_3}$, the mean temperature gradient. We now investigate the validity of this approximation, paying particular attention to those error terms which can lead to systematic correlations of the estimated stresses with the mean flow. Upon decomposition of the field equations into low- and high-frequency components, on the basis of the time scales of the fields, the full heat equation becomes (this is the analog of the buoyancy equation, 4.20, with the addition of a diffusive term):

$$\frac{\partial T}{\partial t} + \bar{u} \cdot \nabla T + \tilde{u} \cdot \nabla \bar{T} \propto (\tilde{u} \cdot \nabla T - \overline{\tilde{u} \cdot \nabla T}) = k \nabla^2 T. \quad (\text{A.2})$$

An overbar indicates an average quantity, K is a thermal diffusion coefficient. The terms represent; time rate of change, Doppler advection by the mean flow, horizontal advection of the mean temperature field by the wavefield, nonlinearities of the wavefield, and thermal diffusion, respectively. To estimate the size of the neglected terms in the heat equation, we consider an estimate of the $u_1 u_3$ cross spectrum. Fourier transforming the variables as

defined in Table 2.1, and denoting the cross-spectrum between x_i and x_j by: (definitions in Table 2.1)

$$C_{ij} + iQ_{ij} = \langle \hat{x}_i \hat{x}_j^* \rangle \quad (\text{A.3})$$

the heat equation becomes:

$$\begin{aligned} \langle \hat{u}_1 \hat{u}_3 \rangle &= C_{13} + iQ_{13} \\ &= -\frac{i\omega}{\Gamma} (C_{1T} + iQ_{1T}) - \frac{\bar{u}_1}{\Gamma} \langle \hat{\alpha}_1 \hat{T} \rangle_{\partial x_1} \\ &\quad - \frac{\bar{u}_2}{\Gamma} \langle \hat{u}_1 \hat{T} \rangle_{\partial x_2} - \frac{C_{11}}{\Gamma} \frac{\partial \bar{T}}{\partial x_1} \\ &\quad - \frac{(C_{12} + iQ_{12})}{\Gamma} \frac{\partial \bar{T}}{\partial x_2} - \frac{\langle \hat{u}_1 \hat{T} \rangle}{\Gamma} \\ &\quad - \frac{K}{\Gamma} \langle \hat{u}_1 \hat{T}^2 \rangle_{\partial x_3} . \end{aligned} \quad (\text{A.4})$$

The simplified heat equation used corresponds to keeping only term 1. A typical magnitude for term 1 is $0.1 \text{ cm}^2 \text{ s}^{-2}$.

The diffusion term can be readily estimated, by considering a wave of vertical length scale H . Estimating an rms vertical displacement, ζ , of 7 m from the Garrett-Munk (1975) model internal wave spectrum, an rms horizontal velocity of 5 cm s^{-1} from the same spectrum, and substituting $K = 1.4 \times 10^{-3} \text{ cm}^2 \text{ s}^{-1}$, we find:

$$(\text{term 7}) \leq 4.9 \text{ cm}^4 \text{ s}^{-2} H^{-2} \quad (\text{A.5})$$

Typical Reynolds stresses observed were about $0.1 \text{ cm}^2 \text{ s}^{-2}$ in

magnitude. For term 7 to contribute less than 1% error, we must have $H > 70$ cm. Most of the internal wavefield has vertical scales in excess of 30 m, so this term is negligible under all circumstances observed.

Term 6 has two contributions; the obvious one is from the correlation of the velocity perturbation, u_1 , with the nonlinear self-advective terms of the wavefield, $u \cdot \nabla T$. For a strictly Gaussian wavefield, or for a horizontally isotropic one, this contribution is zero. Substitution of the order of magnitude of the terms in the triple correlation:

$$\begin{aligned} \frac{u_1 \cdot u_3 \cdot \zeta}{H} &\approx \frac{25 \text{ cm}^2 \text{ s}^{-2} \cdot \frac{f}{N} \cdot u \times 10^2 \text{ cm}}{10^4 \text{ cm}} \\ &\approx 0.025 \text{ cm}^2 \text{ s}^{-2} \end{aligned} \quad (\text{A.6})$$

suggests that if the wavefield nonlinearities are significant, so that the triple correlation approaches one, the terms being considered can approach 25% of the observed stress. However, since total nonlinearity and anisotropy would have to occur in combination to produce an error of this magnitude, the wavefield self-advection is probably negligible.

An implicit source of error which appears in term 6 is due to neglect of the time variation of $\frac{\partial T}{\partial x_3}$ which occurs locally because of vertical advection of temperature microstructure. Eriksen (1976) has compared a direct measurement of u_3 with various estimates computed from $-\frac{\partial T}{\partial t} \left(\frac{\partial T}{\partial z}\right)^{-1}$ where

the temperature gradient was estimated as a function of time from the difference of temperature over various (0.9 - 7 m) vertical separations. Another estimate of u_3 was formed using a constant gradient computed from a 78-hour average over a 7 m vertical spacing. Eriksen found that the best estimate of u_3 was attained using a constant temperature gradient; the error was only increased when attempts were made to estimate the instantaneous gradient. We have used an estimated mean gradient in our estimates of u_3 , and so the estimates are contaminated to some degree by the temperature fine structure. This would not be serious, except that fine structure effects also appear in the current, and the combination could lead to systematic stress errors which are correlated with the mean flow.

In the presence of a mean shear current (see figure A.1) the larger gradients of current and density will tend to occur together. Stewart (1969) and Scorer (1969) give arguments for this. When a high-gradient region (step) is lifted up past the sensors on a current meter, the velocity and temperature perturbations will appear to the instrument as a negative-going step function. The inferred vertical velocity will be a positive pulse. The opposite occurs when the step is advected downward again. The stress error is $u_\alpha^F \frac{\partial T^F}{\partial t} \Gamma^{-1}$, where u_α^F and T^F are the current and temperature contamination. Hence the combined current and temperature fine structure could induce a false stress signal which is

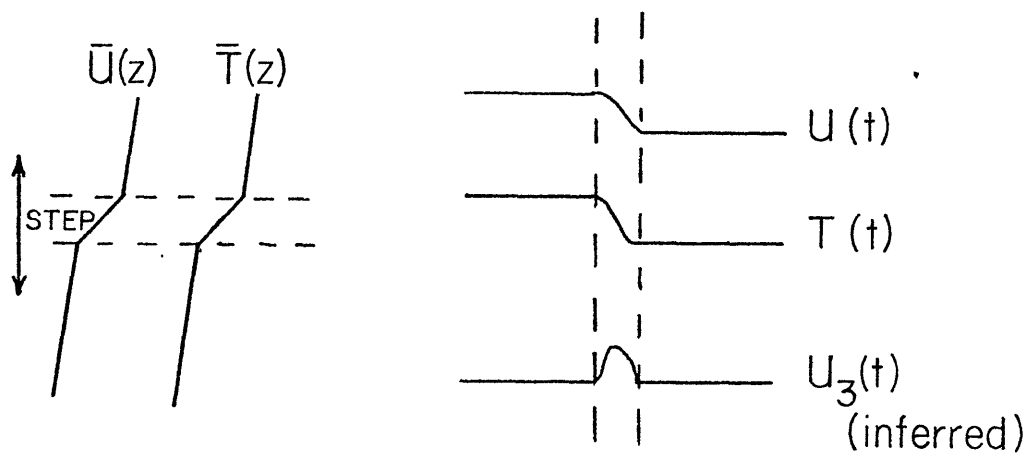


Figure A.1 Sketch of a temperature, density and current shear finestructure step, the measured temperature and velocity signals, and the vertical velocity inferred from temperature.

correlated with the mean shear. The size of this signal will depend on the intensity of the fine structure of both current and temperature, and on how well correlated the current and temperature fine structure signals are.

Joyce and Desaubies (1977, hereafter denoted JD) have compared temperature fine structure and internal wave models to dropped and moored temperature observations, and have estimated the frequency spectrum of the fine structure contamination. For that part of the temperature spectrum which is not due to the displacement of the mean temperature gradient, JD estimate:

$$C_{TT}^F = \frac{\beta A^{1/2}}{2\pi^{1/2}} f^{-3/2} \quad (A.7)$$

where:

$$f = \frac{\omega}{2\pi} \quad (\text{cyclic frequency})$$

$$\beta = 1.81 \text{ C}^2 \text{ m}^{-1}$$

$$A = 1.81 \text{ m}^2 \text{ cph}$$

The parameters β and A are explained in JD. The spectrum of the fine structure contaminated part of the u_3 estimate is then:

$$\begin{aligned} C_{33}^F &= (2\pi f)^2 \left(\frac{\partial \bar{T}}{\partial x_3} \right)^{-2} \\ &= 2\pi^{3/2} \left(\frac{\partial \bar{T}}{\partial x_3} \right)^{-2} \beta A^{1/2} f^{1/2} \end{aligned} \quad (A.8)$$

JD observe $\frac{\partial \bar{T}}{\partial x_3} = 0.18 \text{ C}$ for the mean temperature gradient.

The assumed vertical velocity spectrum is:

$$C_{33}^T = (2\pi)^2 A \quad (\text{A.9})$$

Integrating the true and contamination vertical velocity spectra from the inertial ($f_i = .04 \text{ cph}$) frequency to the buoyancy ($N = 2.5 \text{ cph}$) frequency, we find that the variance of the true vertical velocity is $0.145 \text{ cm}^2 \text{ s}^{-2}$, and the variance of the contamination velocity is $.017 \text{ cm}^2 \text{ s}^{-2}$. Hence the net contamination of the vertical velocity estimates is about 12%, a negligible effect insofar as the spectrum is concerned.

A rough estimate of the velocity fine structure spectrum was made by computing the spectrum of the difference in velocity between two Vector Averaging Current Meters whose sensors were separated in depth by 2 m. (Records 5512 and 5513, at a depth of 2000 m, location 36°N. , 70°W.) The spectrum is shown in figure A.2. Over much of the internal wave range, the difference spectrum is well-fit by a ω^{-1} power law. The form shown on the plot was chosen as an estimate of the fine structure spectrum (divided by two to distribute the difference between the two instruments):

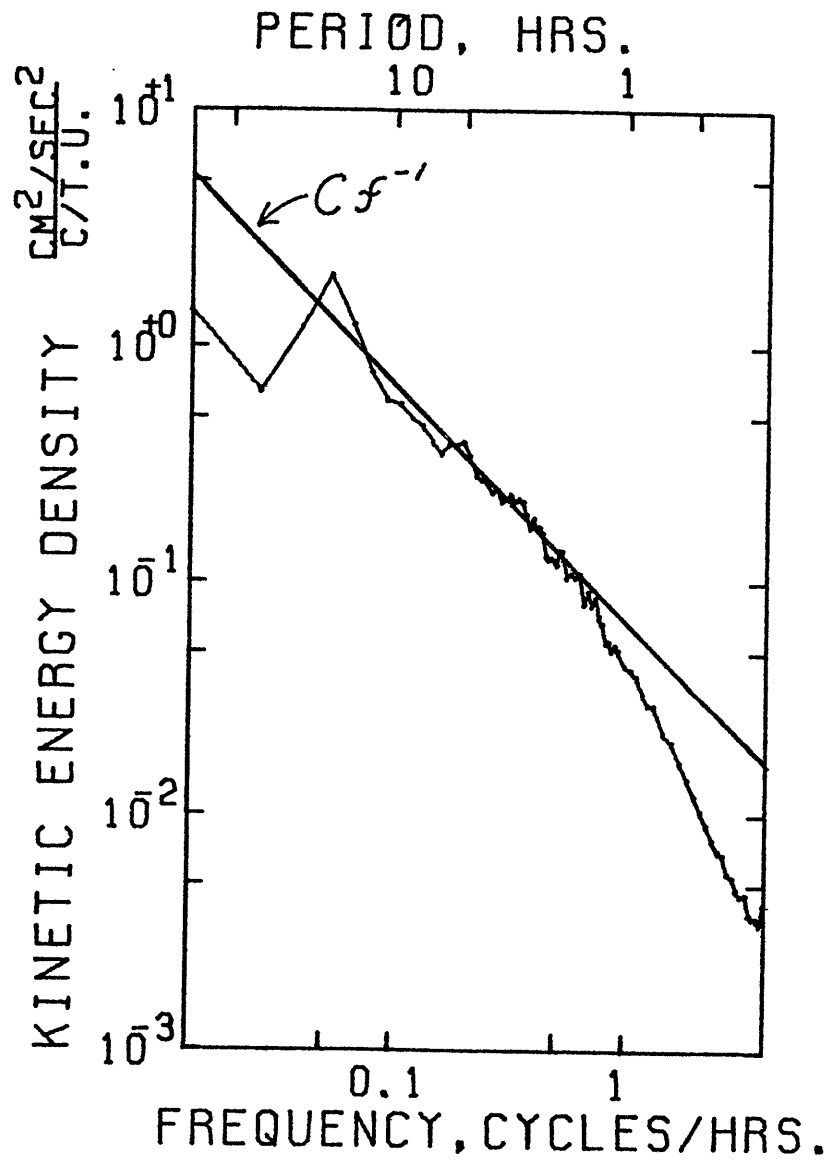
$$P_{uu}^F = C f^{-1} \quad (\text{A.10})$$

where:

$$C = 0.35 \text{ cm}^2 \text{ s}^{-2}$$

JD compute the fine structure temperature and temperature difference spectra, and show that, because of the finite

Figure A.2 Spectrum of velocity difference over 2 m from mooring 551 at 2000 m depth. The ω^{-1} power law used in the estimate of current finestructure contamination is indicated.



correlation scale of the fine structure and the frequency dependence of the internal wave displacements causing the contamination, the difference spectrum is more white. Similarly, we may have underestimated the slope of the current fine structure spectrum by simply using the difference spectrum as an estimate. The effect of an increased spectral slope is an increase in the non-overlapping of the horizontal and vertical velocity contamination spectra, decreasing the stress error. Because of this effect, we are overestimating the stress error.

The records used for the fine structure estimate were taken from a mooring at 2000 m depth, and so the current fine structure level may be underestimated by a factor of two.

Using our estimate of the current fine structure spectrum, and that of JD for the vertical velocity contamination, we can compute a maximum stress error due to the combined current-temperature fine structure effects. This maximum could only occur if the horizontal and vertical velocity errors were perfectly correlated and in quadrature. The error is given by the frequency integral of the geometric mean of the estimated contamination spectra:

$$\begin{aligned}
 \delta C_{13} &= \int_{f_i}^N (P_{uu}^F P_{33}^F)^{1/2} df \\
 &= \frac{4}{3} (2\pi^{3/2} \beta A^{1/2} (\frac{T}{x_3})^{-2} C)^{1/2} (N^{3/4} - f_i^{3/4}) \\
 &= 0.04 \text{ cm}^2 \text{ s}^{-2} \quad (A.11)
 \end{aligned}$$

This stress error might be as large as 40% of the observed stress, or even 80% considering the factor of two. However, the contribution to the stress error should be much smaller than this because u_{α}^F and T^F are expected to be in phase; while the stress error is due to the quadrature of u_{α}^F and T^F . An estimate of how much smaller is at present not possible. Hence, in interpreting the results, it should be kept in mind that the observed stresses might be affected by fine structure effects.

Terms 4 and 5 are due to horizontal advection of the temperature field by internal waves across the tilted mean density surfaces. The terms are formally of higher order in a WKB expansion based on the horizontal length scales of the wavefield and the mean flow (Müller, 1974). However, if the flow is quasigeostrophic, and we assume that the temperature is a good indicator of the density field, we can estimate these terms directly. Assuming that density and temperature isolines are parallel, the geostrophic equations become:

$$\frac{\partial \bar{T}}{\partial x_{\alpha}} \left(\frac{\partial \bar{T}}{\partial x_3} \right)^{-1} = \frac{f}{N^2} \frac{\partial u}{\partial x_3} \quad (\text{A.12})$$

Hence the correction to the cross-spectral estimates due to terms 4 and 5 become:

$$\begin{aligned} C_{13} &= \frac{\omega}{\bar{T}_2} Q_{1T} - C_{11} \frac{f}{N^2} \frac{\partial \bar{u}_2}{\partial x_3} + C_{12} \frac{f}{N^2} \frac{\partial \bar{u}_1}{\partial x_3} \\ Q_{13} &= - \frac{\omega}{\bar{T}_2} C_{1T} + Q_{12} \frac{f}{N^2} \frac{\partial \bar{u}_1}{\partial x_3} \end{aligned} \quad (\text{A.13})$$

Since the expected value of C_{12} is zero for an isotropic wavefield, we expect little change in the eddy viscosity estimate. The primary change is due to the wave spectra which have a finite expected mean value. Hence we expect the observed "cross-viscosity" correlations (a tendency for the estimated wave stress to lie to the left of the shear, section 4.3c) to be reinforced upon correction of the stress. From a mean C_{11} of $25 \text{ cm}^2 \text{ s}^{-2}$, we estimate an increase of $80 \text{ cm}^2 \text{ s}^{-1}$ in the cross-viscosity estimate. As discussed in 4.3c, however, these "cross-viscosity" stresses have no dynamic effect on a quasigeostrophic mean flow, and so were largely ignored. The correction terms listed above were computed on a point-by-point basis, and the stress time series were actually corrected for this advection affect. The correction terms were found to be less than 5% of the original terms. The eddy viscosity estimates were only slightly affected; the change in estimated v_v at 566 was less than $6 \text{ cm}^2 \text{ s}^{-1}$.

The effects of advection of the temperature field by the mean flow are embodied in terms 2 and 3. Because the horizontal velocity of a wave is greatest in a direction parallel to the wavenumber, the larger term is term number 2, which may be written as:

$$-\bar{u}_1 \langle \hat{u}_1^* \frac{\partial \hat{\zeta}}{\partial x_1} \rangle = -\bar{u}_1 T(\omega) \quad (\text{A.14})$$

251

The part which affects the stress estimate is the real part. A rough estimate of this term can be made using the GM76 model spectrum. To facilitate evaluation of the integrals involved, the effects of Doppler shift of the spectrum must be neglected ($\omega - \mathbf{k} \cdot \bar{\mathbf{u}} \approx \omega$). In doing this, we are implicitly assuming that the spectrum is not greatly modified from the GM76 shape by the shear flow. This assumption appears to be invalid for measurements taken at the energetic moorings, and in chapter 4 an alternative estimate of the effects of this term is made.

From the kinematic wavefield model in Appendix B, we can write the cross-spectrum $T(\omega)$ in terms of the energy spectrum of the internal wavefield:

$$\begin{aligned}
 T(\omega) &= -\frac{1}{2} \int_S \int d\alpha \int \frac{d\phi}{2\pi} \frac{\alpha^2}{\alpha^2 + \beta^2} \frac{\beta}{\alpha} \cdot s \frac{\cos^2 \phi}{\omega_0} \epsilon(\alpha, \omega, s) \\
 &= -\frac{1}{4} \int_S \int d\alpha \frac{1}{\omega_0} \frac{\omega_0^2 - f^2}{N^2 - f^2} \left(\frac{N^2 - \omega_0^2}{\omega_0^2 - f^2} \right)^{1/2} \alpha s \epsilon(\alpha, \omega, s)
 \end{aligned}
 \tag{A.15}$$

Neglecting the Doppler effect in the intrinsic frequency, $\omega_0 = \omega - \mathbf{k} \cdot \bar{\mathbf{u}}$, we have $\omega_0 \approx \omega$. We now define Δ in terms of the net vertical flux of energy:

$$\Delta \equiv \frac{\epsilon(k_3 > 0) - \epsilon(k_3 < 0)}{\epsilon(k_3 > 0) + \epsilon(k_3 < 0)}
 \tag{A.16}$$

We will take Δ to be a constant. A positive Δ indicates a net downward energy flux. Substituting for the total energy so that $\epsilon(k_3 > 0) - \epsilon(k_3 < 0) = \Delta \epsilon(\alpha, \omega)$, and substituting for

$\varepsilon(\alpha, \omega)$ from GM76, we obtain:

$$T(\omega) = -\frac{\Delta}{4} \frac{E_O N}{N_O} \frac{\sqrt{(\omega^2 - f^2)(N^2 - \omega^2)}}{(N^2 - f^2)\omega} B(\omega) \int_0^{\alpha_M} d\alpha A\left(\frac{\alpha}{\alpha_*}\right) \frac{\alpha}{\alpha_*} \quad (A.17)$$

where:

$$E_O = 30 \text{ cm}^2 \text{ s}^{-2}$$

$$N(z) = 2 \text{ cph}$$

$$N_O = 3 \text{ cph}$$

$$f = 0.04 \text{ cph}$$

$$B(\omega) = \frac{2}{\pi} \frac{f}{\omega(\omega^2 - f^2)^{1/2}}$$

$$A(x) = \frac{2}{\pi} (1+x^2)^{-1}$$

$$\alpha_* = \frac{j_* \pi}{N_O b} \sqrt{\omega^2 - f^2} ; \quad j_* = 3 .$$

The asymptotic behaviour of the wavenumber integral is α^{-1} and so the integral does not converge unless a cutoff wavenumber is assumed. This is visualized as the largest wavenumber at which internal waves exist; presumably, waves shorter than this have a greater likelihood of breaking. If we choose a minimum absolute wavelength, which is approximately the vertical wavelength, the form of the cutoff wavenumber is found to be:

$$\alpha_M = \frac{j_M}{j_*} \alpha_*(\omega) \quad (A.18)$$

where j_M is the maximum modenumber allowed. Following McComas and Bretherton (1977) we choose the cutoff mode-

number such that the total Richardson number of the wavefield equals 0.5. Then the minimum vertical wavelength is 1 m, and $j_M/j_* = 867$.

The integral then becomes:

$$T(\omega) = - \frac{\Delta}{2\pi} \frac{E_O N(z)}{N_O} \frac{(N^2 - \omega^2)^{1/2}}{N^2 - f^2} \cdot \frac{f}{\omega^2} \alpha_*(\omega) J\left(\frac{j_M}{j_*}\right) \quad (\text{A.19})$$

where:

$$\begin{aligned} J(x) &= \int_0^x x A(x) dx \\ &= \pi^{-1} \ln(1+x) \end{aligned}$$

Consistent with the GM76 model, we neglect ω^2 with respect to N^2 . Then integrating $T(\omega)$ over the frequency limits of the continuum and the total bands described in chapter 2, we find:

$$\int T d\omega = - \frac{E_O \Delta j_* f}{2b N_O^2} \frac{N_O}{N(z)} \int_a^b \frac{(x^2 - 1)^{1/2}}{x^2} dx \quad (\text{A.20})$$

where:

$$a = \begin{cases} 2 & \text{continuum band} \\ 1 & \text{total band} \end{cases}$$

$$b = \frac{N(z)}{f} \sim 50$$

For the values given earlier we find that:

$$\frac{E_O j_* f}{2b N_O^2} = 8.8 \times 10^{-4} \text{ cm s}^{-1} \quad (\text{A.21})$$

204

The correction term is then estimated to be:

$$\delta(C_{13}) = -\bar{u}_1 \Delta \frac{N_O}{N(z)} \cdot 8.8 \cdot 10^{-4} \text{ cm s}^{-1} \cdot \text{I.J.} \quad (\text{A.22})$$

where:

$$\begin{aligned} I &= \int_a^b \frac{(x^2-1)^{1/2}}{x^2} dx \\ &= \left[\ln(2\sqrt{x^2-1} + 2x) - \frac{\sqrt{x^2-1}}{x} \right]_a^b \\ &= \begin{cases} 3.15 & \text{continuum band (a=2, b=50)} \\ 3.61 & \text{total band (a=1, b=50)} \end{cases} \end{aligned}$$

From the wavenumber integral;

$$J(867) = 2.153. \quad (\text{A.23})$$

From Müller, Olbers and Willebrand, (1977), a value of $\Delta = .05$ is a reasonable maximum (52.5% of the total energy going downward, 47.5% going upward).

Substituting these values into the above, we find:

$$C_{13} \begin{cases} -\bar{u}_1 \cdot 3 \times 10^{-4} \text{ cm s}^{-1} & (\text{continuum band}) \\ -\bar{u}_1 \cdot 3.5 \times 10^{-4} \text{ cm s}^{-1} & (\text{total band}) \end{cases} \quad (\text{A.24})$$

At $\bar{u}_1 = 36 \text{ cm s}^{-1}$, the induced stress error is estimated to be $.01 \text{ cm}^2 \text{ s}^{-2}$, or 10% of the observed stress. With the provisions mentioned earlier, that the spectrum is not

greatly modified from the Garrett-Munk form, the effects of advection by the mean flow are negligible.

Because the wavenumber integral has a logarithmic form, the integral is insensitive to the assumed cutoff wavenumber. For example, if the cutoff were moved from 1 m to 1/2 m, the value of J would increase from 2.2 to 2.4, a 10% increase.

Hence the simplified heat equation is a reasonably accurate equation for estimating the Reynolds stresses exerted by a wavefield similar in form to the Garrett-Munk spectrum. However, the effects of temperature and current fine structure on the stress estimates should be more accurately estimated when an adequate dynamical model of current fine structure is available. Although the effects of advection of the wavefield by the mean flow are negligible if the wave spectrum is close to the Garrett-Munk shape, it is shown in chapter 4 that the advective effect on individual waves is $O(\bar{u}/c)$, where c is the horizontal phase speed of the wave. If the stresses are predominantly caused by waves with $c \sim \bar{u}$, then the advection term has a strong effect on the estimated stresses. We investigate this effect in chapter 4.

A.3 Temperature Gradient Estimation

It is shown in A.2 that a reasonably good estimate of the vertical velocity may be obtained from the temperature time series using the simplified heat equation:

$$u_3 = - \frac{\partial T}{\partial t} \left(\frac{\partial \bar{T}}{\partial x_3} \right)^{-1} \quad (A.25)$$

where $\frac{\partial \bar{T}}{\partial x_3}$ is an estimate of the mean temperature gradient. Since there were no differential temperature sensors on the moorings analyzed, an alternative procedure was adopted for estimating the temperature gradient. Since the thermocline tends to heave up and down as a whole, with relatively little stretching or shrinking in the vicinity of the thermocline, we expect the central temperature structure to rise and fall with the thermocline, keeping essentially the same shape. The local temperature gradient would be expected to depend on the position of the thermocline, and so on \bar{T} , which acts as a monitor of the thermocline depth. The temperature gradient was thus estimated as a function of \bar{T} , to allow for the rising and falling of the thermocline, and the associated local change in the temperature gradient.

In figure A.3 are plotted several pieces of information. The dots are the temperature gradient estimated over a 100 m depth interval, plotted against the average value of the temperature. The original data were a combination of bottle and CTD stations, listed in table A.1, which were within 2° of moorings 565 and 566. Although the depth of the thermocline varied by more than 100 m in these stations, the

Figure A.3 Dots: scatterplot of 2-point estimated vertical temperature gradient vs. central temperature for data in Table A.1. The labelled lines are the temperature gradient relations used in computing $\frac{\partial \bar{T}}{\partial x_3}(\bar{T})$, with the observed temperature excursions indicated by the extend of the line. 600 m relation (10°C - 16°C) shows excursion observed at 566. The 543 and 545 temperature gradient relations were estimated from CTD station numbers Chain 116 #20 (543) and Chain 116 #23 (545).

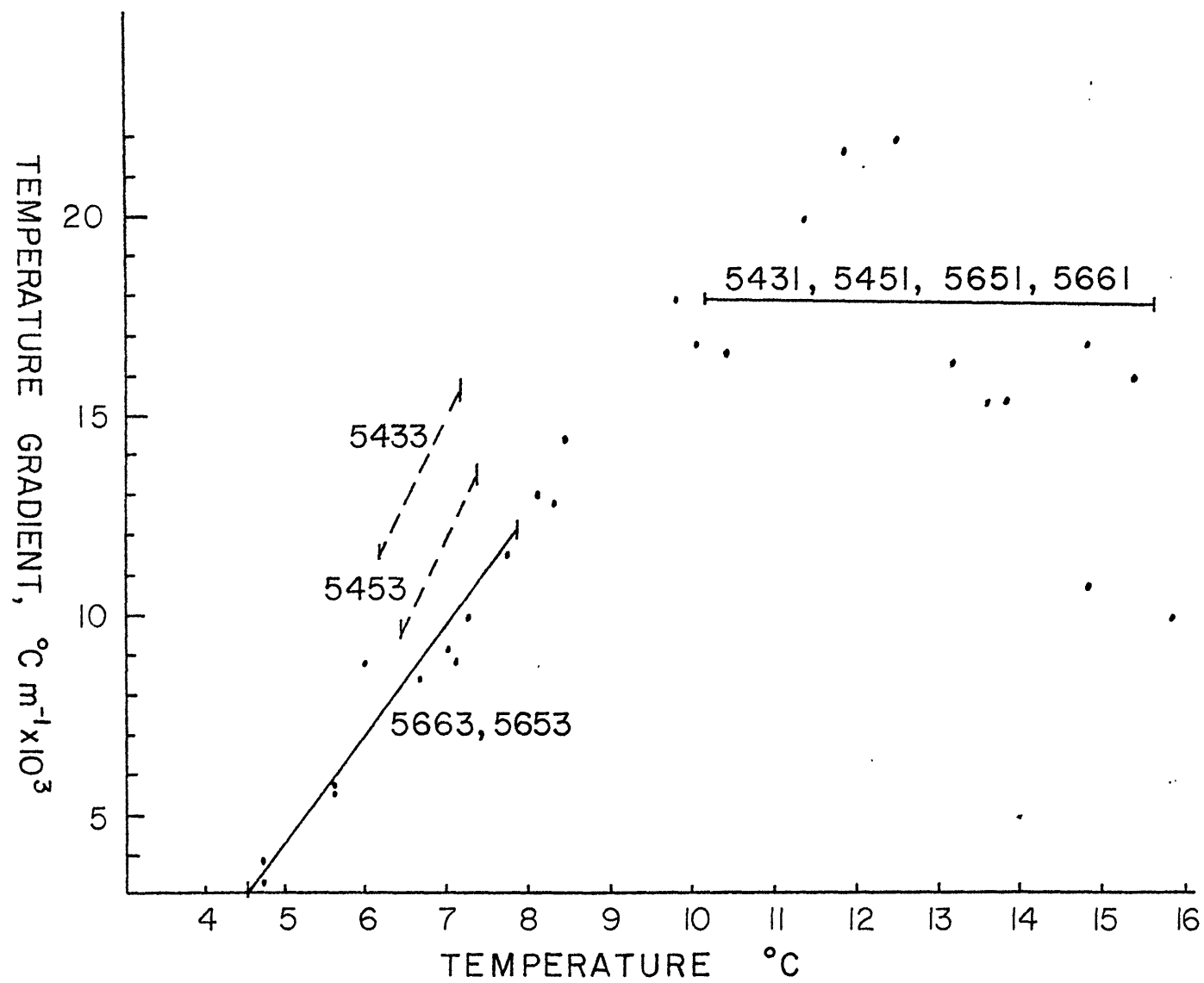


Figure A.3

TABLE A.1

Locations of stations used in figure A.3

CTD Cast

Chain 129, #6	36°30' N 55° W
Chain 129, #12	35° N 55° W

Bottle Cast

Chain 7, #42	36° N 57° W
Chain 7, #43	36° N 55° W
Atlantis 212, #5206	32° N 54° W
Chain 12, #162	35° N 55° W

TABLE A.2

Coefficients c_1, c_2 used to estimate the mean temperature gradient via the equation $\frac{\partial \bar{T}}{\partial x_3} = c_1 + c_2 \cdot \bar{T}$

Data Number	c_1 (m°C m ⁻¹)	c_2 (km ⁻¹)
5453	-17.0	4.105
5433	-13.9	4.1
5663, 5653	-11.25	3.0
5661, 5651 5451, 5431	18.0	0

gradient as a function of temperature was remarkably linear, especially in the 4° - 12° range. At least in the waters below the thermocline, we can accurately estimate the gradient as a function of \bar{T} .

In the 4° - 12° range a linear fit;

$$\frac{\partial \bar{T}}{\partial x_3} = C_1 + C_2 \bar{T} \quad (\text{A.26})$$

works very well, with an accuracy of about 1 m°C m⁻¹ (this is a fit to an exponential temperature vs. depth profile). The fit used for data numbers 5663 and 5653, at 1000 m nominal depth, is shown on figure A.3 for the range of temperatures observed at instrument 5663. In dashed lines just above are the fits for data numbers 5433 and 5453, also at 1000 m. The range of temperatures observed at each instrument is indicated by the extent of the line. Since the range of temperatures observed at these moorings was relatively small, the fit was not as critical. (The gradients are different at these moorings because the moorings are at a different location from 565, 566 and the historical data which are plotted. The gradients were estimated from CTD casts shown in the caption.) We estimate the same gradient error for the 1000 m level at all four moorings: about 1 m°C m⁻¹.

At the upper levels, where the temperature is usually greater than 12°, the gradient is much more variable. The slope $\frac{\partial \bar{T}}{\partial x_3}$ decreases with increasing temperature, but the scatter of the data is so great that a constant gradient of 18 m°C m⁻¹ was found to be about as accurate as a linear fit.

28

(It did not seem worthwhile to attempt a higher order fit.)
For the upper levels, we estimate an error of $\pm 4 \text{ m}^\circ\text{C m}^{-1}$,
or 22%, in estimating the mean gradient.

The values of c_1 and c_2 used in computing $\frac{\partial \bar{T}}{\partial x_3}$ are listed
in table A.2.

A.4 Mooring Motion

A mooring is a dynamic entity, in a continual state of readjustment of forces which arise from the drag of current on the components, the weight and mass of the mooring components, and the buoyancy which holds the mooring up in the face of currents. An introduction to the dynamics of mooring motion is provided by Fofonoff (1969). Internal wave velocities provide a perturbation to the drag forces on a mooring line, and so cause the mooring to move downward whenever the wave velocities reinforce the mean velocities in the region of maximum drag, generally in the upper few hundred meters. The drag law and the mooring response are nonlinear, so we expect the mooring motion to depend in a nonlinear fashion on $\bar{u} + u'$. As a result we expect a false Reynolds stress $(\overline{u_1 u_3})_F$ to be induced in our measurements. This stress will be well correlated with the mean velocity in the upper waters. Since the vertical motions of the moorings at 800 m depth were monitored by a pressure recorder (Wunsch and Dahlen, 1974), it is a fairly simple procedure to correct for this motion, by simply computing the error induced in the u_1 , u_3 cross-spectra and subtracting these error terms from the previous estimates.

An estimate of the magnitude of the problem is obtained by computing the ratio

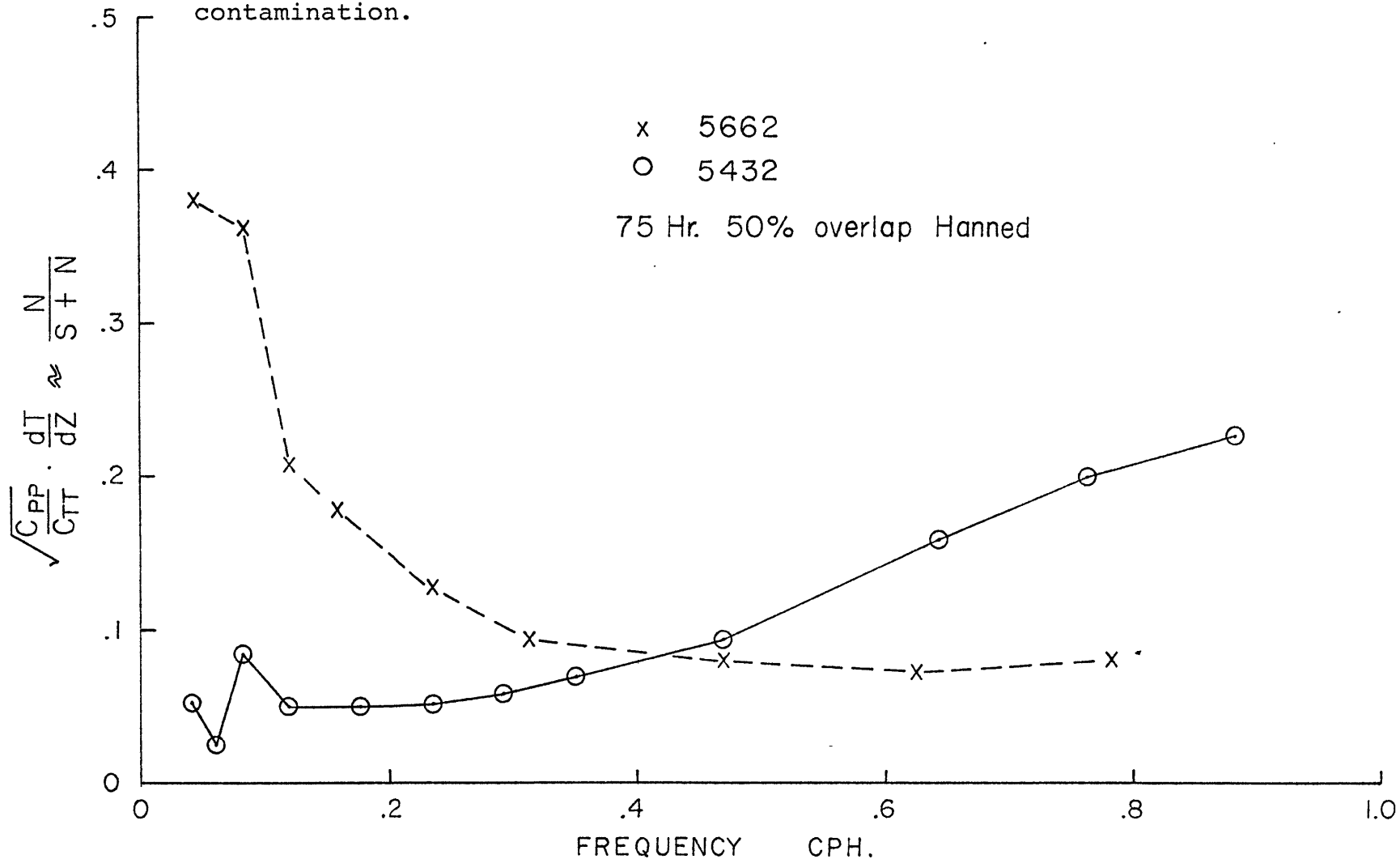
$$\frac{\partial \bar{T}}{\partial x_3} \left(\frac{C_{pp}}{C_{TT}} \right)^{1/2} \sim \left(\frac{N^2}{S^2 + N^2} \right)^{1/2} \quad (A.27)$$

where the pressure is regarded as a source of noise to the temperature signal. Such an estimate is shown in figure A.4, for a "quiet" mooring, 543, and an energetic one, 566.

Mooring 566 is badly contaminated by mooring motion at the low internal wave frequencies, below 0.3 cph. These are the frequencies which contribute most strongly to the stress estimate, and so we expect the stress estimates to be badly contaminated. This is further borne out by looking at the coherence between the pressure and temperature records at 800 m on mooring 566 (figure A.5). The coherence is significant with 180° phase lag at low frequencies, as would be expected if the coherence were caused by mooring motion. Obviously, the observations at the two energetic moorings must be corrected for mooring motion.

Referring back to figure A.4, we see that the mooring motion at 543 is nowhere near as severe at the low frequencies, but appears to become strong at higher frequencies, above 0.5 cph. The reason for this apparent high-frequency problem is that the mooring motion was so slight! The rms mooring motion was less than a meter for this mooring, primarily at tidal frequency. During the 32 minute sample interval, the pressure registered at the instrument tended to change very little. Since the quantizing noise for the pressure recorder (about .01 db, according to Wunsch and Dahlen, 1974) is normally reduced by summing the output of the digital-to-analog converter 64 times in a sample period, the noise is not

Figure A.4 Ratio of rms pressure amplitude divided by rms temperature amplitude, normalized by temperature gradient, vs. frequency for data numbers 5433, 5663. This is an indication of the degree of mooring motion contamination.



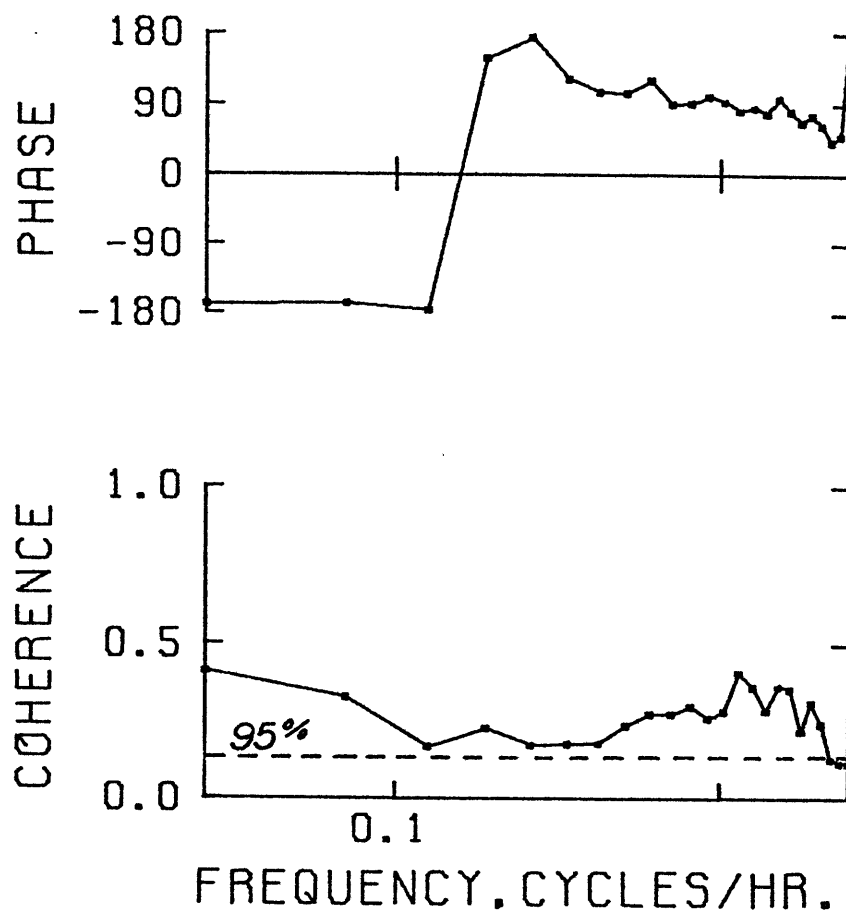


Figure A.5 Coherence between temperature and pressure at 800 m on mooring 566.

reduced as much as usual if the digital pressure value changes very little during the averaging interval. Figure 6 shows the autospectrum of the pressure record from mooring 543. The noisy high-frequency tail, unusual for pressure records from these instruments, is consistent in level with the quantizing noise if there were, on average, only 3 independent estimates of pressure (bit changes, in a sense) per sample interval. The hypothesis of quantizing noise is consistent with the observed temperature-pressure coherence at 543 (not shown), which is below significance levels at frequencies above 0.5 cph. In other words, the high noise-to-signal ratio in figure 4 is unrelated to mooring motion. Although it appears that the quiet moorings do not need to be corrected for mooring motion, the correction was applied to mooring 543 as a check, simply because mooring motion is highly nonlinear, and our measurements are designed to detect such nonlinearities.

The next question to ask is how well-related is the mooring motion at separate depths. Can the pressure record from one depth be used to correct for mooring motion at another? Mooring 557 from Polymode Array II had three T/P recorders of the Wunsch-Dahlen type at depths of 800, 1200 and 2500 meters. These pressure records were Fourier transformed, and the coherence between them was computed. The 800 - 1200 meter coherence is shown in figure 7, and the 800 - 2500 m coherence is shown in figure 8. The coherences

237

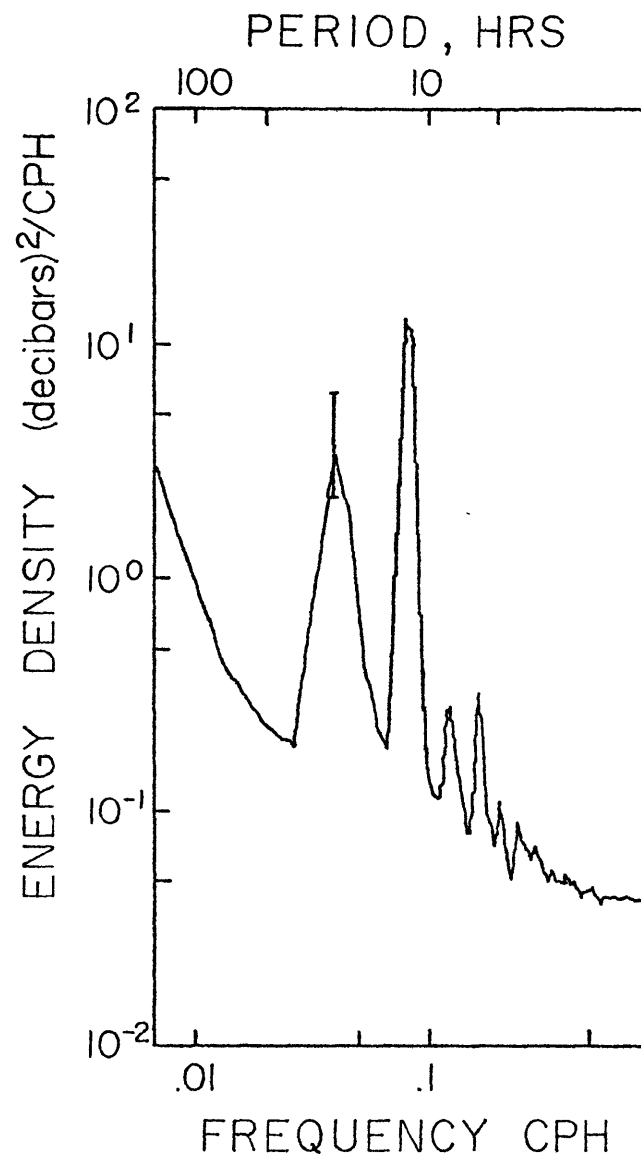


Figure A.6 Pressure spectrum from 800 m on mooring 543.

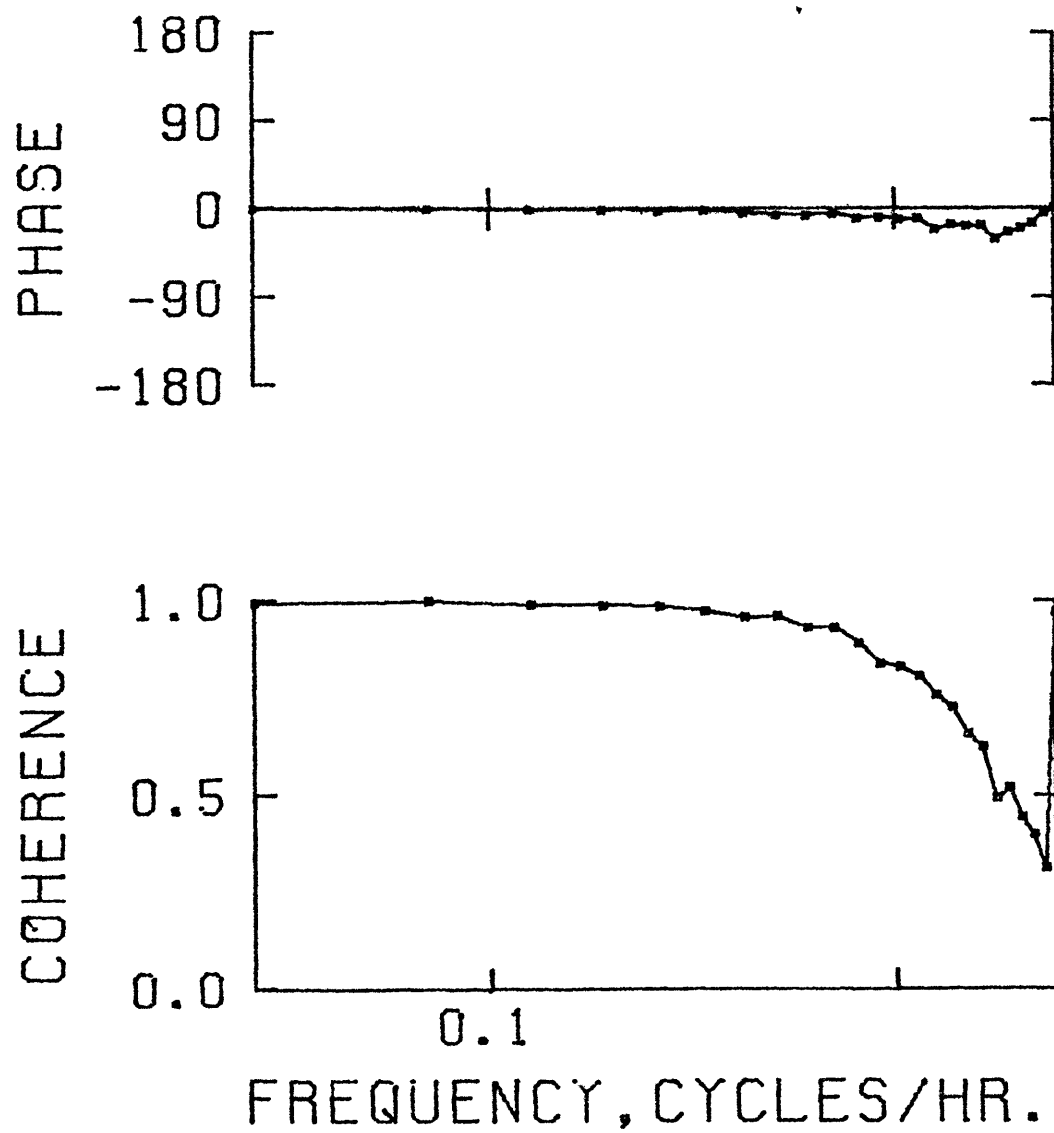


Figure A.7 Coherence between pressure at 800 m and 1200 m on mooring 557.

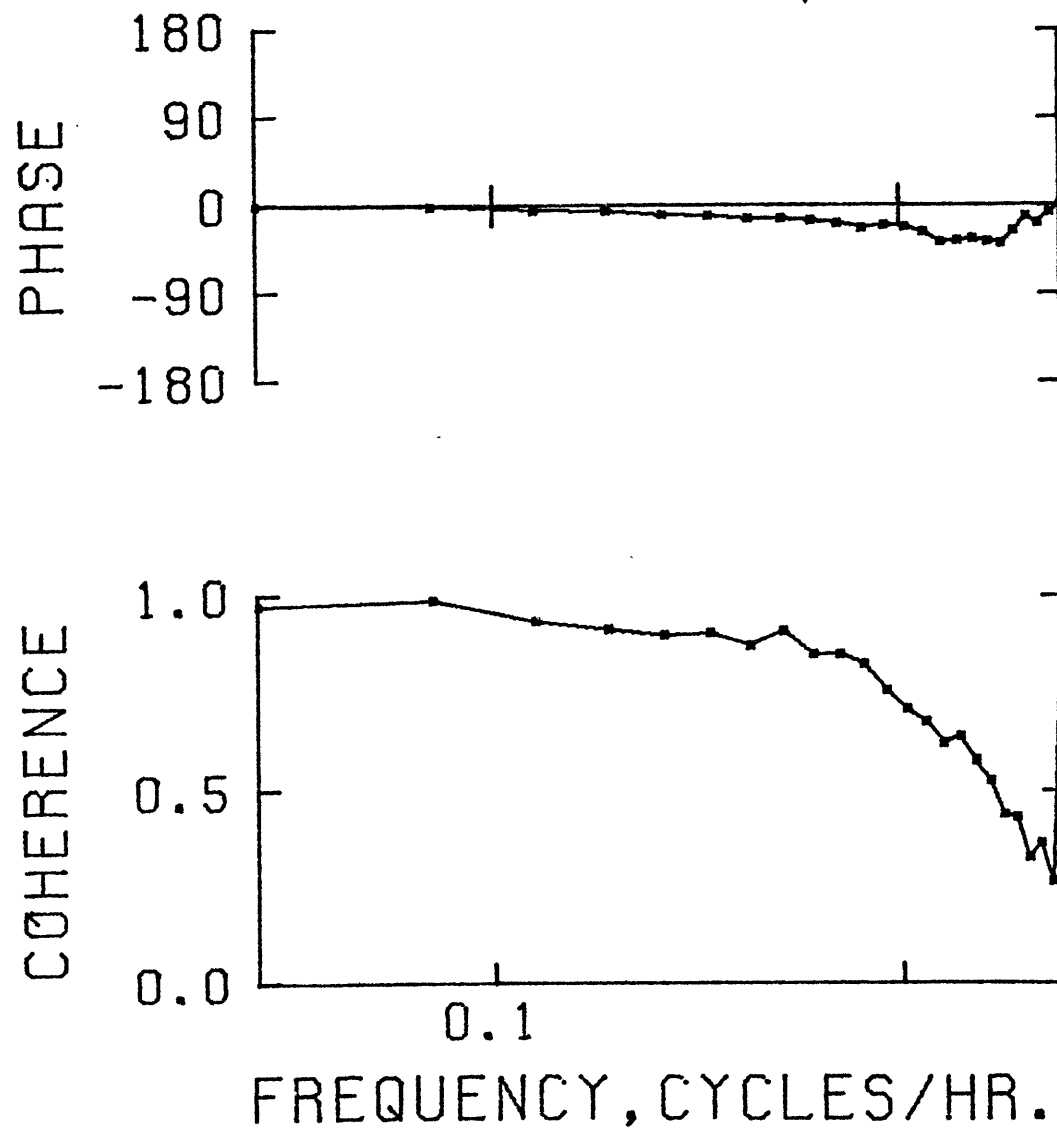


Figure A.8 Coherence between pressure at 800 m and 2500 m on mooring 557.

are extremely high at frequencies below 0.3 cph, the frequencies indicated on figure 4 which are most contaminated by mooring motion. (These pressure spectra fall off as ω^{-4} , with no indication of a noise level as in figure 6.) There is a slight phase lag with increasing depth, corresponding to a delay of about 4 minutes delay from 800 - 1200 m, and about 8 minutes delay from 800 - 2500 m, indicating that the lower part of the mooring tended to respond to time-varying currents a few minutes after the upper part. We have ignored this delay in correcting for mooring motion. Although the coherence was high between levels, the amplitude of the motion was a weak function of depth. Figure 9 shows the pressure auto-spectra from the three levels considered on mooring 557. The relative pressure amplitudes from level to level are not a strong function of frequency, and so it appears permissible to simply scale the 800 m pressure by an amplitude factor to obtain an accurate estimate of the mooring motion in the upper part of the mooring. The amplitude factors were estimated from the spectral ratios in the frequency range .1 - .2 cph, were interpolated and extrapolated to the current meter depths as listed in table A.3. The amplitude factors are probably accurate to 2%.

The following scheme was used to correct for mooring motion:

(a) The 800 m pressure record was interpolated in the frequency domain from a time base of 32 min. to a time base

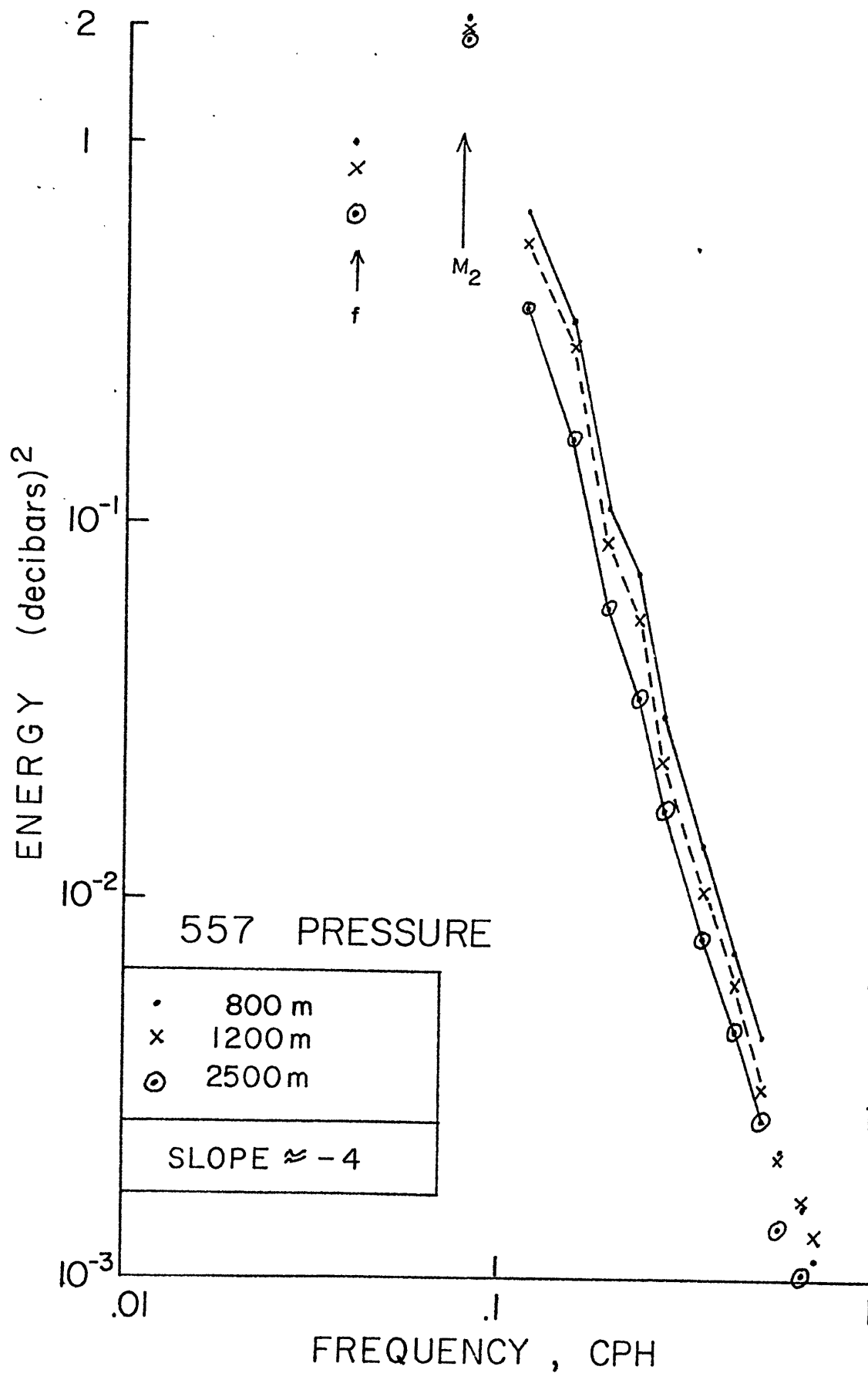


Figure A.9 Pressure spectra from the 800 m, 1200 m and 2500 m level on mooring 557.

of 30 min. The pressure autospectra were compared before and after this operation to ensure equivalent content of the time series.

(b) The internal wave velocity series were low-passed to remove energy at frequencies above 1 cph, and then decimated to a time step of 30 min.

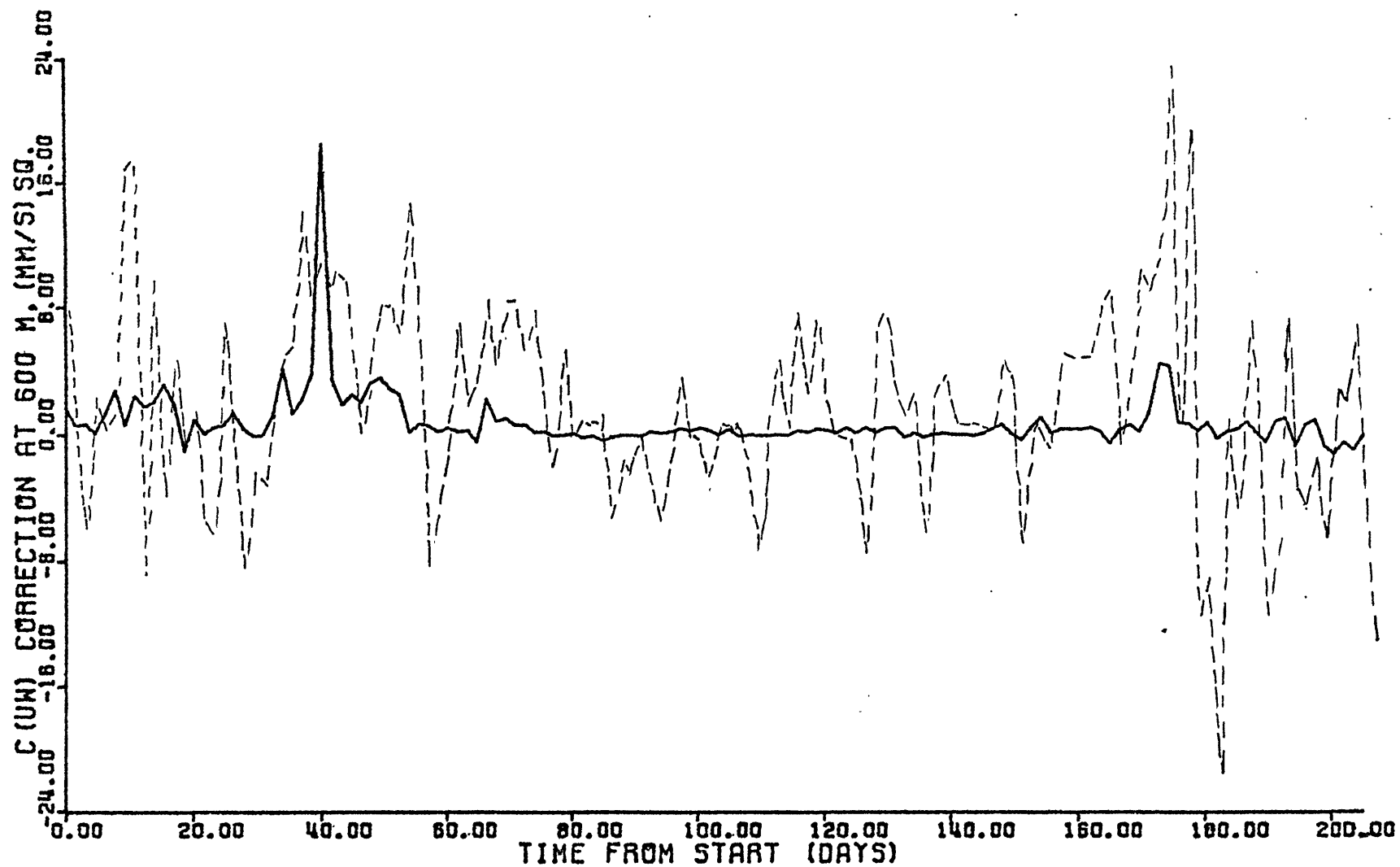
(c) The u' , v' and p' records were Fourier transformed in the manner described in chapter 2.3, except that the summation limits of the frequency bands were altered due to the Nyquist frequency being 1 cph. This resulted in series of correction cross-spectra which were added to the original series of cross-spectra, i.e.,

$$\langle \hat{u}_\alpha * \hat{u}_3 \rangle = -\left(\frac{\partial \bar{T}}{\partial x_3}\right)^{-1} \langle u_\alpha * i\omega \hat{T} \rangle - \left|\frac{\partial p}{\partial x_3}\right|^{-1} \langle \hat{u}_\alpha * i\omega \hat{p} \rangle \quad (\text{A.28})$$

The correction series were found to be extremely small for mooring 543 data, and when the pressure correction was made, the stress-velocity and stress-shear correlations were still found to be insignificant, as before the correction.

The correction terms were not small for mooring 566, however. Comparison of the standard deviations of the original and correction cross-spectra revealed that the correction signals were typically 40% of the original signals at inertial frequency, 20% for the continuum band, and 30% for the total band. This is about as expected from diagram A.4. Figure A.10 compares the corrected stress estimates

Figure A.10 Comparison of 600 m mooring 566 continuum band stress correction series (solid line) with corrected stress (dashed line).



2

(dashed line) with the stress correction term (solid line) for the 600 m continuum band at mooring 566. The correction term is generally small compared to the stress estimate, excepting one rather large correction peak that does not appear to be associated with any burst in the mean flow.

The correction terms were generally well-correlated with the 600 m mean velocity, hence the stress correction tended to reinforce the observed stress-velocity correlations at 600 m, and partially cancel those at 1000 m. As an example, table A.4 lists the continuum band stress-velocity correlation, regression slope, and stress variance (arbitrary units), from before and after the pressure correction was applied. The upper set of numbers is for 600 m stresses; the lower part is for 1000 m. At 600 m, the correlation coefficient, the regression slope, and the stress variance are all larger after correction, while at 1000 m the reverse is true.

All quoted regressions from moorings 565 and 566 are corrected for mooring motion.

275

TABLE A.3

Pressure amplitude factors used for mooring
motion correction

Depth (m)	Scale Factor
600	1.045
1000	0.955
1500	0.865

TABLE A.4

Comparison of continuum band stress vs. 600 m velocity
regression from before and after pressure correction

600 m East velocity vs. Continuum band stress		Before Correction	After Correction
600 m stress	Correlation coefficient	.317	.444
	Regression slope	1.85	2.78
	Stress std. deviation	6.29	6.72
1000 m stress	Correlation coefficient	-.380	-.337
	Regression slope	-2.4	-1.91
	Stress std. deviation	7.99	7.73

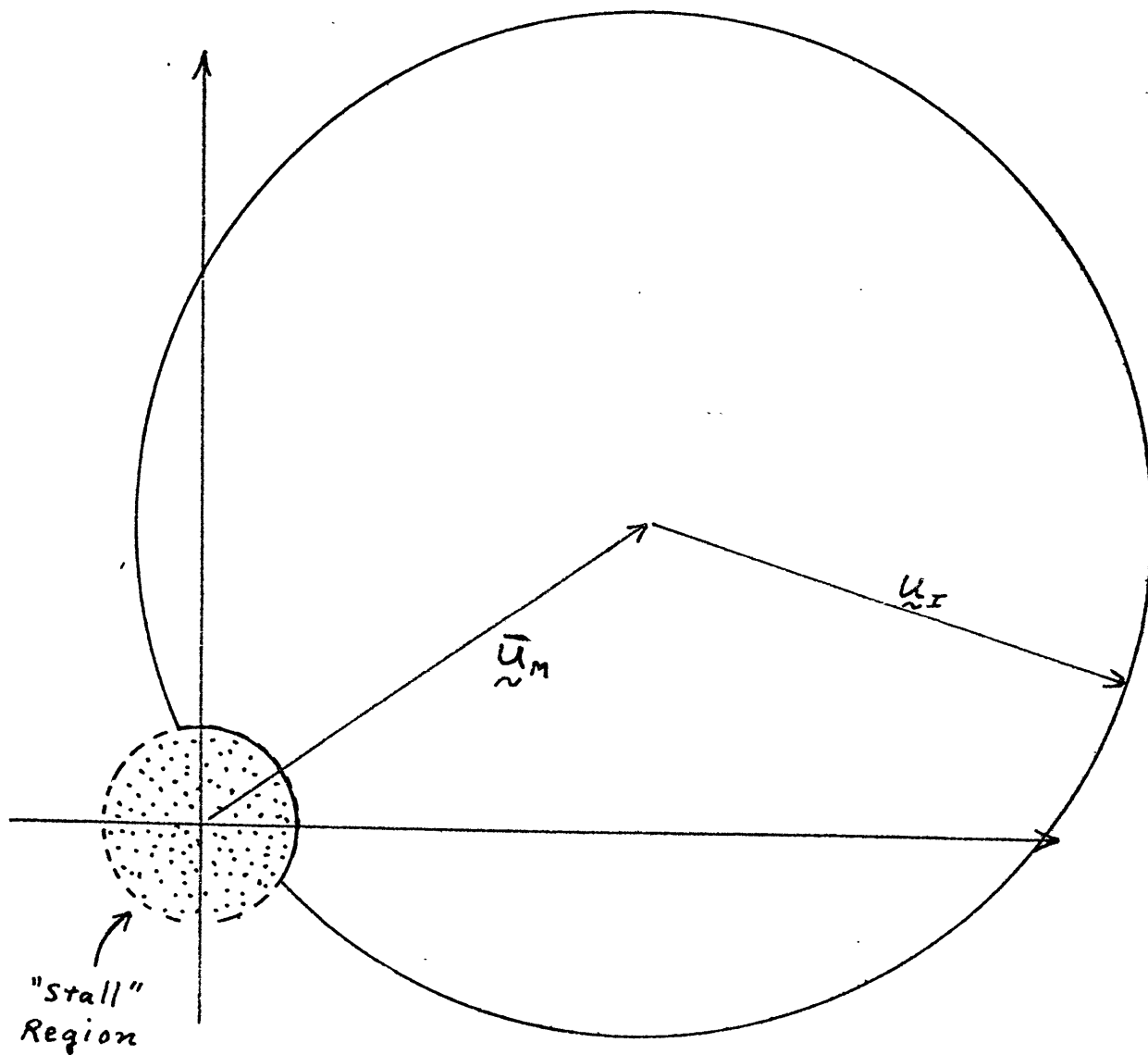
Units of slope and standard deviation are arbitrary

A.5 Rotor Threshold Nonlinearities

The Savonius rotor used on the VACM and 850 current meters to sense the speed has a threshold speed, $U_s \sim 2 \text{ cm s}^{-1}$, below which the rotor does not turn. When the speed is below this value, the instruments record the direction of flow, and set the measured speed equal to U_s . An error is thus introduced into the speed record, of magnitude less than U_s , whenever the speed is below the threshold value. Speeds at moorings 545 and 543 were typically less than 5 cm s^{-1} , and were often below U_s (14.3% of the time for data number 5433, for example). These speed errors are relatively large compared to the typical speeds at these moorings, and could affect the measured internal wave spectra.

A worst-case estimate of the noise due to rotor threshold can be made by assuming that the true velocities are dominated by a mean current, \bar{U}_M and an inertial oscillation, \bar{U}_I of roughly the same amplitude. The vector sum of these currents will pass through the stall region, sketched in figure A.11, once per inertial cycle. When the vector is in the stall region, the measured speed is set to U_s , so the measured velocity vector traces out the solid line in figure A.11. For $|U_I| \gtrsim U_s$, and if the direction of the vane changes slowly (true if $|U_M| \neq |U_I|$), the velocity measured perpendicular to the mean flow is not strongly affected, while the velocity in the direction of the mean flow has an added noise component which is bounded by:

Figure A.11 Sketch of circular path followed by tip of a velocity vector, composed of a mean current, \bar{u}_M , plus a steadily rotating inertial current, u_I .



$$U_N \approx U_S \sin\left(\frac{\pi t}{t_1}\right) H(t-t_1) \quad \text{where } H(X) \text{ is the Heaviside step function}$$

(A.29)

This is in the interval $0 \leq t \leq t_2$, where t_2 is the inertial period. The noise signal is periodic with inertial period, and the fraction of stalled records is given by $A = t_1/t_2$. The noise estimate (A.29) is sketched in figure A.12, to clarify the nature of the signal.

The n th Fourier power coefficient of the noise signal is:

$$\begin{aligned} C_n(A) &= a_n^2 + b_n^2 \\ &= 8 \left(\frac{U_S}{\pi}\right)^2 \frac{A}{1 - (2nA)^2}^2 (1 + \cos 2\pi nA) \\ &= (A U_S)^2 \quad n \neq \frac{1}{2A} \quad (A.30) \\ &\quad n = \frac{1}{2A} \end{aligned}$$

Since the noise signal is continuous, the noise spectrum decays as n^{-4} at high frequencies. If the measured velocity were set equal to zero when the speed was below threshold, the velocity record and noise signal would be discontinuous, causing the spectrum to decay as n^{-2} , making this noise much more of a problem in the high internal wave frequencies. The noise spectrum is plotted in figure A.13 for $U_S = 1.8 \text{ cm s}^{-1}$, as a function of $n = \omega/f$. For $n > (2A)^{-1}$ the spectrum has several zeros which are not plotted; a line connecting the

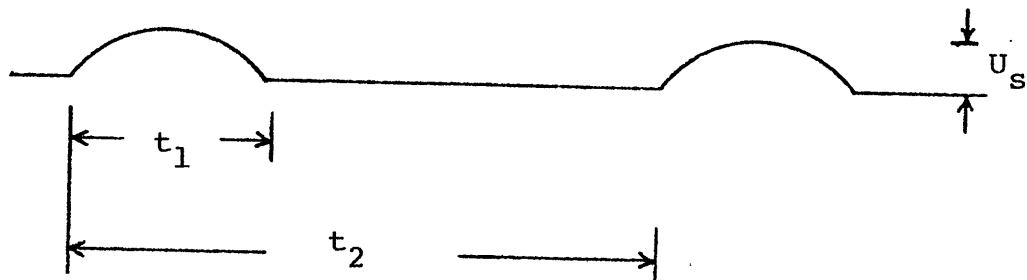
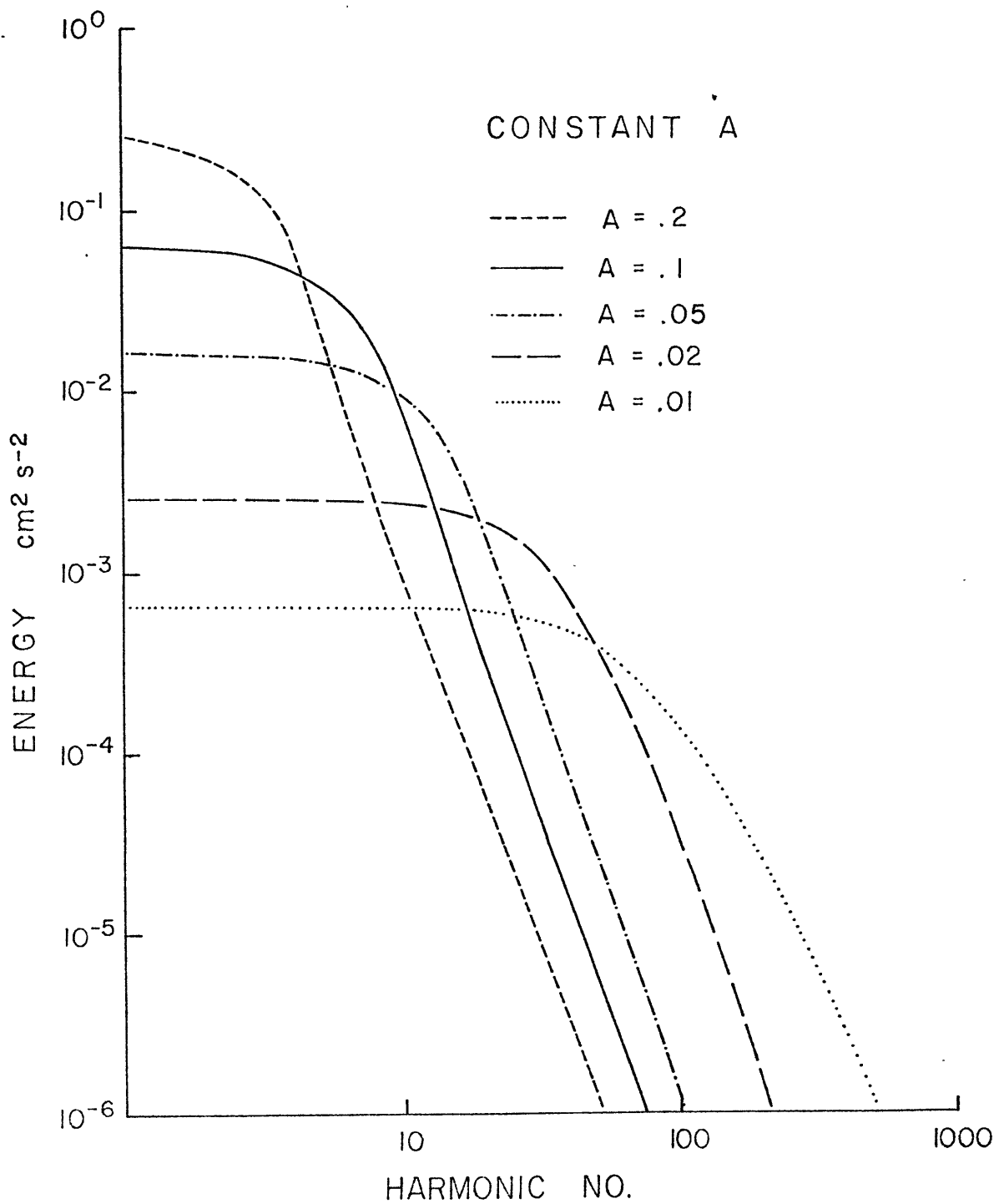


Figure A.12 Sketch of the estimated current measurement error from figure A.11.

Figure A.13 Estimated error spectrum (eq. A.29) vs. harmonic number $n = \frac{\omega}{F}$, for several values of A , where A is the fraction of stalled records.



peaks of the function has been drawn instead. The noise spectrum is nearly flat to about $n = (2A)^{-1}$ (this is just below the half-power point), and falls off rapidly (n^{-4}) beyond this. Hence it may be approximated by band-limited white noise;

$$C_n \approx \left(\frac{2U_S}{\pi}\right)^2 A^2 H\left(n - \frac{1}{2A}\right) \quad (A.31)$$

This underestimates the total variance by about 20%, due to the loss of the high-frequency tail.

Actual current meter records do not have the steady conditions assumed here, but might be visualized as composed of several (P) short (a few inertial periods), "steady" segments, each with its own value of A_p . The power spectrum of the noise is then estimated by:

$$\bar{C}_n = \frac{1}{P} \sum_{p=1}^P C_n(A_p) \quad (A.32)$$

The total noise variance in each piece is proportional to A_p , so the overall variance is simply:

$$\frac{1}{t_2} \int_0^{t_2} |U_N(t)|^2 dt \leq \frac{U_S^2 \bar{A}}{2} \quad (A.33)$$

where \bar{A} is the overall fraction of stalled records. The frequency distribution of this variance depends on the distribution of the A_p . In the limit of a large number of data segments (total record length \gg inertial period), we can

write the estimated noise spectrum in terms of a probability distribution function $f(A)$, of the A 's:

$$\int_0^1 f(A) dA = 1 \quad (A.34)$$

$$\bar{A} = \int_0^1 A f(A) dA \quad (\bar{A} \text{ defined as before}). \quad (A.35)$$

The power spectrum of the noise is:

$$\bar{C}_n(\bar{A}) = \int_0^1 f(A) C_n(A) dA \quad (A.36)$$

Histograms of the A_p from IWEX data (Internal Wave Experiment, Briscoe, personal communication, 1976) suggest two distributions which were tried:

(1) Uniform out to A_0

$$f_1(A) = \frac{1}{A_0} H(A - A_0) \quad (A.37)$$

$$\bar{A} = \frac{A_0}{2} \quad (A.38)$$

The spectral estimate, using the band-limited white approximation for $C_n(A)$, is:

$$\bar{C}_n(\bar{A}) = \begin{cases} \frac{1}{3} \left(\frac{4U_S \bar{A}}{\pi} \right)^2 & n < \frac{1}{4\bar{A}} \\ \frac{(U_S/\pi)^2}{12\bar{A} n^3} & n > \frac{1}{4\bar{A}} \end{cases} \quad (A.39)$$

This is flat out to $n = \frac{1}{4\bar{A}}$ and falls off at n^{-3} above this value. It is sketched in figure A.14, for several values of \bar{A} .

(2) Exponential Distribution

$$f_2(A) = \frac{1}{A_0} e^{-A/A_0} \quad (A.40)$$

$$\bar{A} \approx A_0 \quad (\text{for } A_0 \ll 1) \quad (A.41)$$

The noise estimate is:

$$\bar{C}_n(\bar{A}) = \left(\frac{2U_S\bar{A}}{\pi}\right)^2 \left\{2 - \left[\exp - \left(\frac{1}{2n\bar{A}}\right)\right] \left[\frac{1}{(2n\bar{A})^2} + \frac{1}{n\bar{A}} + 2\right]\right\} \quad (A.42)$$

This is plotted in figure A.15. Oddly enough, for matching values of \bar{A} , the spectra computed from distributions (1) and (2) are nearly identical to within a factor of 2. Both have an n^{-3} falloff at high frequency.

Apparently, the estimated noise spectrum is not strongly sensitive to the distribution of the stall periods, and so may be approximately characterized by the overall fraction, \bar{A} , of threshold-value records.

To compare the estimated noise spectra to spectra of $HKE = \frac{C_{11} + C_{22}}{2}$ we divide the spectra by 2 and normalize by the piece length to get the power density of the noise at frequency $\omega = nf$. The spectrum of horizontal kinetic energy from data number 5433 (1000 m) is plotted in figure A.16 for com-

Figure A.14 Estimated error spectrum (A.38) for several values of \bar{A} (defined in text).

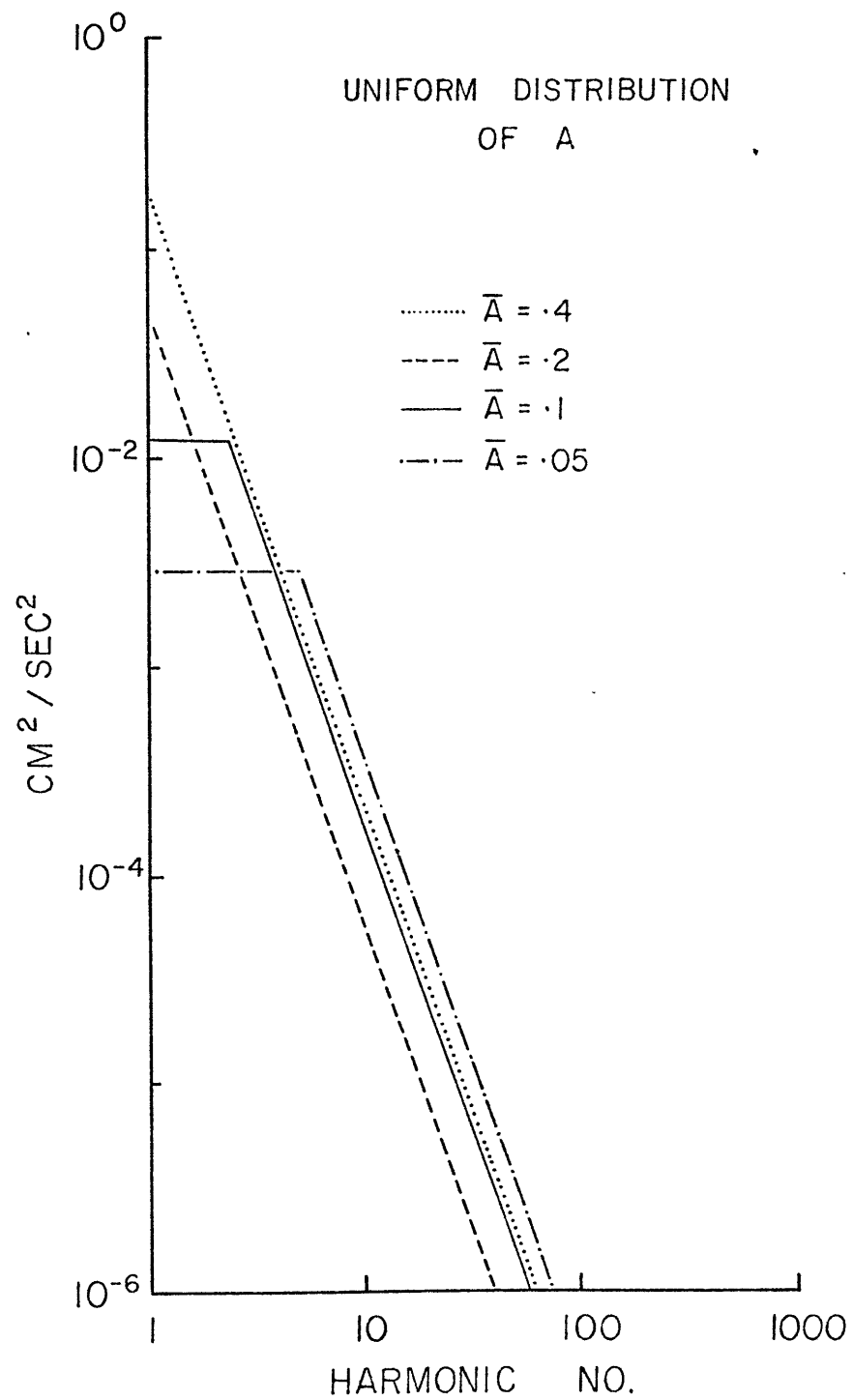
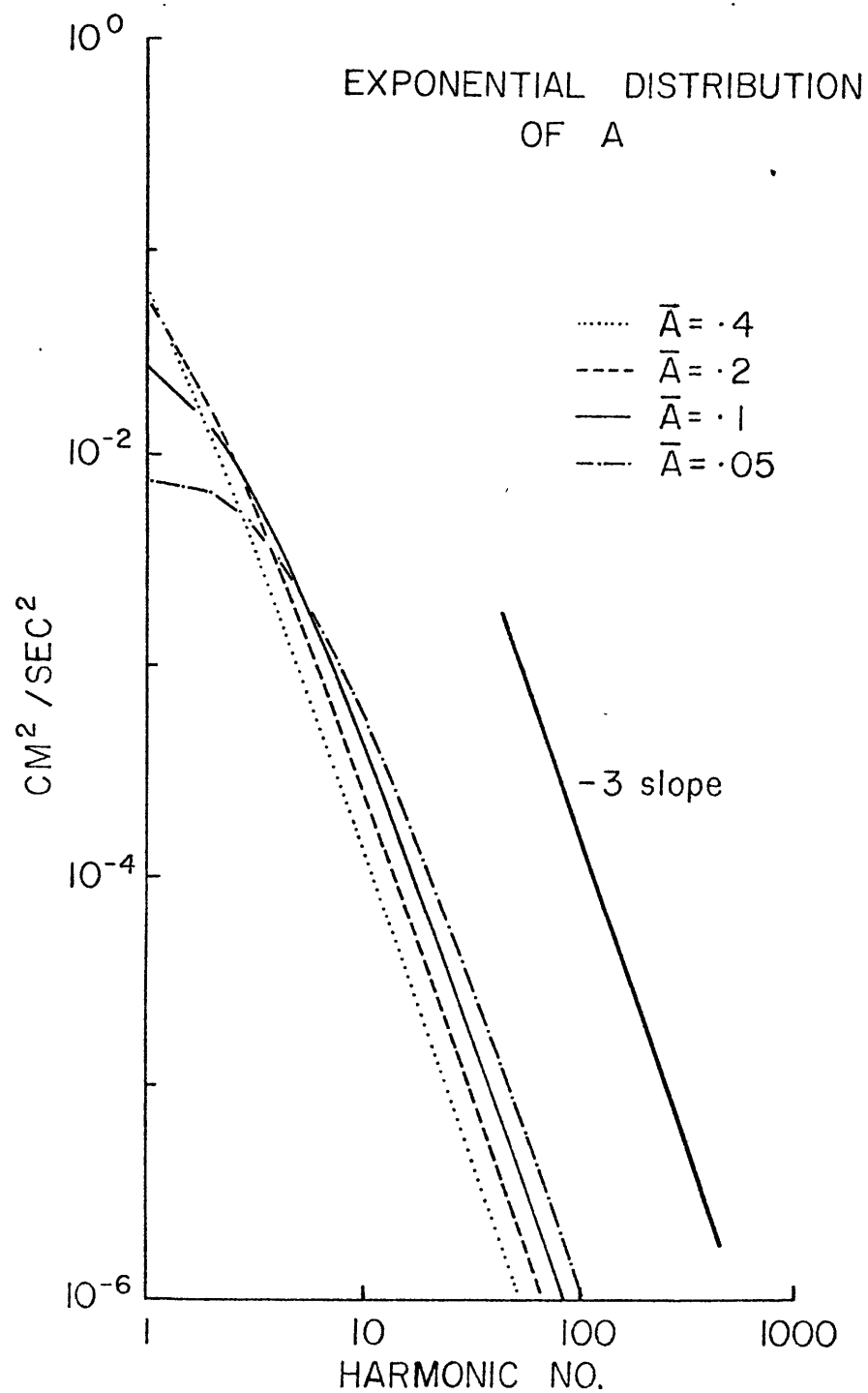
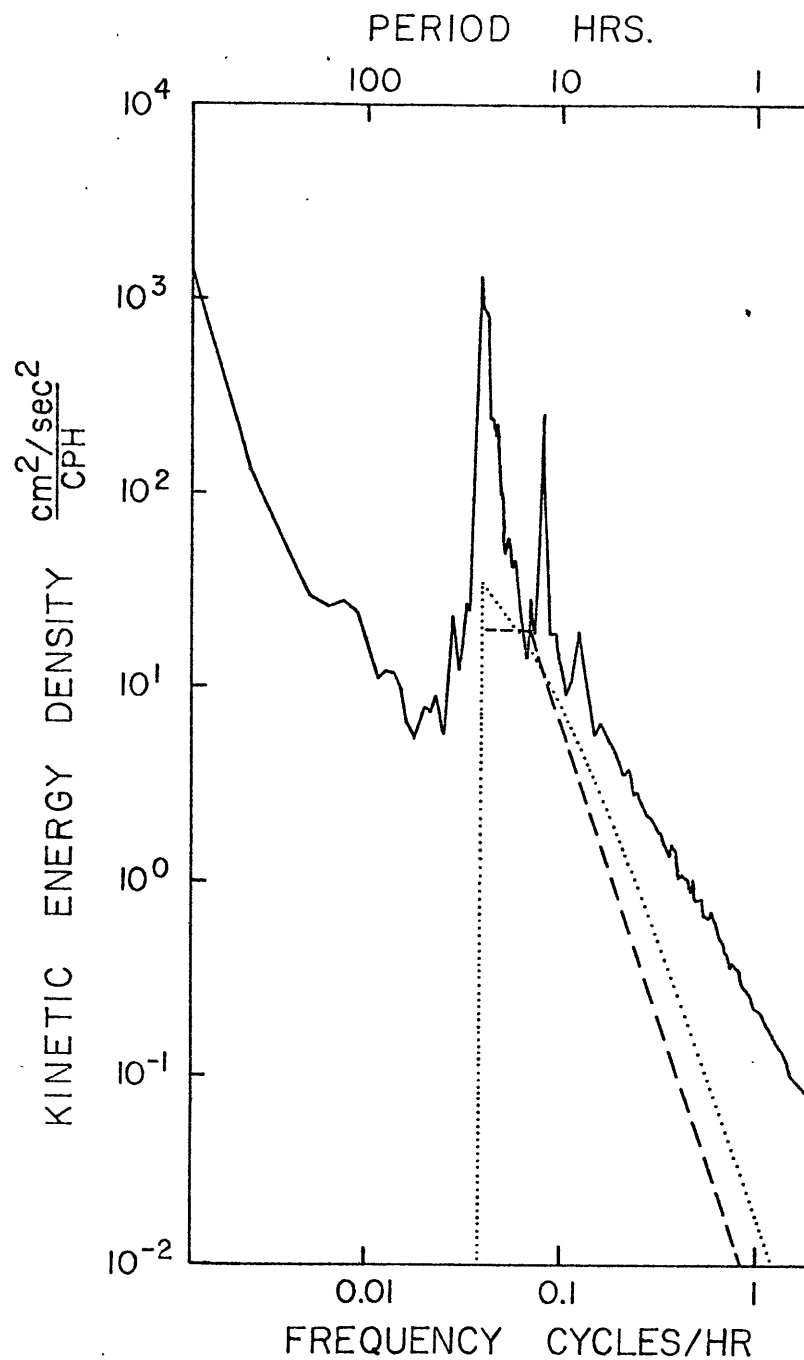


Figure A.15 Estimated error spectrum (A.41) for several values of \bar{A} .



parison with the estimated noise spectra (A.38) and (A.41). The observed value of $\bar{A} = 14.3\%$ was used. The rotor threshold nonlinearity only seems severe in the frequency range $f-2f$. The continuum internal wave frequencies (above 0.1 cph) are relatively unaffected. As the mean speeds increase, so that \bar{A} decreases, the level of this noise drops, so that this noise can be expected to be negligible at the two more energetic moorings which were analyzed.



DATA NO. 5433

14.6% of records at stall speed

..... exponential distribution

----- uniform distribution

Figure A.16 Estimated error spectra (A.38 and A.41) superposed on the HKE spectrum for data 5433, with $\bar{A} = 14.6\%$, as observed.

A.6 Regression Uncertainties

The usual regression model, and the one used in these studies, is:

$$y_i = x_i \cdot a + b + n_i \quad (\text{A.43})$$

where x , y are the two time series, a and b are coefficients estimated in the regression procedure, and n_i is the residual time series, assumed to be uncorrelated with the x_i .

Forcing n to be uncorrelated with x leads to a slope estimate:

$$a = \rho_{xy}(\tau) \frac{\sigma_y}{\sigma_x} \quad (\text{A.44})$$

where:

$\rho_{xy}(\tau), \sigma_x, \sigma_y$ are as given in eqs. 4.44.

A more general regression model allows for noise in both the x and y series (Ricker, 1973). The slope estimate is decreased from the above value, the amount of decrease depending on the noise level in each series. Unfortunately, this is not well known in our case, and so we use the more simple model above.

Comparison of the spectra of the stress and shear time-series in chapter 2.5 shows that the stress timeseries appear to have a definite background noise, with a white spectrum, superposed on the signal. This is of about the correct level to be due to statistical fluctuations in estimating the cross-spectra. The shear estimates have no such apparent noise

level, and indeed, their estimated noise variance is about 2% of the signal. It seems to be a good approximation to neglect the error in estimating the mean velocities, and use the above regression model, with the mean flow quantities regarded as x , and the wavefield quantities regarded as y .

If x and y are random pairs of independent samples drawn from a jointly normal distribution, confidence limits for the regression parameters and correlation coefficient can be computed and are tabulated (c.f. Cooper, 1969). However, the mean flow estimates are certainly not independent at adjacent sample times, and neither are the stress estimates or the residuals (the Hanning data window used to compute the spectra overlaps adjacent estimates by about 50%). It is not even clear that the timeseries involved have a normal distribution. They certainly do not in the energy level correlations described in chapter 4.4.

The problem of autocorrelated residuals was considered by Wold (1950) for Normally distributed data. The classic estimate of the regression error is simply computed as if the series had N/M point pairs, where

$$N \text{ is the number of points in the series,} \quad (A.45)$$

$$M = \sum_{i=-\infty}^{\infty} \rho_x(i) \rho_y(i) \quad (\text{the convolution of the auto-correlation coefficients})$$

This formula also appears in Jenkins and Watts (1969, equation 8.2.6).

An estimate for the standard error of the regression coefficients is derived by Lyttkens (1963), which reduces to the formula of Wold for Normally distributed data, but which involves estimation of the joint fourth moments of the series, and so gives a valid estimate of the errors when the data are non-white and non-normal. The standard error for the slope estimate is:

$$d \approx \frac{\sum_{i=1}^N (x_i - \bar{x})^2 u_i^2 + 2 \sum_{i=1}^{k_0} \sum_{i=1}^{N-k} (x_i - \bar{x}) (x_{i+k} - \bar{x}) u_i u_{i+k}}{\sum_{i=1}^N (x_i - \bar{x})^2} \quad \text{where:} \quad (\text{A.46})$$

$$u_i = y_i - a \cdot x_i - b$$

The formula above was coded as a subroutine (listed in figure A.17) with the parameter k_0 allowed to scan from 1 to $N/2$ so as to maximize the estimate of d . Approximate 95% confidence limits for the regression slope are $1.96 \cdot d$. In a test of the estimator, several artificial time series were generated. The variables were normally distributed, and independent from point to point (white spectrum). Each series was uncorrelated with each of the others, and was 180 data points in length. Several of the series were regressed, one on the other, and the estimate of the correlation coefficient estimator error ($d \cdot \sigma_x / \sigma_y$) was compared to the classical estimate of $1.96 / (N)^{1/2} = 0.15$, and also to the error estimated using Wold's (1950) formula. These comparisons were made for

7

```

1.      SUBROUTINE ERR(X,XB,SX,Y,YB,SY,SL,N,KNBT,R1)
2.      C  COMPUTES R1, THE STANDARD ERROR OF A LEAST SQUARES SLOPE ESTIMATE FROM THE
3.      C  REGRESSION OF Y ON X. SLOPE ERROR BOUNDS ARE ABOUT  $1.96 \cdot R_1$  .
4.      C  NO NORMALITY ASSUMPTIONS HAVE BEEN MADE.  VARIABLES ARE:
5.      C      XB,YB  MEANS
6.      C      SX,SY  STD. DEVIATIONS
7.      C      SL    SLOPE ESTIMATE,DY/DX
8.      C      N     NO. POINTS IN SERIES
9.      C      KNBT  A MAX. SUMMING INDEX
10.     C      KNBT IS SCANNED TO MAXIMIZE R1
11.     C      SEE CHAPTER 3 OF 'TIME SERIES ANALYSIS',ED. BY ROSENBLATT.
12.     DIMENSION X(1),Y(1),U(300)
13.     C  COMPUTE RESIDUALS,U
14.     → DO 10 I=1,N
15.     10 U(I)= Y(I)-YB - SL*(X(I)-XB)
16.     C  DO FIRST SUM
17.     SUM1 = 0
18.     → DO 20 I= 1,N
19.     20 SUM1 = SUM1 + ((X(I)-XB)*U(I))**2
20.     C  DO SECOND SUM
21.     KNBT = N/2
22.     SUM2MAX = 1E72
23.     SUM2 = 0
24.     IF(KNBT.GE.N) OUTPUT'KNBT TOO BIG',R1=0,RETURN
25.     → DO 40 K=1,KNBT
26.     → DO 30 I=1,N-K
27.     30 SUM2 = SUM2 + (X(I)-XB)*(X(I+K)-XB)*U(I)*U(I+K)
28.     IF(SUM2MAX.LT.SUM2) SUM2MAX=SUM2,KMAX=K
29.     IF(K.GE. 2*KMAX .AND.K.GT.10) GO TO 100
30.     40 CONTINUE
31.     100 KNBT = KMAX ←
32.     SUM2 = SUM2MAX
33.     R1 = SQRT(SUM1 + 2*SUM2)/N/(SX)**2
34.     RETURN
35.     END

```

Figure A.17 Listing of the subroutine used to compute the confidence intervals of the regression slopes.

the series as they were generated, after low-pass filtering (filter described in chapter 2), for non-normal series computed as the sum of the squares of a pair of the original series, and for low-passed, non-normal series. The results of the comparison are listed in table A.5. Also shown for comparison are the two largest (absolute values) correlation coefficients computed (out of 35) for each test. The estimator appears to work very well for normally-distributed data, and accounts for autocorrelation in the time series as well as Wold's formula, which is more time-consuming to compute. However, the estimate becomes highly variable for non-normally distributed data, presumably because the fourth-order cumulant becomes important, and the estimation of a higher-order moment is less accurate. Although the estimator may be expected to cope with small non-normality, it appears to run into difficulties with highly non-normal distributions, such as might be expected from time series of energy level. It should be noted that the classical estimates also break down badly for this distribution, and that the Lyttkens estimator at least attempts to account for the non-normal distribution. Hence the estimated regression errors from highly non-normal distributions must be viewed with caution, although the method works quite well for non-white, normally distributed data.

TABLE A.5

Test of Subroutine ERR

DATA	ERR $\Delta\rho$ (95%)	WOLD'S FORMULA		Largest two of 35	
		Convol. ACF's	$\Delta\rho$	#1	#2
Normal, white	.161	1.06	.15	.173	.146
Normal, filtered	.246	3.2	.270	.220	.209
Non-normal, filtered	.283	2.17	.221	.263	.226
Non-normal, white	.108	.924	.15	.189	.170
	.170	1.01	.15	.203	.197
	.242	1.12	.15	.184	.144

A.7 Statistical Uncertainties of Spectral Estimates

The confidence intervals for spectral estimates were computed following Jenkins and Watts (1969), assuming the process from which the data were taken is a Gaussian random variate with a spectrum which varies little in the band of frequencies that contribute to a particular spectral estimate. Jenkins and Watts discuss spectral confidence limits in terms of a smoothing factor, I/T , which they define in terms of the reduction of variance of the spectral estimator. We use the more commonly used term "equivalent degrees of freedom", or EDF to describe a similar quantity. Following Nuttall (1971), the EDF is defined in terms of the reduction of variance of the autospectral estimator and related to Jenkins and Watts' smoothing factor:

$$\text{EDF} = \frac{2[E(C_{xx}(\omega))]^2}{\text{Variance}(C_{xx}(\omega))} = \frac{2T}{I} \quad (\text{A.47})$$

Under the Fourier transform procedures used in this study, spectral estimates at adjacent Fourier harmonics or from adjoining (overlapped) pieces are not statistically independent. Hence the reduction of variance of the estimators is less than the product of the number of pieces and the number of harmonics in the averaged spectral estimate. Using results of Persson (1974) and Nuttall (1971), we derive the following formula for the EDF of a single spectral estimate; computed as the average of N_p 50% overlapped pieces,

215

also averaged over N_b adjacent Fourier harmonics;

$$\text{EDF} = \frac{K}{A} \quad (\text{A.48})$$

where:

$$K = 1.91 N_p - 1.33$$

$$\frac{N_b + 2 \sum_{n=1}^{1/2(N_b-1)} (N_b-n) \rho_n}{N_b^2}$$

$$\rho_0 = .495 \quad (.444)$$

$$\rho_2 = .068 \quad (.028)$$

$$\rho_3 = .005 \quad (0)$$

$$\rho_n \approx 0 \quad (n \geq 4)$$

N_b is assumed to be odd. For a single piece ($N_b = 1$), the correlation coefficients in brackets are used. The values of A used for several of the frequency bands used in the study are tabulated in table A.6. The formulae above will be derived shortly.

Spectral estimates computed over wide frequency bands (i.e., the continuum and total bands) suffer from two effects not considered here, both arising from the non-white frequency dependence of the data. One is the reduction of the amount of averaging which goes into a spectral estimate due to the extra weight given to the more energetic frequencies. This decreases the EDF, in effect allowing the variance of the estimator to remain larger than we would compute from the

296

N # freq. bands	A 1 Piece Hanning Window	EDF 1 Piece; Hanning Window	A 50% Overlap Hanning Window
1	1	2	1
3	.531	3.77	.553
5	.348	5.75	.375
7	.247	8.07	.279
11	.164	12.16	.184
15	.123	16.3	.137
23	.0816	24.5	.0904
31	.0611	32.7	.0675
45	.0424	47.2	.0468
143	.0135	148	.0149
147	.0131	152	.0145

TABLE A.6

Values of EDF; A used for spectral confidence intervals

above. The other effect is a reduction of the maximum value which a cross-spectral estimate can attain due to the non-overlapping in the frequency domain of the two spectra which are involved in the estimate. (One may be large at low frequencies while the other is large at high frequencies, so that the cross-spectrum is never very large.) This effect can be estimated by computing the frequency integral of the product of the two energy spectra, but this was only done for idealized spectra. Hence, confidence intervals computed for the continuum and total frequency bands are inaccurate, and are presented only to provide a rough significance level.

Another potential breakdown of the statistical assumptions is non-Gaussianity of the original fields. However, recent investigation of this indicates it is not a problem. Iida (1975) and Briscoe (1977) showed that internal wave variables u' , v' , and T' are Gaussian "most of the time" if proper allowance is made for the non-white spectrum and the corresponding autocorrelation effects. He found that the times of disobedience to the Gaussian distribution (low kurtosis in velocities, non-zero skewness in T') were times of high variance, leading one to suspect that nonlinearities, either breaking or resonant interactions, are important at these times. However, it does appear that the wavefield has a tendency to relax rather quickly to a Gaussian state.

We now derive the formulae for the EDF for spectra computed under a 50% overlapped Hanning data window.

Averaging of independent data pieces, in imitation of an ensemble average, increases the EDF as $K = 2P$, where P is the number of non-overlapping pieces. The case is slightly different for 50% overlapped Hanning data windows, since each piece is not totally independent of the others. Nuttall (1971) has computed an approximate formula for the EDF of each frequency estimate computed by averaging P pieces plus $(P-1)$ pieces overlapped by 50%; each piece fourier transformed under a Hanning data window, for a total of $N_p = 2P - 1$ pieces:

$$\begin{aligned}
 K &\approx 3.82 P - 3.24 \\
 &= 3.82 \left(\frac{N_p + 1}{2} \right) - 3.24 \quad \begin{array}{l} \text{(50\% overlap} \\ \text{Hanning window)} \end{array} \quad (\text{A.49}) \\
 &= 1.91 N_p - 1.33
 \end{aligned}$$

Note that the EDF is much larger than the corresponding result for a square window:

$$K \approx 2P \text{ (square window)} \quad (\text{A.50})$$

The additional variance reduction is due to the implicit frequency smearing performed by the Hanning data window, giving a variance reduction at a cost in frequency resolution.

Further averaging was performed in the frequency domain, by averaging over a number, N_b , of frequency harmonics. Adjacent spectral estimates computed under a square data window, separated by $(\text{piece length})^{-1}$ in frequency, are uncorrelated, so that averaging over N harmonics reduces the variance of the

estimate by a factor of N . The net EDF is then, for a square window:

$$\text{EDF} = 2 \left(\frac{N_p + 1}{2} \right) N_b \quad (\text{Square Window}) \quad (\text{A.51})$$

Due to the increased Hanning window bandwidth, however, neighboring spectral estimates are not independent, and so frequency averaging is not quite that effective in reducing the variance of the averaged spectral estimate. Perrson (1974) has derived an expression for the variance reduction of a spectral estimate (of white noise) under a single-piece fourier transform estimate, for which a weighted average estimate has been computed:

$$A \equiv \frac{\text{Var}[C_{xx}]}{E^2[C_{xx}]} = \sum_{s=-k}^k \sum_{r=-k}^k \rho(r-s) Q(r) Q(s) \quad (\text{A.52})$$

where:

$N_b = 2k + 1$, as above, is the number of terms
in the average (N_b is assumed odd)
 $Q(r)$ are the weighting factors such that $\sum_{r=-k}^k Q(r) = 1$
 $\rho(r)$ is the correlation coefficient for the data
window (Equations A.57, A.58)

For even weighting, $Q(r) = (2k + 1)^{-1}$ independent of r , and III-C-11 may be simplified. We first realize that the $S = -k$ terms are equal to the $S = k$ terms by virtue of the symmetry of the autocorrelation coefficient.

$$\begin{aligned}
 \sum_{r=-k}^k \rho(r-n) &= \sum_{r=+k}^{-k} \rho(r-n) \\
 &= \sum_{t=-k}^{+k} \rho(-t-n) \\
 &= \sum_{t=-k}^k \rho(-(t+n)) \\
 &= \sum_{t=-k}^k \rho(t+n)
 \end{aligned}
 \tag{A.53}$$

We then write out A explicitly:

$$\begin{aligned}
 (2k+1)^2_A &= \sum_{r=-k}^k \rho_r \\
 &+ 2 \left[\begin{aligned} &\rho_0 + 2\rho_1 + 2\rho_2 + \dots + 2\rho_{k-1} + \rho_k \\ &+ \rho_0 + 2\rho_1 + 2\rho_2 + \dots + \rho_{k+1} + \rho_k \\ &\quad \cdot \quad \cdot \quad \cdot \quad \cdot \quad \cdot \\ &+ \rho_0 + 2\rho_1 + 2\rho_2 + \rho_3 + \dots + \rho_k \\ &+ \rho_0 + 2\rho_1 + \rho_2 + \dots + \rho_k \\ &+ \rho_0 + \rho_1 + \rho_2 + \dots + \rho_k \end{aligned} \right]
 \end{aligned}
 \tag{A.54}$$

The matrix has k rows and $k+1$ columns.

The dividing line between "2" coefficients and "1" coefficients is a diagonal. Then, re-ordering the terms:

$$\begin{aligned}
 (2k+1)^2 A &= \sum_{r=-k}^k \rho_r + 2k \rho_0 + 2(2k-1)\rho_1 \\
 &+ 2(2k-2)\rho_2 + \dots \\
 &\dots + 2(2k-n)\rho_n + \dots \\
 &\dots + 2(k+1)\rho_{k-1} + 2k\rho_k
 \end{aligned}
 \tag{A.55}$$

Then:

$$A = \frac{(2k+1) + 2 \sum_{n=1}^k [2k+1-n]\rho_n}{(2k+1)^2}
 \tag{A.56}$$

The Hanning window autocorrelation coefficients for a single piece are given by Perrson (1974) and Nuttall (1971) as:

$$\begin{aligned}
 \rho_1 &= .444 \\
 \rho_2 &= .028 \\
 \rho_r &\leq 10^{-6} \text{ for } r \geq 3
 \end{aligned}
 \tag{A.57}$$

However, for 50% overlapped windows, Nuttall (1971) finds an increase in the autocorrelation coefficients:

$$\begin{aligned}\rho_1 &= .495 \\ \rho_2 &= .068 \\ \rho_3 &= .005 \\ \rho_4 &\sim 0\end{aligned}\tag{A.58}$$

Thus, in terms of the number of frequency bands, N_b , assumed odd, the decrease in variance is:

$$\begin{aligned}A &= \frac{N_b + 2 \sum_{n=1}^{\frac{N_b+1}{2}} [N_b - n] \rho_n}{N_b^2} \\ &= (2.136 N_b - .646) N_b^{-2} \quad (N_b \geq 3)\end{aligned}\tag{A.59}$$

The net EDF is given by:

$$\text{EDF} = \frac{K}{A}\tag{A.60}$$

with

$$K = \begin{cases} 2 & \text{single piece} \\ 1.91 N_p - 1.33 & \text{Hanning window, } N_p \text{ half-overlapped pieces} \end{cases}$$

It is interesting to note that for large N_b and N_p , the EDF is:

$$\text{EDF} \approx \begin{cases} (N_p + 1)N_b & \text{square window; 50\% overlap} \\ .9 (N_p + 1)N_b & \text{Hanning window; 50\% overlap} \end{cases}$$

(A.61)

so that the Hanning window with 50% overlap achieves nearly the same variance reduction as with no windowing, although the primary purpose of the Hanning data window is to reduce the inter-frequency leakage due to the ω^{-2} falloff of the internal wave spectrum.

A.8 Mean Flow Measurement Errors

Bryden (1975) compared the four-day averaged, low-passed values of current and temperature from current meters separated horizontally by small distances (6 m to 6000 m) on the IWEX mooring. Assuming no velocity difference for horizontal separations, he obtained estimates for the instrumental errors in speed, direction and temperature.

$$\delta S = .35 \text{ cm/sec}$$

$$\delta \theta = .052 \text{ radians} = 3 \text{ deg.} \quad (\text{A.62})$$

$$\delta T = .023^\circ \text{ C} .$$

He found that about half the variance in speed and direction errors could be accounted for by removing a bias for each current meter pair, suggesting that about $2^{-1/2}$, or 71%, of the error is not correctable even by individual instrument calibrations. (However, 93% of the temperature variance was due to offset.)

Owens and McWilliams (1976, personal communication) have estimated the expected error in estimating the shear from a two-point velocity difference. Using Bryden's estimated velocity errors, and assuming 31% of the velocity variance to be in the barotropic mode, 60% in the first baroclinic mode, 6% in the second, and 1.6% in the third, they assumed the modes to be statistically independent and computed the expected error as a function of separation and depth. The

305

error was a minimum at a central depth of 800 m (current meters at 600 and 1000 m), with an rms error of 20%. Approximately the same error was estimated for a 600 m separation, and so is about the same for current meters at 500 and 1000 m.

306

Appendix B

INTERPRETIVE MODEL FOR WAVEFIELD

In order to sensibly interpret the measured internal wave spectra, both in the mean and as a function of time, it will be helpful to use a model of the internal wavefield akin to that of Fofonoff (1969), Garrett and Munk (1972), and Müller (1976), so that the spectra can be regarded as particular integrals in wavenumber space of an energy spectrum. The waves will be regarded as linear and Gaussian (the two assumptions are related), of smaller scale (horizontal and vertical) than the respective scales of variations of the medium in which they propagate, and the concept of vertical modes, in which the net vertical energy transport is zero, is relaxed in order to examine the effects of vertical anisotropy. Vertically propagating near-planewave solutions are explicitly allowed, but the modal solutions are recovered by assuming vertical symmetry in the wavefield; together with fixed phase relationships between up- and downgoing rays, so that two planewaves sum to form a single vertical mode. (This may not be true when nonlinear effects such as weak resonant wave interactions are considered. Considering a resonant triad consisting of three vertical modes to be a coupled pair of triads involving rays could lead to a different result than direct computations would give.)

This model of the internal wavefield is virtually identical to that of Müller (1976) and is reviewed here:

- a) for convenience,
- b) for greater clarity,
- c) to change the Fourier transform definitions so as to conform with the conventions I used,
- d) to investigate the effects of allowing vertically standing modes.

The notation closely follows that of Müller (1976).

Under the above assumptions, the linearized equations of motion for the wavemotions are:

$$\begin{aligned} \left(\frac{\partial}{\partial t}\right) + \bar{\underline{u}} \cdot \nabla) \underline{u}' + \underline{f} \times \underline{u}' - b \hat{x}_3 + \nabla \pi' &= 0 \\ \left(\frac{\partial}{\partial t}\right) + \bar{\underline{u}} \cdot \nabla) b' + N^2(z) u_3' &= 0 \\ \nabla \cdot \underline{u}' &= 0 \end{aligned} \tag{B-1}$$

where:

$\bar{\underline{u}} = (\bar{u}_1, \bar{u}_2, \bar{u}_3)$ mean velocity, slowly varying on wavelength scales

$\underline{u}' = (u_1', u_2', u_3')$ = wave velocity

$\underline{u} = \bar{\underline{u}} + \underline{u}'$ is the total Eulerian water velocity

$\pi' = \frac{1}{\rho_0} \cdot$ (wave-induced pressure perturbation)

$b = - \frac{g}{\rho_0} \cdot$ (wave-induced density perturbation)

$\hat{x}_3 = (0, 0, 1)$ the vertical unit vector.

The above equations, to lowest order in an expansion whose small parameter is the ratio of:

$$\left(\frac{\text{wavelength}}{\text{scale of variation of mean field}} \right)$$

which must be small in both the vertical and horizontal directions, are derived by Müller. (The motions are additionally assumed Boussinesq, inviscid, non-diffusive, and the traditional approximation, $\underline{f} = f \hat{x}_3$, has been made.)

Ignoring the boundary conditions, Müller writes down locally planewave solutions (altered to match our Fourier Transform definitions):

$$\psi(x,t) = \begin{bmatrix} u_1 \\ u_2 \\ u_3 \\ b \end{bmatrix} = \{ a(\underline{k}) \Psi(\underline{k}) e^{-i(\underline{k} \cdot \underline{x} - \omega t)} \} + \text{c.c.} \quad (\text{B-2})$$

where:

$a(\underline{k})$ is the amplitude (complex)

c.c. denotes complex conjugate (also *)

$\underline{k} = (k_1, k_2, k_3)$ is the wavenumber

$$\omega = \underline{k} \cdot \underline{u} + \left(\frac{N^2 \alpha^2 + f^2 \beta^2}{\alpha^2 + \beta^2} \right)^{1/2}$$

= frequency of the wave.

(This equation defines the dispersion relation.)

As in Garrett and Munk (1975) we define;

$$\alpha = (k_1^2 + k_2^2)^{1/2}$$

$$\beta = |k_3|.$$

The local complex amplitude factors are given by:

$$\Psi = \begin{bmatrix} U_1 \\ U_2 \\ U_3 \\ B \end{bmatrix} = \left(\frac{\alpha^2}{\beta^2 (\alpha^2 + \beta^2)} \right)^{1/2} \begin{bmatrix} -\left(\frac{\beta^2}{\alpha^2}\right) (k_1 - i \frac{f}{\omega_0} k_2) \\ -\left(\frac{\beta^2}{\alpha^2}\right) (k_2 + \frac{if}{\omega_0} k_1) \\ k_3 \\ + i k_3 \frac{N^2}{\omega_0} \end{bmatrix} \quad (B-3)$$

Ψ is normalized so that:

$$U_1^2 + U_2^2 + U_3^2 + \frac{B^2}{N^2} = 2.$$

The linearity of the system of equations (1) allows us to write the full solution as a sum of planewaves:

$$\Psi = \left\{ \sum_{\text{ALL } \tilde{k}} a(\tilde{k}) \Psi(\tilde{k}) e^{-i(k_i x_i - \omega t)} \right\} + \text{c.c.} \quad (B-4)$$

As the number of waves becomes very large, the summations approximate to a three dimensional integral over all \tilde{k} :

310

$$\psi = \int d^3 \underline{k} \{ a(\underline{k}) \Psi(\underline{k}) e^{i(\underline{k} \cdot \underline{x} - \omega t)} \} + c.c. \quad (B-5)$$

The assumed Gaussianity of the wavefield is invoked at this point in describing two statistical relations between expected values of products of wave amplitudes at differing wavenumbers:

$$\langle a(\underline{k}) a(\underline{k}') \rangle = 0 \quad \underline{k} \neq \underline{k}' \quad (B-6)$$

where $\langle \rangle$ denotes ensemble averaging. This describes the randomness of phase of the waves, since if $\underline{k} = \underline{k}'$:

$$\langle a(\underline{k}) a(\underline{k}) \rangle = \langle |a|^2 e^{2i(\text{Phase})} \rangle = 0 \quad (B-7)$$

The energy density spectrum, describing the expected value of the wave amplitudes, is defined below:

$$\begin{aligned} \langle a^*(\underline{k}) a(\underline{k}') \rangle \\ = \frac{1}{2} \epsilon(\underline{k}) \delta(\underline{k}_1 - \underline{k}_1') \delta(\underline{k}_2 - \underline{k}_2') \delta(\underline{k}_3 - \underline{k}_3') \end{aligned} \quad (B-8)$$

where $\delta(\underline{x} - \underline{x}')$, the Dirac δ -function, is defined by:

$$\int_{x^-}^{x^+} f(u) \delta(u - x) du = f(x) \quad (B-9)$$

The conservation of action density, $\frac{aa^*}{\omega - \underline{k} \cdot \underline{u}}$ for individual wavetrains was established, for no rotation, by

30

Garrett (1968) and, in the case of rotation, by Müller (1976). Both derivations accounted for the presence of an Eulerian mean flow. The generalization to an ensemble of wavetrains, discussed in 5.2, results in the radiation balance equation (RBE), a transport-type equation for the action density spectrum, $n(\underline{k}, \underline{x}) = \epsilon / (\omega - \underline{k} \cdot \underline{u})$. The RBE and its associated boundary conditions are discussed in Müller and Olbers (1975). It conceptually closes the problem and thus gives the action density spectrum from which the physical properties of the wavefield may be calculated.

Using (9) the expected values of the internal wave spectra may be derived in terms of integrals over an energy spectrum. Letting ψ_j, Ψ_j , denote the j^{th} component of ψ, Ψ respectively, we have, using the definitions in Table 2-1 ($\hat{}$ denotes Fourier Transform):

$$\begin{aligned} \Gamma_{jk} &\equiv \hat{\psi}_j^* \hat{\psi}_k = C_{jk} + i Q_{jk} \\ &= \int dt e^{i\omega t} \psi_j \int dt' e^{-i\omega t'} \psi_k \quad (\text{B-10}) \\ &= \int dt \left[\int dt' e^{-i\omega(t'-t)} \psi_j \psi_k \right] \end{aligned}$$

(Note that ψ is a real quantity.)

We substitute ensemble averaging $\langle \rangle$ for the time average $\int dt$, and use eq. 5:

$$\begin{aligned}
C_{jk} + iQ_{jk} &= \int_{-\infty}^{\infty} d\tau e^{-i\omega''\tau} \left\langle \psi_j(t) \psi_k(t+\tau) \right\rangle \\
&= \int d\tau e^{-i\omega''\tau} \int d^3\tilde{k}' \Psi_j^* \Psi_k \left\langle a^*(\tilde{k}) a(\tilde{k}') \right\rangle \\
&\quad \cdot e^{-i[(k_1' - k_1)x_1 - (\omega' - \omega)t]} \cdot e^{ia'\tau} \\
&\quad + \text{c.c.} \tag{B-11}
\end{aligned}$$

The terms involving $\left\langle a(\tilde{k}) a(\tilde{k}') \right\rangle$, $a^*(\tilde{k}) a^*(\tilde{k}')$ are zero by eq. (6). We substitute for $\left\langle a^*(\tilde{k}) a(\tilde{k}') \right\rangle$ using 8 and 9:

$$\begin{aligned}
\Gamma_{jk}(\omega'') &= C_{jk}(\omega'') + i Q_{jk}(\omega'') \\
&= \frac{1}{2} \int_{-\infty}^{\infty} d\tau e^{-i\omega''\tau} \int d^3\tilde{k} \epsilon(\tilde{k}) [\Psi_j^*(\tilde{k}) \Psi_k(\tilde{k}) e^{i\omega\tau} + \text{c.c.}] \\
&= \frac{1}{2} \int_{-\infty}^{\infty} d\tau e^{-i\omega''\tau} \int_{-\infty}^{\infty} dk_1 \int_{-\infty}^{\infty} dk_2 \sum_{s=\pm} \int_f^N d\omega \frac{\epsilon(k_1, k_2, k_3(\omega))}{\left| \frac{\partial \omega}{\partial k_3} \right|} \left[\right] \\
&= \frac{1}{2} \int dk_1 \int dk_2 \sum_{s=\pm} \frac{\epsilon(k_1, k_2, k_3(\omega''))}{\left| \frac{\partial \omega}{\partial k_3} \right|} \Psi_j^* \Psi_k \tag{B-12}
\end{aligned}$$

The integration region has been mapped from $\tilde{k} = (k_1, k_2, k_3)$ to (k_1, k_2, ω, s) using the dispersion relation from B-2. The index s indicates $k_3 \gtrless 0$ for upward and downward (in phase) propagating waves. We have used the Hermitian symmetry of Ψ with respect to ω , $(\Psi(k_1, k_2, -\omega, s) = \Psi^*(k_1, k_2, \omega, s))$, and then used the Fourier integral theorem.

3/3

Re-defining the energy density spectrum:

$$\epsilon^s(k_1, k_2, \omega) = \frac{\xi(k_1, k_2, k_3(\omega))}{\left| \frac{\partial \omega}{\partial k_3} \right|_{s = \frac{k_3}{|k_3|}}} \quad (B-13)$$

we obtain:

$$C_{jk}(\omega) + iQ_{jk}(\omega) = \frac{1}{2} \sum_{s=\pm} \int dk_1 \int dk_2 (\Psi_j^* \Psi_k) \epsilon^s. \quad (B-14)$$

The integration region may also be put into cylindrical coordinates:

$$k_1 = \alpha \cos \phi$$

$$k_2 = \alpha \sin \phi$$

$$C_{jk} + iQ_{jk} = \frac{1}{2} \sum_s \int d\phi \int d\alpha (\Psi_j^* \Psi_k) \alpha \epsilon^s(\alpha \cos \phi, \alpha \sin \phi, \omega) \quad (B-15)$$

Using the dispersion relation from eq. 2, several expressions for cross-spectra may be found; for example, with $j = 1$, $k = 2$, and using

$$\frac{k_3 k_3}{k_i k_i} = \frac{N^2 - \omega_o^2}{N^2 - f^2} \quad \text{where } \omega_o = \omega - \alpha(\bar{u} \cos \phi + \bar{v} \sin \phi)$$

$$\begin{aligned}
c_{u_1 u_2} &= \int d\alpha \int d\phi \left(1 + \frac{f^2}{\omega_o^2}\right) \left(\frac{N^2 - \omega_o^2}{N^2 - f^2}\right) \xi(\alpha, \phi, \omega) \\
&\approx \left(1 - \frac{f^2}{\omega^2}\right) \left(\frac{N^2 - \omega^2}{N^2 - f^2}\right) \int_0^\infty d\alpha \alpha \xi(\alpha, \omega) \int_0^{2\pi} d\phi \cos \phi \sin \phi \\
&= 0 \text{ for a horizontally isotropic spectrum; if} \\
&\quad \text{Doppler shift is small enough so } \omega \approx \omega_o.
\end{aligned}
\tag{B-16}$$

Effect of vertically standing modes.

We now consider the wavefield to be composed of vertically standing modes, with no net vertical energy propagation and satisfying a rigid lid boundary condition at $z = 0$. The previously independent up and downgoing waves become phase-locked. Formally, eq. B-8 becomes:

$$\begin{aligned}
&\langle a^*(\tilde{k}) a(\tilde{k}') \rangle \\
&= \frac{1}{2} \epsilon(\tilde{k}) \delta(k_1 - k_1') \delta(k_2 - k_2') [\delta(k_3 - k_3') + \delta(k_3 + k_3')]
\end{aligned}
\tag{B-17}$$

$\epsilon \neq 0$ for $k_3 > 0$ only.

To satisfy both top and bottom boundary conditions, there ought to be an extra delta-function $\delta(k_3 - \beta(\eta, z))$, representing the fact that k_3 can only take on discrete values, $\beta(\eta, z)$, where η is the mode number. This will be smeared

315

out in an "equivalent continuum" procedure akin to that of GM 72. The vertical phase-locking results in some extra terms in eqs. 11-14, since each upgoing wave is accompanied by a downgoing one with a fixed amplitude and phase relationship. Carrying the algebra through, eq. 14 becomes:

$$\begin{aligned} \Gamma_{jk}(\omega) &= C_{jk}(\omega) + iQ_{jk}(\omega) \\ &= \int dk_1 \int dk_2 (\Phi_j^* \Phi_k) \epsilon(k_1, k_2, \omega) \end{aligned} \quad (B-18)$$

where:

$$\Phi_j = \Psi_j(k_1, k_2, k_3) e^{ik_3 z} + \Psi_j(k_1, k_2, -k_3) e^{-ik_3 z} \quad (B-19)$$

Effectively, the ray amplitude factors, Ψ , have been altered to modal amplitude factors, Φ . Explicitly:

$$\Phi = \left(\frac{\alpha^2}{\beta^2 (\alpha^2 + \beta^2)} \right)^{1/2} \begin{bmatrix} -\frac{\beta^2}{\alpha^2} (2 \cos \beta z) (k_1 - i \frac{f}{\omega_0} k_2) \\ -\frac{\beta^2}{\alpha^2} (2 \cos \beta z) (k_2 + i \frac{f}{\omega_0} k_1) \\ i \beta^2 \sin \beta z \\ -\beta \frac{N^2}{\omega_0} 2 \sin \beta z \end{bmatrix}$$

(B-20)

The main changes are, as expected:

- (1) the absence of vertical phase propagation,
- (2) the 90° phase shift in u_3 .

It seems possible to extend this model to allow rays and modes simultaneously. Probably there is some coherence between the ray and modal part of the field, and even a time-variable relation between up and downgoing rays, due to vertical reflection from (slowly) time-varying microstructure. The possibilities (and free parameters involved) are many; however, the above model demonstrates the necessary points, and will not be carried further.

Appendix C

THE RELATIONSHIP BETWEEN ACTION, MOMENTUM,
AND BUOYANCY FLUXES

Non-rotating:

The equivalence of Reynolds stress and "momentum flux" was investigated by Bretherton (1969), in the case of no Coriolis force. He found that a horizontal momentum equal to the horizontal wavenumber times the action of the wave packet can be associated with the wave packet. The key word is "associated," an internal wave does not carry momentum with it, it merely exerts a stress which transfers momentum in the mean. However, the transfer is such that if the wave packet is totally dissipated, the integrated (space and time) stress divergence is equal to the momentum associated with the packet.

Muller (1974) has discussed the analog of this for a spectrum of internal waves. For waves propagating in the absence of Coriolis forces, he demonstrated that:

1) The effect of the wavefield on the mean flow may be written as the divergence of a stress tensor in the Eulerian mean momentum equation

$$\left(\frac{\partial}{\partial t} + \bar{u}_j \frac{\partial}{\partial x_j}\right) \bar{u}_i + \dots = - \frac{\partial}{\partial x_j} (\overline{u_i' u_j'} + \bar{p}_w \delta_{ij}) \quad (C-1)$$

where ... indicates the usual terms omitted for clarity

u_i' is the i^{th} component of the internal wave velocity,

\bar{p}_w is the mean wave-induced pressure perturbation.

2) The wave stresses may be simply written:

$$\overline{u_i' u_j'} = \int d^3 \underline{k} \, n \begin{bmatrix} v_1 k_1 & v_2 k_1 & v_3 k_1 \\ v_1 k_2 & v_2 k_2 & v_3 k_2 \\ v_1 k_3 \frac{\alpha^2}{\beta^2} & v_2 k_3 \frac{\alpha^2}{\beta^2} & v_3 k_3 \frac{\alpha^2}{\beta^2} \end{bmatrix} \quad (C-2)$$

Since the vertically acting stresses are balanced by small mean vertical displacements (Bretherton, 1969), the interpretation is as though waves traveling at velocity $\underline{v} = (v_1, v_2, v_3)$ were transporting a horizontal momentum density equal to $(k_1, k_2, 0)$ times their action density.

Rotating:

Jones (1967) has investigated propagation and critical level absorption for inertio-gravity waves in a vertical shear flow. He found that, except near critical levels, where $\omega - \underline{k} \cdot \underline{u} = \pm f$, the quantities

$$\overline{u_1' u_3'} - f \overline{\xi_2 u_3'} \quad (C-3)$$

$$\overline{u_2' u_3'} + f \overline{\xi_1 u_3'}$$

were constant with height. ξ_1, ξ_2 are the x_1, x_2 displacements of a material particle from its semi-Lagrangian mean position, i.e.,

$$\begin{aligned}\frac{D\xi_\alpha}{Dt} &= \left(\frac{\partial}{\partial t} + \bar{\mathbf{u}} \cdot \nabla\right) \xi_\alpha = u_\alpha' \\ \bar{\xi}_\alpha &= 0\end{aligned}\tag{C-4}$$

Jones identified the conserved quantities as being proportional to the vertical flux of angular momentum, which is also conserved. He also noted that, as $(\omega - \mathbf{k} \cdot \bar{\mathbf{u}})^2 \gg f^2$ the conserved quantities reduced to the vertical fluxes of horizontal linear momentum (Eliassen and Palm, 1961).

Since the study was on an f-plane, the orientation of the x-axis is arbitrary and we may rotate the coordinate system so that the horizontal wavenumber coincides with the x-axis. The y-gradients are now zero, and so:

$$\frac{Du_2'}{Dt} = \frac{D^2\xi_2}{Dt} = -fu_1' \tag{C-5}$$

$$\xi = \frac{f}{\omega_0^2} u_1' \tag{C-6}$$

Then a relation exists between what might be called the "effective" vertical flux of horizontal momentum (the conserved quantity) and the actual momentum flux, which is not conserved:

$$\overline{(u_1' u_3')}^E = \overline{u_1' u_3'} - f \xi_2 u_3' = \overline{u_1' u_3'} \left(1 - \frac{f^2}{\omega_0^2}\right) \tag{C-7}$$

This relation is derived, without using the WKB approximation in the vertical, in Chapter 4.2.

Müller (1976) has shown that, for the WKB approximation to be consistent for internal waves propagating in a mean flow, the mean flow must be quasigeostrophic. Then the relevant dynamical equation for the mean flow is the vorticity equation. Müller writes, for the mean streamfunction, ϕ (defined by $\frac{\partial \phi}{\partial x_1} = \bar{u}_2$; $\frac{\partial \phi}{\partial x_2} = -\bar{u}_1$):

$$\left(\frac{\partial}{\partial t} + \bar{\mathbf{u}} \cdot \nabla \right) \left(\nabla_H^2 + \frac{\partial}{\partial x_3} \frac{f^2}{N^2} \frac{\partial}{\partial x_3} \right) \phi = -\epsilon_{\alpha\beta 3} \frac{\partial}{\partial x_\alpha} \frac{\partial}{\partial x_\beta} T_{\beta j} \quad (\text{C-8})$$

where:

$$\epsilon_{123} = +1$$

$$\epsilon_{213} = -1$$

$$\epsilon_{\alpha\beta 3} = 0 \text{ otherwise}$$

$$\alpha, \beta \quad \text{sum over } 1, 2$$

$$T_{\alpha j} = \overline{u_\alpha' u_j'} - \epsilon_{\alpha\beta 3} \frac{f}{N^2} b' u_\beta' \delta_{j3} .$$

Substituting from the dispersion relation and eq. B-3, and rewriting in terms of the group velocity, Müller finds:

$$-\epsilon_{\alpha\beta 3} \frac{\partial}{\partial x_\alpha} \frac{\partial}{\partial x_\beta} T_{\beta j} = -\epsilon_{\alpha\beta 3} \frac{\partial}{\partial x_\alpha} \frac{\partial}{\partial x_\beta} \left[\int d^3 k \, k_\beta v_j \eta \right] \quad (\text{C-9})$$

This simple form suggests that we define an effective wavestress, or momentum flux:

$$Q_{\alpha j} = \int d^3k \, k_{\alpha} \, n V_j \quad (C-10)$$

where:

$$\alpha = 1, 2$$

$$j = 1, 2, 3$$

(Note that $T_{12} \neq Q_{12}$, but that upon taking the gradients, the two tensors are equivalent.)

The mean flow equations are then redefined to be:

$$\frac{\partial \bar{u}_{\alpha}}{\partial t} + \dots = - \frac{\partial}{\partial x_j} (Q_{\alpha j}) \quad (C-11)$$

$$\frac{\partial \bar{u}_3}{\partial t} + \dots = 0 \quad (C-12)$$

$$\frac{\partial \bar{b}}{\partial t} + \bar{u} \cdot \nabla \bar{b} + N^2 \bar{u}_3 = 0 \quad (C-13)$$

Q combines the effects of the physical stresses and the buoyancy fluxes into one effective stress tensor. The $\overline{u_1 u_3}$ stress and the $\overline{b u_2}$ buoyancy flux are linked, through the Coriolis force. Since the mean flow is quasigeostrophic, the $\frac{\partial \bar{u}_1}{\partial x_3}$ shear component is also linked to a horizontal mean buoyancy gradient. The effects of the buoyancy flux (the ability

to tilt the mean density gradient) partially cancel the effects of the Reynolds stress, so that the net effect on the mean flow is expressed by the effective stress tensor, Q .

It is apparent then, that for the purposes of computing the effect on the (quasigeostrophic) mean flow, an effective momentum equal to the horizontal wavenumber times the wave action may be associated with the wave, as in the non-rotating case.

It is easily shown that the relation between the physical wave stresses and the effective wave stresses are:

$$\overline{u_1' u_3'} = \int d^3 k \, k_1 \eta V_3 \frac{\omega_o^2}{\omega_o^2 - f^2} \quad (C-14)$$

$$\overline{u_2' u_3'} = \int d^3 k \, k_2 \eta V_3 \frac{\omega_o^2}{\omega_o^2 - f^2} \quad (C-15)$$

$$\begin{aligned} \overline{u_1' u_2'} &= \overline{u_2' u_1'} \\ &= \int d^3 k \, k_2 \eta V_1 \frac{\omega_o^2 + f^2}{\omega_o^2 - f^2} \\ &= \int d^3 k \, k_1 \eta V_2 \frac{\omega_o^2 + f^2}{\omega_o^2 - f^2} . \end{aligned} \quad (C-16)$$

REFERENCES

- Bell, T.H. (1975). Topographically generated internal waves in the open ocean. *J. Geophys. Res.* 80, 320-327.
- Bell, T.H. (1976). The structure of internal wave spectra as determined from towed thermistor chain measurements. *J. Geophys. Res.* 81, 3709-3714.
- Berteaux, H.O. (1976). *Buoy Engineering*. John Wiley and Sons, New York, N.Y.
- Booker, J.R., and F.P. Bretherton (1967). The critical layer for internal gravity waves in a shear flow. *J. Fluid Mech.* 27, 513-539.
- Breeding, R.J. (1970). A non-linear investigation of critical levels for internal atmospheric gravity waves. *J. Fluid Mech.* 50, 545-563.
- Bretherton, F.P. (1966). The propagation of groups of internal gravity waves in a shear flow. *Quart. J. Roy. Met. Soc.* 92, 446-480.
- Bretherton, F.P. (1969a). On the mean motion induced by internal gravity waves. *J. Fluid Mech.* 36, 785-803.
- Bretherton, F.P. (1969b). Momentum transport by gravity waves. *Quart. J. Roy. Met. Soc.* 95, 213-243.
- Bretherton, F.P. (1969c). Waves and turbulence in stably stratified fluids. *Radio Science* 4, 1279-1287.
- Bretherton, F.P. (1970). The general linearized theory of wave propagation. *Lectures in Appl. Math.* 13.
- Bretherton, F.P. and C.J.R. Garrett (1968). Wavetrains in inhomogeneous moving media. *Proc. Roy. Soc. A*, 302, 529-554.
- Briscoe, M.G. (1975a). Preliminary results from the trimooored internal wave experiment. *J. Geophys. Res.* 80, 3872-3884.
- Briscoe, M.G. (1975b). Internal waves in the ocean. *Rev. Geophys. and Space Phys.* 13, 591-645.
- Briscoe, M.G. (1977). Gaussianity of internal waves. In Press, *J. Geophys. Res.* 82. (May, 1977).
- Bryden, Harry (1975) W.H.O.I. internal memo to J. Dean, J. McCulloch, and R. Payne entitled "Precision of low frequency estimates of current and temperature." Unpublished document.
- Cairns, J.L., and Williams, G.O. (1976). Internal wave observations from a midwater float, 2. *J. Geophys. Res.* 81, 1943-1950.

REFERENCES (Cont.)

- Cooper, B.E. Statistics for Experimentalists. Pergamon Press, New York, N.Y., (1969). 336 pp.
- Desaubies, Y.J.F. (1976). Analytical representation of internal wave spectra. J. Phys. Oceanogr. 6, 976-981.
- Eliassen, A. and Palm, E. (1961) On the transfer of energy in stationary mountain waves. Geofys. Publik. 22, 1-23.
- Fofonoff, N.P. (1969a). Spectral characteristics of internal waves in the ocean. Deep Sea Res. 16, 58-71.
- Fofonoff, N.P. (1969b). "Buoy system motions", in Handbook of Ocean and Underwater Engineering. McGraw-Hill, New York, N.Y.
- Frankignoul, C.J. (1970). The effect of weak shear and rotation on internal waves. Tellus 22, 194-203.
- Frankignoul, C.J. (1974). Observed anisotropy of spectral characteristics of internal waves induced by low-frequency currents. J. Phys. Oceanogr. 4, 625-634.
- Frankignoul, C.J. (1976). Observed interaction between oceanic internal waves and mesoscale eddies. Deep Sea Res. 23, 805-820.
- Frankignoul, C.J. and E.J. Strait (1972). Correspondence and vertical propagation of the inertial-internal wave energy in the deep sea. Memoires Societe Royale des Sciences de Liege 4, 151-161.
- Garrett, C.J.R. (1968). On the interaction between internal gravity waves and a shear flow. J. Fluid Mech. 34, 711-720.
- Garrett, C.J.R., and Munk, Walter (1972a). Space-time scales of internal waves. Geophys. Fluid Dyn. 2, 225-264.
- Garrett, C.J.R., and Walter Munk (1972b). Oceanic mixing by breaking internal waves. Deep Sea Res. 19, 823-832.
- Garrett, C.J.R., and Walter Munk (1975). Space-time scales of internal waves: a progress report. J. Geophys. Res. 80, 291-297.
- Gonella, J. (1972). A rotary-component method for analyzing meteorological and oceanographic vector time series. Deep Sea Res. 19, 833-846.
- Grimshaw, R. (1974). Internal waves in a slowly varying, dissipative medium. Geophys. Fluid Dyn. 6, 131-148.

References (Contd.)

- Grimshaw, R. (1975a). Internal gravity waves: critical layer absorption in a rotating fluid. *J. Fluid Mech.* 70, 287-304.
- Grimshaw, R. (1975b). Nonlinear internal gravity waves in a rotating fluid. *J. Fluid Mech.* 71, 497-512.
- Hasselmann, K. (1968). Weak interaction theory of ocean waves. *Basic Development in Fluid Dynamics.* 2, 117-182.
- Hazel, P. (1967). The effect of viscosity and heat conduction on internal gravity waves at a critical level. *J. Fluid Mech.* 30, 775-783.
- Hendry, R.M. (1975). The generation, energetics, and propagation of internal tides in the Western North Atlantic Ocean. Ph.D. Thesis, M.I.T.-W.H.O.I. Joint Program in Oceanography.
- Hines, C.O., and A. Reddy (1967). On the propagation of atmospheric gravity waves through shear. *J. Geophys. Res.* 72, 1015-1033.
- Howard, L.N. (1961). Note on a paper of John Miles. *J. Fluid Mech.* 10, 509-512.
- Iida, Lucio (1975). A study of the non-white Gaussianity of the trimooored internal wave experiment (IWEX) current data. W.H.O.I. Technical Report #75-67.
- Jenkins, G.M., and D.G. Watts (1969). Spectral analysis and its application. Holden-Day, San Francisco.
- Jones, Walter L. (1967). Propagation of internal gravity waves in fluids with shear flow and rotation. *J. Fluid Mech.* 30, 439-448.
- Jones, W.L. and D.D. Houghton (1971). The coupling of momentum between internal gravity waves and mean flow: A numerical study. *J. Atmos. Sciences* 28, 604-608.
- Joyce, T.M., and Y.J.F. Desaubies (1977). Discrimination between internal waves and temperature finestructure. *J. Phys. Oceanogr.* 7, 22-32.
- Leaman, K.D. (1976). Observations of vertical polarization and energy flux of near-inertial waves. *J. Phys. Oceanogr.* 6, 894-908.
- Lindzen, R.S. (1972). Wave-mean flow interactions in the upper atmosphere. *Boundary Layer Meteorology* 4, 327-343.
- Lyttkens, E. (1963). Standard errors of regression coefficients in the case of autocorrelated residuals. In "Time Series Analysis", S. I. A. M.

References (Contd.)

- Magaard, L. (1968). Ein Beitrag zur theorie der internen Wellen als Störungen geostrophischer Stromungen. Deutsche hydrographische Zeitschrift, 21, 241-278.
- Marion, J.B. (1970). Classical dynamics of particles and systems. Academic Press, N.Y. (2nd Ed.)
- Maslowe, S. (1973). Finite-amplitude Kelvin-Helmholtz billows. Boundary Layer Meteorology 5, 43-52.
- Mooers, C.N.K. (1975a). Several effects of a baroclinic current on the cross-stream propagation of inertial-internal waves. Geophys. Fluid Dyn. 6, 245-275.
- Mooers, C.N.K. (1975b). Several effects of baroclinic currents on the three-dimensional propagation of inertial-internal waves. Geophys. Fluid Dyn. 6, 277-284.
- Miles, J. (1961). On the stability of heterogeneous shear flows. J. Fluid Mech. 10, 496-508.
- MODE-I Dynamics Group (1975). Dynamics and the analysis of MODE-I. Report to the MODE-I Scientific Council, March, 1975.
- Murray, J. (1892). On the temperature of the salt- and fresh-water Lochs of the West of Scotland at different depths and seasons during the years 1887 and 1888. Proc. Roy. Soc. Edinburgh 18, 139-228.
- Müller, P. (1974). On the interaction between internal waves and larger scale motions in the ocean. Hamburger Geophysikalische Einzelschriften 23.
- Müller, P. (1976). On the diffusion of momentum and mass by internal gravity waves. J. Fluid Mech. 77, 789-823.
- Müller, P. (1977). Spectral features of the energy transfer between internal waves and a larger scale shear flow. In press.
- Müller, P., and D.J. Olbers (1975). On the dynamics of internal waves in the deep ocean. J. Geophys. Res. 80, 3848-3860.
- Müller, P., D.J. Olbers, and J. Willebrand (1977). Inverse analysis of IWEX. In press, Geophysical Institute, University of Hamburg.
- McCulloch, J.R. (1975). Vector averaging current meter speed calibration and recording technique. WHOI Technical Report, WHOI-75-44.
- McWilliams, J. (1972). Observations of kinetic energy correspondences in the internal wavefield. Deep Sea Res. 19, 793-811.

References (Contd.)

- Nuttall, A.H. (1971). Spectral estimation by means of overlapped Fast Fourier Transform processing of windowed data. Report 4169 of the Naval Underwater Systems Center, New London, Conn. 06320.
- Olbers, D.J. (1976). Non-linear energy transfer and the energy balance of the internal wavefield in the deep ocean. *J. Fluid Mech.* 74, 375-399.
- Olbers, D.J. (1974). On the energy balance of small-scale internal waves in the deep sea. *Hamburg. Geophys. Einzelschriften* 24.
- Perkins, H. (1976). Observed effect of an eddy on inertial oscillations. *Deep Sea Res.* 23, 1037-1042.
- Perrson, Jan (1974). Variability and covariability of modified spectral estimators. *I.E.E.E. Transactions on Acoustics, Speech and Signal Processing*, April, 1974.
- Phillips, O.M. (1966). The dynamics of the upper ocean. Cambridge University Press.
- Phillips, O.M. (1971). On spectra measured in an undulating layered medium. *J. Phys. Oceanogr.* 1, 1-6.
- Rhines, P. (1973). Observations of the energy-containing oceanic eddies, and theoretical models of waves and turbulence. *Boundary Layer Meteorology* 4, 345-360.
- Richman, J. (1976). Kinematics and energetics of the mesoscale mid-ocean circulation: MODE.. Unpublished Ph.D. Thesis, 205 pages.
- Ricker, W.R. (1973). Linear regressions in fishery research. *J. Fisheries Res. Board Can.* 30, 409-434.
- Sabinin, K.D. (1976). Certain features of the space spectrum of short-period internal gravity waves in the ocean. *Okeanologia* 16, 782-786.
- SCOR Working Group 21. An intercomparison of some current meters, III. *Unesco Technical Papers in Marine Science*, #23.
- Scorer, R.S. (1969). Billow mechanics. *Radio Science* 4, 1299-1308.
- Sanford, T.B. (1975). Observations of the vertical structure of internal waves. *J. Geophys. Res.* 80, 3861-3871.
- Smith, Ronald (1973). Evolution of inertial-frequency oscillations. *J. Fluid Mech.* 60, 383-389.
- Stewart, R.W. (1969). Turbulence and waves in a stratified atmosphere. *Radio Science* 4, 1269-1278.

References (Contd.)

- Taylor, G.I. (1921). Diffusion by continuous movements. Proc. London Math. Soc. 20, 196- .
- Thorpe, S.A. (1975). The excitation, dissipation and interaction of internal waves in the deep ocean. J. Geophys. Res. 80, 328-338.
- Uchupi, L. (1971). Bathymetric atlas of the Atlantic, Caribbean, and Gulf of Mexico. W.H.O.I. Ref. 71-72, unpublished manuscript.
- Whitham, G.B. (1965). A general approach to linear and non-linear dispersive waves using a Lagrangian. J. Fluid Mech. 22, 273-283.
- Wold, H. (1950). On least-square regression with autocorrelated variables and residuals. Bull. Inst. Int. Statist. 32, No. 2.
- Wunsch, C. (1975a). Geographical variability of the internal wavefield: a search for sources and sinks. J. Phys. Oceanogr. 6, 471-485.
- Wunsch, C. (1975b). Deep ocean internal waves: what do we really know? J. Geophys. Res. 80, 339-343.
- Wunsch, C., and J. Dahlen (1974). A moored temperature and pressure recorder. Deep Sea Research, 1974, 21, 145-154.

Biographical Note

The author was born on June 1, 1949 in Victoria, British Columbia, Canada. He grew up in Brantford, Ontario, Dartmouth, Nova Scotia and Victoria, B.C. He earned a B.Sc. in Honours Physics at the University of Victoria in June, 1971. He held a summer student fellowship at the Woods Hole Oceanographic Institution during the summer of 1971, before entering graduate school in physical oceanography that fall. He is married to the former Lorraine Ann Johnson and will be going to Australia to work this July.